Università Politecnica delle Marche
Scuola di Dottorato di Ricerca in Scienze dell'Ingegneria
Curriculum in Ingegneria Civile, Ambientale, Edile e Architettura

---

Methods and Measurement Systems in Photoelastic Analysis of Scintillating Crystals.
PWO and LYSO crystals

Ph.D. Dissertation of:

Pier Paolo Natali

Advisor:

Prof. Fabrizio Davì

Co-advisors:

Prof. Daniele Rinaldi

Prof. Karl Ziemons

Curriculum supervisor:

Prof. Stefano Lenci

XVII edition - new series

Università Politecnica delle Marche
Dipartimento di Ingegneria Civile, Ambientale, Edile e Architettura
Via Brecce Bianche — 60131 - Ancona, Italy

Abstract

A material with the capability to scintillate means that is able to convert the energy of a radiating particle, that interact within its volume, into light. This mechanism starts when there is an interaction between different kinds of radioactivity or energy interaction and the scintillating material. This interaction is able to excite the electrons enough to allow them to jump to a higher energy band. The scintillation process happens when these electrons turn back to their equilibrium state, producing a release of photons in the visible (or near visible) range. The incident energy to the scintillating crystal, as happens for all kinds of energy conversion, is higher than the energy belonged to the group of photons emitted. This energy conversion produces as output usually monochromatic light. The quality of this light emitted, in terms of wavelength, stability, polarization and coherence, is a key point. This aspect can be explained considering that these materials are involved in fields like the nuclear and high energy physics (for instance, CERN-Geneva or PANDA project), biomedical imaging (PET-positron emission tomography for cancer diagnosis), geologic research, security and laser technology. Inside all that different kinds of fields, the performance behaviour of the instruments is ruled by the scintillators. Therefore, an improvement of scintillating materials involves a direct instrumentation efficiency improvement. Moreover, the quality of the material itself and the production efficiency, determine the cost and the feasibility of the above-mentioned activities. Considering all these aspects, a depth knowledge of the material is crucial to predict the behavior of the crystals, from the mechanical to the optical aspects. Therefore, results useful the creation of tools, aimed to improve the efficiency and efficacy of the larger and larger production of these crystalline scintillators from the production point of view, and aimed to check their quality from the utilizers point of view. To cover these aspects, in this thesis is presented a work voted to the development of non-invasive, therefore non-destructive, methods and systems useful to assess the crystal quality. The main purpose to investigate the crystals is the determination of the residual stress state, whose presence is a signature of the whole quality degradation due to different origins. The development methods are based on optical crystallography and then on the Photoelasticity. These allow, using optical measurement techniques, to develop non-destructive tools that allow to a very detailed analysis providing sensitivity and spatial resolution. In order to provide more flexibility on the crystals characterization, the measurement techniques have been developed along different directions with respect to the crystal optic axes. To enrich the set of

developed methods, a new faster technique named Sphenoscopy was studied, which provides reliable inspection of the crystal in a simplified way whatever orientation of the crystallographic and optic axes. The developed tools are based, using different techniques, on the acquisition of fringe images. Therefore, hand in hand, the systems have been provided of dedicated algorithms to process and analyze accurately the fringe patterns, developing techniques voted to the measurement error reduction. A new technique was then developed, using observations in collimated light in direction normal to the optic axis, with the different purpose of analysing the sample from a dimensional point of view, with the aim of determining any non-coplanarity between the surfaces, which is an aspect that may disturb the previous measurement techniques. This technique has been treated by comparing it with the mathematical model presented and used for the Conoscopy, with the direct geometrical measurements of the surfaces and with the theories of the optical crystallography. Concluding, it is important to remark that the information carried out by these methods are useful for both research bodies and industries, crystal producers and users, since they are crucial feedbacks to better understand the material behavior, develop predictive math models and set properly the production parameters.

Abstract

Un materiale ha la capacità di scintillare quando è capace di convertire l'energia delle particelle radianti, che interagiscono con il volume in esame, in luce. Questo meccanismo ha inizio quando c'è un'interazione tra differenti tipi di radioattività o energie e il materiale scintillatore. Questa interazione è capace di eccitare gli elettroni abbastanza da permettergli di passare ad una banda di energia più alta. Il processo di scintillazione avviene quando questi elettroni tornano al loro stato di equilibrio, producendo un rilascio di fotoni nel campo visibile (o vicino). L'energia incidente al cristallo scintillatore, come accade in ogni tipo di conversione di energia, è più alta dell'energia appartenuta al gruppo di elettroni emessi. Questa conversione di energia produce, come uscita, usualmente luce monocromatica. La qualità di questa luce emessa, in termini di lunghezza d'onda, stabilità, polarizzazione e coerenza è un punto chiave. Questo aspetto può essere spiegato considerando che questi materiali sono utilizzati in campi come la fisica nucleare e delle alte energie (per esempio al CERN di Ginevra o nel progetto PANDA), in campo biomedicale (PET per la diagnosi del cancro), ricerche geologiche, sicurezza e tecnologia nella produzione dei laser. All'interno di questi campi, l'andamento delle performance degli strumenti è legato agli scintillatori. Quindi, un miglioramento nei materiali scintillatori si traduce in un diretto miglioramento nell'efficienza della strumentazione. Inoltre, la qualità del materiale stesso assieme all'efficienza di produzione, determinano il costo e l'utilizzo delle attività appena menzionate. Considerando tutti questi aspetti, una conoscenza profonda del materiale risulta cruciale al fine di prevedere il comportamento dei cristalli, dal punto di vista meccanico e ottico. Perciò risulta utile la creazione di strumenti con il fine di migliorare, dal punto di vista dei produttori, l'efficienza e l'efficacia della grande produzione di questi cristalli e con il fine di controllare la qualità, dal punto di vista degli utilizzatori dei cristalli. Per coprire questi aspetti, in questa tesi è presentato un lavoro finalizzato allo sviluppo di tecniche non invasive, e quindi non distruttive, utili per controllare la qualità del cristallo. Il principale scopo per caratterizzare il cristallo, è la determinazione del suo stato tensionale, la cui presenza è sinonimo di degradazione della qualità, dovuta a differenti cause. I metodi sviluppati sono basati sulla cristallografia ottica, e quindi sulla Fotoelasticità. Questi permettono, osando tecniche di misura ottiche, di sviluppare strumenti non distruttivi, che consentono di ottenere una analisi molto dettagliata e sensibile del materiale. Al fine di avere flessibilità nella caratterizzazione di questo tipo di materiali, le tecniche di misura sono state sviluppate al fine di poter operare lungo differenti direzioni rispetto a quella dell'asse ottico del cristallo. Al fine di arricchire l'assieme di tecniche di

misura sviluppate, è stata studiata una nuova tecnica di misura più veloce, chiamata Sfenoscopia, la quale fornisce una tecnica di ispezione semplice e affidabile, indipendente dalla direzione di osservazione rispetto all'asse ottico del cristallo. I sistemi sviluppati, sono basati sull'acquisizione di frange da parte dell'utente. Per questo, di pari passo con lo sviluppo della tecnica, sono state sviluppati algoritmi di processamento dei differenti pattern di frangia, con il fine di ridurne il più possibile l'errore di misura. È stata quindi sviluppata una nuova tecnica, utilizzando le osservazioni in luce collimata in direzione normale all'asse ottico, con il fine differente di analizzare il campione da un punto di vista dimensionale, allo scopo di determinare qualsiasi non-complanarità tra le superfici, il quale è un aspetto che disturba le precedenti tecniche di misurazione. Questa tecnica è stata trattata confrontandola con il modello matematico presentato e utilizzato per la Conoscopia, con le misurazioni geometriche dirette delle superfici e con la teoria inerente alla cristallografia ottica. In conclusione, è importante sottolineare che le informazioni ottenibili da questi metodi sviluppati, sono utili sia per la ricerca che l'industria, per i produttori e gli utilizzatori di cristalli, poiché forniscono gli strumenti per capire meglio il comportamento del materiale, sviluppare modelli matematici predittivi e facilitare la scelta dei parametri di produzione

Thesis guidelines

The problem

The scintillating Crystals represent the sensitive measurement element in fields like Biomedical imaging (PET-positron emission tomography for cancer diagnosis), the nuclear and high energy physics (for instance, CERN-Geneva or PANDA project), geologic research, security and laser technology. Cause of that, the performance behaviour of the instruments is ruled by the scintillators. An improvement of that materials leads directly an efficiency enhancement of the instrumentation. Moreover, the cost and the feasibility of the activities where the Scintillating Crystals have a role, are determined by the quality of the material itself and the production efficiency. To cover all these aspects, in order to predict the behaviour of the crystal, a depth knowledge of the material is crucial. This must be achieved through a study from the mechanical to the optical point of view. Connected to the material knowledge, results useful, from the production point of view, the creation of tools aimed to improve the efficiency and efficacy of the larger and larger production of these crystalline scintillators, and aimed to check their quality from the utilizers point of view.

Thesis originality

The thesis is based on the crystal optics, and in particular on Photoelasticity. The previous works starts from the diffused light polariscope to implement new systems named laser Conoscopy and laser Sphenoscopy in direction parallel to the optic axis. These new techniques were studied deepen in order to introduce, as innovative contribution, an optimization from the measurement system to the data analysis point of view. Furthermore, was implemented, about these techniques, a new field of application, by creating the possibility of applying the Conoscopic and the Sphenoscopic analysis systems in direction orthogonal to the optic axis. The limitations of these techniques were therefore won, allowing analyses no longer confined to a specific crystallographic direction. To do this, specific mathematical models have been created, together with the new measurement and data analysis systems. Using these new developments as measurement techniques, was studied a new measurement system, that use collimated light in direction orthogonal to the optic axis, to investigate the non-coplanarity degree between the crystal surfaces. Going to the applications point of view, these new techniques was used to test and characterize a PWO from a pre-series, in order

to implement what was discovered in the analysis of crystal quality. Furthermore, was evaluated piezo optic parameters and photoelastic constant in Tetragonal PWO, going to a deepen knowledge of this type of crystal. Moreover, was performed comparative analysis between Photoelastic measurements and timing properties measurements on LYSO samples, on order to find a correlation between these two aspects.

Publications

Part of the work described is concentrated in these publications:

- P. P. Natali, L. Montalto, F. Davi, N. Paone, D. Rinaldi, and L. Scalise, "Optimization of the photoelastic fringe pattern processing for the stress evaluation in scintillating anisotropic media," in I2MTC 2017 - 2017 IEEE International Instrumentation and Measurement Technology Conference, Proceedings, 2017 [1].
- P. P. Natali, L. Montalto, D. Rinaldi, F. Davi, N. Paone, and L. Scalise, "Noninvasive Inspection of Anisotropic Crystals: Innovative Photoelasticity-Based Methods," IEEE Trans. Nucl. Sci., vol. 65, no. 8, 2018 [2].
- P. P. Natali, L. Montalto, F. Davì, P. Mengucci, A. Ciriaco, N. Paone, D. Rinaldi, "Theoretical and experimental evaluation of piezo-optic parameters and photoelastic constant in tetragonal PWO," Appl. Opt., vol. 57, no. 4, p. 730, 2018 [3].
- L. Montalto, P. P. Natali, F. Daví, P. Mengucci., N. Paone, and D. Rinaldi, "Characterization of a defective P_bWO_4 crystal cut along the a-c crystallographic plane: structural assessment and a novel photoelastic stress analysis," J. Instrum., vol. 12, no. 12, p. P12035, 2017 [4].

Thesis Layout

Regarding the state of the art described in this thesis, in the first chapter are introduced the main field of applications of scintillating crystals. In particular are described the applications in high energy physics, in biomedical field and industrial applications. Then are outlined the main production procedure of crystals. In the second chapter is described the crystal optics necessary for this work, from the light and polarization concept to the optical indicatrix and the Bertin surfaces. Then in the chapter three is outlined the Photoelasticity concept next to the piezo optic effect and is introduced the diffused light polariscope. From the fourth chapter are introduced the innovative contribution on the Photoelastic techniques. In this chapter are described the laser techniques

named Conoscopy and Sphenoscopy, optimized in direction parallel to the optic axis, and developed to be used in direction orthogonal to the optic axis. Then is described a new technique that use collimated laser light in direction normal to the optic axis. The Chapter five is the applications chapter, where is described the evaluation performed of piezo-optic parameters and photoelastic constant on Tetragonal PWO, the results of testing and characterization of PWO sample from a pre-series, and a comparative analysis between Photoelastic measurements and timing properties in LYSO samples.

Contents

List of Figures

Chapter 1

1 Introduction

A material with the capability to scintillate means that is able to convert the energy of a radiating particle, that interact within its volume, into light. This mechanism starts when there is an interaction between different kinds of radioactivity or energy interaction and the scintillating material. This interaction is able to excite the electrons enough to allow them to jump to a higher energy band. The scintillation process happens when these electrons turn back to their equilibrium state, producing a release of photons in the visible (or near visible) range. In order to introduce the scintillation mechanism, it is governed by the same phenomenon of phosphorescence and luminescence, the differences are due to the internal mechanisms involved and by their decreasing time scales [5]. Some of the main features used to describe the scintillation process are the Light Yield (LY), rise and decay time (τ), wavelength and energy resolution (ER) [5]. Briefly describing these aspects: LY is the number of photons (light intensity) produced with respect to the energy interaction, rise time and decay time describe the duration of the scintillation phenomenon (the rise of intensity and the decay respectively), the energy resolution describe how narrow is the peak in the emission energy spectra (narrower the peak, better the capability to discriminate the incoming energy of the radiation.) [5]. The incident energy to the scintillating crystal, as happens for all kinds of energy conversion, is higher than the energy belonged to the group of photons emitted. This energy conversion produces as output usually monochromatic light. The quality of this light emitted has great quality in terms of wavelength stability, coherence and polarization. Considering these peculiarities, it is obvious that the scintillating crystals find place in several applications as primary transducers of sophisticated and complex systems. In fact, they are involved in fields like the nuclear and high energy physics (for instance, CERN-Geneva or PANDA project), biomedical imaging (PET-positron emission tomography for cancer diagnosis), geologic research, security and laser technology. Inside all of that different fields, the performance behaviour of the instruments is ruled by the scintillators; therefore, the feasibility of the above-mentioned activities is strictly related to the quality of the material itself and the production efficiency, which determine the costs of production and use. In summary, the applications, by their growing demand in space and time resolution, light production, sensitivity and general improvement of the quality, prompted the increased performance of the Scintillators. Therefore, a deepen characterization voted to a better knowledge of the material is crucial, to predict the behaviour of the crystals covering from the

mechanical to the optical point of view. Considering that the production request of the scintillator is larger and larger and that the production process is quite complex, delicate and time consuming, industry needs tools to improve the efficiency and efficacy in order to improve productivity while keeping production costs under control [6]. Also from the crystal utilizer point of view, are necessary tools to assess the crystal quality before the utilization, in order to check the performances required. Returning to the point of high production costs, the methods and systems necessary to assess the crystal quality must be non-invasive. The following work present a series of non-destructive methods aims to analyse the crystal quality through the determination of the residual stress state that can be the signature of the whole quality degradation, due to different origins. The information carried out by these methods are useful for both research bodies and industries, crystal producers and users, since they are crucial feedbacks to better understand the material behaviour, developing predictive math models, and to set properly the production parameters. The conceptual process will be presented starting from the state of the art which is the base of the developed methods. Then the innovative contribution will be treated, and eventually direct applications will be presented of what has been achieved. Hereafter, some paragraphs will outline briefly the main fields in which scintillating crystals are involved, their principal production techniques and criticalities.

1.1 Main fields of application

There are many application areas about scintillator crystals, from physics to high energies and biomedical. In fact, the scintillators are more used where there is no need of destructive analysis.

1.1.1 Spinthariscope

The first scintillation detectors were invented at the beginning of 1900 from sir William Crooks that created the “Spinthariscope” [7]. It consists of a metal cylinder with at opposite ends an eyepiece lens and a fluorescent screen of zinc sulphide on the other. In front of the latter was placed the radioactive source to scan: alpha particles were observed in this way which, by interacting with the screen, produced scintillations, observed in a microscope. The device was placed in a dark room, and for its simplicity of construction was soon spread to all campuses.

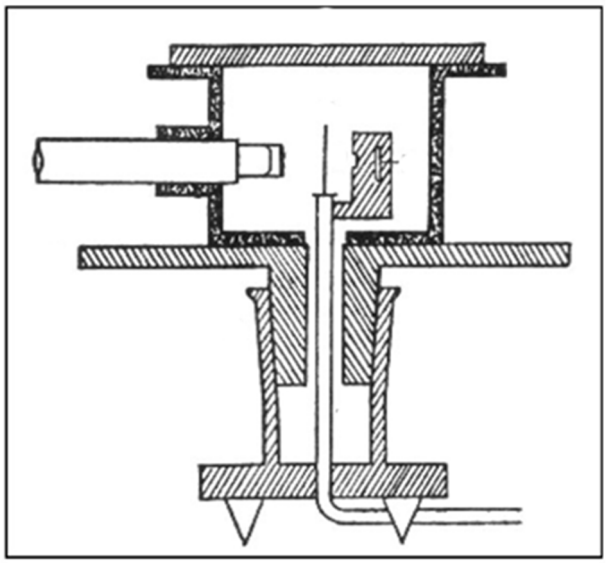

Fig. 1. 1: Spintariscope scheme.

It was also used by Rutherford in his experiment that led him to develop the first theory of atomic structure.

1.1.2 Application in high energy physics

The scintillators are used in the detection system of particle accelerators, that allow to register the results from the collision of particle swarms accelerated by electric fields [8]–[10]. They can measure, in addition to the particle passage:

- The energy;
- The position;
- The momentum;
- The particles number;
- The instant traversal;
- The type of particle.

1.1.2.1 Calorimeters

The calorimeters are detectors of the particle energy running through them. There are two types of division: one transversal, for the identification of the direction of the particle swarm and one longitudinal for the identification of the particle type based on the shape of the swarm itself that causes. They are sensitive to both the neutral and charged particles and can reveal even muons (particles that leave an ionisation signal) or neutrinos (detectable only indirectly through an energy

balance). The mechanism of how these detectors consists in the formation of Hadronic or electromagnetic cascades in order to convert the energy of the particle. The electromagnetic cascade forms when high-energy charged particles affect thick absorbers initiating a series of creation of electron-positron pairs from photon and electromagnetic radiation for the phenomenon of Bremsstrahlung (emitted by charged particles after impact). This cascade continues until is reached a certain level of energy, called critical, above which become predominant energy loss by radiation than for collision. The Hadronic cascade instead concerns precisely the impact loads or neutral hadrons with the absorber, whose nuclei partially generate electromagnetic cascade and fragment in heavy secondary particles.

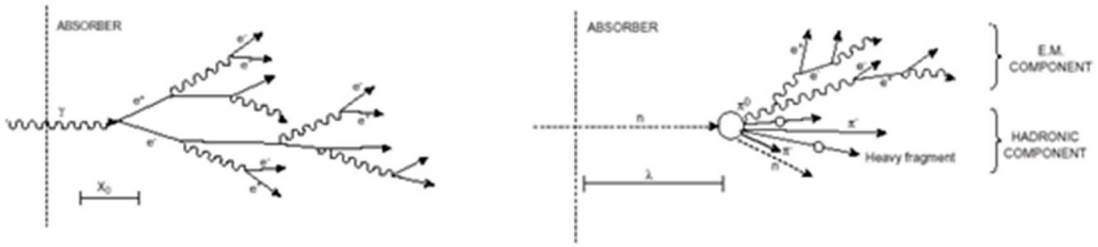

Fig. 1. 2: Scheme of electromagnetic hadronic falls.

There are two configurations of calorimeters:

- Homogeneous calorimeter: particle absorption and the production of the signal are obtained by a single material (scintillator); they have good energy resolution, but poor;
- heterogeneous or sampling calorimeters: consist of several layers of materials with different functions, in particular the heavy materials (such as uranium); they act as shock absorbers while the scintillators are the active part; do not have a good energy resolution because part of the radiation is lost in the transition from one layer to another, but a great space.

1.1.2.2 DaMa (Dark Matters)

DaMa is a project dedicated to the study of dark matter and other rare [11] and uses crystals scintillators that have the characteristic of being very radiopure materials: they are, therefore, been made by removing most traces of radioactive substances in order to optimize the sensitivity. Sodium iodide crystals are particularly sensitive to the particles that make up the dark matter, and when they are crossed by these produce scintillation light. Detection technique of checkers is based on marking, or annual modulation identification, and requires that they be satisfied at the same time a

large number of specific requirements. Since the earth rotates around the Sun, and the Sun revolves around the Galactic core, the first will be exposed to a wind of dark matter particles whose intensity varies cyclically throughout the year. This change should only exist in low energy, where the dark matter particles can produce a signal and only in events where a single crystal spark. DAMA/NaI, over a period of seven annual cycles, showed a periodicity that meets all the requirements of the marking.

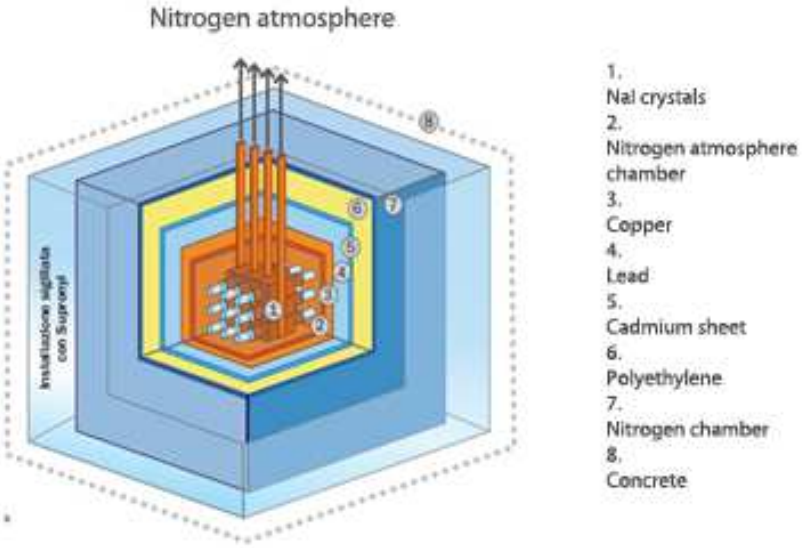

Fig. 1. 3: Experimental set up (DAMA) for the study of dark matter.

1.1.2.3 AGATA (Advanced GAmma Tracking Array)

Agata is a next-generation gamma ray detector [12]: is a research and development project to build a spectrometer 4π, that can capture and report the particles produced in nuclear reactions, in any direction being issued. Its goal is to study the structure of atomic nuclei analysing precisely gamma rays they emit when they decay. The detector has a spherical structure, consisting of 12 regular pentagons and hexagons, containing 8 Germanium crystals 180 centimetres in diameter and 10 long) encapsulated in a very thin aluminium container and placed in to preserve the modularity and reduce inter-modular space from each other. The crystals themselves are divided electronically in 36 segments. The inner radius of the matrix is 17 centimetres, and the total solid angle covered by the crystal is the 80% of the maximum. The efficiency of photopeak is so high to reach the 50% for a single gamma ray by 1 MeV. The peculiar characteristic of Agate is the high sensitivity, which is unprecedented in the history of the detectors, and consequent high precision in determining the

trajectory of particles. In addition to numerous applications in physics and Astrophysics, agate is also useful in medical imaging and security.

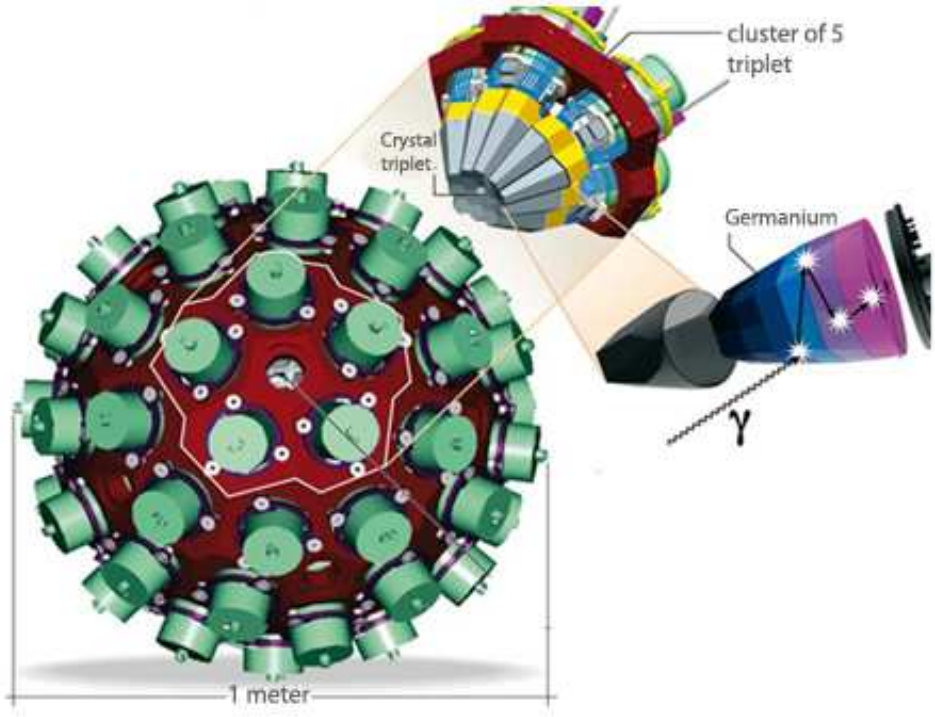

Fig. 1. 4: AGATA detector scheme.

1.1.2.4 GLAST (Gamma-ray Large Area Space Telescope)

The Fermi GLAST telescope is designed to detect electromagnetic radiation in the range of energies between the 8 keV and 300 GeV, or gamma rays [13], and includes two scientific instruments:

- LAT (Large Area Telescope) sensitivity Ile to gamma radiation between 20 MeV and 300 GeV;
- GBM (Gamma-ray Burst Monitor) for the study of phenomena that occur at relatively lower energies, among 40 keV and 8 MeV.

In particular the LAT consists of a modular system of 16 towers (dimensions 37x37 cm^2) arranged in a 4 x 4 matrix, supported by a lightweight yet sturdy, grid structure that provides the necessary stiffness. Each tower consists of a tracker and Silicon converter, with alternating with thin slabs of tungsten, and by an electromagnetic calorimeter with Caesium iodide crystals CsI, organized into 12 floors from 8 crystals each. The telescope's operation is as follows: gamma rays incidents are converted to electron-positron pairs in tungsten and plotted by silicon detectors; This allows to

trace, event to event, at the direction of the incident photon. Finally, couples are absorbed in the calorimeter, which measures the energy.

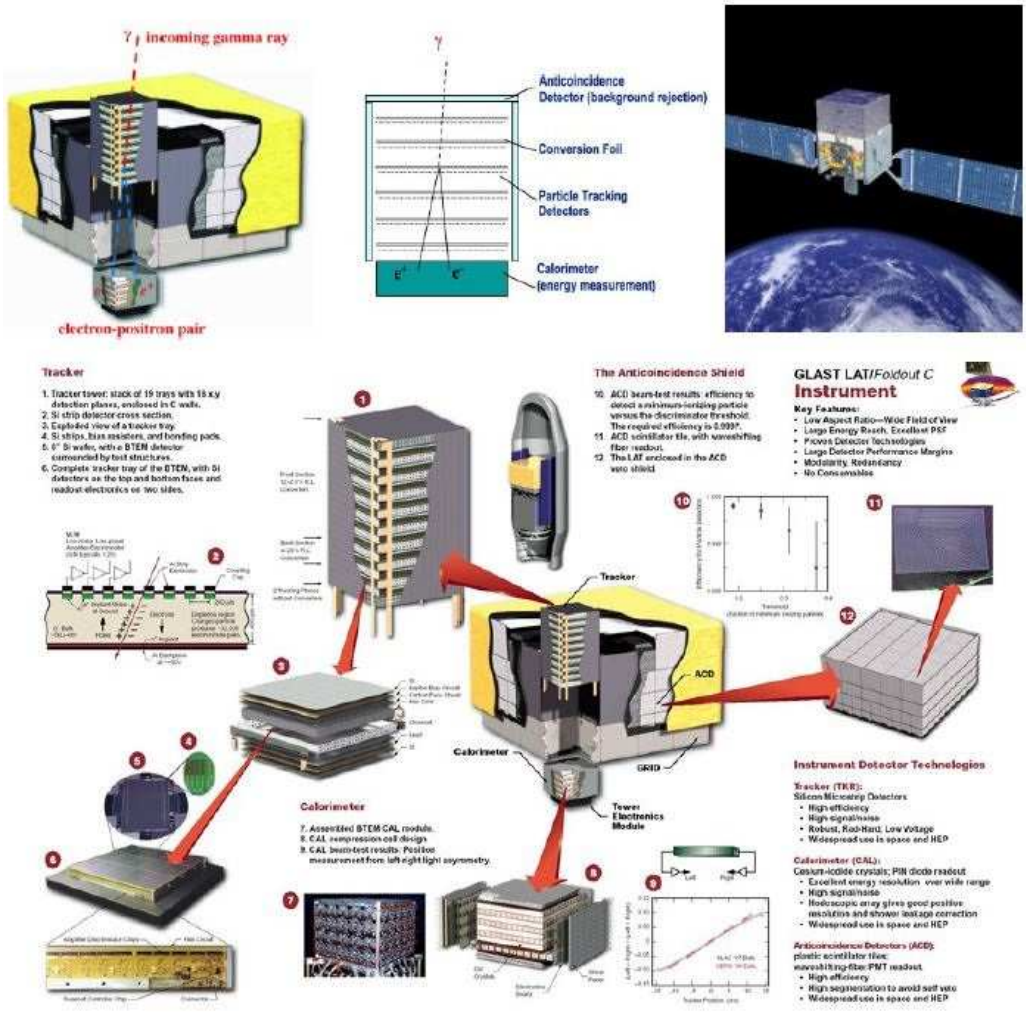

Fig. 1. 5: GLAST working images.

1.1.3 Biomedical imaging applications

Scientific discoveries and technological innovations soon travel through all search fields. An example is the following: the use of Crystal scintillators developed by CERN for high energy physics [8], [9] in the biomedical field, with Diagnostics address but not only. The tools described below are based on the use of the Anger Camera, tools for the detection of gamma radiation. Consist of two basic elements: the collimator and a localization system Photonics. The collimator is a sheet of absorbent material (lead) on which were performed several parallel channels with each other and with axis perpendicular to the plane of the plate, so that only the rays moving in que is direction. The width

and the length of the holes determine the definition of the image; the hole geometry can be of various types:

- Parallel-hole (actual size of images);
- Converging-hole;
- Diverging-hole (increases the field of view of the Crystal);
- Pin-hole (enlarge the scanned image).

After the scope there are crystals and the photomultipliers, which convert the scintillation light into an electrical signal, and localization Photonic system. The fact that the sparks are detected by the sensor even if not perfectly centred on, it gives the spatial lack of linearity acquisition system.

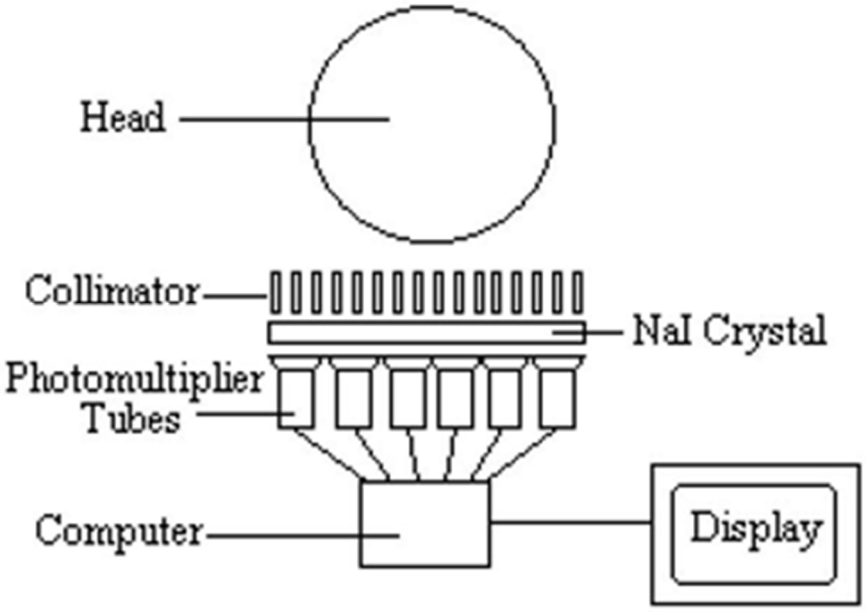

Fig. 1. 6: General scheme of a detector used in biomedical imaging.

1.1.3.1 PET

PET (Positron Emission Tomography) [14]–[16] is a medical imaging technique based on administration to the patient of radio pharmaceuticals, labelled with radionuclides produced by particle accelerator (cyclotron) machines. Radiopharmaceuticals Positron emitting isotopes contain β + (the antiparticle of the electron). The positrons emitted annihilate electrons of matter by generating pairs of photons moving in the opposite direction and have energy of 511 keV. Below are the most important radioisotopes β + stations.

Radioisotope	Half-life (minutes)	Energy (MeV)	Maximum penetration range of matter (mm)
^{15}O	2,03	1,723	8,3
^{11}C	20,38	0,960	5,4
^{18}F	109,8	0,635	2,4
^{13}N	9,96	1,190	5,4

Tab. 1. 1: Example of properties for some radioisotopes.

The annihilation process works this way: the radioactive isotope becomes a Proton into a neutron and Positron nucleus, so that the atom maintains its relative atomic mass but decreases its atomic number of 1. Positron is ejected, and it annihilates with an electron; the energy associated with the mass of the two particles (electron and Positron) is 120 MeV, according to the law of Einstein:

$$E = mc^2 \qquad (1.1)$$

where c is the speed of light and m the mass. This energy is then divided equally between the two gamma photons generated by the annihilation process, which run each other on the same line but in opposite directions.

$$e^- + e^+ = 2\, photons\, \gamma \qquad (1.2)$$

When two photons are recorded simultaneously by a pair of detectors the annihilation that produced them must be located on the line joining the two detectors. If a photon is scattered the joint is incorrect. After the annihilation 100000 or more events have been recorded, the location of Positron-emitting tracers is calculated using tomographic reconstruction procedures [16]. Crux of the technique is the simultaneous detection of pairs of photons. It is possible to measure the likelihood of revealing a pair of photons with these simple formulas [16]:

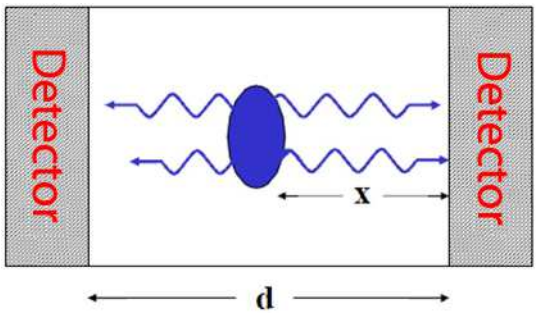

Fig. 1. 7: Measure of the probability of detection of a pair of photons.

$$P = P_1 * P_2 = e^{-\mu x} e^{-\mu(d-x)} = e^{-\mu d} \quad (1.3)$$

where P1 and P2 are the probability of detection of two single photons. The success of the technique is because the organs and cells are equipped with highly specific receptors to capture details certain molecular shapes; in fact, radiopharmaceuticals are metabolic active molecules, also known as "carrier", heading and accumulate towards the tissues to be analysed. In the radiopharmaceutical the concentration of radionuclide is present in such low concentrations that they have no chemical effect on the cell while maintaining its capacity for radiation. Finally, the radionuclides are widely used not only in the diagnosis of the disease, but also in the care. The detection system consists of a ring of coupled to photomultiplier scintillator crystals, just as in high energy physics applications. The detectors must have 100% efficiency close to because the sensitivity of the apparatus is proportional to the square of that value. More circular SEPTA are placed in parallel the next to each other, thereby creating a pipe that will contain the entire body of the patient. If the photons are revealed with the same crystals 2D images are obtained, otherwise ring by removing the separation between the crowns is possible to get 3D images.

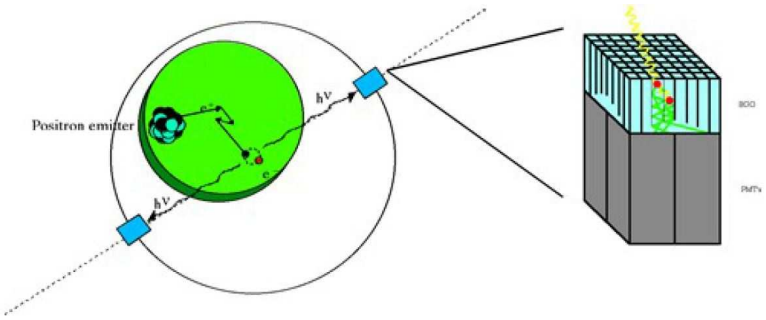

Fig. 1. 8: Schematization of the operation of PET: the energy generated from the annihilation is detected by scintillators.

The crystals used in PET detectors must have basic requirements; the first important among these is to have a high degree of stopping power to be able to detect gamma rays. The PWO is not intended for use in the application, because it heavy and fast but with low light output. The sensitivity is very critical parameter as it reflects the number of useful events per unit dose injected to the patient; greater sensitivity means a smaller dose injected in the patient or a better image contrast. Crystals NaI (Tl) and CsI (Tl) were the most widely used biomedical imaging detectors. The BGO is introduced in this field because of its high density and conversion efficiency, despite a very minor light yield of NaI. Many of the PET scanner constructed in recent times have been designed with BGO crystals. Finally, do not underestimate the importance of the cost of these crystals so that

they make available on the market at an affordable price. It can be said that the Lu based scintillator (LuAP, LSO, LYSO, LuAP) remain the top-quality materials. The design for "individual coupling" is capable of very high resolution, and since the schema is parallel (all photomultiplier tubes and crystals from scintillation operate independently. The disadvantages of this type of project are the requests of many expensive photomultiplier tubes. Also connect the photomultiplier tubes rectangular Crystal ring-shaped door problems in rectangular crystals and photo-packed circular tubes with a diameter small enough to form a solid ring. For this most modern PET scanner for whole body uses an arrangement of detectors which is generally based on a block of glittering items read by a small number of photomultiplier tubes. This configuration, called "block detector design" allows much lower costs. There are also some drawbacks, mainly due to the inevitable uncertainty in the exact determination of the coordinates of the point of annihilation and the limitation of the number of counting due to the inability to process more than an event characteristic scintillation falloff over time. Digital encoding scheme: in the block, two-layer five photomultiplier tubes are paired with eight scintillators. Whenever one of the four photomultiplier tubes come on stream, a photon from 511 Kev interacted with one of two crystals attached to the photomultiplier tube; photomultiplier tube control unit is then used to determine whether it was the Crystal stressed was that more internal or external.

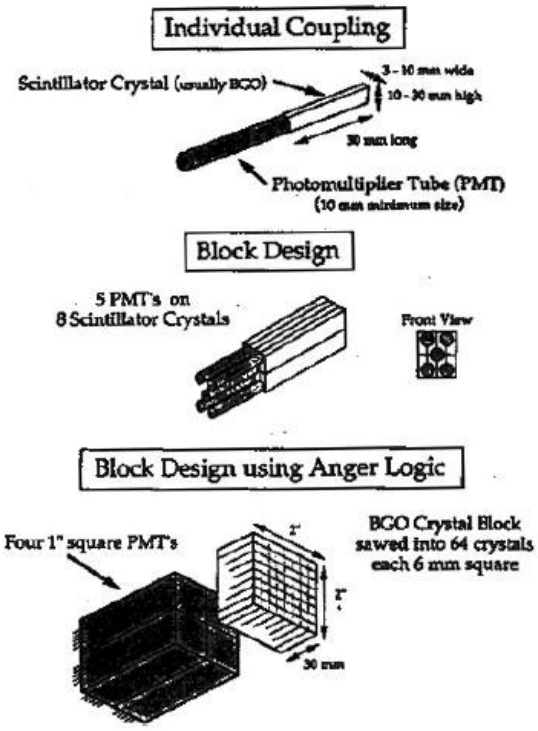

Fig. 1. 9: Different configurations of the scintillator Crystal blocks.

Compared to other sophisticated imaging (ultrasound, CT, MRI), with PET are obtained in a non-invasive and in vivo, only qualitative and quantitative information about physiological type and maps of functional processes in the body.

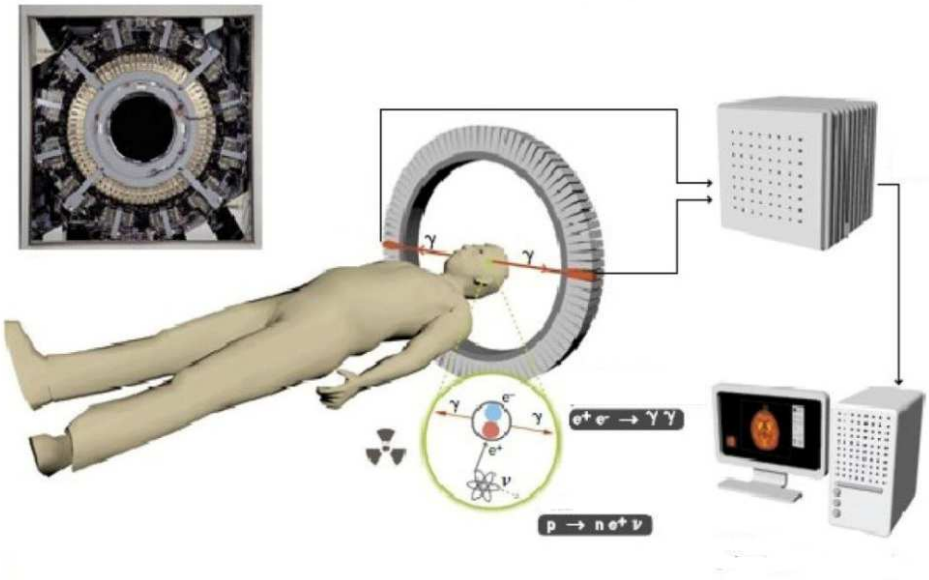

Fig. 1. 10: Scheme of the PET exam.

1.1.3.2 SPECT

SPECT (Single photon emission computed tomography, or single photon emission Tomography) is a diagnostic technique very similar to PET, but difference is just about using radioactive compounds that emit gamma rays directly [14], [17]. For example, it makes extensive use of 99mTc which isomer decaying emits a single photon; This has a peak at around 140 keV and half-life of 6 hours. After injection of radioactive substances, a device that can detect gamma radiation rotates around the patient acquiring images that are processed on a computer. They take many different projections Planar images obtained at defined points during the rotation, typically every 3-6 degrees of arc. In many cases, is performed a rotation of 360 degrees, allowing to obtain a 3D reconstruction. The time taken to obtain each projection is variable but is typically a period of 15-20 seconds. This results in a total time of scanning approximately 15-20 minutes. One of the sources of error in SPECT is due to the attenuation of photons coming from the tissues. In fact, the emitted photons inland areas are more likely to be deflected scattering and change energy, therefore more photons arrive from the outer layers. The most widely used method for correcting (method of Chang) is based on the approximate calculation of the mean attenuation of photons according to their location within the body. SPECT has 100 times less efficient to PET and a worse image resolution but also cost 10 times

less, which makes them very popular in the territory of pets. An advantage is the ability to provide three-dimensional measurement SPECT cerebral blood flow for a long time even after the injection of the radiopharmaceutical.

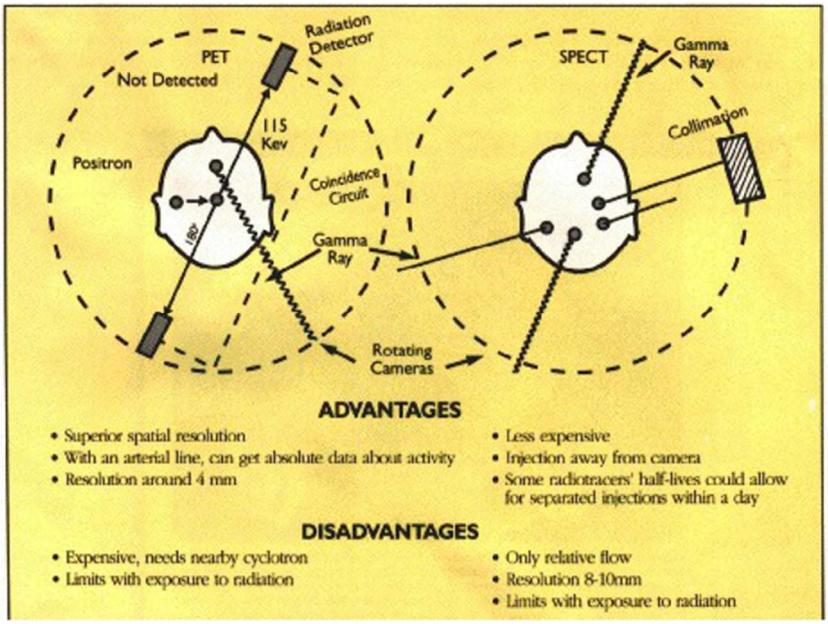

Fig. 1. 11: Comparison of PET and SPECT.

1.1.3.3 Bronchial scanner

Research is ongoing with the objective of designing miniature transverse size detectors minor sub-centimetre. The interest lies in the possibility of promising probes scintigraphy can operate within catheters and able to localize lesions based on the metabolic characteristics of tissues and organs examined. Invasiveness would be minimized because the probe may use led "catheterizable" of the human body and because, operating from within and without the collimation doses of radioactivity necessary would be considerably smaller than those of PET and SPECT.

1.1.4 Applications in security inspections

For security inspections [18] means the detection of offensive weapons and hidden materials, as well as personal belongings of individuals and groups to cross checkpoints. Over the years, different x-ray imaging techniques have been adapted in response to the specific composition and structure of these articles. In these devices the scintillators and photodiodes assembled work the same way in which operate the detectors used in the counting of events. The scintillators are also widely used for detection of explosives by measuring the concentration of nitrogen contained in objects. Among the main challenges ahead of technology based on the mechanisms of scintillation in this field,

including the development of fast and high-resolution spectrometers based on x-rays. Fast scintillators are required for these applications (with less than 50 ns decay time), having a high atomic number and energy resolution comparable to this of the NaI.

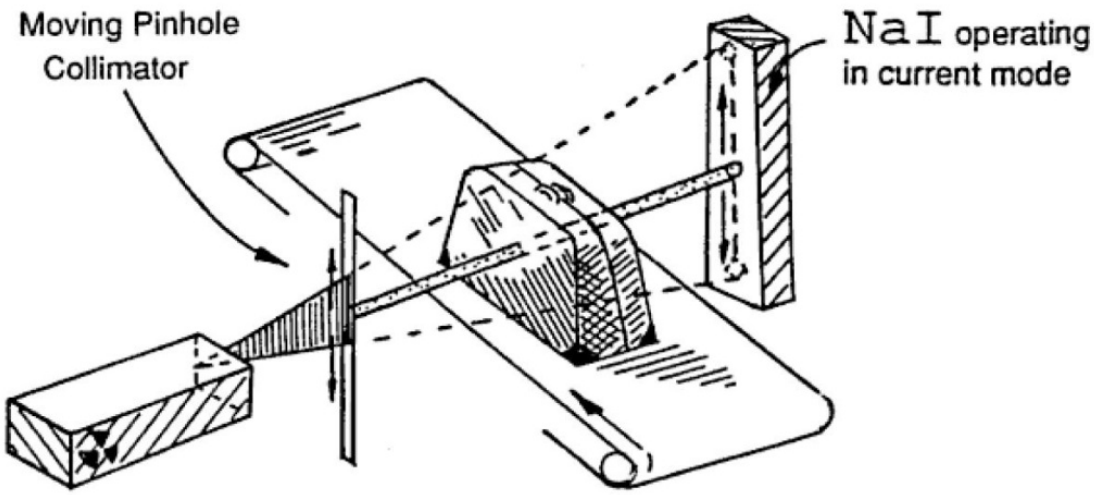

Fig. 1. 12: Application of NaI in security inspections.

The basic techniques of these two nuclear detection systems and x-ray-based; they are complementary in that the first reveals mainly low atomic number objects as chemical explosives, while the second is much more applicable to reveal small amounts of materials with high atomic number, like detonators and batteries. As regards the detection of chemical explosives and bombs, the techniques developed are since these are mainly formed by concentrated density of nitrogen and oxygen. The detector must perform his work in a quick, automatic, non-destructive, with a high probability of success and a very low probability of false alarms. The system must also be able to be inserted into the airport environment without producing detectable radiations and maintain an affordable cost.

1.1.5 Industrial applications

Scintillation detectors are used in a wide variety of industrial applications including the detection of gamma rays and x-rays. These applications can be grouped into five categories: process control and measurement of the thickness, inspection of containers, mineral processing, analysis during production of coal and drilling of oil wells.

	Detector efficiency (r, Z)	Decay time	Light output	Energy resolution	Rugged	Temper-ature response
Process control/ gauging		X			X	
Container inspection	X	X				
Mineral processing		X	X	X	X	
Coal analysis		X	X	X	X	
Oil well logging	X	X	X	X	X	X

Tab. 1. 2: Schematization industrial applications.

Applications / Properties	Tomography CT, PET	Nuclear medicine SPECT	High-energy physics	Industry	Security	Environment
High density and atomic number	++	+	+++	++	+	++
High light yield	+++	++	+++	+	–	++
Fast response	+	–	++	–	–	–
High transparency	+	–	+++	+	–	–
Convenient emission range	+	–	++	+	++	++
Radiation stability	–	–	+++	–	–	+
Large size of single crystal	+++	–	+++	–	–	–
Low cost	+++	+++	+++	++	++	+

Tab. 1. 3: Schematization industrial applications.

1.1.5.1 Process control and measurement of the thickness

The transmission of gamma rays and x-rays are used in the control of changes to determine the presence or positioning parts in containers where no visual inspections, to determine the level of the liquid inside these containers and the presence of fair coverage. Radiation sources range from chemical sources as 241Am or 137Cs for inspections on a small scale until electron accelerators which produce gamma rays of a few MeV on a larger scale. The most widely used scintillators in these applications are in NaI (Tl) and CsI (Tl). Nuclear measurements are used to control precisely the thicknesses in the manufacture of sheet metal, such as aluminium or steel, but also in the production of paper, plastic and thin films. There are two techniques: The first uses chemical sources of gamma rays and scintillators as NaI (Tl), CsI (Tl), CsI (Na). The second using both sources of beta rays together with plastic scintillators and x-ray sources or low-energy gamma rays with inorganic

scintillators. The Fig. 1. 13 shows the thickness control of an aluminium plate with both techniques, with accuracy of +/-0.2%, regardless of the composition of the alloy.

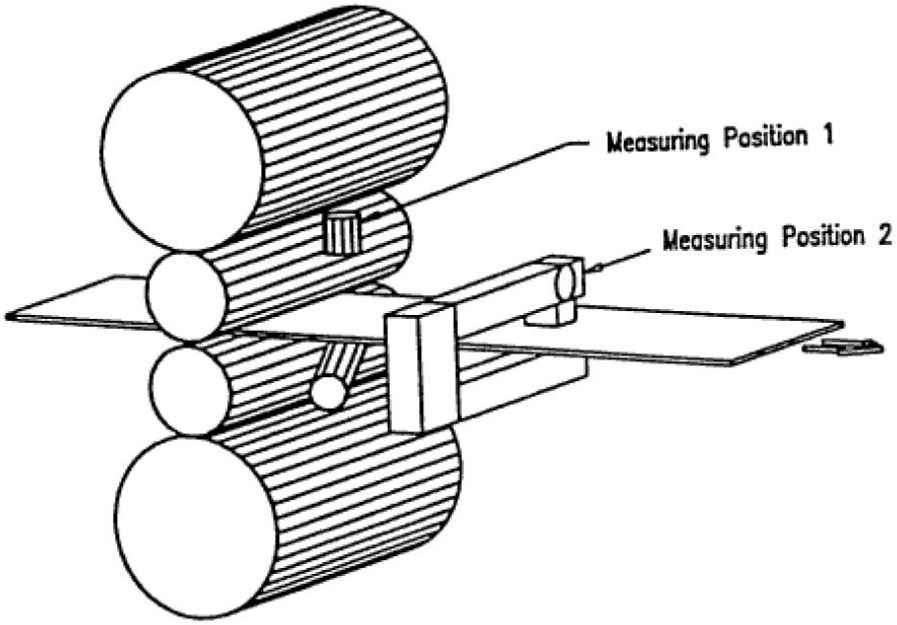

Fig. 1. 13: Scheme of the LET technique for the thickness measurement.

1.1.5.2 Analysis coal production stages

On-line analysis in the production process of coal include the determination of ash content but also the measure of humidity after washing. These techniques are based on the interaction of gamma rays or x-rays and on the fact that the ash has an effective atomic number greater. The main interaction of gamma rays are photoelectric absorption and atomic number-dependent production of pairs. The measuring technique LET (low energy gamma-ray transmission) is based on the dependence of the intensity of a beam of gamma radiation (high and low energy) on weight per unit area of the coal and atomic number. The intensities are detected by scintillators positioned opposite the radiation source by comparing the output represented by the height of the pulses. Sources of error are due to the variation of the constituents of the ashes and that applies especially for coal; they are also due to the low weight per unit area. Advantages of this method are the ability to measure directly on the conveyor belt, the short time of measurement and the low cost.

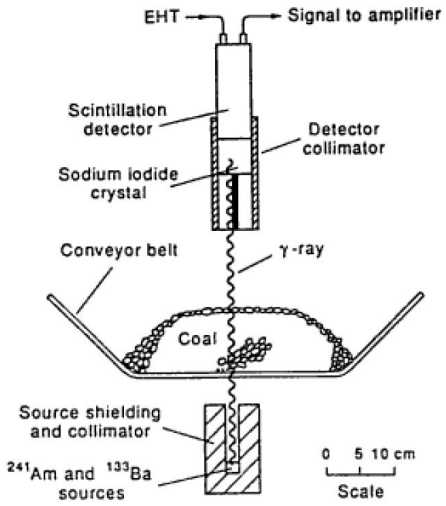

Fig. 1. 14: LET technique for the coal production analysis.

The measuring technique PP is based in the dependence of retro diffuse gamma-ray intensity from production of couples and by scattering Compton. The intensities of the gamma ray interactions are determined separately by the two non-through analysis of pulse height outgoing from Crystal scintillator, so comparing to determine the ash content. The advantage of this technique is less sensitive than LET (at least 4 times) the composition of coal.

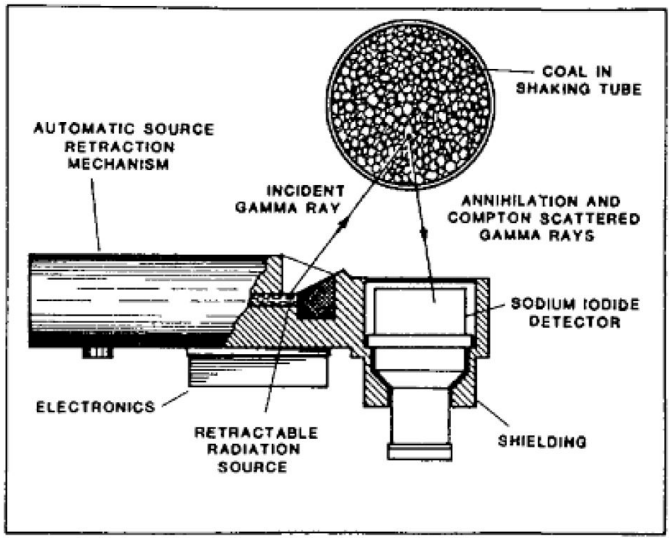

Fig. 1. 15: Operating scheme of the PP technique.

1.1.5.3 Drilling of oil wells

The drilling of wells is the composition of subsoil geological properties. The simplest technique is to use a scintillation detector for measure natural radioactivity of soil composition. In other crafts, the probes carry with them the sources of gamma-rays, such as 137Cs to radiate the soil composition,

or a neutron source to induce the reaction of production of gamma-rays and a detector to measure the rays coming back towards the probe after scattering. The utility of a scintillator crystal depends on both his physical characteristics both from those of scintillation. These ones are modified by temperature variability in the wells, while the physical ones are important due to shock, vibrations and limited space. The NaI(Tl) is still the most widely used in this field of application.

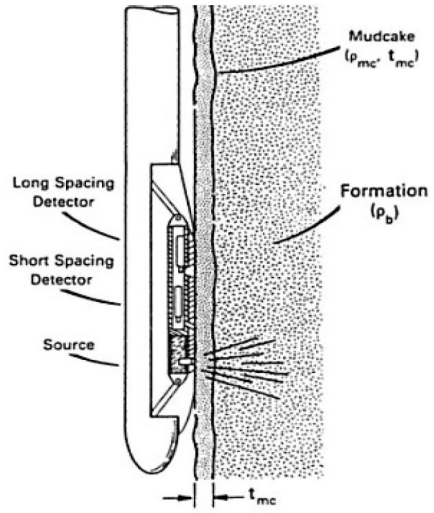

Fig. 1. 16: Scheme of utilisation for oil wells drilling.

1.2 Outline of the main production procedures

Scintillating crystal production cover a field from the chemical laboratory to the industrial scale. Crystals are produced by growth methods specific (optimal) for every chemical compound, part size and quantity [19]. A variety of techniques is used to grow scintillating inorganic crystals. They are all derived by two main methods, which are named Czochralsky and Bridgman [20]. At first the preparation of raw materials is a mandatory prerequisite for crystal quality. This because the purity must be controlled, affecting scintillation (afterglow, light yield) transparency (colour centres) radiation resistance and built-in stress level (cell distortion). The responsible for the lightning performances and production are the dopant species and quantity. The dopant fraction in a Crystal is usually of a few percent. They must be chosen to match to the best the lattice properties (crystal symmetry, lattice parameters). The two possible obstacles that must be faced in order to optimize the crystal production are: segregation, which makes light production uneven over the crystal volume, and lattice distortion, that may induce mechanical stress and be detrimental to the production yield.

1.2.1 Czochralsky method

In the Czochralsky method, illustrate in Fig. 1.17, the raw materials are molten in a metallic crucible and kept slightly above fusion point. A small crystal of the same material (seed) is put in contact with this molten bath and pulled up to lift a small meniscus of liquid by capillarity. Solidification occurs at a position and at a rate ruled by several parameters [21].

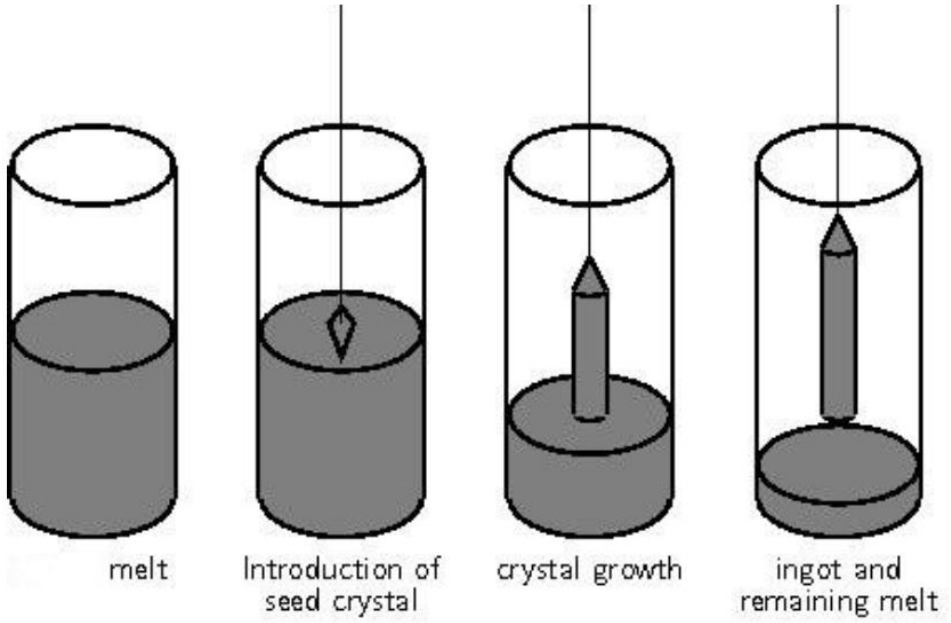

Fig. 1. 17: A schematic representation of the Czochralsky growth method; a hot melt of raw material is put in contact with a pure crystalline seed (slightly colder), generating a meniscus where the melt starts to solidify. Then the growth crystalline part is pulled up (or down) slowly so to produce the boule.

The thermal gradient is regulated by an induction loop heating the melt with the help of the crucible mass. The melt temperature must be homogenized by crucible regulation. The rising solidified bulk takes the shape of the desired ingot (or boule) and the pulling rate gives the ingot its conical top and bottom ends and its cylindrical overall shape. The optimal conditions choice leads to turn the full melt into the ingot volume. As an example, in order to give a view of the production difficulties, the growth of a 1kg PWO ingot take a time of the order of 1 day. The ingot shape may be facetted or oval, depending on the crystal lattice and on the seed orientation. The latter is a critical parameter.

1.2.2 Bridgman method

A scheme of this method is presented in Fig. 20a. Bridgman is an evolution of the fusion zone refining method [21]; the hot zone moves along the length of the furnace while the crystal growths. The raw

material, in powder form, is shaped to the final part proportions with an extra thickness, considering the mechanical processing to follow. A monocrystalline seed is placed at one end and the shape is usually an elongated prism (Fig. 1.18b). This assembly is contained in a thin (a few tenths of a mm) metallic envelope, usually made of platinum.

Fig. 1. 18: A scheme of a possible Bridgman setup (left). In this case, it is the heater that moves along the crucible length. The seed is placed at a side of the crucible and the powder of raw material first melts and then crystallizes while the heater goes back and forth several times. The technique allows to prepare a multiple crucible shaped more or less like the requested final geometry.

One or several of these assemblies are positioned in the furnace enclosure. The fusion zone (thermal gradient) moves from the seed interface along the ingot length by combining several induction loops. The gradient displacement velocity is comparable to the Czochralsky growth rate, but contrariwise the operation must be repeated several times (at the week scale) to reach monocrystallinity and purity at the required level. The Bridgman process can compete with the Czochralsky method only using multiple ingot furnaces, so to have a parallel production. The advantage is that the technique allows to prepare a multiple crucible shaped more or less like the requested final geometry.

1.2.3 Annealing

The solidification process produces thermally-induced stresses. The supposed profile of this stresses is parabolic, with moderate compression in the core, and higher tension at the periphery. The last consideration must be taken with great care as crystals are especially prone to breaking in tension (crack opening). Annealing is necessary to reduce these tensions. The annealing temperature is very close to the melting point to ease dislocation movements and elimination. The thermal effect is sometimes combined with the presence of a chemical element in a controlled atmosphere, because

is expected that a chemical correction is able to restore the crystal lattice equilibrium. In this case, annealing time is governed by diffusion and may take several days. Cause of this, the annealing furnace is a complex temperature-controlled device and annealing is a time-consuming operation and consequently costly in term of money. Moreover, the annealing step is performed to recover the radiation damage too; since in this process the thermal time gradient could be faster, the distribution of the eventual residual stress can be critical in this case.

1.2.4 Machining

A delicate part in the Crystal s production is the cut and shape according to the needs. In this phase the key points are: to avoid material wasting or induced stress and not produce bad surface condition. The ingots are high cost materials used for expensive parts tightly specified in shape and dimensions. Essentially the mechanical processing is designed to achieve these two goals.

- For calorimeters, ingots are usually dimensioned for the yield of one piece. Attempts were made to get two and even four pieces out of an ingot.
- The tiny pixels for medical imaging are either obtained from a single ingot or cut from fibres.

1.3 Scope of this work

In this work, starting from the theories inside the Optical Crystallography and inside the Photoelasticity [22]–[25], which leads to the Diffused Light Polariscope concepts [26], [27], will be defined the process that conduces to the laser Photoelasticity, that involves the conoscopic technique [28]. It will be demonstrated that this technique allows to obtain a detailed stress distribution map inside the whole sample geometry [4]. In this work, this technique will also be applied to crystallographic directions different from the optical axis, to make this measurement technique more flexible [2], [4]. Moreover, will be presented, to enrich the set of developed methods, a new faster technique named Sphenoscopy, which provides reliable inspection of the crystal in a simplified way whatever orientation of the crystallographic and optic axes [2], [4], [29], [30]. The developed tools are based, using different techniques, on the acquisition of fringe images. Therefore, in parallel, the systems have been provided of dedicated algorithms to process and analyse accurately the fringe patterns, developing techniques voted to the measurement error reduction [1], [2]. A new technique will then have developed, using observations in collimated light in direction normal to the optic axis, with the different purpose of analysing the sample from a dimensional point of view, with the aim of determining any non-coplanarity between the surfaces,

which is an aspect that may disturb the previous measurement techniques. This technique will be treated by comparing it with the mathematical model presented and used for the Conoscopy, with the direct geometrical measurements of the surfaces and with the theories of the optical crystallography.

Chapter2

2 Crystal optics

On the correct interpretation of the phenomenon of light there are two different theories: that corpuscular, proposed by Newton, who sees the light as a stream of microscopic particles emitted from light sources and that rippling proposed by Huygens, which sees the light as a wave. The main difference between them is that the first theory states that the light transpose matter, instead the second one states that light transpose energy. At the end of '800s Maxwell confirmed that light is an electromagnetic wave whose disruption consists of electromagnetic fields and the oscillations propagate even into the void. In 1905 Einstein studied the photoelectric effect and returned the corpuscular nature to light composed, according to this theory, by particles called photons. It is now believed that both models are valid because they describe different characteristics of light, that coexist and are no longer considered antithetical to each other. With this work the characteristics that affect are related to wave nature of light. With "light" means that portion of the electromagnetic spectrum visible to the human eye, with wavelength between 400 and 700 manometers and frequency of order 1015 Hz. Visual sensitivity varies from person to person, but generally the visible range is limited below by the colour purple (λ = 380 nm) and superiorly from red (λ = 730 nm). By definition, a light that contains all of the visible wavelengths is called white light, while a light consists of a single wavelength is called monochromatic light. Electromagnetic waves are described as swing of electric field E and magnetic field H vectors: these are in phase and oscillate perpendicularly to each other in the plane normal to the direction of wave propagation, as shown in Fig. 2. 1 [22], [24].

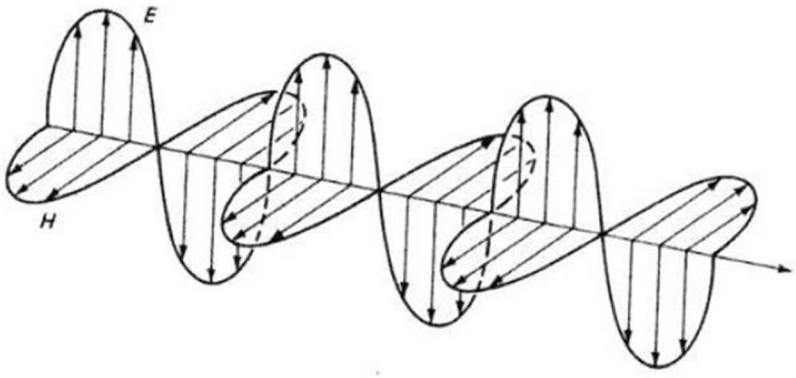

Fig. 2. 1: Variation of magnetic field vector and the electric field vector in an electromagnetic wave.

The behaviour of the electromagnetic waves is described by Maxwell's equations, a system of four differential equations that govern the spatio-temporal evolution of the electromagnetic field; These four laws are [24]:

- Gauss law for E (electric field flux through a closed surface is proportional to the total charge contained in volume: the lines of force depart from positive charges and end up on the bad ones);
- Gauss law for B (the magnetic induction field flux through a closed surface is always null: the lines of force are closed);
- Faraday law (circling of the electric field is proportional to the time derivative of the magnetic flux through any of the infinite surfaces that have the line as border);
- Ampère law (adapted to take account of displacement current using the term added by Maxwell, states that the magnetic induction field circuitry is proportional to the sum of two terms, the first of which contains the total current passing through a surface bounded by the closed loop and the second term contains the temporal derivative of electric field flux through a surface bounded by the curve considered).

The following are the mathematical formulations of physical laws described above; in addition to the E vector, already known, appear:

- $B=\mu_0 H$ is the electromagnetic vector;
- $\mu_0 = 4\pi * 10^{(-7)} N*A^{(-2)}$ is the magnetic permeability of free space [22];
- $\varepsilon_0 = 8.854 * 10^{(-12)} F*m(-1)$ is the permittivity of free space [22];
- ρ is the charge density;
- $j = \sigma E$ is the vector current density (σ is the conductivity of the matter).

Integral form	Differential form	
$\oiint E \cdot dS = \frac{1}{\varepsilon_0} \iiint \rho dV$	$divE = \frac{\rho}{\varepsilon_0}$	Gauss law for E
$\oiint B \cdot dS = 0$	$divB = 0$	Gauss law for B
$\oint E \cdot dl = \frac{-d}{dt} \iint B \cdot dS$	$rotE = \frac{-\partial B}{\partial t}$	Faraday law

$\oint B \cdot dl = \mu_0 [\iint j \cdot dS + \varepsilon_0 \frac{d}{dt} \iint E \cdot dS]$	$rotB = \mu_0 [j + \varepsilon_0 \frac{\partial E}{\partial t}]$	Ampère modified law

Tab. 2. 1: Scheme for the Faraday, Gauss and Ampere laws in integral form.

The electromagnetic field can exist even in the absence of sources, i.e. in the absence of electrical charges (ρ = 0) and electric currents (j = 0), as the magnetic field is generated by variation of the electric field and vice versa. The equations below show these conditions:

Using divergence and rotor	Using derivates	
$divE = 0$	$\frac{\partial E_x}{\partial x} + \frac{\partial E_y}{\partial y} + \frac{\partial E_z}{\partial z} = 0$	Gauss law for E
$divE = 0$	$\frac{\partial B_x}{\partial x} + \frac{\partial B_y}{\partial y} + \frac{\partial B_z}{\partial z} = 0$	Gauss law for B
$rotE = \frac{-\partial B}{\partial t}$	$\frac{\partial E_z}{\partial y} - \frac{\partial E_y}{\partial z} = \frac{-\partial B_x}{\partial t}$ $\frac{\partial E_x}{\partial z} - \frac{\partial E_z}{\partial x} = \frac{-\partial B_y}{\partial t}$ $\frac{\partial E_y}{\partial x} - \frac{\partial E_x}{\partial y} = \frac{-\partial B_z}{\partial t}$	Faraday law
$rotE = \mu_0 \varepsilon_0 \frac{\partial E}{\partial t}$	$\frac{\partial B_z}{\partial y} - \frac{\partial B_y}{\partial z} = \mu_0 \varepsilon_0 \frac{\partial E_x}{\partial t}$ $\frac{\partial B_x}{\partial z} - \frac{\partial B_z}{\partial x} = \mu_0 \varepsilon_0 \frac{\partial E_y}{\partial t}$ $\frac{\partial B_y}{\partial x} - \frac{\partial B_x}{\partial y} = \mu_0 \varepsilon_0 \frac{\partial E_z}{\partial t}$	Modified Ampère law

Tab. 2. 2: Scheme for the Faraday, Gauss and Ampere laws.

Solving Maxwell's equations in vacuum and in the absence of sources are derived the equations of electromagnetic wave vector, as follows [24]:

$$\nabla^2 E = \mu_0 \varepsilon_0 \frac{\partial^2 E}{\partial t^2} \quad (2.1)$$

$$\nabla^2 B = \mu_0 \varepsilon_0 \frac{\partial^2 B}{\partial t^2} \quad (2.2)$$

Where $c = \frac{1}{\sqrt{\mu_0 \varepsilon_0}}$ is the light speed equal to 10^8 * 2.99792458 m/s. These equations connect the temporal derivates of E and B to its temporal derivates. Besides the fields E and B are related by the relation E = BxC, proving that they are mutually perpendicular. The electromagnetic field equation that satisfy the first of them is [22]:

$$E = E_0 e^{i(kr-\omega t)} \quad (2.3)$$

where E_0 is the vector width, k is the wave vector that have width equal to $2\pi/\lambda$ and direction parallel to that of propagation, r is the translation vector and ω is the angular frequency or pulse and amounts to $2\pi f$.

The fundamental parameters associated with electromagnetic waves are:

- Frequency f (number of peaks of the wave at a point per unit of time);
- Wave length λ (spatial distance between two successive wave peaks);
- Speed (in void is equal to c).

These are related by the relation $\lambda \cdot f = c$. From the standpoint of geometric parameters to be considered are:

- Wave front (locus of points, on different directions of propagation, which, at a given instant, show the same amplitude of the electric field and/or magnetic);
- Radius (line normal to the wave front and indicating the direction of wave propagation).

For three-dimensional waves, which propagate from one point in all directions, the wave fronts are spheres and the spokes are radial lines. In this case, as the wave moves away from the origin the amplitude of the vibration is reduced; in the far distance, also, the curvature of the wave fronts is such that we can consider plane. Finally is possible to define the Pointing vector stated by [22]:

$$P = \frac{E \times B}{\mu} \quad (2.4)$$

whose direction is equivalent with the direction of wave propagation. Considering a one-dimensional plane wave which further along the z direction with speed c, electromagnetic wave function can be written as [22]:

$$E = E_0 \cos\left(\frac{2\pi}{\lambda}(z - ct)\right) \quad (2.5)$$

A representation of this electromagnetic wave, called harmonic wave, in two successive moments is shown in the following Fig. 2. 2.

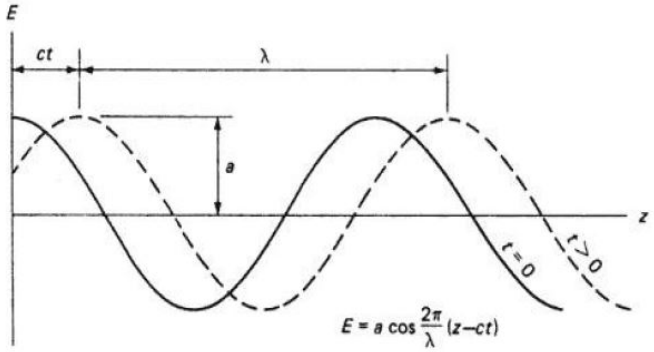

Fig. 2. 2: Performance of an electromagnetic wave in space, represented with two different phase delays.

Another important physical quantity associated with the waves is the initial phase d. The following illustration shows three waves with same amplitude and wavelengths, but different initial phase [22]:

$$E = E_0 \cos(\frac{2\pi}{\lambda}(z - ct)) \tag{2.6}$$

$$E_1 = E_0 \cos(\frac{2\pi}{\lambda}(z + \delta_1 - ct)) \tag{2.7}$$

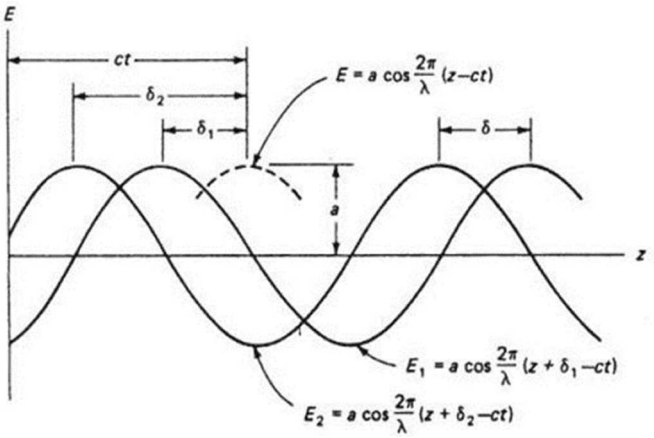

Fig. 2. 3: Three electromagnetic waves with same amplitude but different values of initial phase.

$$E_2 = E_0 \cos(\frac{2\pi}{\lambda}(z + \delta_2 - ct)) \tag{2.8}$$

The difference defined by the equation:

$$\delta = \delta_2 - \delta_1 \tag{2.9}$$

is called linear phase difference or delay, while is called phase angle the size:

$$\phi = (z + \delta)\frac{2\pi}{\lambda} \quad (2.10)$$

The three equations can be written as:

$$E = E_0 \cos(\phi - \omega t) \quad (2.11)$$

$$E_1 = E_0 \cos(\phi_1 - \omega t) \quad (2.12)$$

$$E_2 = E_0 \cos(\phi_2 - \omega t) \quad (2.13)$$

A real wave cannot be perfectly harmonious because the latter extends infinitely in either direction along the axis of propagation and has no starting or ending instant. Common natural sources of light are composed by molecules glowing a series of short pulses, with clearly defined start and end both in space and in time. However, a wave in nature can often be approximated as a harmonic because its extension in space is much greater than its wavelength. a wave with this characteristic is called wave train. Each pulse emitted by the real source is the collection of a series of oscillations, whose duration is approximately 10-8 seconds, called the wave train together. Each train is, in General, the composition of many vectors, each with different values of E0, k, r, and phase to: in this case we speak of incoherent light, can be represented as in the following illustration. When, instead, the atoms (or molecules) emit light in a coordinated manner, the wave trains are being and with equal frequency, amplitude and floor vibration: in this case we speak of coherent light. The laser is a typical example of coherent light, with monochromatic wave trains and in phase.

2.1 Light and Polarization

Polarization of light is about how the light wave vibrates along its propagation path. The harmonic light waves (defined as the oscillation of the Electric Field E) can vibrate in a plane, then is linear polarized or plane polarized but can also vibrate generating a circular or elliptic helix (circular and elliptic polarization Fig. 2.3b and c), or randomly (unpolarised) like most the light sources.

The Polarization can be obtained by the composition of the light waves which vibrate in planes mutually orthogonal (Fig. 6). These waves are defined with the harmonic motions:

$$E_x = E_{0x} \cos(\phi_x - \omega t) \quad (2.14)$$

$$E_y = E_{0y}\cos(\phi_y - \omega t) \tag{2.15}$$

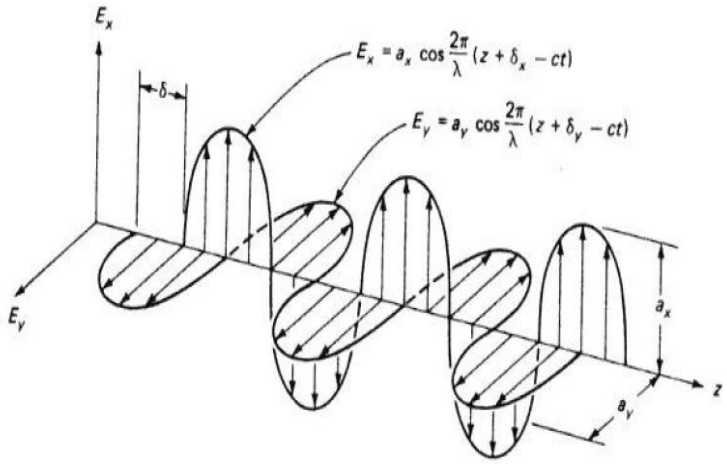

Fig. 2. 4: Linearly polarized waves mutually orthogonal.

They can be rearranged, so to eliminate the time and see what the tip of the resulting vector E describes on the plane orthogonal to the propagation [23].

$$\frac{E_x}{E_{0x}} = \cos(\omega t) \tag{2.16}$$

$$\frac{E_y}{E_{0y}} = \cos(\omega t)\cos(\phi) + \sin(\omega t)\sin(\phi) \tag{2.17}$$

By substituting:

$$\frac{E_y}{E_{0y}} = \frac{E_x}{E_{0x}}\cos(\phi) + \sqrt{1 - \frac{E_x^2}{E_{ox}^2}}\sin(\phi) \tag{2.18}$$

Transposing and squaring:

$$[\frac{E_y}{E_{0y}} - \frac{E_x}{E_{0x}}\cos(\phi)]^2 = [1 - \frac{E_x^2}{E_{0x}^2}]sin^2(\phi) \tag{2.19}$$

$$(\frac{E_y}{E_{0y}})^2 + (\frac{E_x}{E_{0x}})^2 - 2\frac{E_y E_x}{E_{0y}E_{0x}}\cos(\phi) = sin^2(\phi) \tag{2.20}$$

This is the equation of an ellipse in the plane X-Y: therefore, this light is elliptically polarized (Fig. 2.5).

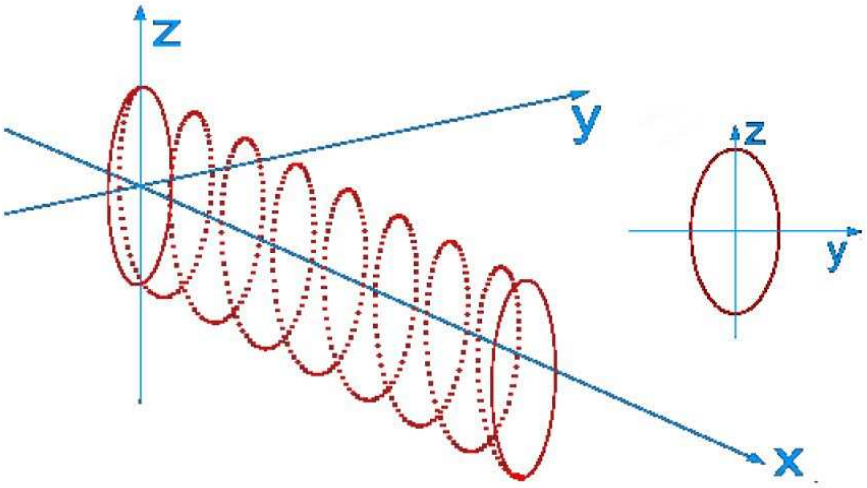

Fig. 2. 5: Representation of the elliptical polarization.

When the two interfering waves has $\phi = \pm\frac{N\pi}{2}$ or $\delta = \frac{N}{4}\lambda$ with N odd integer number, and if E_{0x} and E_{0y} have the same amplitude, then the previous equation becomes:

$$(\frac{E_y}{E_{0y}})^2 + (\frac{E_x}{E_{0x}})^2 = 1 \qquad (2.21)$$

This is the equation of a circle, so we talk about circular polarization. In particular, if the direction of rotation is clockwise we talk about circular right-turning polarization, whereas if the direction of rotation is counter clockwise we talk about circular left-turning polarization. One last special case of elliptical polarization is obtained when $\phi = \pm N\frac{\pi}{2}$ and $\delta = N\frac{\lambda}{4}$, with n an integer. In this case the equation (2.20) reduces to:

$$[\frac{E_y}{E_{0y}} \pm \frac{E_x}{E_{0x}}]^2 = 0 \qquad (2.22)$$

$$E_y = \pm\frac{E_{0y}}{E_{0x}}E_x \qquad (2.23)$$

This is the equation of a line: therefore, we're back in the case of linear polarization or plane (Fig. 2.6).

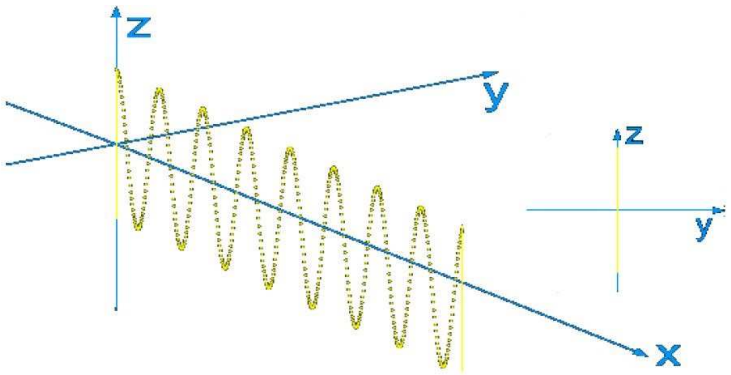

Fig. 2. 6: Representation of linear polarized light.

The orientation of the plane of vibration depends on the ratio of the amplitudes of the waves originating and delay: for δ = 0, λ, 2λ ... this plan lies in the first and third quadrant; for δ = λ/2, 3λ/2, 5 λ /2 ... lies in the second and fourth quadrant.

2.2 Refractive Indices and Optical Indicatrix

Some of the phenomena linked to the interaction between matter and light waves are reflection, refraction and absorption [22]. Here the focus is on light propagation through the media, without considering the phenomena at the interfaces. When the oscillating electric fields passes through a substance, interacts with atoms and ions perturbating the electric atmosphere. An oscillation is forced in the substance particles and the restoring forces of the induced vibrating dipoles (due to the substance and crystal structure) rule the propagation of the electromagnetic wave [31]. The interaction depends by the direction of the oscillation of the electric fields [24] and by the bonding forces of the structure [31]. Considering the magnetic and dielectric properties of the material [24] (2.24), it is obtained that the speed of the electromagnetic light wave when it passes through a medium is slower than the speed in vacuum [22].

$$v = \frac{1}{\sqrt{\mu\varepsilon}} \tag{2.24}$$

The ratio between the speed of light in vacuum c and the speed in the material is named refractive index n [22]. Since in this case the constant μ is the same as in the vacuum, the definition of the refractive index is (for further details see [22]–[24]):

$$n = \sqrt{\varepsilon} \tag{2.25}$$

Or, considering the dielectric impermeability $B = \frac{1}{\varepsilon}$ [24]:

$$n = \frac{1}{\sqrt{B}} \tag{2.26}$$

In case of isotropic material, the refractive index is the same for each direction of the propagation while, in optically anisotropic material there is a distribution of the refractive indices with respect to the direction of the light. In fact, light transmitted energy depends by the arrangement of the dipoles that is linked to the crystal requirements of internal symmetry [31]. Because of this isometric crystals structures (e.g. cubic ones) or amorphous material transmit the energy in an isotropic behaviour, while om the contrary not isomeric structures (e.g. hexagonal or rhombohedra) have anisotropic transmission of light. In these last materials, the refractive indices are represented by a positive-definite and symmetric tensor [32]. The light transmitted through the anisotropic media is represented by the (2.27) in which D is the electric displacement vector (for further details see [24], [27], [31]).

$$\begin{pmatrix} D_x \\ D_y \\ D_z \end{pmatrix} = \begin{bmatrix} \varepsilon_{xx} & \varepsilon_{xy} & \varepsilon_{xz} \\ \varepsilon_{yx} & \varepsilon_{yy} & \varepsilon_{yz} \\ \varepsilon_{zx} & \varepsilon_{zy} & \varepsilon_{zz} \end{bmatrix} \begin{pmatrix} E_x \\ E_y \\ E_z \end{pmatrix} \tag{2.27}$$

That is in another notation:

$$(D) = [\varepsilon](E) \tag{2.28}$$

The principal refractive indices, which describe the optical behaviour of the media, can be derived from the eigenvalues of $[\varepsilon]$

$$n_x = \sqrt{\varepsilon_x}\,,\ n_y = \sqrt{\varepsilon_y}\,,\ n_z = \sqrt{\varepsilon_z} \tag{2.29}$$

By the [22], [27], considering that $[\varepsilon^{-1}](D) = (E)$, the dielectric energy is defined as follow [24], [27], [31]:

$$U = \frac{1}{2}[\varepsilon^{-1}](D) \cdot (D) \tag{2.30}$$

In the most general case the surface with constant energy is an ellipsoid [31].

$$\frac{x^2}{\varepsilon_x}+\frac{y^2}{\varepsilon_y}+\frac{z^2}{\varepsilon_z}=C \tag{2.31}$$

$$\frac{x^2}{n_x^2}+\frac{y^2}{n_y^2}+\frac{z^2}{n_z^2}=C \tag{2.32}$$

$$B_x x^2+B_y y^2+B_z z^2=C \tag{2.33}$$

This ellipsoid describes the distribution of the refractive indices and it is named as Fresnel ellipsoid, index ellipsoid or optical indicatrix [23]. By (2.31), three cases can be distinguished with respect to the light transmission, according to the eigenvalues of (2.27): isotropic behaviour, anisotropic uniaxial behaviour and anisotropic biaxial behaviour.

2.2.1 Uniaxial crystals

In anisotropic crystals less symmetry of the arrangement of Atomic bonds affect the speed of the light waves, which varies according to the direction of propagation. When a beam of light affects the surface of an anisotropic crystal, generating two rays refracted (phenomenon of double refraction), polarized linearly with vectors E that vibrate at right angles to each other [22], [23], [31]. Because of the different directions of vibration, also the speed of the two rays will be different. However, there are the directions of wave propagation (matching certain crystallographic directions) along which the two speeds are equal. This direction is called optic axes. In uniaxial crystal there is only one optic axis [23], [33]. The ray-speed surface for similar crystals consisting of two figures: a sphere, for the so-called ordinary Ray (whose speed is equal in any direction) and an ellipsoid for the so-called extraordinary Ray (whose speed varies with the direction). The two surfaces are touching in two places, at the optical axis (denoted by the letter c), because along the optical axis the two speeds are the same. Along any other direction, however, the two speeds differ [23], [33]. Also, if the speed of ordinary beam is greater than that of the extraordinary Ray it is said that the Crystal is optically positive (left), otherwise it is said optically negative (right). The distance along a given direction, between the two surfaces is proportional to the difference between the two speeds [22], [23].

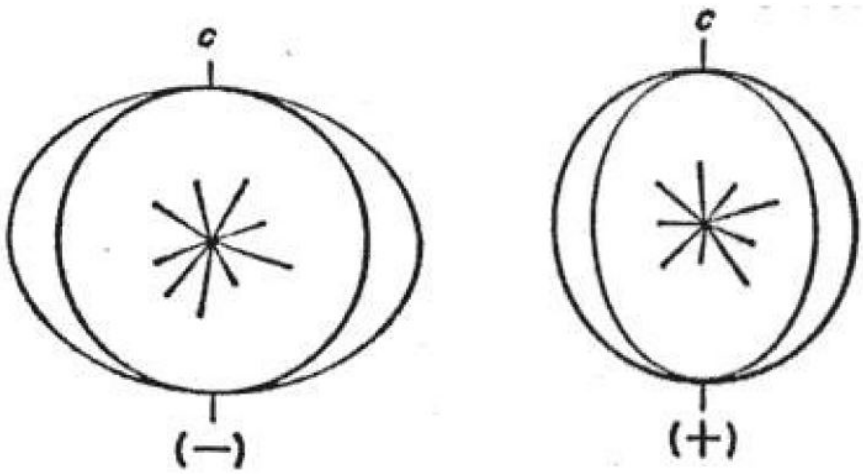

Fig. 2. 7: Surface of single-axis anisotropic crystals negative rate (left) and positive (right).

In uniaxial case, there are two main indexes, called refractive ordinary index $n_0 = n_x = n_y$ and extraordinary refractive index $n_e = n_z$. The optical index, then, is an ellipsoid of rotation, where the major and minor axes are proportional to n_e and n_0. If $n_e > n_0$ the crystal is called positive uniaxial. If ne<n0 it is called negative uniaxial. Optical index equation is [22]:

$$\frac{x^2+z^2}{n_0^2} + \frac{y^2}{n_e^2} = 1 \qquad (2.34)$$

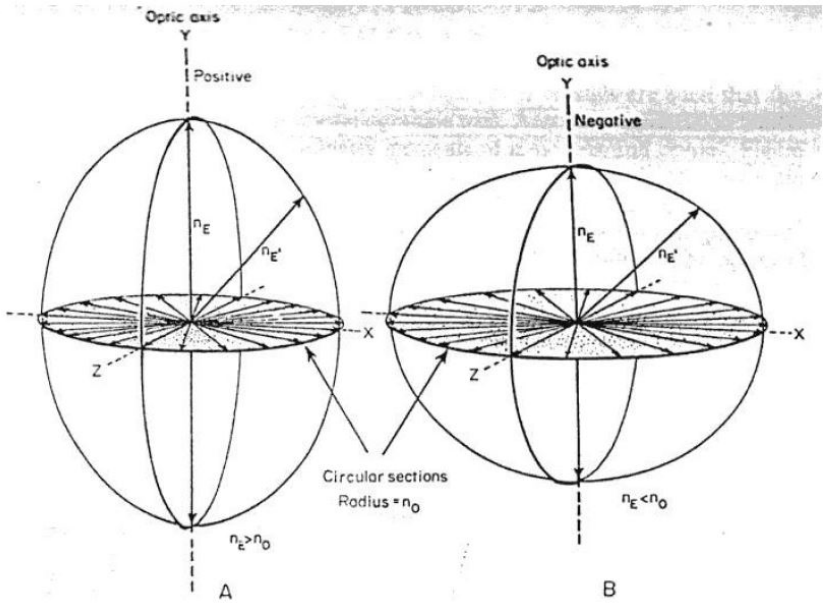

Fig. 2. 8: Optical indicator for negative unassial anisotropic crystals (right) and positive (left).

When a wave passes through the Crystal in a certain direction (s), the electric field propagates according to the dielectric constants relating to the portion of its ellipsoid orthogonal to the direction of the wave: this section will be an ellipse with n_0 and n_e as semi-axes with intermediate

value between n_0 and n_e. The plane containing the optical axis OZ and vector s is called the main plane [23].

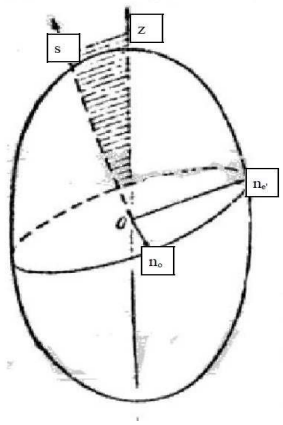

Fig. 2. 9: Representation of the directions of vibration of ordinary ray and extraordinary ray.

The ordinary wave associated with the wave under consideration will vibrate in the plane of the ellipse located along a normal to the main section (so this the refractive index associated is precisely equal to n_0), while the extraordinary wave vibrates in plan of the ellipse, but normally the ordinary wave (it will be associated with the index n_e). Special case occurs when a wave passes through the crystal in the direction of the optical axis: in this case, it happens that the orthogonal ellipse degenerates to a circle of radius equal to n_0, and then the crystal will act as if it were isotropic (but only in this particular direction) because the two beams will travel with the same speed of propagation. The ordinary beam vibration direction is normal to the plane containing the optical axis and the radius itself, while the extraordinary ray lies in the plane containing the optical axis and the radius. The two components of the wave will come out from the Crystal with a time delay dependent on the difference in speed of each of the two inside the medium, resulting in a phase shift from what value will depend on the type of interference (constructive or destructive), depending on the thickness of the stroke path. This will form the basis of the formation of special interference patterns, which will allow the internal analysis of the crystal [22], [23], [27].

2.2.2 Biaxial crystals

In biaxial anisotropic crystals there are two optical axes: exist two preferential directions along which the ordinary ray and the extraordinary one has the same speed of propagation; the optical indicator is a Triaxial ellipsoid. Optical axes, in the reference frame chosen in Fig. 2. 10, and non-restrictive assumption that $n_x<n_y<n_z$, they lie in the plane ZX, called optical plane [23]. The y-axis,

normal to such a plan is said normal optics. Between the two optical axes there is an angle (acute), denoted by 2β, said optic angle [23]. The bisector of that angle is said acute positive bisector Bx_a: in positive crystal this bisector is Z axis, in the negative is X axis. The bisector of the angle between the two optical axes (obtuse) it says obtuse angle bisector Bx_0 [23]. The triaxial index has the property that the normal sections optical axes are circular with a radius of n_y: so, a wave that propagates along the optical axis will behave as if it's moving in a medium isotropic, and two waves that are generated for birefringence are the same. Any other section is elliptical: a wave in motion along a direction different from optical axes, then splits into two rays, with vibration directions respectively parallel to major and minor semi-axes of the ellipse [23], [34].

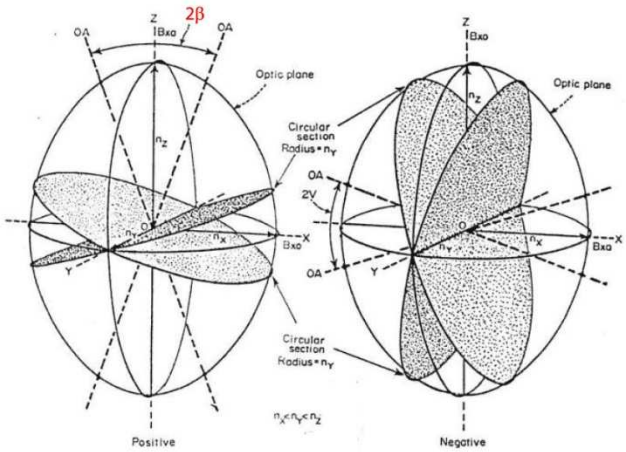

Fig. 2. 10: Optical index of biaxial anisotropic crystals.

The difference n_z–n_x it says double refraction, while n_z–n_y and n_y–n_x are said to partial birefringence. The value of the opening angle can be determined experimentally, but there are some approximate formulas to calculate it according to the value of the indices of refraction [22]:

$$tan^2\beta = \frac{\frac{1}{n_x^2}-\frac{1}{n_y^2}}{\frac{1}{n_y^2}-\frac{1}{n_z^2}} \qquad (2.35)$$

In the last two anisotropic cases, the media have an isotropic behaviour only in the direction of the optical axes. In any other direction, it has been demonstrated by theory and proven by experiments that, any electromagnetic perturbation consists in the sum of two plane and mutual orthogonally polarized light waves [23]. These waves are affected by different forces that act to restore the vibrating dipoles, and therefore, they travel with different velocities [22]. In fact, for these directions the refractive indices are represented by the axis of their cross section. These anisotropic material

are naturally birefringent [33]. It is worth to remind that the combination of such waves gives a resulting wave with a polarization which depends by the relative delay. In general, for the anisotropic media, the light propagation is conditioned by the fact that the electric field E and the displacement vector D are not parallel except along the direction of the optical axes. To get the idea of the behaviour, a sort of Huygenian construction [23] is presented. It starts from considering that the axes of the index ellipsoid are the direction of vibration of the waves, which move with a velocity related to that axis (inversely proportional to the refractive index). It is helpful to introduce the "surface velocity", which is related to the optical indicatrix as mentioned above. This means that the velocity surface about the ordinary (governed by the ordinary index) and the extraordinary light waves (velocity proportional to $\frac{1}{n_e}$) are respectively a sphere and an ellipsoid. Some section of this surfaces are presented and the wave front behaviour explained in the Fig. 2.11 [33];

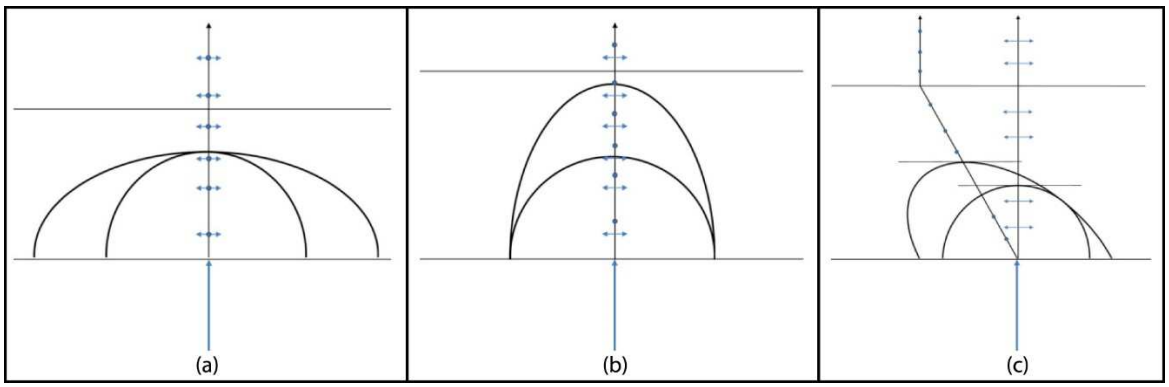

Fig. 2. 11: In the image are shown sections of the ray velocity propagation surfaces, which are related to the optical indicatrix (velocity is proportional to 1/n), moreover in the figures the trace of the refracted rays is drawn. When the vibration is normal to the section, the polarization is indicated as dots; is instead indicated with doubled arrows lines when the vibration is parallel to the section. The light impinges normally to the surface. In (a) the ray is not refracted and go through the crystal thickness along the optical axis; therefore, a uniform and isotropic behaviour is recognized. In (b) the light crosses the crystal along the orthogonal direction with respect to the optic axis. Even if the light has a single path, a birefringent effect is present. That because the resulting wave is composed by the sum of two orthogonally polarized waves which run with different velocities, that are respectively one with V proportional to 1/no and the other with V proportional to 1/ne. Therefore, the light emerges from the outlet surface with a phase delay. In (c) we have the case were the crystal is cut randomly. The ray normal to the inlet surface is divided in two rays. The ordinary ray, that is not refracted, follows the spherical propagation and the extraordinary, that is refracted, follows the elliptical one. In the image the wave fronts are draw as tangent to the ray velocity surfaces. Then, the overall electromagnetic perturbance is composed by two waves which have different velocity and run through different paths. At the outlet surface the extraordinary ray is refracted again. The emerging rays have achieved a phase delay.

2.4 Bertin Surfaces

It has been outlined., in the previous paragraphs, how the delay between interacting light waves affects the resulting one. In our case the delay is generated by the birefringent material and it is ruled by their optical indicatrix (refractive indices distribution) and the relative ray velocity surfaces. Resuming the discussion from the Fig. 2.11b, in this case the two waves are travelling the thickness

of the crystal along the same path, mutually orthogonal polarized, but with different velocities. At the outlet surface they get a delay, due to the thickness and to the different refractive indices (17), which is, defining the dimension of the thickness as d:

$$\delta = n_e d - n_o d \tag{2.36}$$

It is convenient, here, to express the delay in two manners: as optical path difference (related to the wavelength λ) and as phase delay $\phi = \frac{2\pi}{\lambda}\delta$:

$$N\lambda = d(n_e - n_o) \tag{2.37}$$

$$\phi = \frac{2\pi}{\lambda} d(n_e - n_o) \tag{2.38}$$

About the delay (optical path or phase delay) it is possible to trace points with same phase delay and optical delay (in terms of number of wavelength). These points compose the so called Bertin Surfaces [23], [33], that is, the loci of point where the refracted waves get the same phase delay. In Fig. 2.12 is reported the trace of the surfaces in 2D and 3D construction for the uniaxial crystals.

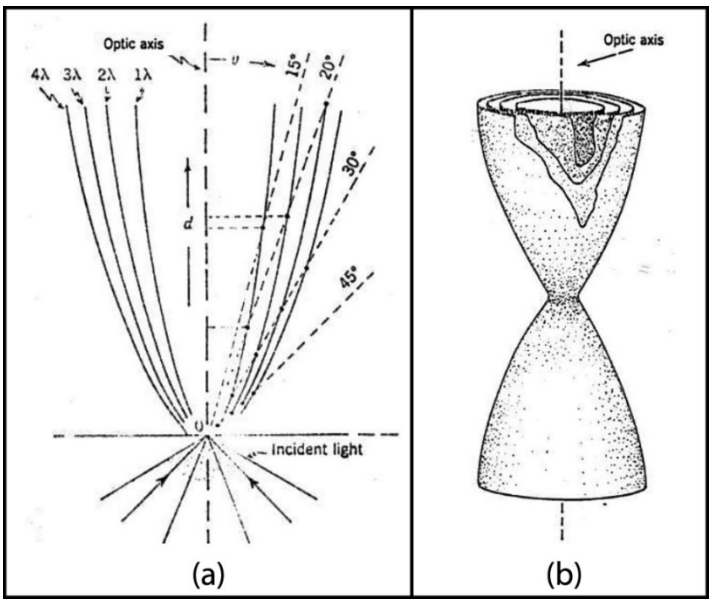

Fig. 2. 12: Construction of the Bertin surfaces [18]. (a) Plane representation of the equal delay or optical path difference as function of the angle of refraction. (b) Volume reconstruction of the Bertin surfaces by means of the circular symmetry of the light behaviour around the optic axis.

Considering a small angle between the ordinary and the extraordinary ray [22] the Fig. 2.12a can be represented with an equation from (2.37) and (2.38):

$$\phi = \frac{2\pi d}{\lambda cos\theta_m}(n_e - n_o)sin^2\theta \quad (2.39)$$

Where θ is the angle between the refracted ray and the optic axis, whereas θ_m is the angle between the optic axis and the bisector of the ordinary and extraordinary ray. In our case, where is considered a small angle between the ordinary and the extraordinary ray, can practically considered θ_m=θ. The same equation is achievable for the optical path difference.

$$N\lambda = \frac{d}{cos\theta_m}(n_e - n_o)sin^2\theta \quad (2.40))$$

Using the same principles, Bertin surfaces can be traced for the biaxial crystals. Hereafter are reported, for the three planes of symmetry of the optical indicatrix, the construction of the curves [22], [23] (Fig. 2.13), described with mathematical approach in the same way as (2.37).

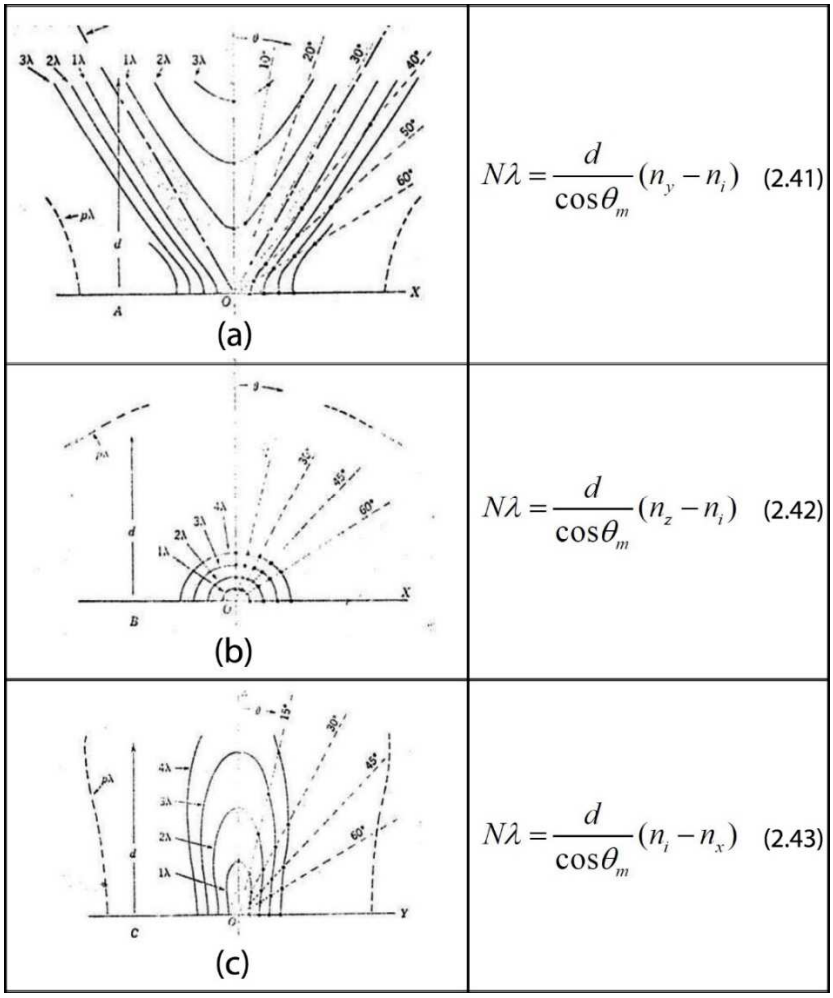

$$N\lambda = \frac{d}{\cos\theta_m}(n_y - n_i) \quad (2.41)$$

$$N\lambda = \frac{d}{\cos\theta_m}(n_z - n_i) \quad (2.42)$$

$$N\lambda = \frac{d}{\cos\theta_m}(n_i - n_x) \quad (2.43)$$

Fig. 2. 13: Two-dimensional trace of the biaxial Bertin surface for the three planes of symmetry (a) (b) (c) of the optical indicatrix. On the left are reported the graphic trace of each plane of symmetry, with on the right the relative equation for the optical path difference.

The evaluation of n_i has been made for each angle by the (2.44) [23]:

$$(n_i)^2 = \frac{(n_z)^2(n_x)^2}{(n_x)^2 sin^2\theta + (n_z)^2 cos^2\theta} \quad (2.44)$$

By the Fresnel treatment [22], the Bertin curves can be represented by a relation obtained as (2.40), but taking into account that the refracted middle ray has an angle from each optic axis (θ_1 and θ_2).

$$N\lambda = \frac{d}{cos\theta_m}(n_z - n_x) sin\theta_1 sin\theta_2 \quad (2.45)$$

The mathematical relations with the relative curves are at the construction base of the biaxial Bertin surfaces (Fig. 2.14).

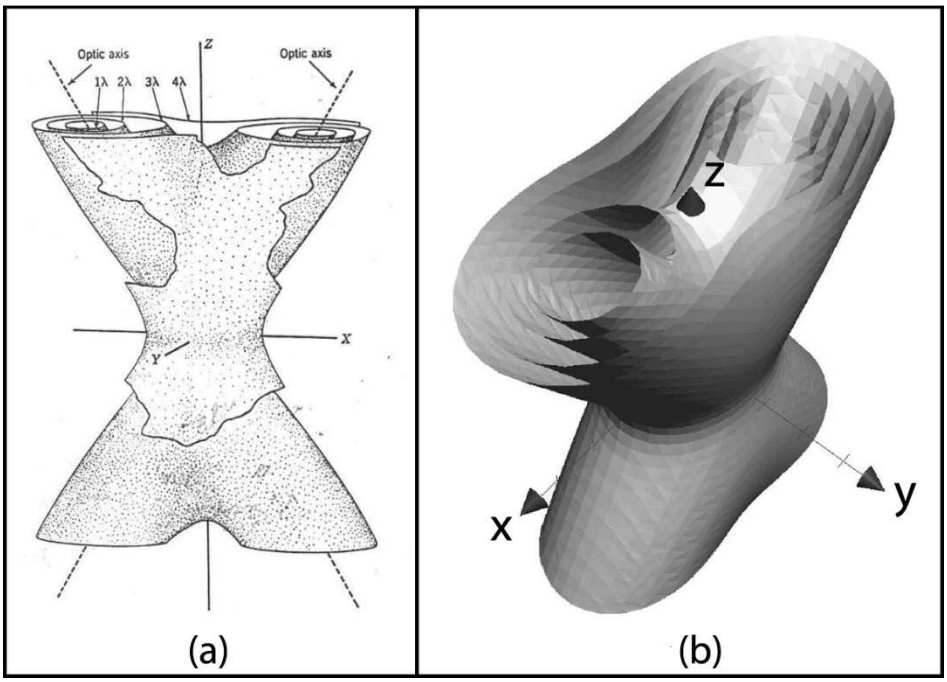

Fig. 2. 14: (a) Three-dimensional reconstruction of the equal path difference curves in biaxial crystals extracted by [35]**. (b) Computer simulation of the Bertin surfaces, obtained starting from the model in** [35]**.**

Starting from this, a fourth-order polynomial expression representing the Bertin surfaces has been found in [27], [36] (2.46):

$$(N\lambda)^2 = (x^2 + y^2 + z^2)(n_x - n_z)^2 \left(1 - \frac{[z \cdot cos\beta + x \cdot sin\beta]^2}{x^2 + y^2 + z^2}\right)\left(1 - \frac{[z \cdot cos\beta - x \cdot sin\beta]^2}{x^2 + y^2 + z^2}\right) \quad (2.46)$$

Starting from the (2.46) is possible to create a three-dimensional representation of the described model, which is shown in Fig. 14b.

2.5 Conoscopic Fringe Patterns

To determine and understand the optical path difference and the phase delay of light waves traveling through a birefringent crystal, is helpful the mathematical concepts of the Bertin surfaces. Using polarized light and optical systems, fringe patterns are observed. The morphology of those patterns is due to the path difference; therefore, they are directly related to the Bertin surfaces. Polarizers are the optical accessories which have the capability to absorb linear polarized light that has an angle with respect to polarizer transmission axis [37] (Fig. 15). They are at the bases of numbers of optical systems like polarized microscopes [23] and polariscopes [38] used, classically, for photoelastic observation (Fig. 2.15).

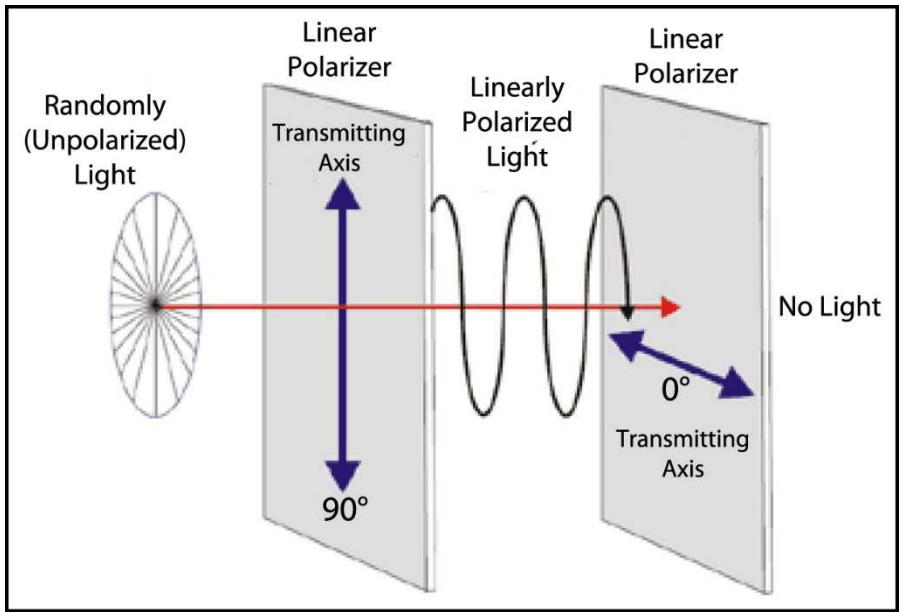

Fig. 2. 15: A scheme of the polarizer behaviour. In typical optical devices like polariscopes or polarized microscopes, the light are polarized by the first polarizer, the second present polarizer (0°) is called analyser. In this case the system works with linear polarization.

A simple and helpful method using vectors is presented (see for details [23]), to evaluate the light transmitted by the analyser when it is crossed by $\pi/2$ with respect to the polarizer (Fig. 2.16).

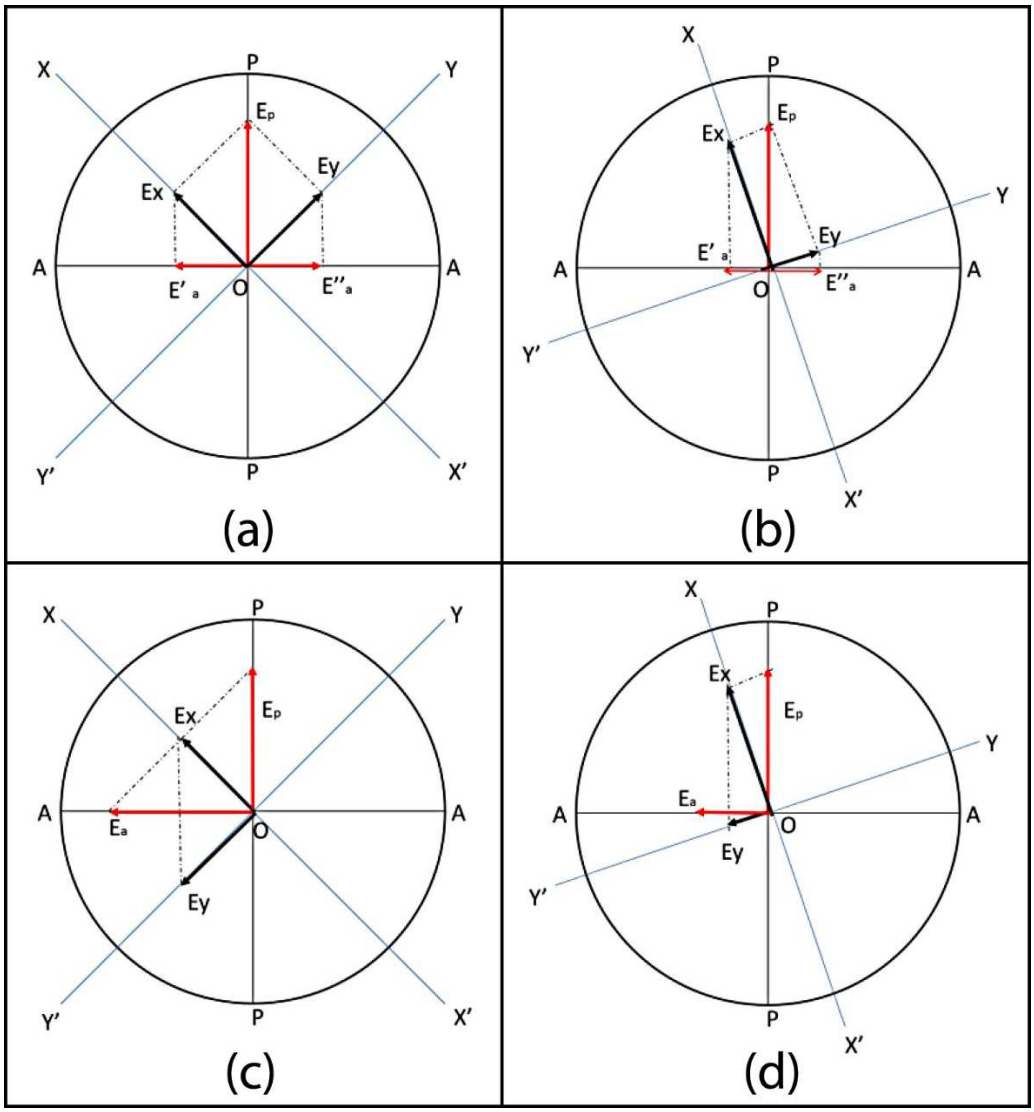

Fig. 2. 16: A scheme to evaluate the light, emerging from the crystal outlet surface transmitted by the analyser. The direction of the plane of vibration of the light waves are named XX' and YY', PP and AA instead are the polarizer and the analyser. The polarized electric field is represented by E_p, starting from this E_x and E_y are its component along the vibration planes. In (a) and (b) the wave components, represented in black, have a Nλ path difference, therefore they are in the same positive quadrant X-Y. The resulting vectors on the analyser are equal and in opposition, therefore no light is transmitted. In (c) and (d), the path difference of the components is (N/2)λ with N odd number. In this case E_y is in the negative part of YY', hence the resulting vectors on the analyser are in the same direction. Thus, intensity is transmitted due to the constructive interference.

In Fig. 2.16, polarizer and analyser are named PP and AA, while XX' and YY' are the traces of the vibration planes of the light emerging from the crystal (the axis of the relative ellipse obtained as a section of the optical indicatrix normal to the light ray). The electric field amplitude emerging from the polarizer (P) is represented by E_p. When crosses the crystal, the light is composed by two rays vibrating along XX' and YY' (E_x and E_y). The electric field amplitude, transmitted by the analyser, is named as E_a. In the case (a) and (b) of the Fig. 2.16, the vectors of the electric fields parallel to the analysers are equal and opposite, since the delay is Nλ, with N a whole pair number. In this case a destructive interference is obtained. In (c) and (d) instead, the path difference is (N/2)λ (N an odd

number). Thereafter the component on YY' is opposite to the one in (a) and (b) (this is in accord with the (2.34). Therefore, a constructive interference is carried out, being the electric fields vectors on the analyser equal and in the same direction. In the case (d) the transmitted intensity is lower. Using convergent polarized light to illuminate a crystal, like in the scheme of Fig. 2.12a and 2.12b, the plane of vibration of the emerging ray in Fig. 2.17 are obtained.

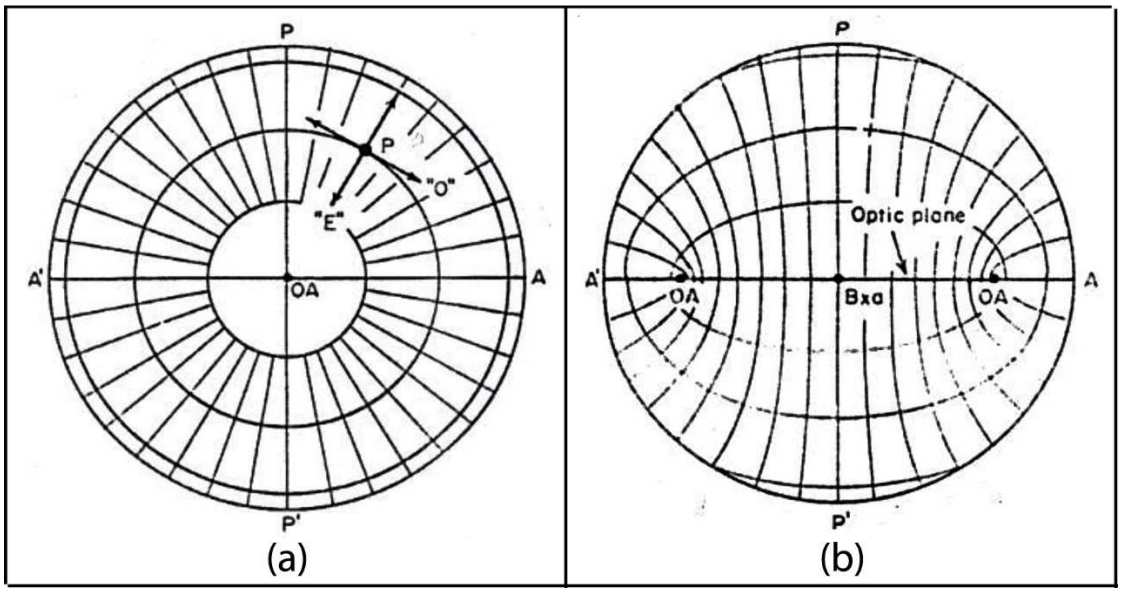

Fig. 2. 17: The trace of the vibration planes for each direction angle of diverging light inside the crystal are represented by the lines. (a) Representation of uniaxial crystal observed along its optic axis. (b) Biaxial crystal observed along its acute bisector.

Using the system in Fig. 2.18, each couple of parallel rays that comes from the analyser vibrating on orthogonal plane, are recombined on the focal plane. Their optical path difference (or phase delay), that is described by the Bertin surface, determine if the interference is destructive or constructive.

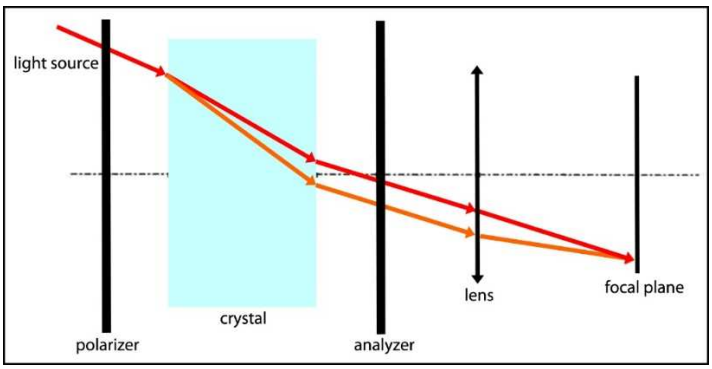

Fig. 2. 18: Observation scheme of a typical plane polarizer. The sample is between two crossed polarizers in dark field. The parallel rays emerging from the sample that crosses the analyser, are converged by the lens on the focal plane. An interference is carried out on the focal plane.

The typical fringe patterns carried out are shown in Fig. 2.19. These patterns can be imagined and as the intersection of the Bertin surfaces with a plane representing the edge surface of the crystal.

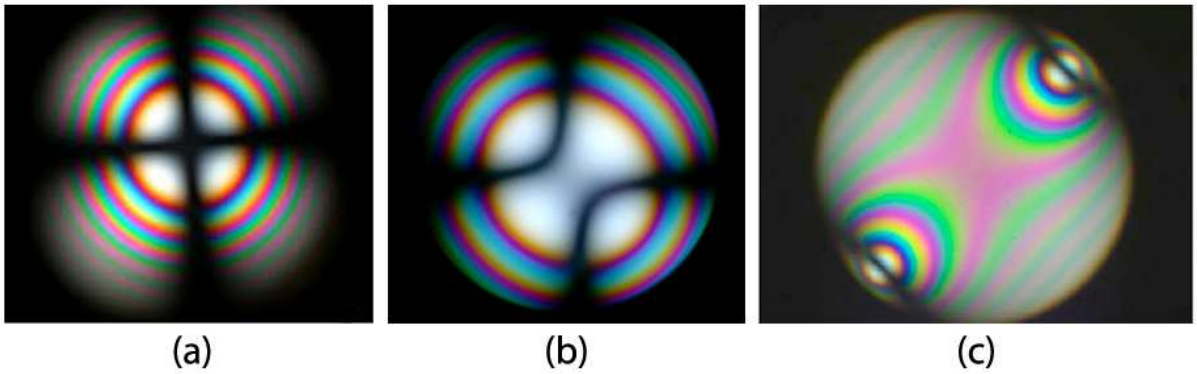

Fig. 2. 19: Conoscopic fringe patterns for uniaxial (a) and biaxial (b and c) crystals observed along the optic axis. The black fringes, that is in particular a cross in (a), is present because the planes of vibration coincide with the polarizer and analysers axis, therefore, no light is transmitted.

Chapter 3

3.Photoelasticity

Photoelasticity is a classical measurement technique suited to observe stress in transparent isotropic materials [14]. The birefringence induced by the stress leads to an estimate of the stress condition by the appearing of fringe patterns due to the induced refractive indices difference [37]. The presented research deals with naturally birefringent media in which a fringe structure is already present even when the stress is not present [23]. Usually these patterns are symmetric. Then, in case of stress it is observed a modification or distortion of the symmetries of the patterns due to the deformation of the stressed lattice [37]. Hereafter are outlined, briefly, the principles governing Photoelasticity of naturally birefringent materials and the piezo-optic behaviour of the anisotropic transparent media as well as the diffuse light polariscope technique; its strength and its limitation will be underlined.

3.1 Piezo optic effect

In each transparent material a stress condition changes its optical properties. In isotropic materials the stress tensor, named Lamè ellipsoid, [39] interacts with the structure modifying the spheroid indicatrix to become an ellipsoid (Fig. 3.1).

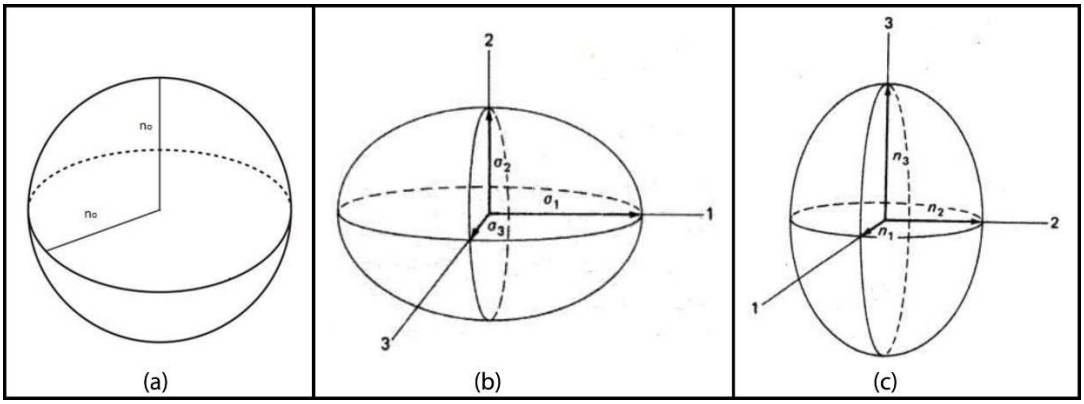

Fig. 3. 1: A graphical representation of the isotropic optical indicatrix interaction (a) with the stress tensor (b) named Lamè ellipsoid [39]**. The spherical indicatrix (a), when a stress state is applied, turns in a general ellipsoid (c).**

The induced birefringence is governed by the Photoelastic constants as follow:

$$n_1 - n_0 = f_1\sigma_1 + f_2(\sigma_2 + \sigma_3)$$

$$n_2 - n_0 = f_1\sigma_2 + f_2(\sigma_1 + \sigma_3) \tag{3.1}$$

$$n_3 - n_0 = f_1\sigma_3 + f_2(\sigma_1 + \sigma_2)$$

Where f_1 and f_2 are the elasto-optic coefficients. Taking into account the last considerations, a stressed isotropic material behaves as a birefringent substance. Managing the equations (3.1) to eliminate n_0, is possible to obtain the following relations:

$$n_2 - n_1 = f(\sigma_1 - \sigma_2)$$

$$n_3 - n_2 = f(\sigma_2 - \sigma_3) \tag{3.2}$$

$$n_1 - n_3 = f(\sigma_3 - \sigma_1)$$

Where f is the relative photoelastic constant. Starting from the equations (3.2), the path difference and the ellipsoid of Fig. 3.1 can be traced and linked to the stress tensor [37]. The crystal lattice symmetries distortion, due to the stress tensor, leads to a change in the light transport and transmission, influencing the electronic displacement. Due to this distortion, the electromagnetic atmosphere is modified, and the light perturbation faces different restoring forces of the oscillating dipoles. The refractive indices distribution changes and the relative optic indicatrix modifies its shape. What is being discussed is actually named Piezo - Optic effect. The magnitude and the shape of this distortion depends on the Piezo-Optic π matrix characteristic [32]. This matrix links the stress tensor to the deformation of the refractive indices distribution and to the dielectric impermeability tensor deformation B [23]. It governs the interaction of the tensile ellipsoid (Lamè Tensor) [40] with the index ellipsoid (Fig. 3.1). An example for tetragonal crystals (the π tensor belongs the point group 4, 4, 4/m) is given in the equation (3.3) [32].

$$\begin{pmatrix} \Delta B_{xx} \\ \Delta B_{yy} \\ \Delta B_{zz} \\ \Delta B_{xz} \\ \Delta B_{yz} \\ \Delta B_{xy} \end{pmatrix} = \begin{bmatrix} \pi_{xxxx} & \pi_{xxyy} & \pi_{xxzz} & 0 & 0 & \pi_{xxxy} \\ \pi_{yyxx} & \pi_{yyyy} & \pi_{yyzz} & 0 & 0 & -\pi_{xxxy} \\ \pi_{zzxx} & \pi_{zzyy} & \pi_{zzzz} & 0 & 0 & 0 \\ 0 & 0 & 0 & \pi_{xzxz} & \pi_{xzxz} & 0 \\ 0 & 0 & 0 & -\pi_{xzxz} & \pi_{xzxz} & 0 \\ -\pi_{xyxx} & \pi_{xyxx} & 0 & 0 & 0 & \pi_{xyxy} \end{bmatrix} \begin{pmatrix} \sigma_{xx} \\ \sigma_{yy} \\ \sigma_{zz} \\ \sigma_{xz} \\ \sigma_{yz} \\ \sigma_{xy} \end{pmatrix} \tag{3.3}$$

The resulting [B] tensor is than given (in a shorter notation) by the expression [35]:

$$[B] = [B_0] + [\Delta B] = [\varepsilon]^{-1} \tag{3.4}$$

The optical indicatrix will modify in with respect to the (2.33). The resulting eigenvalue and eigenvectors of [B] will warp the index ellipsoid by relation $n_i = \frac{1}{\sqrt{B_i}}$ due to the piezo-optic effect. Remembering the relation (2.35), here reported $tan^2\beta = \frac{(\frac{1}{n_y})^2-(\frac{1}{n_x})^2}{(\frac{1}{n_z})^2-(\frac{1}{n_y})^2}$, a variation of the optic angle is observed whenever stress is present. Considering a uniaxial crystal, where $n_x=n_y=n_o$, it becomes biaxial ($n_x=n_o \neq n_y=n_e$) in case of plane stress orthogonal to its optic axis (Fig. 3.2).

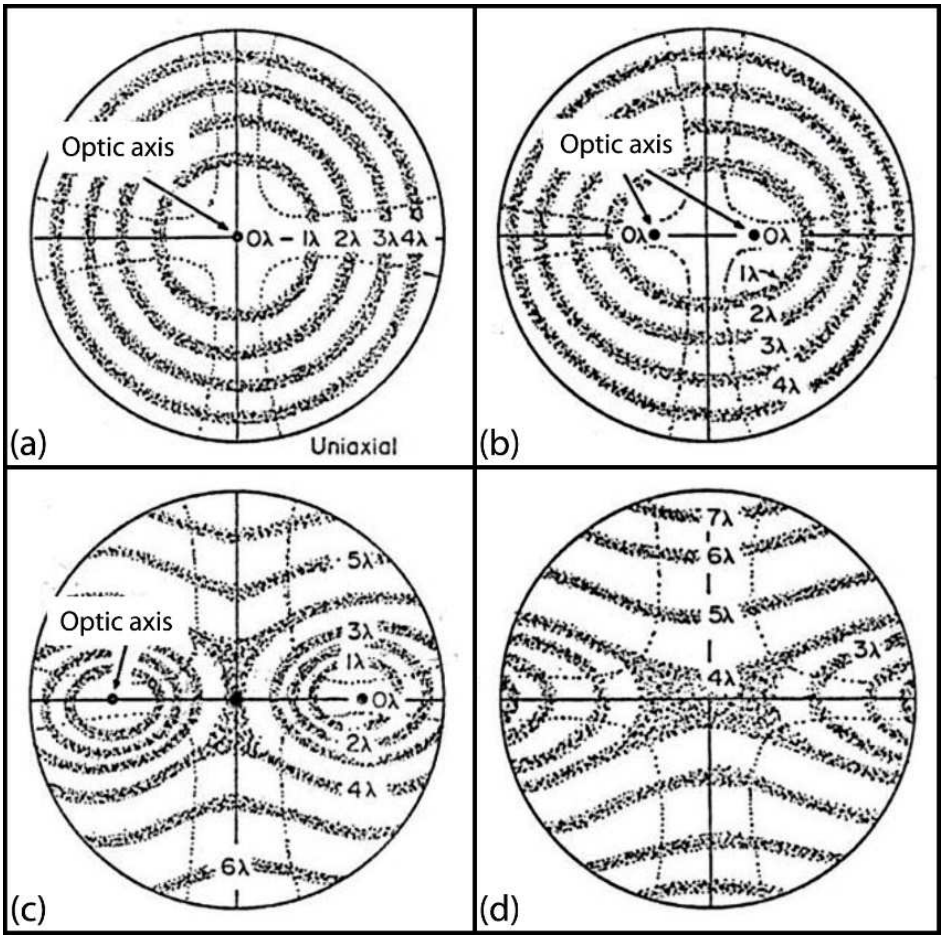

Fig. 3. 2: In the image the induced biaxial behaviour for a uniaxial crystal is shown. The fringes are due to the intersection of the Bertin surfaces with a plane orthogonal to the optical axis. The load increases from (A) to (D), the image clearly shows that the angle between the induced optic axes increases as well.

The construction of the entire Bertin surfaces changes due to the warping of the optical indicatrix [36] (2.37 – 2.46), as it is reported in Fig. 3.3 by the simulation obtained from the expression (2.46).

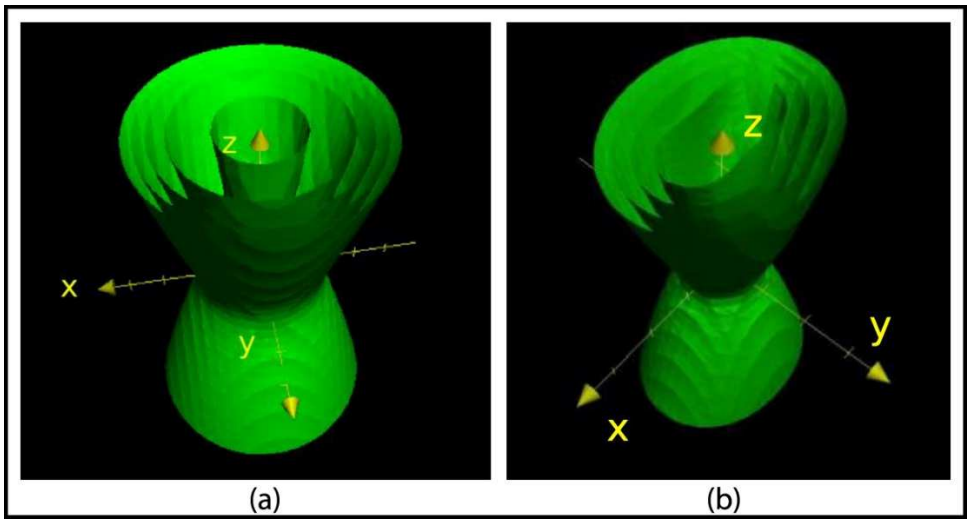

Fig. 3. 3: Simulation of the Bertin Surfaces distortion [36] **by the model in eq. 2.45. In (a) the initial uniaxial state and in (b) the induced biaxial deformation. In (b), the axes are not indicated but the Z direction of the optical indicatrix which coincide with the original uniaxial direction.**

3.2 Diffused light Polariscope

The polariscope is an optical instrument that uses the properties of polarized light [37]. Depending on the type of polarization of the light, it is called plane polariscope and circular polariscope. In plane polariscopes polarizers are used plans or linear: the component parallel to the polarization axis is transmitted, the normal one is absorbed or subjected to total internal reflection. The intensity of the radiation transmitted, if it was polarized, is equal to:

$$E_a = a\cos(\omega t)\cos(\alpha) \tag{3.5}$$

where α is the angle between the vector light and polarization axis. The most common configuration is one in which the axes of the two polarizers are orthogonal to each other: in this case we speak of cross-or dark-field polariscope. The advantage of this arrangement is that all that is observed in the polariscope is due to the interaction between light and crystal: the light not subjected to phenomena of birefringence cannot exceed the analyser since the angle between the light from the polarizer and the analyser is π/2 and so, form the previous equation we obtain E_a=0 (IE dark). If the analyser is parallel to the polarizer, the plane polariscope can be named bright field, with obvious meaning of the term.

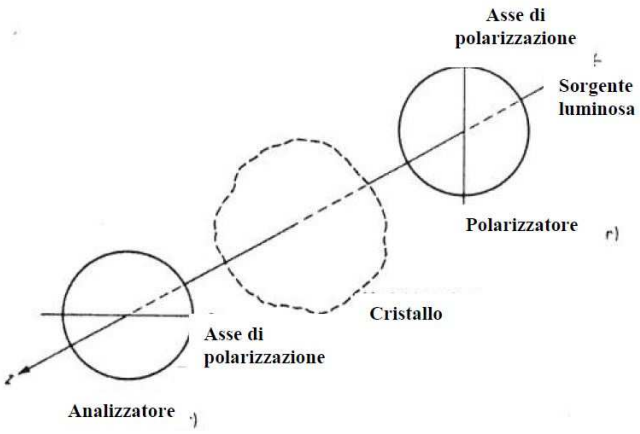

Fig. 3. 4: Plane polariscope scheme

Is possible also to use circular polarization to analyse the optical anisotropy of a material or a crystal. This is achieved by inserting, immediately after the polarizer, of a plate λ/4 oriented +π/4 than the polarizer. This plate is nothing but a slab of anisotropic material in the plane orthogonal to the axis of the polariscope with a "fast" and "slow" axis along which is decomposed the incoming polarized wave. The thickness is such that, for a certain wavelength, the phase shift of the two output components gives rise to circular polarization, as is clear from the composition of with phase difference of π/2. Then add a second λ/4 plate after the sample that is oriented so that the “fast” axis and the “slow” axis are parallel respectively to the “slow” axis and to the “fast” axis of λ/4 plate fast in order to reverse the effect of the first retardant foil. What is possible to see after the analyser is only given by the passage in photoelastic sample. Circular polariscope scheme is represented in the following Fig. 3. 5.

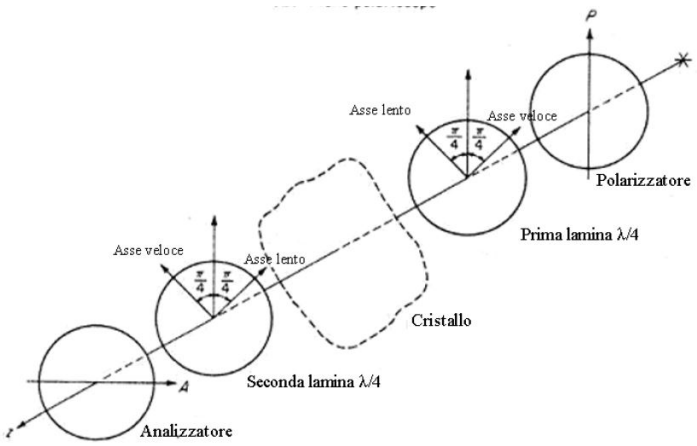

Fig. 3. 5: Circular polariscope scheme

3.1.1 Isotropic materials

In isotropic is not observed the phenomenon of birefringence, unless they are charged. Also in the isotropic, bonding forces, and then the speed of light, are the same in all directions; in this case the surface speed of rays and the optical indicator will be spheres.

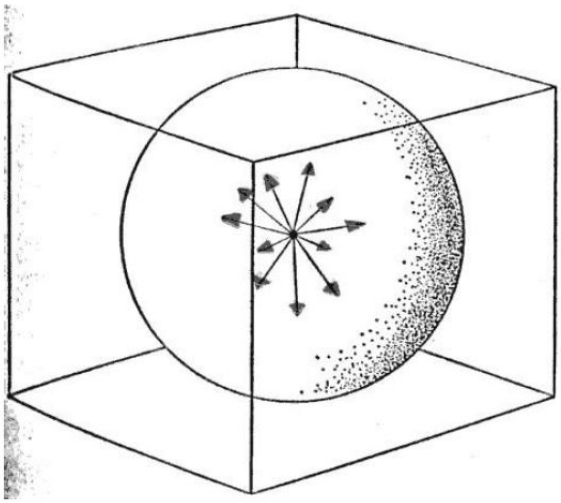

Fig. 3. 6: Velocity surface of isotropic crystals.

3.1.2 Birefringent crystals

For uniaxial crystals this phenomenon can be described by the following diagram:

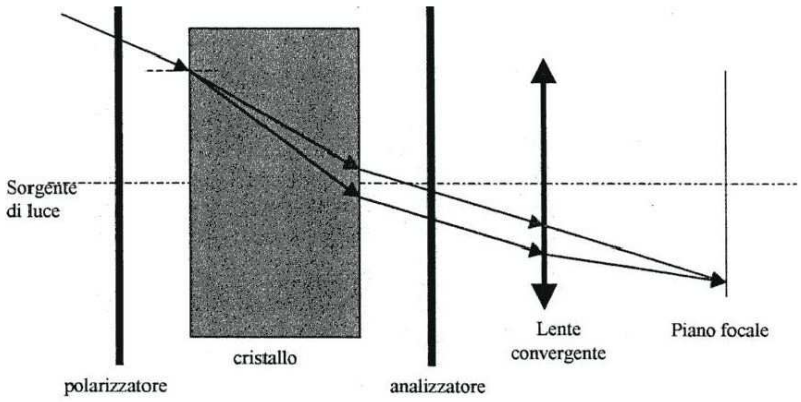

Fig. 3. 7: Phenomenon of birefringence in uniaxial crystals.

The phenomenon is due to two different refractive indices in a crystal if the light beam passing through it is not directed along the optical axis as we have above explained via the index ellipsoid. When the two rays are reassembled on the focal plane, their overlap generates an intensity which depends on the phase shift Δ equal to [23], [28], [41]:

$$\Delta = \frac{2\pi h}{\lambda cos\vartheta_2}(n_e - n_0) \quad (3.6)$$

where h is the thickness of the crossed crystal, θ2 is the angle formed by the median trajectory of the rays refracted, and n_o and ne ar_e the two refractive indices, λ is the wavelength of light. To express the indices n ' and n ' ' according to the main indexes of the crystal, we use Fresnell equation [22], [24]:

$$\frac{S_x^2}{v_v^2 - v_x^2} + \frac{S_y^2}{v_v^2 - v_y^2} + \frac{S_z^2}{v_v^2 - v_z^2} = 0 \quad (3.7)$$

where s = (s_x ,s_y ,s_z) is the vector indicating the direction of wave propagation (through its components along coordinate axes), $v_k = \frac{c}{\sqrt{\mu\varepsilon_k}}$ (with k = x, y, z) is the speed along the three main axes and $\overline{v_v} = \frac{c}{n}\bar{s}$ is the phase speed. Whit Fresnell equation written in terms of refractive indices, we have [28]:

$$\Delta = \frac{2\pi\rho}{\lambda}(n_e - n_0)sin^2\vartheta \quad (3.8)$$

Where $sin^2\vartheta = S_x^2 + S_y^2$

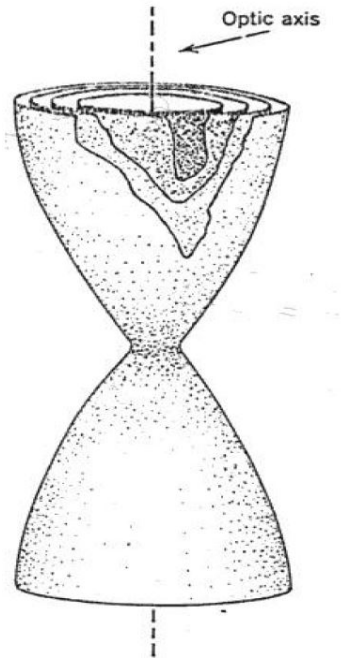

Fig. 3. 8: Surfaces of Bertin or equal delay for a uniaxial Crystal.

This means that propagation directions which give rise to the same phase shift are axisymmetric from the optical axis. Extending such consideration to any space is possible to get a set of surfaces that focus in the optical axis, known as Bertin surfaces (Fig. 3.8) representing the places where is present equal delay Δ and presented to the side [35]. These curves are called isocromate because in case of polariscope with white light source, the surfaces with equal delay present the same colour (chromatic dispersion phenomenon). Observing the interference patterns by collecting light from them coming on a focal plane is making sections of these surfaces that vary in shape with the orientation of the plane of observation. If the observation takes place parallel to the optical axis the fringes will have a circular profile (section of isocromate orthogonal to the optical axis) (Fig. 3.9).

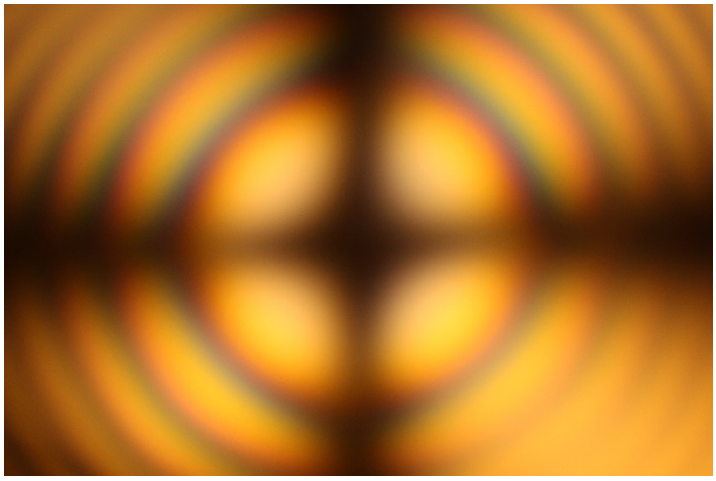

Fig. 3. 9: Example of acquisition with diffused light polariscope for an uniaxial crystal.

In this work we will always try to observe the interference fringes parallel to the optical axis or in the direction of acute bisectrix of optical axes in case of biaxiality. If it increases the thickness of the crystal through, observe the interference patterns is equivalent to dissect the curves of Bertin at greater distance along the axis: the isocromate will widen. We must distinguish between enlargement of the image of interference due to the thickness of the Crystal and what happens away from the surface of emergence of light, due to the refraction of the light leaving the Crystal which has generally significantly higher refractive index than air. In addition to isocromate, the plane polariscope forms another sort of interference pattern that overlap at isocromate: the isogyres. They are black or grey overlapping areas at isocromate, and constitute the locus of points in the same direction of vibration waves [28], [35]. If the optic axis of the crystal in question coincides with the axis of the polariscope, and then the surface from which emerge the light rays is normal to this axis, the isogyres appear as a black cross. The accuracy of this cross will be used in this work as an

index of alignment with the optical axis. For the phenomena of double refraction in biaxial crystals is possible to repeat analytical assessments mentioned for the uniaxial case [35]. The biaxial Bertin Surfaces representation are in Fig.3.10.

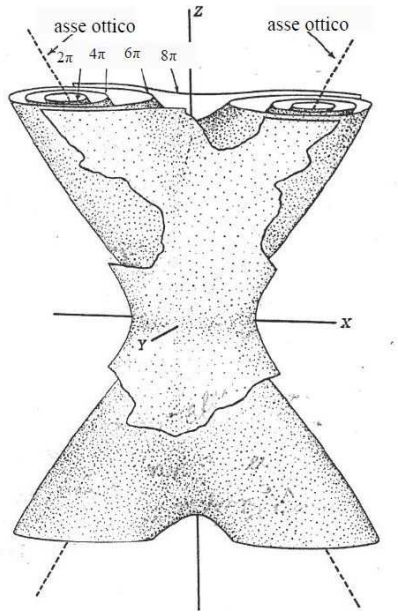

Fig. 3. 10: Bertin surface representation for biaxial crystals.

Observing a biaxial Crystal through the Conoscopy, we obtain the following images, different depending on the type of light source and type of polarization (Fig. 3.11).

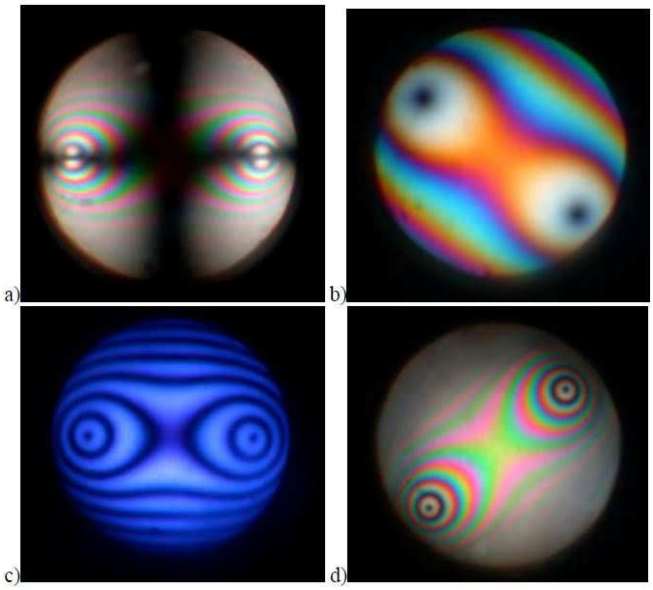

Fig. 3. 11: a) White light and plane polarization, b, d) white light and circular polarization oriented 45° c) monochromatic light and Circular Polarizer.

Is already described in the piezo optic effect that the optical axes give an interference pattern of the type shown in the Fig. 3.12:

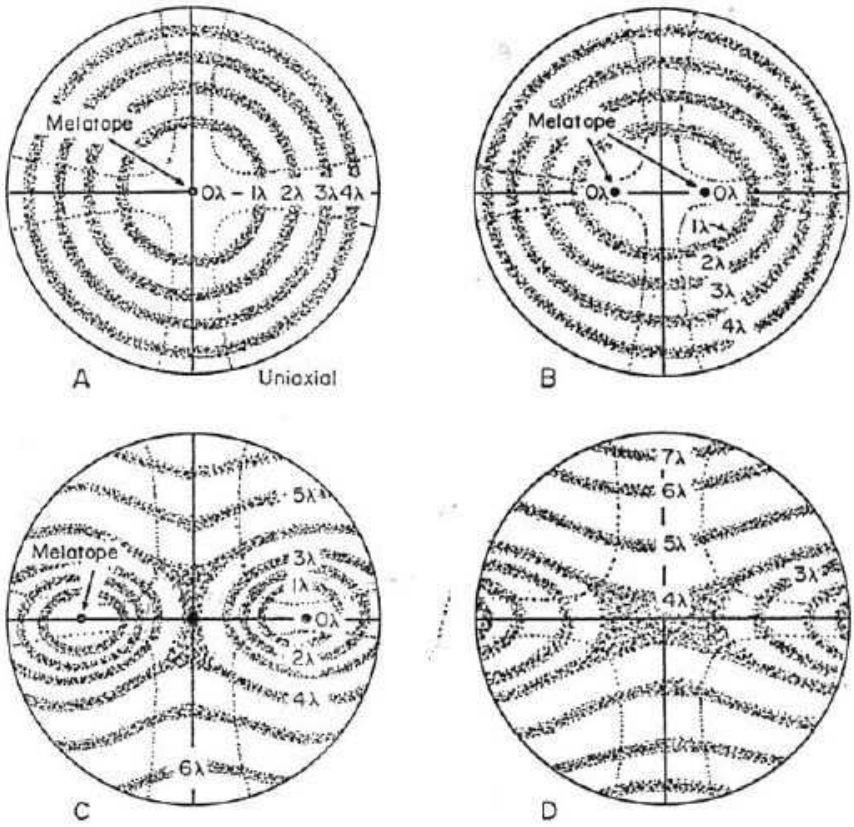

Fig. 3. 12: Isochromatic curves for biaxial crystals, with different optical corners.

If the Crystal of PWO is in a stress-free condition, is possible to see a Fig. 3. 12a type. The load induces changes of the indexes, and then changes on the angle between the optical axis. So, the fringes shape of a crystal, passing from a low to a heavy load, becomes gradually from the B type to the D type. In fact, stress state deforms the Bertin surface and induces the biaxial behaviour accordingly to [27]. Consequently, the fringe pattern becomes like one of the possible example situations in Fig. 3.9 - 3.11. This pattern can be considered composed by Cassini like curves, expressed like follow:

$$[(x - a^2) + y^2][(x + a^2) + y^2] = b^4 \quad (3.9)$$

Where a and b are the fringe parameters described in Fig. 3.13.

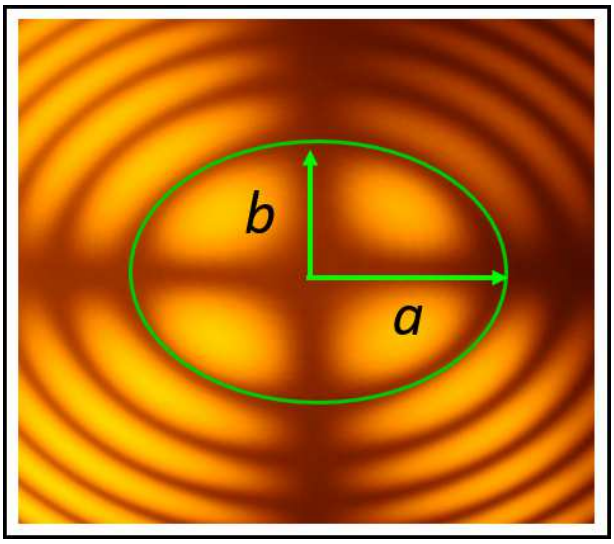

Fig. 3. 13: Fringe pattern acquired with diffused light polariscope, with superimposed the distances a and b of the major and the minor semi axis.

In case of the distortion is not too high, as it usually is the residual strain fields encountered in crystals, is possible to consider the induced Cassini curves as ellipses with negligible error, therefore it is convenient relate the stress to the ellipticity of the fringes [42] as:

$$\Delta\sigma = \frac{C}{f_\sigma} \tag{3.10}$$

Where f_σ is the photoelastic constant measured in the calibration step [26] which depends by the π matrix and, linearly by the thickness or optical path [26] and C is the ellipticity evaluated by the ratio of the major and minor ellipses semi axis (Fig. 3.13) and as [42]:

$$C = \frac{b}{a} - 1 \tag{3.11}$$

However, if we have a more complex stress distribution, the fringes pattern will be complex as well [27]. An example of this cases is shown in Fig.13. It is possible to explain these observed non symmetrical patterns, by inducing a known stress distribution by a four points bend test [28] (Fig. 14a). In this manner is possible to observe a pear-like shape, which is physically related to the stress gradient along the vertical axis of the sample (Fig.15b).

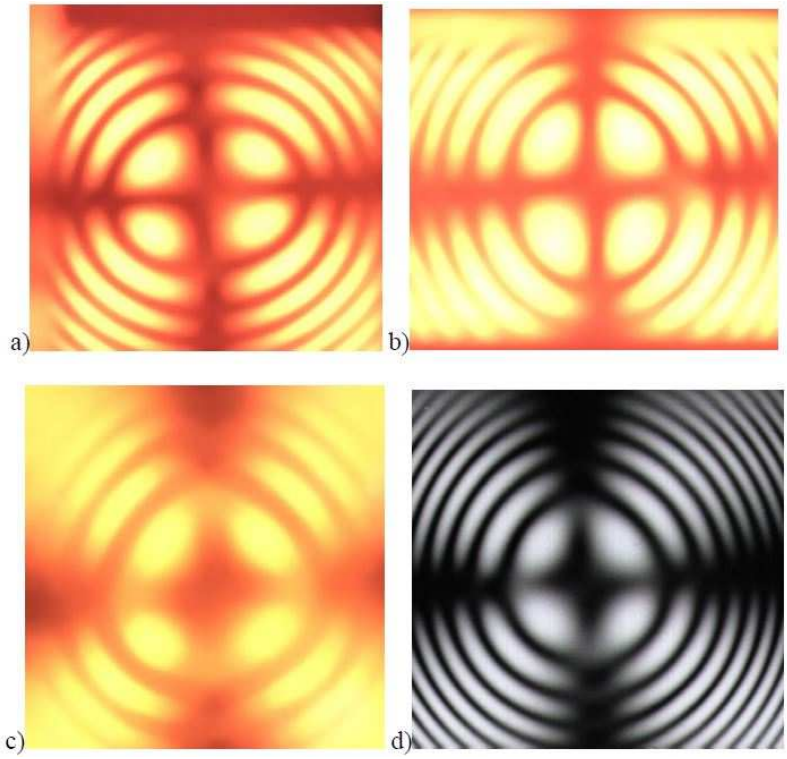

Fig. 3. 14: Sample subjected to various load levels.

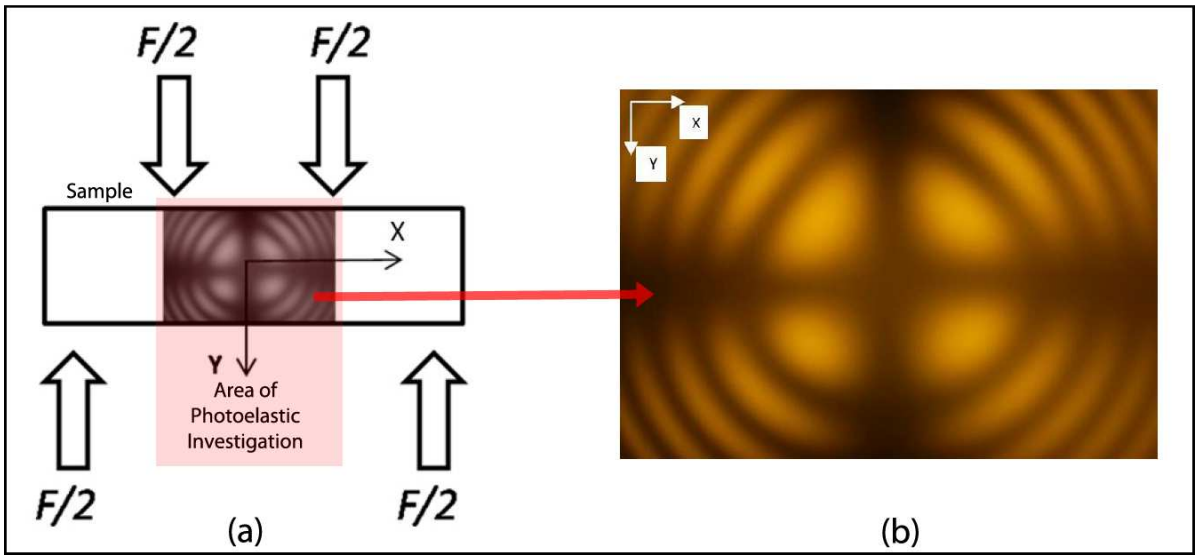

Fig. 3. 15: a) Scheme of a four-point bend test applied on a crystal in order to induce a stress gradient. B) Photoelastic acquisition of the relative stressed area of the sample.

The fringe pattern is due to the classical antisymmetric distribution of σ_x along the Y axis and has been modelled in [27]. However, from an image like this, it remains difficult to extract the actual stress distribution in the sample. For example, it is not easy to detect the position of the neutral axis (σ_x =0) in the fringe pattern. It is clear, therefore, that a complex stress distribution is coupled to complex fringe shape to analyse. [27]. Moreover, in the case of internal stress this technique

“mediates” the stress on a relative large volume so punctual magnitude is difficult to be detected, being this method, as demonstrated, sensitive to the overall condition of the crystals. The environmental conditions like vibration, temperature and crystal surfaces polishing are not critical for this measurement system but it presents some limitation listed hereafter:

- Considering that the Crystal is fully illuminated, it is difficult to refer the pattern to a specific location inside the crystal volume. Considering this, the method is definable intrinsically a volume method, and does not allow for a spatially resolved local inspection. This affects negatively the spatial resolution of the measurement [41].
- Regarding the sensitivity, considering what mentioned above, it is difficult to detect concentrated stress, smooth variation and local distribution of the residual stress. These condition, as well as local defect, are averaged on the overall probe volume producing a unique pattern from the entire volume [28].
- Moreover, as already mentioned, from a complex stress distribution, a complex shape of the fringe pattern derives. Therefore, it is difficult to analyse it so to get information about the spatial distribution of stress and identify local defects [29].

These aspects negatively affect the measurement sensitivity and spatial resolution. But therefore, it remains a method to have a reliable but coarse evaluation of the birefringent media condition.

Chapter 4

4 Innovative contribution: Laser techniques

In this chapter, the contribution and the developed methods to overcome the limitation introduced in the previous section, will be given in detail. The developed methods and systems have improved the capability of a reliable and precise analysis. The systems are provided of a dedicated algorithm so as to analyse the fringe pattern images with a low uncertainty. In the first step, the sensitivity and the resolution of the Photoelastic measurement has been improved by the developed laser conoscopic method, supplied with the analysis of the fringes acquisition system. Then, the new conoscopic method in has been adapted to observe uniaxial crystals orthogonally to the optic axis. To achieve this, a new theory has been developed that allows us to understand the new different type of observable fringe pattern. With the new type of fringe pattern, is also presented the new fringe acquisition system. The following step is about the development of a technique (Sphenoscopy) which fastens the inspection and simplifies the analysis of the crystal state in each direction of observation. At the end is presented a new technique developed for the detection of geometrical non-coplanarity inside the samples.

4.1 Laser Conoscopy along the c crystallographic axis.

4.1.1 The technique

The advantage to use a laser light source is that it allows us to control the probe volume into the birefringent media and to form a fringe pattern which depends on the local stress state. This is obtainable by illuminating the crystal with light rays originating from a point and forming a cone of light[2], [28], [41]. In case of uniaxial crystals, the theory of the conoscopic observation leads to the following analytic equation that expresses the loci of points where the recombined rays get an equal delay Δ [23], [28], [41]:

$$\Delta = \frac{2\pi h}{\lambda cos\theta_m}(n_e - n_o)sin^2\theta \qquad (4.1)$$

where θ and θ_m are, respectively, the incident angle of the light rays bundle and the middle angle between ordinary and extraordinary rays, h is the crystal thickness, λ is the light wave length of the

laser source, and finally n_o and n_e are respectively the ordinary and extraordinary refraction indices. Considering this [41]:

$$\Delta = 2\pi N \qquad (4.2)$$

dark fringes are obtained if N is an integer [23]. A qualitative representation of the iso-delay curves is represented in Fig. 4.1 where it can be observed that the delay depends on θ and h for a given refractive indices, which depends on the crystal type.

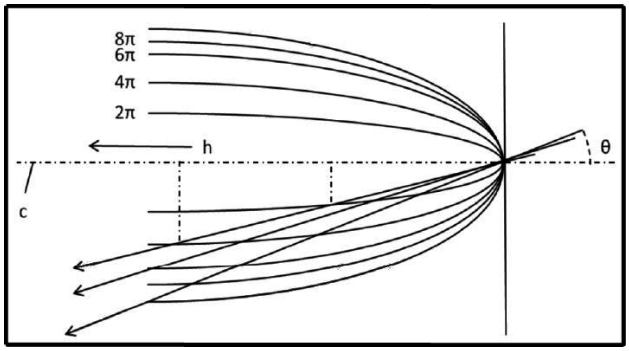

Fig. 4. 1: The isodelay curves are labelled with the 2πN and the optic-axis is the dotted line (c); with a given refractive indices difference, that is a characteristic of the crystal specie, the number of fringes observed depends by the thickness h and by the angle of the impinging light θ.

The optical system that realize the concept is designed and arranged with the intent to have the possibility to measure the tensional states with a controlled spatial resolution. The measurement system[2], [28], [41], schematized in Fig. 4.2, is then composed by a laser polarized light source (a) collimated and coherent. After the source is mounted the lens (b) and (c) that represents the optical beam expander that increases the beam dimensions. Then, between the sample and the beam expander, is aligned a converging lens (d) that turns the beam into a cone of light, converging the rays at its focal point.

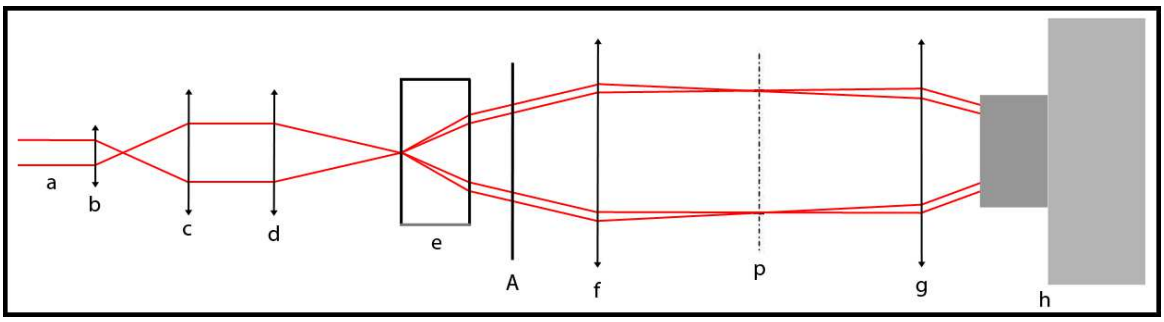

Fig. 4. 2: Set up of the laser polariscope for the conoscopic technique. (a) the starting laser beam of coherent monochromatic polarized light represented as a pair of parallel lines is enlarged by a beam expander system composed by the two converging-diverging lens (b) and (c). Then the laser beam is focused by (d) on the sample surface, producing the conoscopic probe volume

inside the crystal. The rays that emerges from the specimen pass through the analyser (A) in dark field respect to the laser polarization. Then the lenses (f) and (g), that have the same focal plane (p), makes the rays parallel and directed to the macro lens of the camera (h). This camera lens is set with the focal to the infinity, therefore the conoscopic fringes are formed on the C-MOS sensor of the camera.

The rays that emerges from the crystal surface, pass through the analyser (A). Then the lenses (f) and (g), that have the same focal plane (p), makes the rays parallel and directed to the macro lens of the camera (h). This last lens is focused to the infinity, thus the conoscopic fringes are formed on the C-MOS sensor (Fig. 4.3) [22].

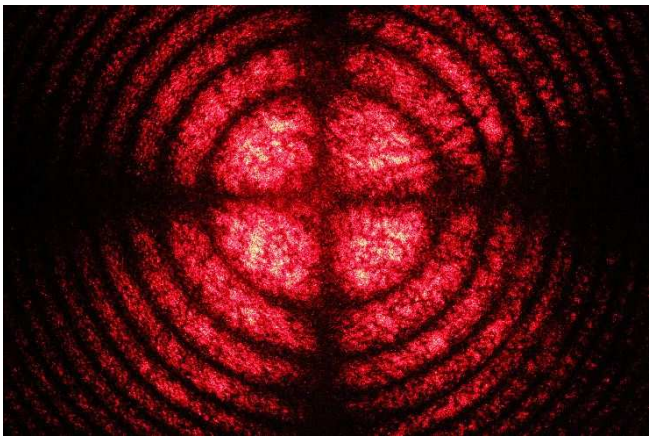

Fig. 4. 3: Example of interference fringes acquired with the laser conoscopic system. From this acquisition it is possible to see three fringe order.

The technique has numerous advantages. The first is that the pattern is due uniquely to the illuminated volume (Fig. 4.4) which can be managed reducing its dimension [2], [28], [41]. In this manner the sensitivity and the spatial resolution are largely enhanced.

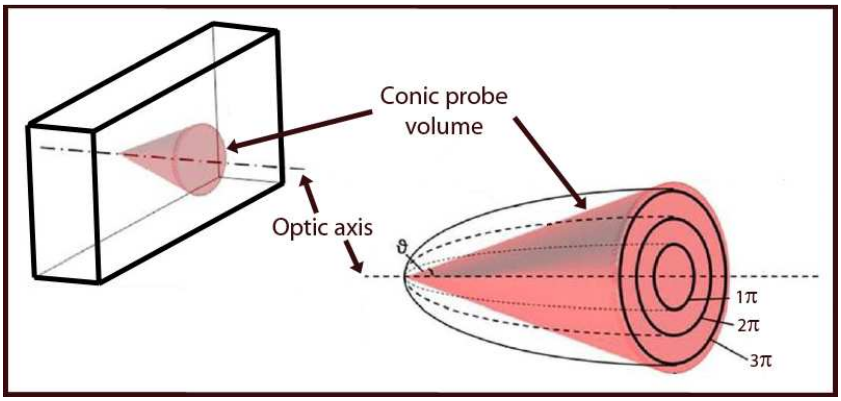

Fig. 4. 4: Schematic representation of the conic probe volume and the generation of the relative fringe pattern (observation along the optic axis). Differently from the diffuse light polariscope, by laser Conoscopy the light is confined in a specific part of the sample volume and with known angles. By the Bertin surfaces, the fringe pattern is due to the angle of incidence and the thickness of the sample. The phenomenon is schematically represented in the right side of the figure.

In order to be more precise, the spatial resolution is determined by the dimension of the inlet spot diameter and the outlet spot diameter, which are defined by the cone angle, the diffraction indices and the thickness [22], [28], [41]. In fact, due to the diffraction, the cone tip is not a point, but it is rather a small circle, having diameter depending on focusing optics and laser wavelength, in the order of 1mm. Regarding the refractive indices influence, these are a limit for the maximum spatial resolution. In fact, referring to Eq. 2, if the difference between the refractive indices decreases, the angle of the light cone must be increased to observe the first fringe order. Concerning instead the sample thickness, with reference to the same Eq. 2, if the thickness h is large, then the cone angle could be reduced to observe the first order. Another advantage of using this technique, always linked to the reduction of the measuring cone, is that concerning the distribution of stress within the sample [28], [41]. Whatever the stress distribution is, the volume can be reduced in dimension until the stress can be approximated uniform inside the probe cone. Therefore, in this condition, no complex pattern shapes are expected[28]. In particular in this condition of observations along the optic axis only circles and ellipses are expected. This controllable probe volume again, as ulterior advantage, allows to get a precise study and characterization of the material; e.g. the number of fringe orders to generate can be decided a priori verifying the mathematical model. In order to summarize, using the advantages of the increased spatial resolution and the easiest pattern shapes (circles and ellipses), a very detailed map of stress distribution can be carried out from a sample by scanning a grid of points [4]. The spatial resolution of the grid is principally limited only by the position system of the crystal, being the maximum optical resolution of the cone very high respect to the position system resolution. By considering the load homogeneous in each observed point, it is possible to carry out a local evaluation of the stress by using the (3.10). Point by point, the fringes have an ellipticity ratio C that depends on the value of the local stress. In particular, in a load condition (Fig. 4.5a), the measured ellipticities C vary along the stress gradient observable along y [41].

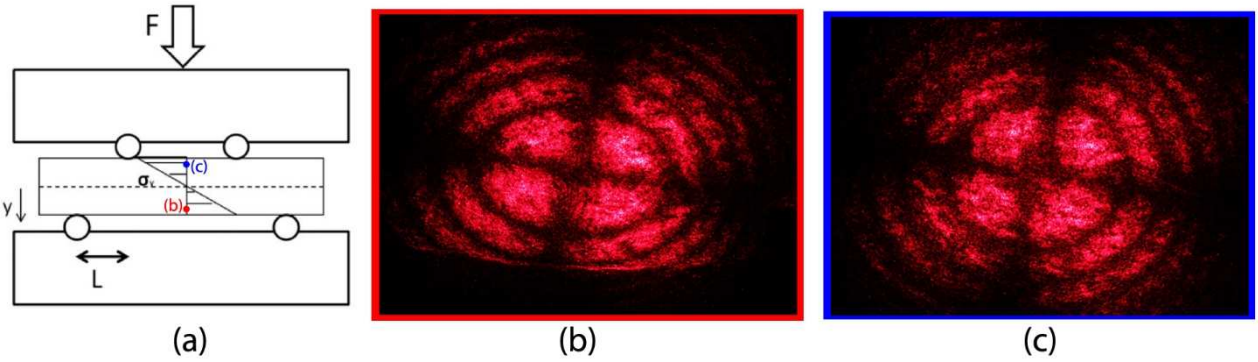

Fig. 4. 5: (a) using a four points bend test is possible to obtain Images from the tensile area (b) and the compressive area (c). In this way it is possible to observe how the ellipticity parameter varies with stress, observing two different points. Moreover, being in the condition of two different states of stress (tensile and compressive), the π/2 rotation of the ellipse axes is evident.

Furthermore, the ellipses in a tensile stress condition (Fig. 4.5b) is rotated by π/2 with respect to the ellipses belonging to the compressive zone (Fig. 4.5c). Therefore, the fringe pattern contains complete information on the stress magnitude and sign of the investigated point.

4.1.2 Fringe analysis Algorithm

The development and the optimization of the fringe analysis algorithm is useful for a better stress evaluation and a more accurate material knowledge. This type of measurement is pointwise; accordingly, a complete material inspection needs a lot of images acquired and a lot of time for their processing. Furthermore, respect to the diffused light polariscope, laser polariscope images are affected by speckle noise (Fig. 4.6) [1].

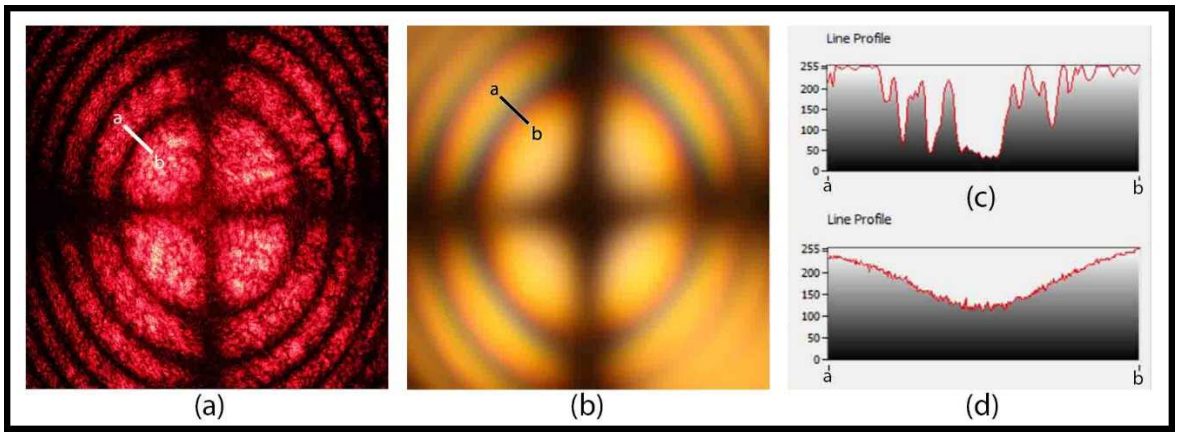

Fig. 4. 6: Different acquisitions coming from (a) laser light Conoscopy and diffused light polariscope (b). In each image source a segment AB that cross an interference fringe is traced. By the study, in each case, of the light intensity distribution along these segments, it si possible to observe different behaviours. In (d), that corresponds to the diffused light case, we have a smooth curve without noise. Contrarywise in (c), that correspond to the laser case, it is possibe to observe a lot of noise that disturbs the trend of the curve. This noise is called spackle noise and must be removed in order to obtain information from the image.

Considering these aspects, the key points to obtain an optimized fringe analysis algorithm are, principally, the speckle noise reduction and find a comfortable way to manage the big number of acquisitions. All with the final aim of uncertainty reduction of the measurement system. The first step in order to calculate the ellipticity value is to define a measurement area called region of interest (ROI). This area can be defined manually by the user, but in this case the selection is not repeatable since it depends by the user sensitivity. This aspect is overcome if the system is able to find that region of interest automatically. An algorithm that is capable to find a desired area is the pattern matching system [1], [43], [44]. This kind of method works by superimposing a template over the image until it matches the required feature (Fig. 4.7).

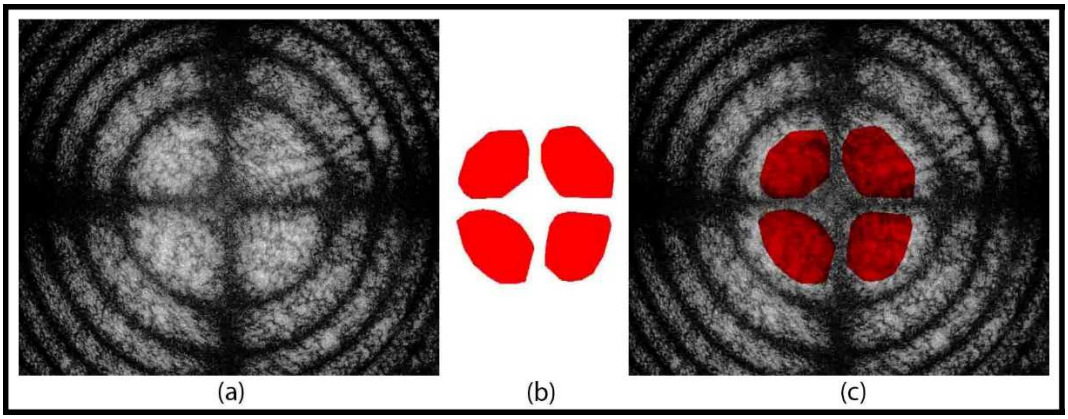

Fig. 4. 7: Pattern matching system used to find automatically the region of interest inside the image. Starting from the acquired image with a single-color plane (a), is used a template (b) in order to find in the acquisition source the desired feature. The system superimposes the template over the image until it finds the better correspondence (c).

In our case the requested reference feature, to find the desired ROI, is the area enclosed from the smallest elliptical fringe. In order to to make the system working, it is strictly important to find a right template for the pattern matching that works with all types of images. This aspect is crucial because the required feature has no regular geometry that changes between an image with the others. Obtained the layout with the best template, the software can work completely autonomously to find the desired area. In this good results in terms of uncertainty reduction have been achieved. Once that the pattern matching worked, the system finds the ROI of interest where the system will carry out further calculations (Fig. 4.8).

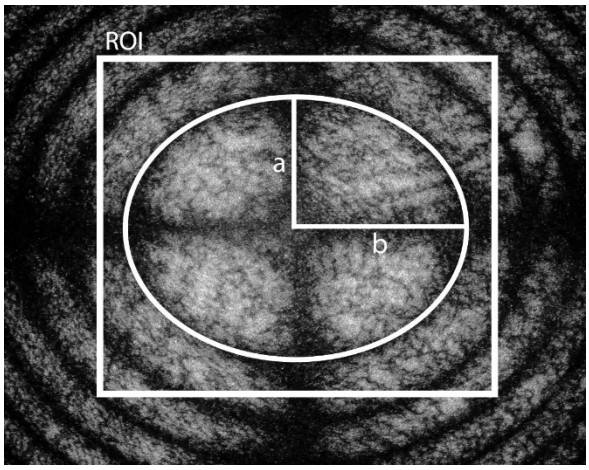

Fig. 4. 8: Acquisition source with superimposed the automatically detected ROI where the system will perform further calculus operations.

Through removal of the human factor from the ROI selection, as well as obtaining a more precise system, it is also possible to perform a sensitivity analysis by software, being every operation automatic and repeatable. Now that the area that enclose the first isocromate fringe is fixed, it is possible to start finding the best fitted ellipse. In order to proceed in this way many points are necessary from the first order fringe, that can be extracted using the tool that estimate the pixel light intensity level along a drawn line on the image [43], [44]. The system therefore draws several lines inside the ROI that cross the first fringe order (Fig. 4.9a). Then, studying the line profile of light intensity level inside each drawn line, the points that belongs the first fringe order are found as points of minimum light intensity (Fig. 4.9b) [1].

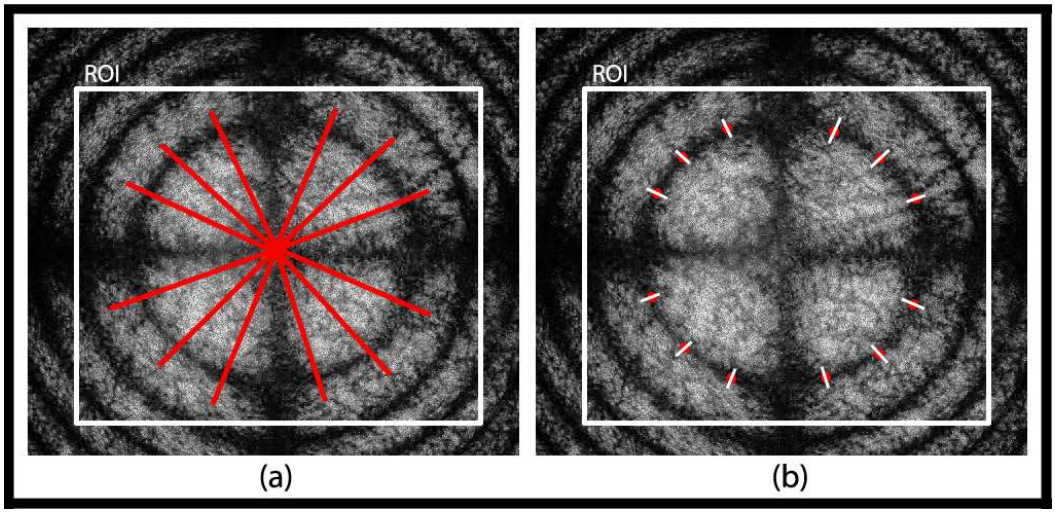

Fig. 4. 9: Starting from the found ROI, (a) the system draws several lines that cross the first fringe order inside this area. (b) Whereupon, using the tool that estimate the pixel light intensity level along a drawn line on the image, the points that belongs the first fringe order are found as points of minimum light intensity.

The problem that involves this operation is that this type of images is affected by spackle noise (Fig. 4.6a -c). So, it becomes crucial, before of the operations aimed to find the minimum points of light intensity, to manage the image with the right filters that reduce this type of noise. Otherwise it is impossible to determine with a good uncertainty the minimum from the line profile of light intensity. The image processing starts with the colour plane extraction that corresponds with the laser source wavelength [43], [44]. In our case the laser is He-Ne type, so the red plane is extracted. Then the algorithm works on the grayscale using a look up table to increase the contrast [1], [43], [44]; it is strictly important to set the right parameter in this type of filter otherwise is possible to lose some information about the minimum of line profiles and consequently the uncertainty increase(Fig. 4.10).

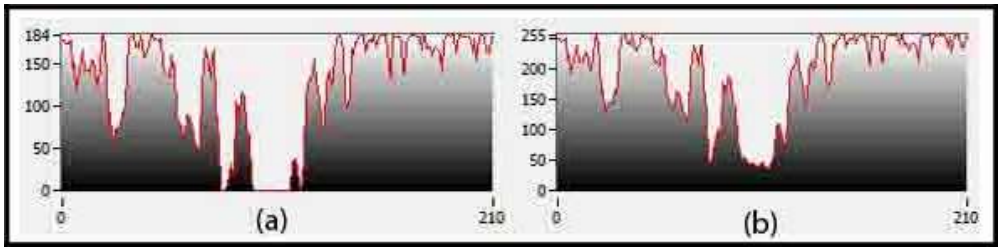

Fig. 4. 10: Different level of contrast applied on the same area and studied with the line profile of light intensity. In (a) we have a bad application of the filter that produces a saturation on the minimum level. In this case is not identifiable the minimum of light intensity. Contrarywise in (b), where the filter is applied in the right manner; we have no light saturation, but nevertheless there is an excellent level of contrast between the maximum and minimum brightness values.

In Fig. 4.10a we have a bad application of the contrast regulation, instead of a point of minimum light intensity we have a flat area that correspond to the zero value of luminosity. In Fig. 4.10b, instead, we have no light saturation, but nevertheless there is an excellent level of contrast between the maximum and minimum brightness values. The next step is the application of a low-pass filter called median to the image [1], [43], [44]. This filter allows us to obtain an image with considerable noise reduction without significant alterations of the features passing from Fig. 4.11a to Fig. 4.11b.

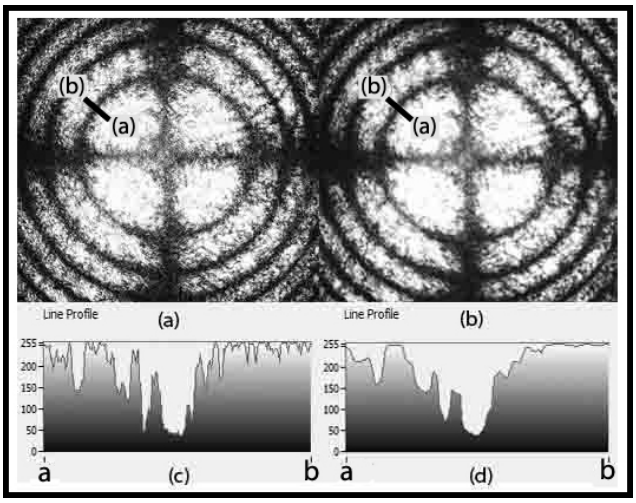

Fig. 4. 11: Comparison between the images before the application (a) and after the application of the median filter (b). In each image is traced the same segment AB that cross an interference fringe. In this manner is possible to study the differences in the line profiles of light intensity relative to the image without (c) and with median filter (d). This type of filter is principally used to remove the spackle noise from an image. This type of noise can be interpreted as quick variations of light intensity. These very fast variations, that are visible in the left line profile, can have an amplitude lower than the minimum light intensity of a dark fringe. In the right line profiles these quick spikes are transformed in a smoother line through the median filter. It is important to not exceed with the median filter to remove completely the noise because it is also important to not modify too much the line profile as it would alter the measurement results.

This type of filter mainly works by assigning to each pixel the median value of its neighbourhood, removing isolated pixels. Principally it is used to remove the speckle noise from an image, without disturbing the clean pixels. This peculiarity is opposed to linear low pass filters, that will also reduce the noise, but spreading out the effect of noisy pixels rather than isolating and removing them. It is important to specify that, passing from the condition in Fig. 4.11c (before the filter application) to the condition in Fig. 4.11d (after the filter application), the line profile curve doesn't become completely a smooth curve. This because, with the filtering operation, is important to remove the spackle noise that can be interpreted as a quick variation of light intensity. These variations together may produce in the line profile graph spikes highest than the searched minimum of light intensity. These are the peaks that must be removed but taking into account also that it is important to not modify too much the line profile as it would alter the measurement results [1]. Beyond that, the dimensions and the shape of the median filter must be chosen considering also the acquisition parameters, the dimension of the image and its resolution. This process of image improvement is aimed to fit an ellipse equation by the line profiles that cross the first order fringe, with an acceptable uncertainty level. The next step is therefore a test of the fitting system to understand how many points are needed to fit an ellipse with an acceptable level of uncertainty. To obtain this parameter, starting from a defined ellipse, a random noise with a standard deviation of 0.03 is

added. Then, starting from this noisy source, a number of increasing points are chosen to fit the ellipse (Fig. 4.12).

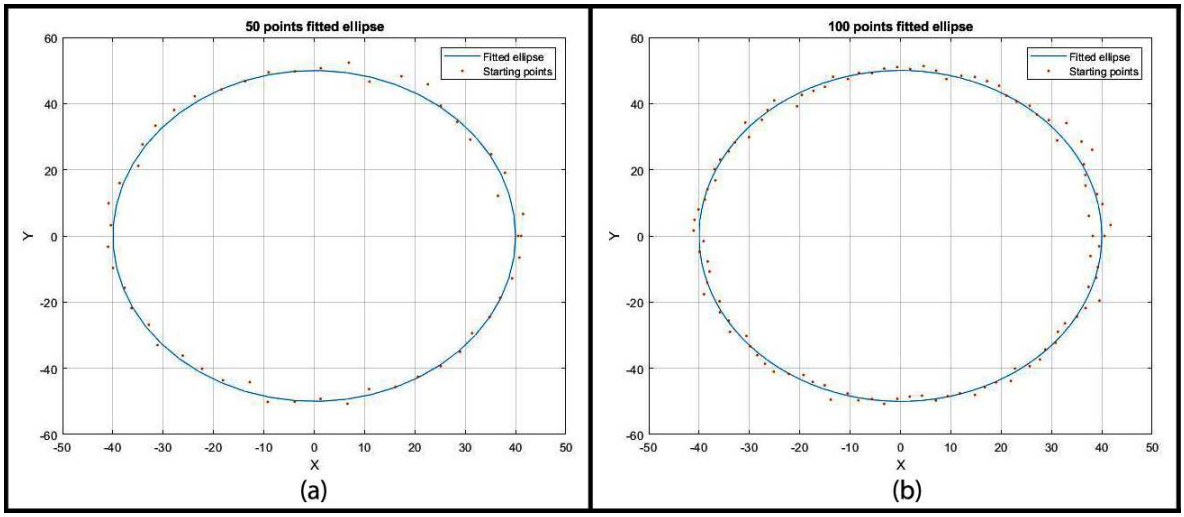

Fig. 4. 12: Representation of the same ellipse fitted using different number of points. In (a) the ellipse is fitted using 50 points, instead in (b) the ellipse is fitted using 100 points.

By iterating this process using several ellipses with the same defined noise, is studied the relation between the number of points used to fit the ellipses and the ellipticity standard deviation of the fitted ellipses, respect to the defined starting ones (Fig. 4.13).

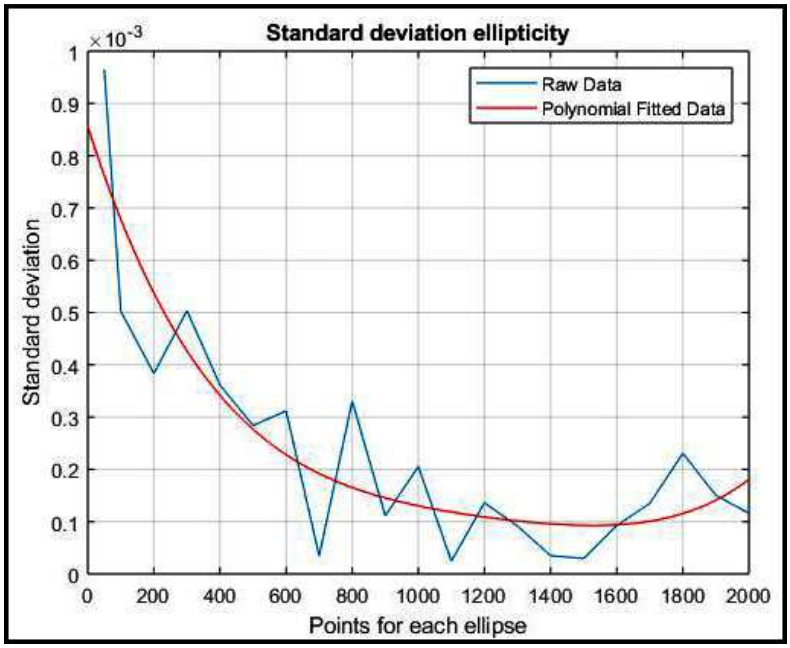

Fig. 4. 13: In the graph is studied the correlation between two parameters. The first one is the standard deviation between the fitted and the real ellipse. The second one is the number of points used to fit the ellipse. In is clear that until the 1000 points is possible to obtain an improvement of the standard deviation. Exceeding this parameter, the standard deviation become not stable, therefore the computation time increases without obtaining any advantage.

Using 1000 points is possible to obtain a standard deviation level that is not improvable, even duplicating the numbers of points. Therefore the system, once the ROI has been automatically selected and the necessary filters are applied, searches for 1000 points to fit the searched ellipse. This ellipse, obtained through the fitting of the points detected as described in Fig. 4.9, is defined by five parameters that are the two coordinates (x, y) of the centre, the length of the mayor and the minor axis and the angle of rotation with respect of the horizontal line. The next step is aimed to a better choice of the ellipse function, in order to reduce further the uncertainty on the ellipse detection. Regarding the five parameters that defines the first attempt ellipse, they are randomly varied in order to generate several ellipses closes to the starting one with a selected number of iterations [1]. The goal of this approach is to find the ellipse with the lowest pixel intensity value along its full boarder. This is achieved by an optimization process that is composed by two similar phases [1]. In the first one, the algorithm generates numbers of ellipses and select the one with the minimum total intensity. The second optimization phase evolves like the first, but the new ellipses produced are close to the best ellipse founded in the previous phase (Fig. 4.14).

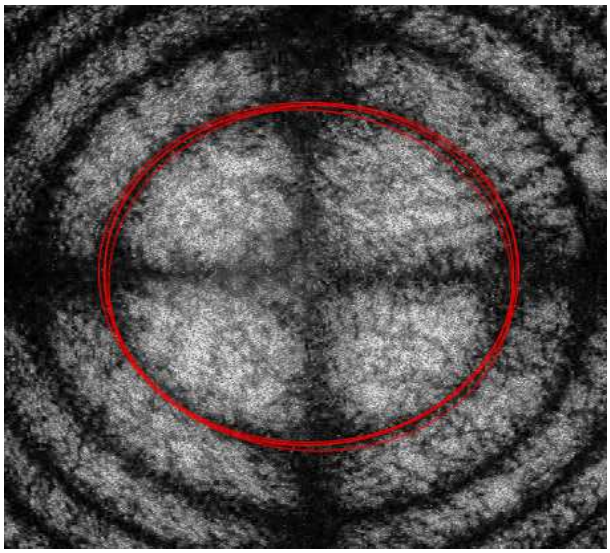

Fig. 4. 14: Starting from the first tentative ellipse, numbers of ellipses are generated next to the starting one in order to find the one that match the first dark fringe. The ellipse with the lowest pixel intensity value along its full boarder is then chosen.

These steps are finalized to find in an iterative way the ellipse function that match the first dark fringe so to reduce the uncertainty. To find the correct number of iterations to perform in each optimization phase it has been carried out a sensitivity analysis [1]. The parameters to keep under control in this analysis are the elaboration time of each image and the standard deviation [45]. In particular it has been studied the trend of the standard deviation on the measurements, in function of the number of the iterations N in each process of optimization. The right number of iterations is

obtained when by increasing N a significant improvement of the standard deviation is not achievable anymore. In this manner the processing times are not prolonged uselessly to achieve a negligible improvement in standard deviation.

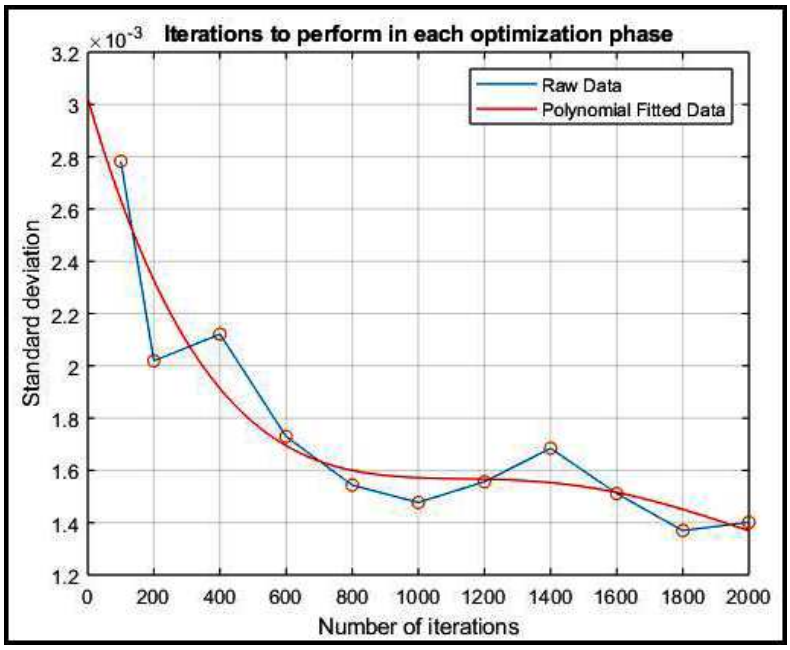

Fig. 4. 15: An iterative test is performed on a group of images in order to calculate the standard deviation of the ellipticity value obtained using a fixed number of iterations. The same test is performed changing this parameter to correlate the standard deviation with the number of iterations applied.

In our case with 1000 iterations we obtain a level of standard deviation which is hardly improvable (Fig. 4.15). Analysing image sources coming from a crystal with well-polished surfaces, acquired with a 24 megapixel C-Mos sensor, it is possible to achieve a standard deviation of 1.5×10^{-3} on the ellipticity parameter [1], [45].

4.2 Laser Conoscopy in direction orthogonal to the optic axis

4.2.1 The technique

In our studies we focalize our attention on PWO crystal, but the following analysis is applicable with care at all birefringent crystals. PWO is a body-centred tetragonal crystal, point group 4/m, and its piezo-optic **Π** tensor in the crystallographic frame of Fig. 4.17b can be written as [35], [46]:

$$\Pi = \begin{vmatrix} \pi_{11} & \pi_{12} & \pi_{13} & 0 & 0 & \pi_{16} \\ \pi_{12} & \pi_{11} & \pi_{13} & 0 & 0 & -\pi_{16} \\ \pi_{31} & \pi_{31} & \pi_{33} & 0 & 0 & 0 \\ 0 & 0 & 0 & \pi_{44} & \pi_{145} & 0 \\ 0 & 0 & 0 & -\pi_{45} & \pi_{44} & 0 \\ \pi_{61} & -\pi_{61} & 0 & 0 & 0 & \pi_{66} \end{vmatrix} \quad (4.3)$$

The growth process can cause lattice distortions, which induce a residual stress distribution. This residual stress, as the applied loads, modify the ***B*** tensor as follows:

$$\boldsymbol{B} = \boldsymbol{B}_0 + \Pi[T] \quad (4.4)$$

Were T is the Cauchy symmetric stress tensor.

The Bertin surfaces associated to **B** can be written in the following form [27], [36]:

$$cos^4\beta x^4 + y^4 + sin^4\beta z^4 + 2cos^2\beta x^2y^2 + 2sin^2\beta z^2y^2 - 2sin^2cos^2\beta z^2x^2 - N^2H^2(x^2 + y^2 + z^2) = 0 \quad (4.5)$$

with:

$$H = \frac{\lambda}{n_e - n_o} \quad (4.6)$$

Where β is the semi-angle between the optical axes, λ is the wavelength and N is an integer number that represent the fringe order.

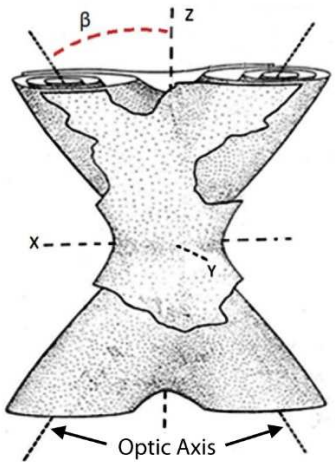

Fig. 4. 16: Bertin surfaces which represent the loci of points where the light rays, crossing the sample, have the same delay. In the figure the general case of surface in biaxial crystal is represented. This condition is natural in a biaxial crystal, but likewise can also be induced by the presence of residual or applied stress in a uniaxial crystal.

The relative surfaces of the Bertin equation (4.5) are shown in Fig. 4.16, which represents the classical Bertin equal delay surfaces for each N integer value. This surfaces shape is due to a biaxial condition of a crystal sample which can occur naturally (depending on the crystal system) or when a uniaxial crystal undergoes to specific load directions.

Following the Wahlstrom [23] we can evaluate:

$$cos\beta = \sqrt{\frac{B_{2,1}-B_3}{B_{1,2}-B_3}} \tag{4.7}$$

$$sin\beta = \sqrt{\frac{B_{1,2}-B_{2,1}}{B_{1,2}-B_3}} \tag{4.8}$$

with $B_3 > B_2 > B_1$ and $B_3 > B_1 > B_2$ respectively. The values $B_{(i)}$, with i=1,2,3, are the eigenvalues of **B** that, with the corresponding eigenvectors, define shape and direction of the optic indicatrix [35], [47]. In order to implement an elasto-optic model we need two reference systems, one intrinsic to the Bertin surfaces named x'-y'-z', and one that refer to the crystallographic directions a b and c which correspond to the axes x-y-z as reported in Fig.4.17 [22], [27], [36].

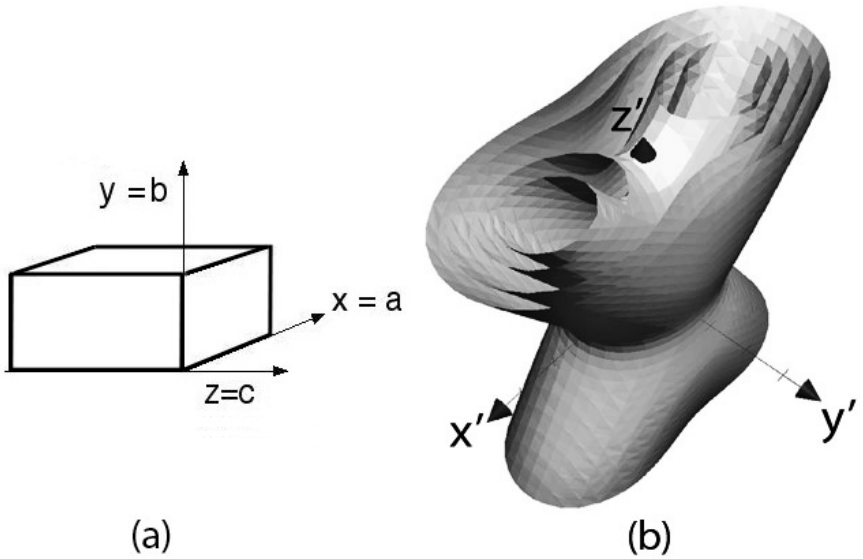

Fig. 4. 17: Reference frames used in the elasto-optic model: (a) crystallographic reference x-y-z corresponding to the crystallographic directions a, b, c, (b) reference frame x'-y'-z' intrinsic to the Bertin surfaces.

Given the specimen shape, the observations are carried out along the x-axis, which corresponds to the 'a' crystallographic direction of the PWO tetragonal lattice. Taking this into account, we may assume that the stress components associated with the observation direction, namely σ_{xx} τ_{xy} τ_{xz}

cannot be detected if present. To be more precise, the photoelastic technique used for the investigations integrates the terms σ_{xx} τ_{xy} τ_{xz} over the specimen thickness and, being residual stress, they have zero mean value. Accordingly, we may safely assume that the only measurable residual stress will be the plane stress σ_{yy}, σ_{zz}, τ_{yz}. Under such hypotheses, from (4.3) and (4.4) follows:

$$\Pi[T] = \begin{bmatrix} \sigma_{yy}\pi_{12} + \sigma_{zz}\pi_{13} & 0 & -\tau_{yz}\pi_{45} \\ \bullet & \sigma_{yy}\pi_{11} + \sigma_{zz}\pi_{13} & \tau_{yz}\pi_{44} \\ \bullet & \bullet & \sigma_{yy}\pi_{31} + \sigma_{zz}\pi_{33} \end{bmatrix} \quad (4.9)$$

We deal with linear Photoelasticity; therefore, we can assume that |Π[T]|<<|B(i)-B(j)|. Taking into account the consideration of Sirotin [46], the eigenvalue problem associated with (4.4) admits the following solution, to within higher-order terms:

$$B_1 = B_x + \sigma_{yy}\pi_{12} + \sigma_{zz}\pi_{13}$$

$$B_2 = B_y + \sigma_{yy}\pi_{11} + \sigma_{zz}\pi_{13} \quad (4.10)$$

$$B_3 = B_z + \sigma_{yy}\pi_{31} + \sigma_{zz}\pi_{33}$$

In our case the rotation of the associated principal directions is negligible [32]; by taking into account that for small stress the acute bisector of 2β remains the eigenvector of B_3 [22], [47] we obtain:

$$sin^2\beta(\sigma_{yy}, \sigma_{zz}) = \frac{\pm\sigma_{yy}D(\Pi)}{\Delta B + \sigma_{yy}G_{\pm}(\Pi) + \sigma_{zz}H(\Pi)} \quad (4.11)$$

Where $\Delta B = B_x - B_z$, $D(\Pi) = \pi_{12} - \pi_{11}$, $G_+(\Pi) = \pi_{12} - \pi_{31}$, $G_-(\Pi) = \pi_{11} - \pi_{13}$ and $H(\Pi) = \pi_{13} - \pi_{33}$. The sign ± depends on $B_3 > B_1 > B_2$ or $B_3 > B_2 > B_1$ respectively [22].

When $B_2 > B_1$ the frame x', y', z' intrinsic with the Bertin surfaces (Fig. 4.17a) coincides with the crystallographic frame x, y, z (Fig. 4.17b). Consequently, the optic angle lies in the plane (x - z) which correspond to (x' – z').

Therefore, starting from the Bertin equation (4.5), we set the variable x' ≡ x equal to the parameter d that describe the sample thickness, obtaining:

$$y^4 + z^4(sin^4\beta) + y^2(2cos^2\beta d^2 - NH^2) + z^2(-2sin^2\beta cos^2\beta d^2 - NH^2) + z^2y^2(2sin^2\beta) + cos^4\beta d^4 - NH^2d^2 = 0 \quad (4.12)$$

This operation is finalized to get the interference fringes as a section of the Bertin surfaces with the observation plane x' ≡ x ≡ d, which is parallel to y – z plane. In this manner, by varying the integer value N, it is possible to obtain two families of interference fringes, as shown in Fig. 4.18.

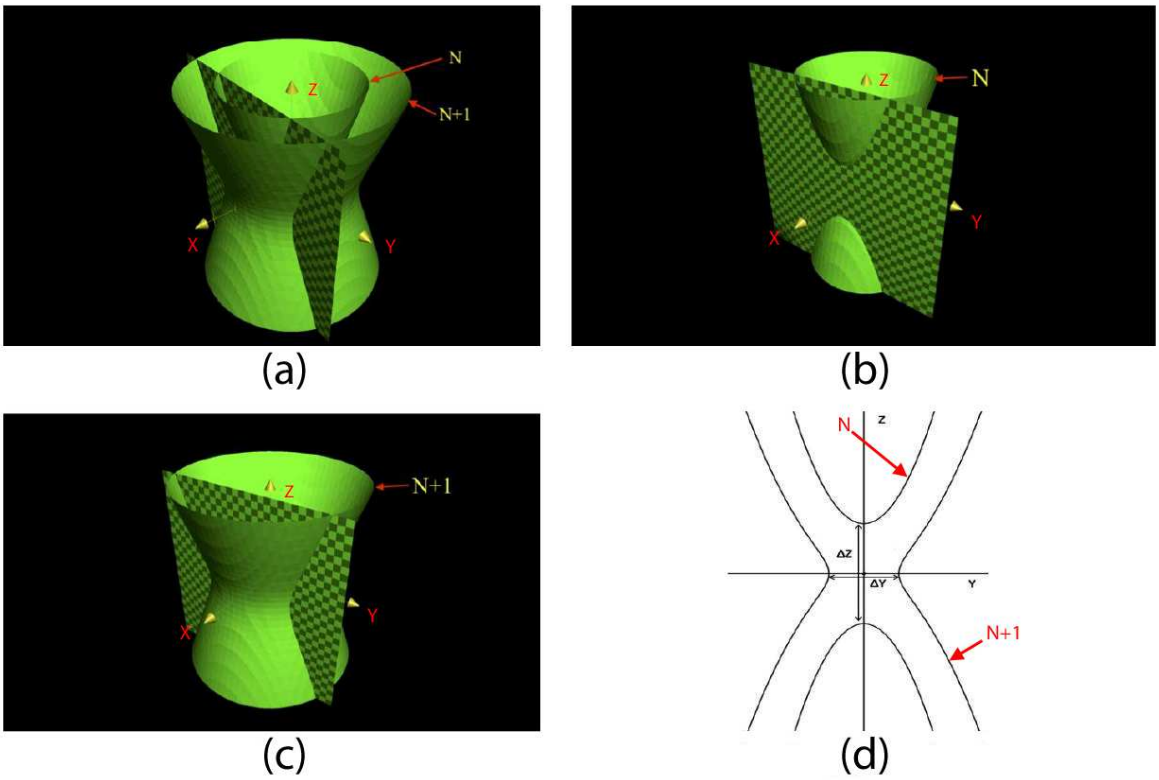

Fig. 4. 18: Scheme of the Bertin surfaces in uniaxial condition (a) for two orders (N;N + 1) and the intersection plane. To be more precise in (b) we plot only the intersection with the N order, and in (c) with the N +1 order. In (d) both the intersection curves between the plane and the Bertin surfaces with different orders N and N+1 are plotted. They represent the shape of the fringes which can be observed in the (a - c) plane observation. The two measurable quantities, ΔY and ΔZ, are also indicated. Those quantities are a function of the state of stress.

By increasing the value of the fringe order to a certain N index, we obtain the interference fringes family of the type described in Fig. 4.18b, for the values corresponding to N + 1 and subsequent we obtain the interference fringe family represented Fig. 4.18c. Considering values of the fringe order up to N, the intersection of the interference fringes with the plane form a pair of symmetrical curves with respect to the y axis; for indexes higher than N, there are symmetrical pairs of curves with respect to the z axis(Fig. 4.18d). As experimentally measurable quantity we assume the distances Δz and Δy between the apex of the curves which results by sectioning the Bertin surfaces (Fig. 4.18d).

To obtain Δz we have to start from equation (4.12) and set the variable y equal to zero ($y = 0$). After a few steps it is possible to obtain the relation:

$$\Delta z = \frac{\sqrt{2}NH}{sin^2\beta}\sqrt{2sin^2\beta cos^2\beta\xi^2 + 1 - \sqrt{1 + 4sin^2\beta\xi^2}} \quad (4.13)$$

where ξ is defined by:

$$\xi = \frac{d}{NH} \quad (4.14)$$

This relation (4.13) is true for N values corresponding to the numeric range:

$$N \leq cos^2\beta d \quad (4.15)$$

To obtain the other quantity Δy we have to start from the same equation (4.12) and set the variable z equal to zero ($z = 0$). After a few steps it is possible to obtain as the same:

$$\Delta y = \sqrt{2}NH\sqrt{1 - 2cos^2\beta\xi^2 + \sqrt{1 + 4sin^2\beta\xi^2}} \quad (4.16)$$

This relation is true for N values corresponding to the numeric range:

$$N \geq cos^2\beta d \quad (4.17)$$

Considering that the condition:

$$N = cos^2\beta d = \widehat{N} \quad (4.18)$$

is true for both the equations that describes the quantities Δy and Δz, this relation represents the limit state for each equation (4.13) and (4.16). In fact, substituting the (4.18) inside the (4.12) and using a sample test thickness (d) of 10mm and a fixed value for β of 10°, we obtain the graph showed in Fig. 4.19a. Starting from $\widehat{N}$, rounding its value up to the first successive integer number, it is possible to obtain the first fringe order $N^{(+)}$ corresponding to the ΔY distance. Rounding $\widehat{N}$ down to the first precedent integer value it is possible to obtain contrariwise the first fringe order $N^{(-)}$ corresponding to the ΔZ distance. (Fig. 4.19b)

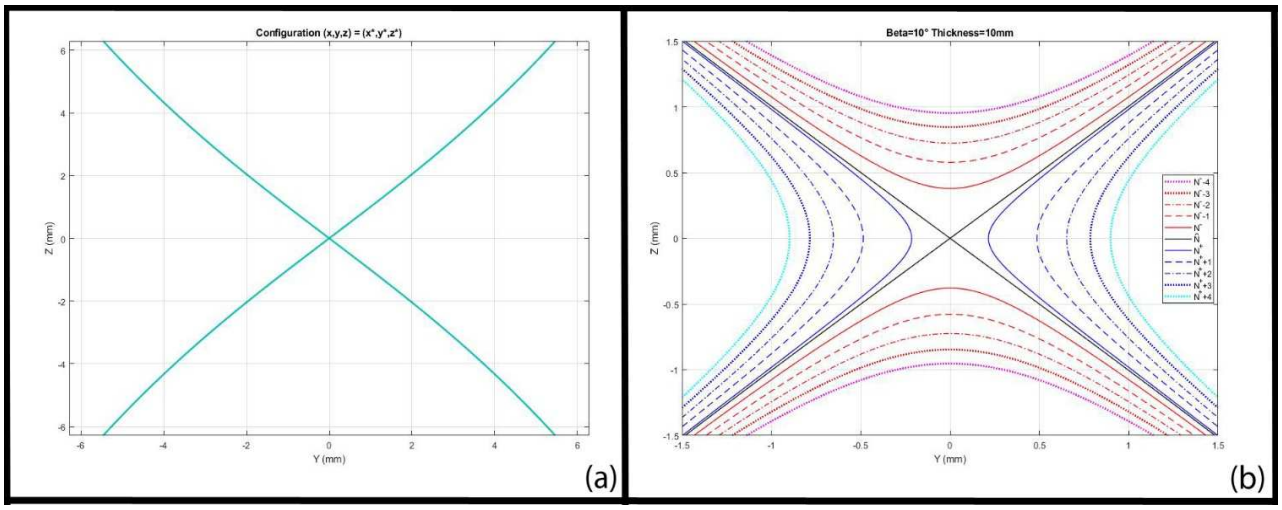

Fig. 4. 19: Graph representation of the interference fringes in the case of $B_2 > B_1$. In (a) we have the limit condition that makes equal to zero both the equations for the calculation of the parameter ΔY and ΔZ. In (b) are represented the first order fringes closest to the Z and Y axes, with fringe orders named respectively $N^{(+)}$ and $N^{(-)}$. Adding integer values to $N^{(+)}$ we obtain gradually the other fringe orders with the same orientation. For the outer orientation we must subtract integer values to $N^{(-)}$.

In this manner, with the fringe order $N^{(+)}$ we have the couple of fringes closest and symmetric with respect to the Z axis. Adding integer values in ascending order to $N^{(+)}$, we obtain the other fringe orders that produces interference fringes with same orientation but always more distant from the Z axis (Fig. 4.19b). Contrariwise, with the fringe order $N^{(-)}$ we have the couple of fringes closest and symmetric with respect to the Y axis. In this case, to produce interference fringes with same orientation but more and more distant with the Y axis, we have to subtract integer value in descending order from $N^{(-)}$ (Fig. 4.19b). To proceed with the analysis, we choose the fringe order $N^{(-)}$ for ΔZ and for ΔY the fringe order $N^{(+)}$. This choice is to obtain these two distances from the fringe pairs closest to the axes Y and Z.

$$\Delta z(\beta) = \frac{\sqrt{2}N^{(-)}H}{sin^2\beta}\sqrt{2sin^2\beta cos^2\beta\xi^2 + 1 - \sqrt{1 + 4sin^2\beta\xi^2}} \qquad (4.19)$$

$$\Delta y(\beta) = \sqrt{2}N^{(+)}H\sqrt{1 - 2cos^2\beta\xi^2 + \sqrt{1 + 4sin^2\beta\xi^2}} \qquad (4.20)$$

where in each equation we have the only variable defined by the β angle.

Starting from this and changing the β parameter inside each equation it is possible to obtain the graph of ΔY and ΔZ in function of the beta angle, using a sample test thickness of 10mm. (Fig. 4.20a - b)

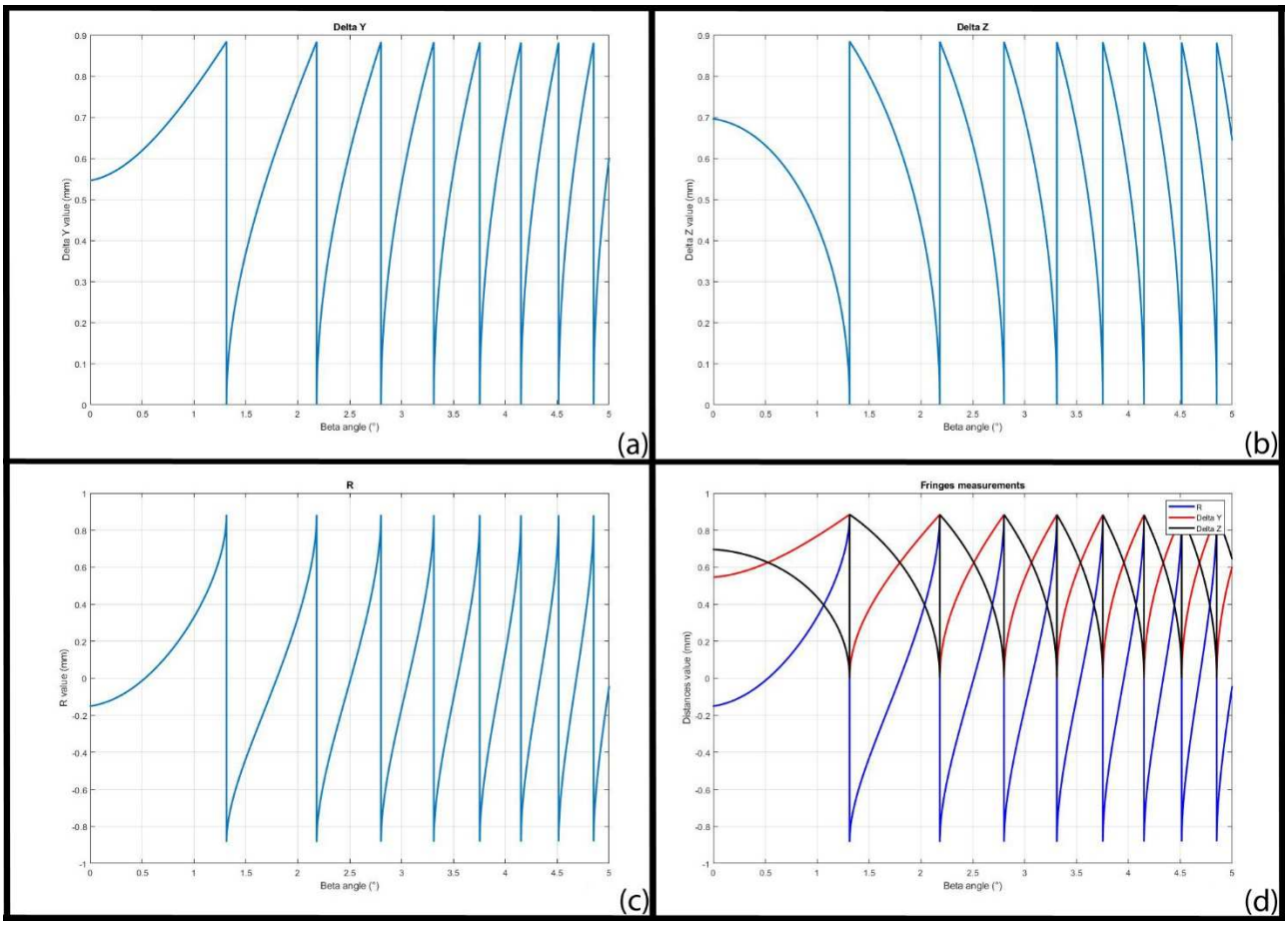

Fig. 4. 20: Trend of the measurement parameters when the beta angle changes. We have in (a) Δy, in (b) Δz, in (c) the parameter R and in (d) the summary of all the parameters together.

Now that we have the only quantity β to measure, it is important to define only one measurable parameter from the fringes shape. So, in order to have only one equation that is function of the semi angle between the optic axes, we chose the parameter R(β) that is described by the equation:

$$R(\beta) = \Delta y - \Delta z \qquad (4.21)$$

This quantity is graphed in Fig. 4.20c.

The shape of R parameter in function of β is not completely linearizable because the limit condition $\widehat{N}$ is also function of the β parameter. Because of this, increasing the value of the angle, the value of $\widehat{N}$ decrease. (Fig. 4.21a) Considering that the values of $N^{(+)}$ for ΔY and $N^{(-)}$ for ΔZ are taken respectively as the rounding up of $\widehat{N}$ to the successive integer and down to the precedent integer, their trend are shown in Fig. 4.21b,c,d for a sample test thickness (d) of 10mm. The jumps in the graphs of Fig. 20a,b,c, that correspond to the jumps of the relative fringe order in Fig. 21b,c for the Δy and Δz trend simulation, occur when the critical value $\widehat{N}$ coincides with an integer value, and

therefore represents a fringe order itself. In this case where $\widehat{N}$ is an integer value, the two fringe distances Δy and Δz, following the results in the Fig. 20 from (4.19) and (4.20), collapses both to the zero value.

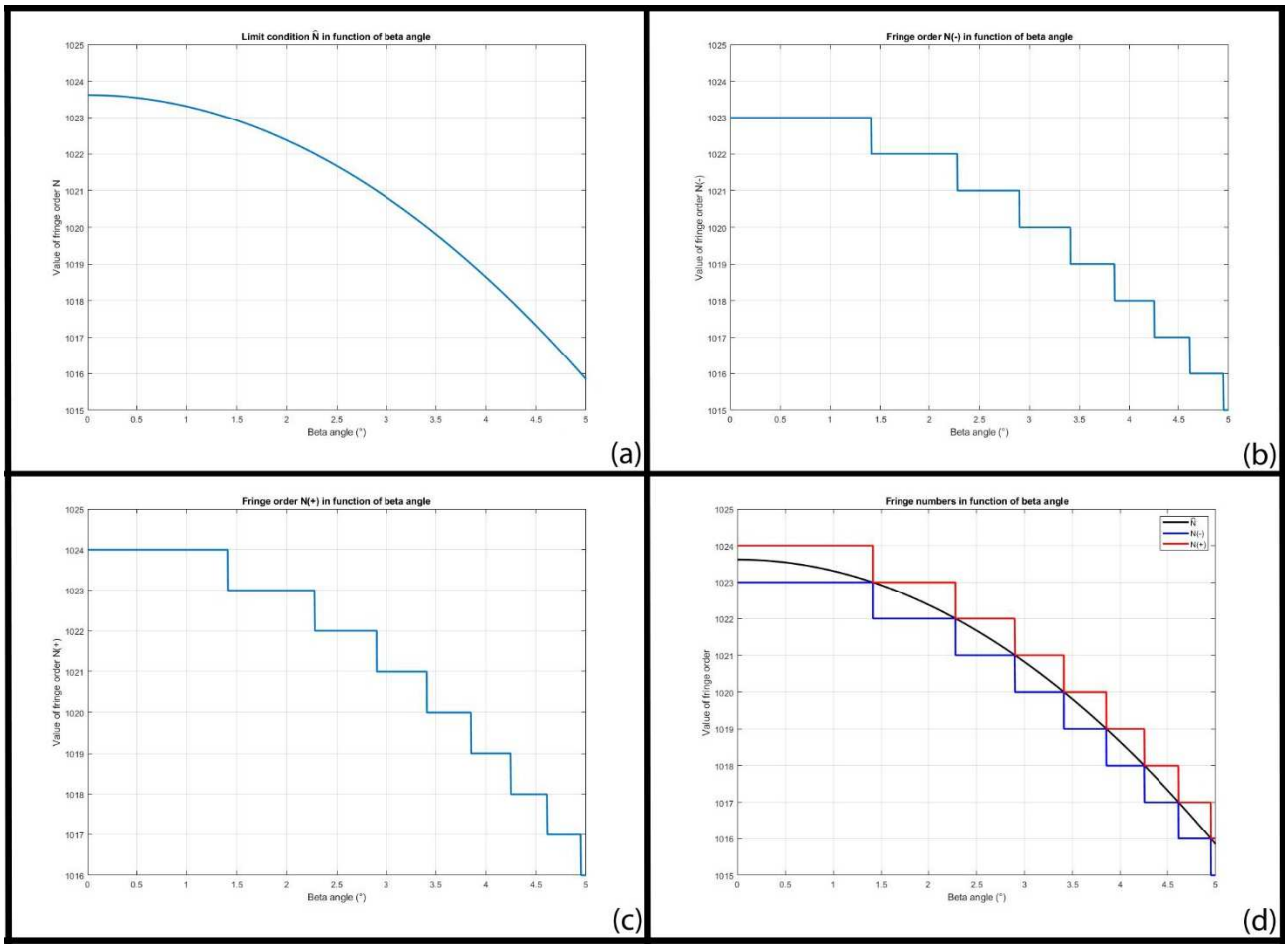

Fig. 4. 21: (a) State of the limit condition $\widehat{N}$ by varying the value of the beta angle; (b)(c) relative trend of the parameters N(+) and N(-) obtained as different roundings from $\widehat{N}$; (d) summary of the all precedent parameters.

However, if the angle variation does not involve an alteration of the fringe orders $N^{(+)}$ and $N^{(-)}$, we can consider the shape of R(β) linearizable for small variation of the beta angle. (Fig. 4.22)

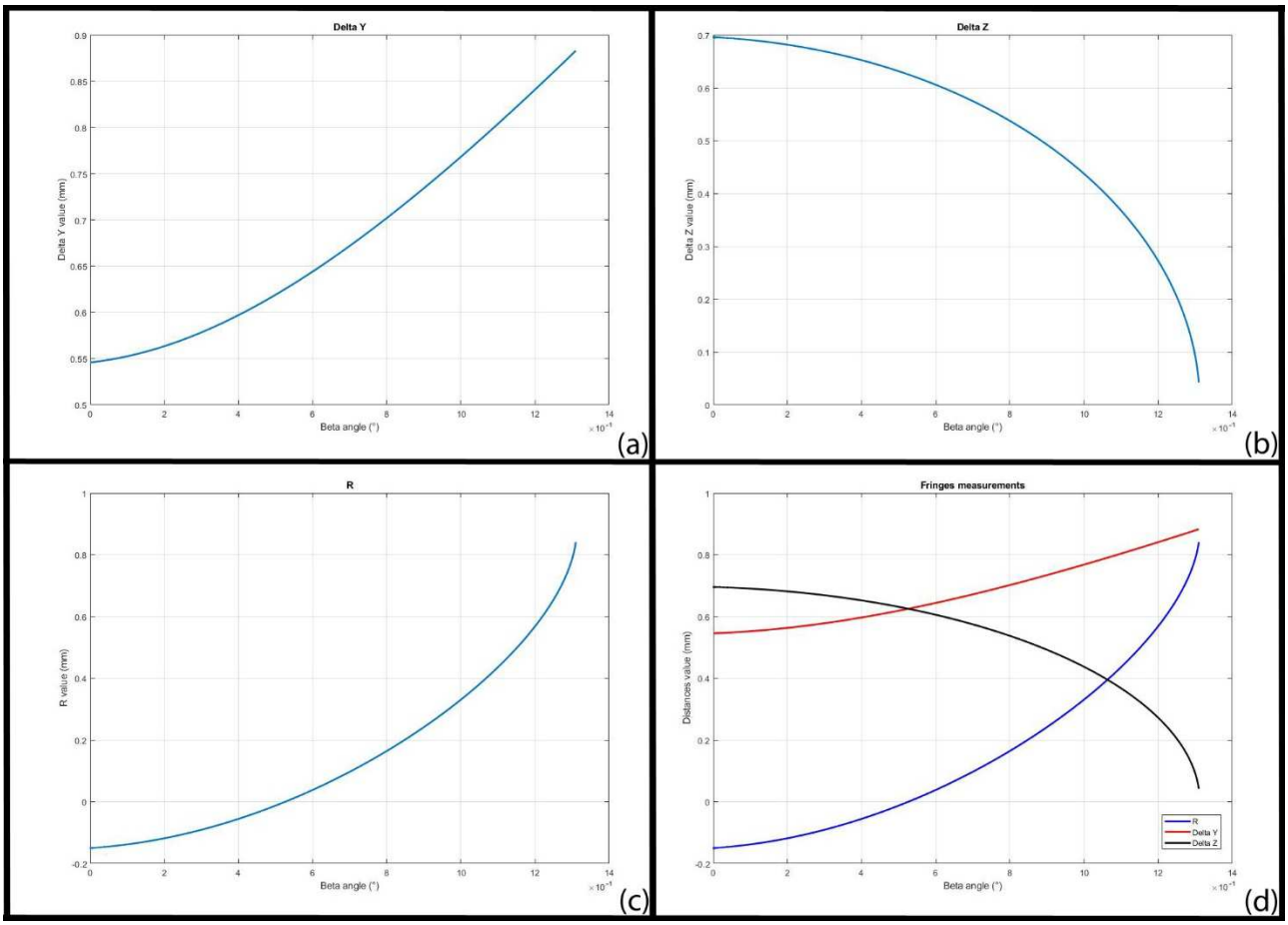

Fig. 4. 22: Shape of the parameters (a) Δy, (b) Δz, (c)R for small variation of the beta angle. In (d) the summary of all the parameters together is represented.

Coming back to the eigenvector solution, when contrariwise $B_1 > B_2$ the frame x', y', z' intrinsic with the Bertin surfaces does not coincides with the crystallographic frame x, y, z. In this case the optic angle, which is defined in the plane x' – z', is instead located on the on the crystallographic plane y-z. In order to be clearer, the two reference system x', y', z' and x, y, z have the z' and z axes coincident ($z' \equiv z$) but they are respectively rotated of $\frac{\pi}{2}$ respect to the common axis z. Likewise, starting from the Bertin equation (4.5), we set in this case the variable y' ≡ x equal to the parameter d that describe the sample thickness, in order to get the interference fringes as a section of the Bertin surfaces with the observation plane. Therefore, starting from (4.5) and inserting the relation y' = x =d we obtain:

$$y^4(cos^4\beta) + z^4(sin^4\beta) + y^2(2cos^2\beta d^2 - NH^2) + z^2(2sin^2\beta d^2 - NH^2) + z^2y^2(-2sin^2\beta cos^2\beta) + d^4 - NH^2d^2 = 0 \quad (4.22)$$

To obtain the measurable quantity Δz we have to start from equation (4.22) and set the variable y equal to zero ($y = 0$). After a few steps it is possible to obtain the relation:

$$\Delta z = \frac{\sqrt{2}NH}{sin^2\beta}\sqrt{1 - 2sin^2\beta\xi^2 - \sqrt{1 + 4sen^4\beta\xi^2 - 4sin^2\beta\xi^2}} \quad (4.23)$$

This relation is true for N values corresponding to the numeric range:

$$N \leq d \quad (4.24)$$

In order to obtain the other measurable quantity Δy we have to start from (4.22) applying the relation $z = 0$. After few steps we achieve:

$$\Delta y = \frac{\sqrt{2}NH}{cos^2\beta}\sqrt{1 - 2cos^2\beta\xi^2 + \sqrt{1 + 4sen^4\beta\xi^2 - 4sin^2\beta\xi^2}} \quad (4.25)$$

This relation is contrariwise true for N values corresponding to the numeric range:

$$N \geq d \quad (4.26)$$

Even in this case we have the common condition that represent the limit state for ΔY and ΔZ that is:

$$N = d = \widehat{N} \quad (4.27)$$

Substituting the value of (4.27) inside the (4.22) and using a sample test thickness (d) of 10mm and a fixed angle β of 10°, in fact, we obtain the Fig. 4.23a.

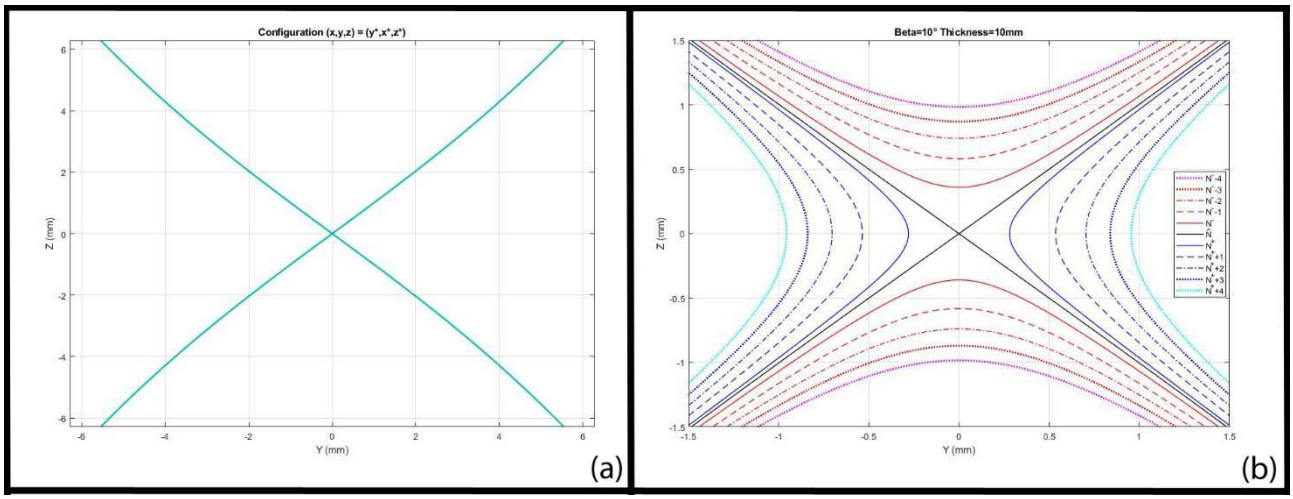

Fig. 4. 23: Graph representation of the interference fringes in the case of $B_1 > B_2$. In (a) we have that condition that makes equal to zero both the equations for the calculation of the parameter ΔY and ΔZ. In (b) are represented the two types of interference fringes. With the fringe order named $N^{(+)}$ we have the couple of fringes closest and symmetric to the Y axis. Adding integer value to $N^{(+)}$ is possible to obtain the fringe order for the outer interference fringes with same orientation. With the fringe order named $N^{(-)}$ we have the couple of fringes closest and symmetric to the Z axis. So, on the contrary, the outer interference fringes with same orientation are obtained subtracting integer value from $N^{(-)}$.

As in the previous case then, it is possible to obtain the values of $N^{(+)}$ and $N^{(-)}$ respectively as the rounding up of $\widehat{N}$ to the successive integer and down to the precedent integer. In this way, by substituting $N^{(+)}$ and $N^{(-)}$ within (4.22), it is possible to obtain the shape of the first two symmetrical interference fringes with respect to the z and the y axis respectively (Fig. 4.23b). It is therefore possible to obtain the function that binds ΔZ with β using the fringe order $N^{(-)}$, and the function that binds ΔY with β using the order $N^{(+)}$:

$$\Delta z(\beta) = \frac{\sqrt{2}N^{(-)}H}{sin^2\beta}\sqrt{1 - 2sin^2\beta\xi^2 - \sqrt{1 + 4sen^4\beta\xi^2 - 4sin^2\beta\xi^2}} \qquad (4.28)$$

$$\Delta y(\beta) = \frac{\sqrt{2}N^{(+)}H}{cos^2\beta}\sqrt{1 - 2cos^2\beta\xi^2 + \sqrt{1 + 4sen^4\beta\xi^2 - 4sin^2\beta\xi^2}} \qquad (4.29)$$

It is important to consider that in this case there is no correlation between the parameter $\widehat{N}$ and the angle β. Therefore, if a specified thickness (d) is fixed, changing the value of the angle β we measure ΔY and ΔZ always respect to the same fringe orders $N^{(+)}$ and $N^{(-)}$. The trends of the parameters ΔY, ΔZ and R are then presented in Fig. 4.24a - b. Considering that from (4.11) we have a relation that gives $sin^2\beta$ as a function of stress components σ_{yy} and σ_{zz}, the quantity $R(\beta)$,measurable in each case of axes orientation, can be used as an indirect measure of the internal stress. Taking into account that is possible to assume [4], [46]:

$$|\Delta B| \gg |\sigma_{yy}G_{\pm}(\pi) + \sigma_{zz}H(\pi) \qquad (4.30)$$

Therefore, considering the relation (4.30), expanding in Taylor series $sin^2\beta$ given from (4.11) we obtain [4]:

$$sin^2\beta = \frac{\pm\sigma_{yy}D(\pi)}{\Delta B}[1 - \varepsilon + \varepsilon^2 + o(\varepsilon)] \qquad (4.31)$$

that is in term of the dimensionless parameter $\varepsilon = \frac{\sigma_{yy}G_{\pm}(\pi)+\sigma_{zz}H(\pi)}{\Delta B}$.

Considering the equation (4.31), it seems that at the first order $sin^2\beta$ depends linearly from $\sigma_{y.}$ Therefor the measure of R appear particularly sensitive to the stress component σ_y, and the dependence from σ_z happens only at higher order terms. So, at the end we obtain locally [4], [48]:

$$R(\sigma_{yy}, \sigma_{zz}) = k_0 + k\sigma_{yy} + o(\sigma_{yy}, \sigma_{zz}) \qquad (4.32)$$

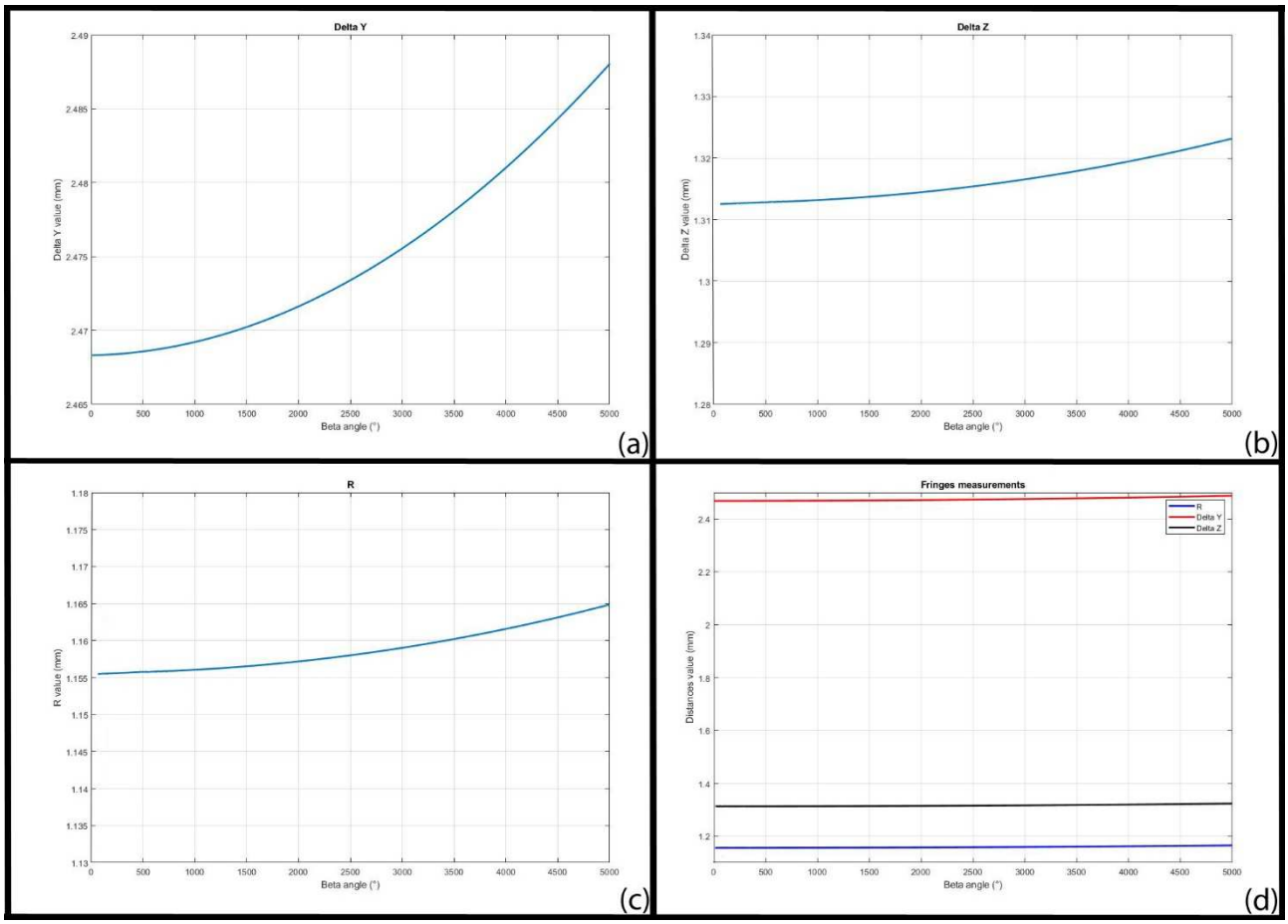

Fig. 4. 24: Trend of the measurement parameters when the beta angle changes. We have in (a) Δy, in (b) Δz, in (c) the parameter R and in (d) the summary of all the parameters together.

4.2.2 Fringe analysis Algorithm

The observations obtained by conoscopic technique, carried out along the 'a' crystallographic axis (orthogonal to the optic axis), produce acquisitions that are like those in Fig. 4.25. In this type of images, the black shapes represents the Bertin interference fringes [2], [4].

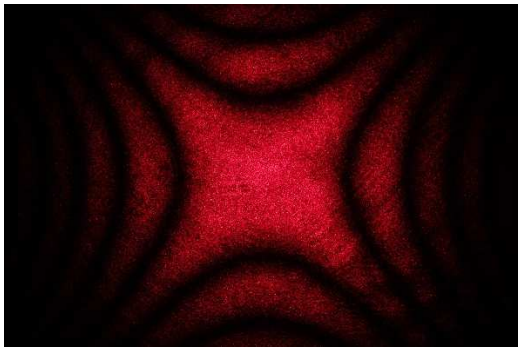

Fig. 4. 25: Example of conoscopic acquisition obtainable observing the sample in direction perpendicular to the optic axis. In particular that acquisition was obtained looking along the 'a' crystallographic axis.

In order to extract the interference fringes shape from the images, it is useful at first to manipulate the images trough filters. This is to make more precise the identification of the minimum light intensity points.

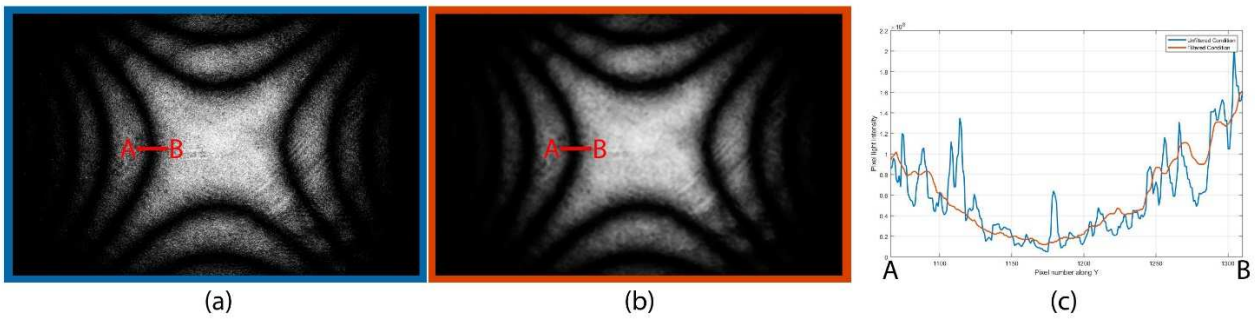

Fig. 4. 26: Example of an image in different conditions. In (a) we have an image acquired from which is extracted only one colour plane of interest. in (B) we have the same image but with applied a Median filter. In (A) and in (B) it is tracked the same segment crossing a dark fringe. In each case it was studied the trend of pixel light intensity along the segment. That in order to study the differences after and before the application of the Median filter. In (C) it is possible to see that with that filter (red line) the spackle noise does not affect the trend of pixel light intensity, removing only the isolated spikes of disturb. In this manner, using that filter is possible a more precise detection of the points of minimum light intensity.

Starting from the acquired image, only the colour plane of interest is extracted (Fig. 4.26a). In our case red is chosen, that is the colour of the laser acquisition. Starting from this results, it is applied a median filter [43], [44]. The Median Filter belongs at the family of lowpass filter. Mainly works by assigning to each pixel the median value of its neighbourhood, removing isolated pixels. Principally it is used to remove the speckle noise from an image, without disturbing the clean pixels. This peculiarity is opposed to linear low pass filters, that will also reduce the noise, but spreading out the effect of noisy pixels rather than isolating and removing them. The first step in order to apply this type of filter is to define the size S of a square pixel array (Tab. 4.1), where the central pixel is the pixel in exam, in which the filter result will be applied. Once that S is defined, this type of filter sort in increasing order the value of the central pixel together with its neighbourhood contained inside the square pixel array.

$P_{(i-1,\ j-1)}$	$P_{(i,\ j-1)}$	$P_{(i+1,\ j-1)}$
$P_{(i-1,\ j)}$	$P_{(i,\ j)}$	$P_{(i-1,\ j)}$
$P_{(i-1,\ j+1)}$	$P_{(i,\ j+1)}$	$P_{(i+1,\ j+1)}$

Tab. 4. 1: Example of a 3 S size array for the application of the Median filter.

For each pixel value in ascending order is given a ranking N, that goes from 0 for the lowest pixel value to (S^2-1) for the higher pixel value. The last step, hence, is to find the pixel value corresponding to the ranking $\overline{N}$ defined by the equation (4.33) [43], [44]:

$$\overline{N} = \frac{S^2-1}{2} \tag{4.33}$$

This pixel value corresponding to $\overline{N}$ is the result of the filtering operations and must be replaced at the original value of the central pixel coming from the size S pixel array. These operations are iterated for each pixel inside the image source. The result of these operation with the median filter is visible in Fig. 4.26b. With the aim of study the quality improvement from the Fig.4.26a (without filter) to the Fig. 4.26b (with filter), in each figure the same line profile of the pixel light intensity from the point A to B is tracked. The two line profiles are illustrate superimposed inside the graph in Fig. 4.26c. It is clearly visible that, passing from the unfiltered to the filtered image, the effect of the spackle noise has decreased, without however substantially modifying the original line profile trend but removing the isolated spikes. Now that the points of minimum light intensity are clearly recognizable, they can be extracted in order to reconstruct mathematically the Bertin interference fringes [2], [4]. To be more precise, over each dark fringe of interest are traced a series of segments that cross with the interference fringe (Fig. 4.27a). By studying the pixel light intensity along each segment, it is possible to extract points of the interference fringe as the minimum of pixel light intensity in each line profile of each segment (Fig. 4.27b).

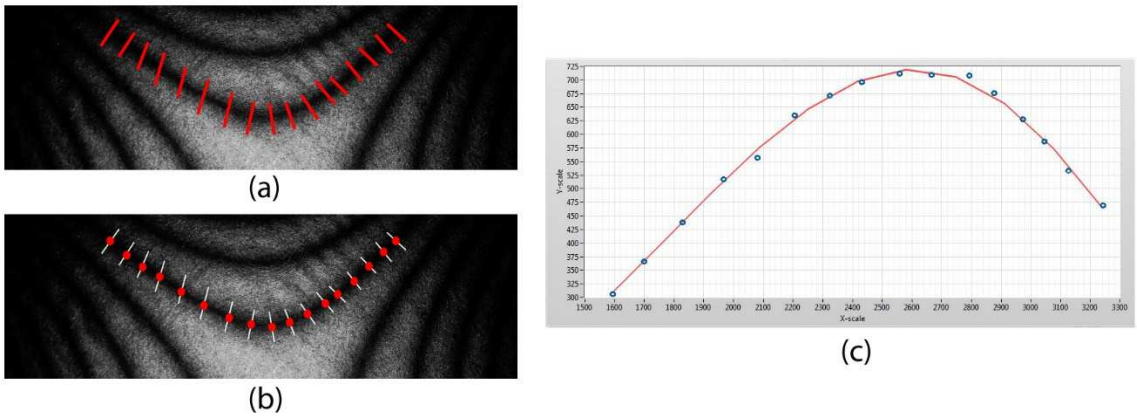

Fig. 4. 27: In (A) are tracked crossing the fringe of interest a series of segments. Along each segment the minimum of light intensity is detected (B). With these points it is possible to digitalize the shape of the investigated fringe(C).

Putting together the points detected, it is possible to reconstruct the fringe shape numerically (Fig. 11c). As known from the mathematical model, the fringes are described numerically as quartic

curves. In fact, once known if we are in the conditions to apply the equation (4.12) or (4.22), substituting inside this equation the sample thickness (d) and a plausible value of the beta value (β) corresponding to the semi angle between the optic axes, it is possible to generate a series of interference fringes that coincides with the fringes inside the images. Starting from an acquisition (Fig. 4.28a) and generating a series of fringe order from the mathematical model (Fig. 4.28b), it is possible to superimpose the mathematical model with the image source (Fig. 4.28c).

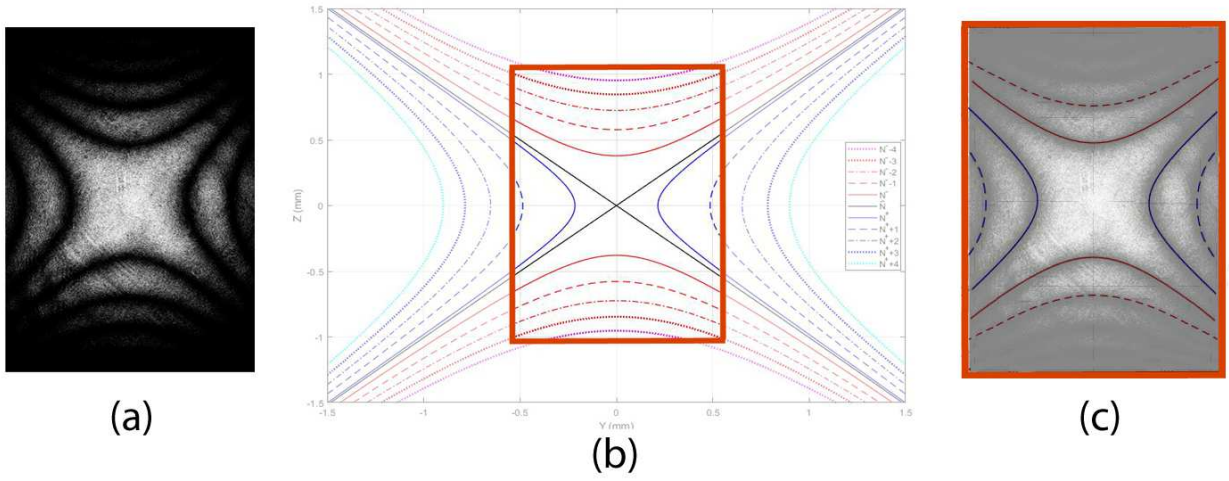

Fig. 4. 28: With the mathematical model of the interference fringes it is possible to generate a series of quartic curves, once established a value of the semi angle beta parameter (b). In this manner, starting from an acquired image of interference fringes (a), and using a certain value of beta, it is possible to superimpose the shapes of the interference fringes inside the image source with the quartic curves shape (c).

The problem is that, starting from a series of acquired points belonging to the same fringe order, it is hard to generate and manipulate a fit of the equations (4.12) or (4.22). This because that equations are quartic trigonometric curves, and their parameters detection, even if possible, is difficult and very time consuming by software. Considering that the parameters we want to get from the images are the distances Δy and Δz between the first two symmetrical interference fringes with respect to the z and the y axis respectively, it could be useful to find an equation that approximates the quartic curves (4.12) and (4.22) in the area surrounding the two vertices of the symmetrical interference curves. This approximation curve must be simple and fluent to use, in order to make the fit easily obtainable starting from the data points extracted from the acquired images. Furthermore, this curve must give the same results in term of the parameters Δy and Δz, respect to the corresponding quartic curves. To find these curves we have to start extracting data points of minimum light intensity from each couple of interference fringes as in Fig. 4.27 for a single fringe.

Then each group of points coming from each couple of interference fringe are used to fit a conic equation defined by the relation [49]:

$$\Gamma(x,y) = ax^2 + 2bxy + cy^2 + 2dx + 2ey + f \tag{4.34}$$

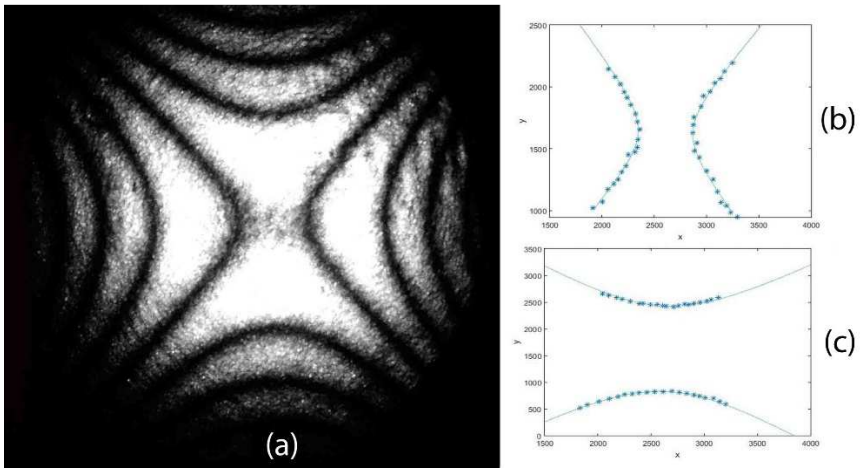

Fig. 4. 29: In (a) we have an acquired image, where the points belonging the two couple of fringes nearest the center are acquired and fitted as hyperboles (b). This type of process is made in order to find an easy equation that approximate well the interference fringes shape.

In this manner, starting from an image source (Fig. 4.29a) it is possible to obtain the coefficients of each conic equation respect to the data points. We have thus obtained, for each fringe orientation, a rototranslated hyperbole equation as shown in Fig. 4.29b and Fig. 4.29c. Each conic equation is also defined by the matrix A (4.35) composed by the coefficients of the curve [49].

$$A = \begin{bmatrix} a & b & d \\ b & c & e \\ d & e & f \end{bmatrix} \tag{4.35}$$

Knowing that the found hyperbola equation is rototrasled type, through the matrix A it is possible to obtain the hyperbola equation in canonical form. This is possible making diagonal the matrix A obtaining the matrix A_d defined by [49]:

$$A_d = \begin{bmatrix} \lambda_1 & 0 & 0 \\ 0 & \lambda_2 & 0 \\ 0 & 0 & \lambda_3 \end{bmatrix} \tag{4.36}$$

So, the new Hyperbole equation is defined by the formula [49]:

$$\Gamma_c(x,y) = \lambda_1 x^2 + \lambda_2 y^2 + \lambda_3 \tag{4.37}$$

Now that both the hyperboles are in the canonical form, they are one symmetric respect to the y axis and one respect to the axis z. In this configuration, it is useful to compare the quartic equation with the hyperbola equation in the same orientation condition. It is important to observe these comparisons at different ranges of measure. In fact, regarding the curves symmetric respect to the y axis, for a large scale (Fig. 4.30c) the two different order equations seem to have different behaviour. But looking in a small scale the area near the Δz distance detection, the two curves has the same curvature and they can be overlapped (Fig. 4.30a).

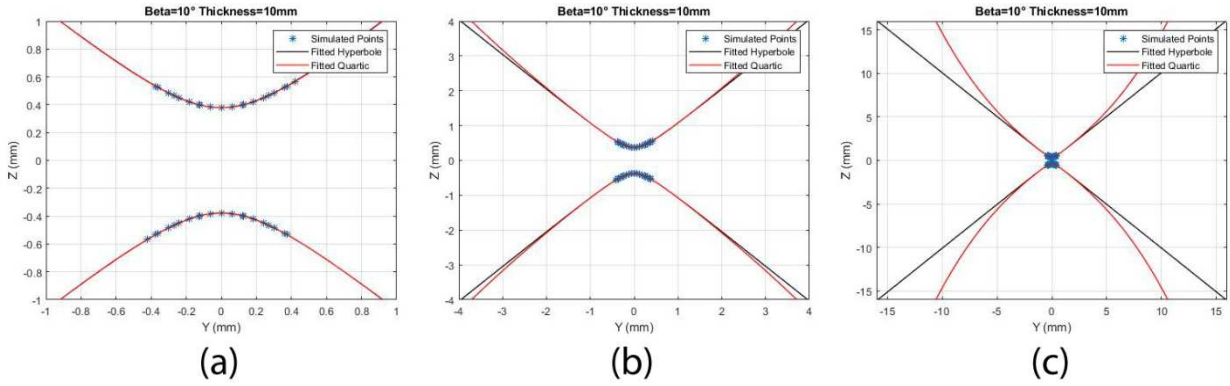

Fig. 4. 30: In each graph we have the points belonging to a couple of fringes symmetric respect to the Y axis. With those points we have therefore the fitted hyperbole (blue line) and the fitted quartic (red line) that comes from the mathematical model. In the area near the smallest distance between the couple of fringes , that is the area of interest, (a), the two type of curves overlap perfectly. Passing to a bigger and bigger scale (b)(c) it is possible to see that the behaviour of the two different type of equations changes more and more as moving from the area shown in (a) to more distant regions in the graph. Summarizing, the two equations has a different trend on large scale, but in the region of interest can both be used to fit the points.

Likewise happens regarding the curves symmetric respect to the z axis. Near the smallest distance between the two branches, the two equations can be superimposed (Fig. 4.31a), regarding instead a bigger area (Fig. 4.31c) it is visible the effect of the differences between the two equations.

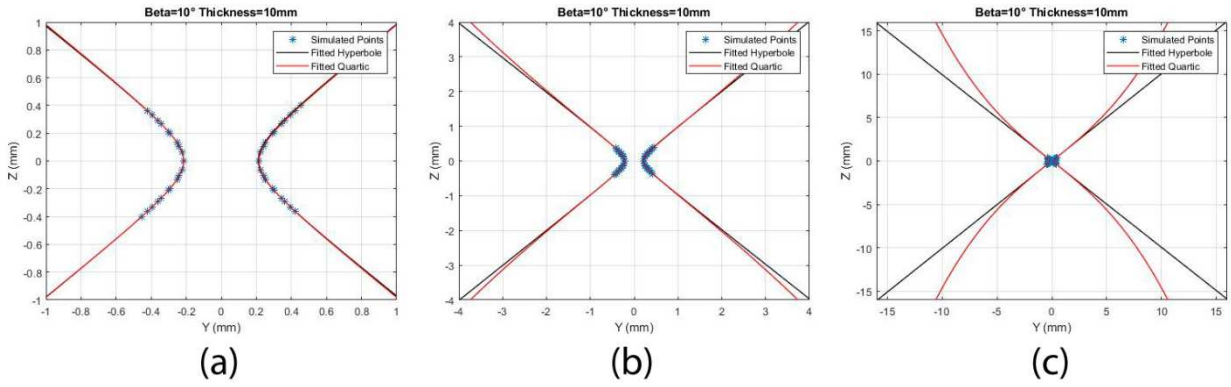

Fig. 4. 31: Here we have presented the same results for a couple of fringes symmetric respect to the Z axis. As above, we have in each graph the acquired points, the fitted hyperbole (blue line) and the fitted quartic (red line). Likewise, for a small scale, that is the region of interest, the two curves can be overlapped.But for the surrounding regions, the thend fo the two curves changes observing ever greater scales (b) (c).

4.3 Sphenoscopy

4.3.1 Observation along the optic axis direction

The starting purpose is to realize a new type of inspection for the birefringent crystals, which must be faster than the precedent techniques. In order to realize that goal, the idea is to substitute, inside the conoscopic system, the solid cone of light with a wedge of light [29], [30], [48]. A wedge of light can be created using cylindrical lenses instead of spherical ones, and it focuses into a line of light at the crystal surface, thus realizing an observation along a line (Fig. 4.32a). In Conoscopy, instead, the cone of light is focused onto a point of the crystal surface (Fig. 4.32b [30].

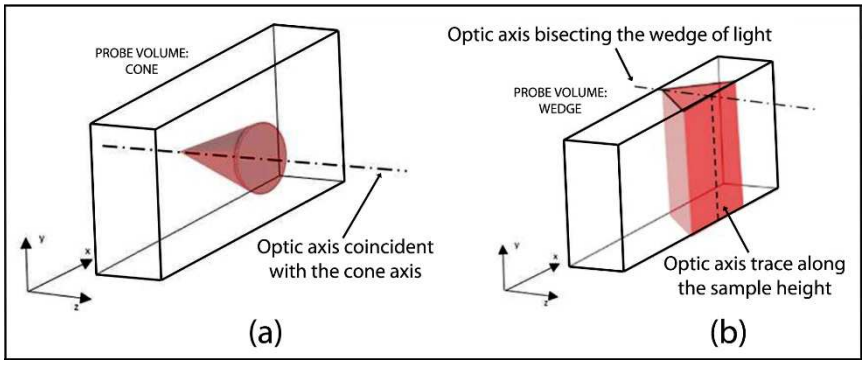

Fig. 4. 32: Representation of the different type of light focusing. In (a) the light beam is focused into a point, that is proper to the conoscopic technique. In (b), by the Sphenoscopic technique, the light is focused in a line. In the first case, that is punctual, the probe volume inside the sample is a cone; in the second we have a wedge of light.

The produced wedge of light by Sphenoscopy can be thought as the superimposition of light sheets piled up one over the others and all with the same common edge of departure, which is the focus of the wedge. Each light sheet, that spans along the crystal thickness d, contains a slice of the fringe pattern [30], [48], as represented in Fig. 4.33b.

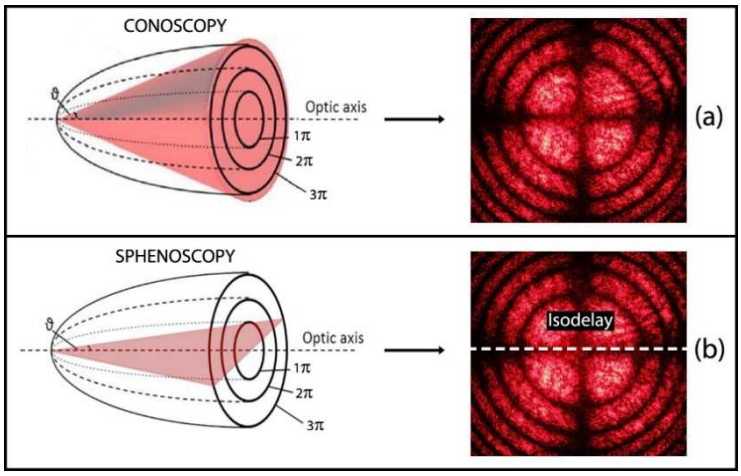

Fig. 4. 33: (a) By laser Conoscopy the light is confined in a specific part of the sample volume and with known angles. Starting from the Bertin surfaces, the fringe pattern is due to the angle of incidence and the thickness of the sample. In (b), instead, we have the intersection between the Bertin surfaces and the plane of light that crosses the crystal, that generates the loci of isodelay on this plane.

Looking at the Fig. 4.33b it is possible to observe how a light sheet intersects the Bertin surfaces. Starting from this consideration, the intersection of the Bertin surfaces with a plane orthogonal to the optic axis does not generate the complete conoscopic fringe pattern (Fig. 4.33a) but just points with different intensity depending on the phase delay [30]. To be more precise, we observe the intensity profile across a section of the isocromate fringe pattern. By the superposition of several planes like the one just described, it is generated a wedge of light with a controlled aperture θ_s and height t, which depend on the lens geometry. By this decomposition into planes, it is possible to understand the behaviour of the optic axes and the Bertin surfaces. The optic axis generates a plane, due to the superposition of the optic axis of each light sheet along the height, and the Bertin surfaces become planes which are symmetric to that plane (Fig. 4.34b) [30], [48].

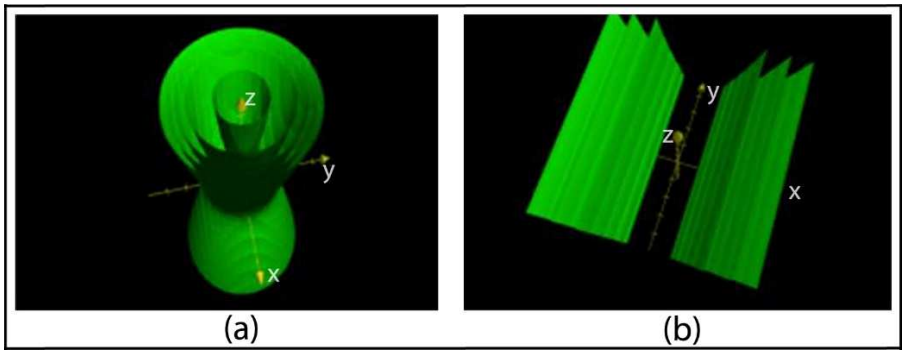

Fig. 4. 34: In (a) we have the computer simulation of the isodelay surfaces, which are generated inside the conic probe volume of the Conoscopy. The shape of these surfaces is a peculiarity of the point in exam. In (b) we have the numerical simulation of the isodelay curves for Sphenoscopy, generated by the several planes of light superimposed.

In particular, Fig. 4.34b show the numerical simulation of the Bertin surface for an observation in Sphenoscopy. By the model in [27] from (2.45)(2.46) the one-one dimensional expression can be achieved as [30]:

$$H^2(n_x)N^2(x^2+z^2)(1+tan^2\beta)^2 = (x^2 - z^2 tan^2\beta)^2 \quad (4.38)$$

It is easy to see, by a comparison with the numerical simulation of the Bertin surface in Conoscopy (Fig. 4.34a), that using Sphenoscopy it is possible to inspect a larger crystal volume without the need for scanning. As confirmed in the numerical simulation, the fringe patterns observed in Sphenoscopy are parallel lines if no stress gradient occurs in the crystal sample along the probe volume (Fig. 4.35) [30], [48].

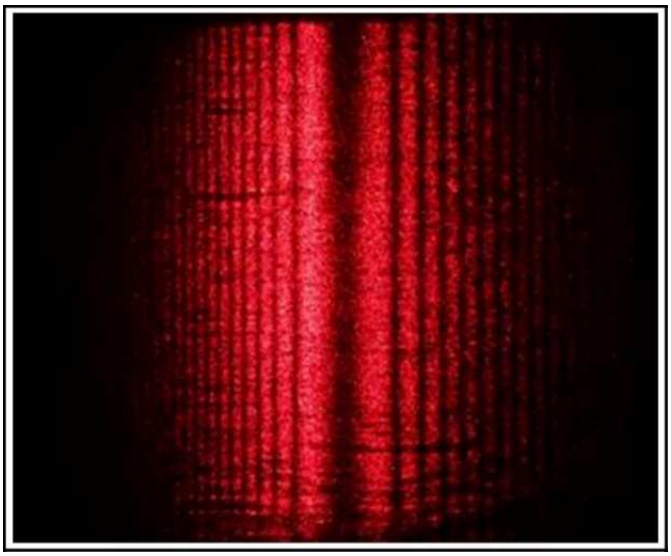

Fig. 4. 35: Example of Sphenoscopic acquisition, obtained in direction parallel to the optic axis. It is clearly visible in the middle the vertical dark fringe that is the trace of the optic axis due to the superposition of the optic axis of each light sheet along the height of the light focus. The other fringes, following, are the trace of the isodelay of each light sheet. Thae fact that all the fringes are vertical parallel line is a signature of no stress gradient presence.

The presence of defects or stress inside the crystal volume appears as variation of the interference fringes shape. In the sphenoscopic case, if a stress gradient exists along the probe volume, then fringe spacing will vary, so to produce curved fringes (Fig. 4.36d) [30], [48]. It is important to remark that the main characteristic of Sphenoscopy is that an entire height of the sample can be inspected with just one acquisition giving an easy interpretation of the crystal quality status.

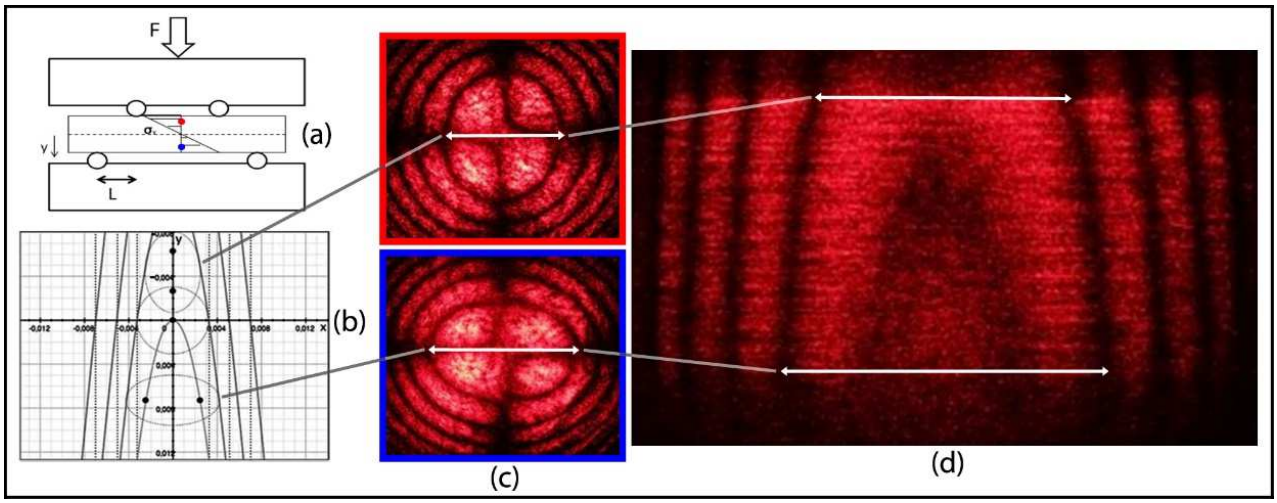

Fig. 4. 36: By using a four point bend test (a) is possible to induce a stress gradient that is linear along y, passing from a tensile stress in the bottom side, to a compressive stress in the top side. In (c) are shown two conoscopic acquisition respectively of the compressive state stress (red box) that correspond to the red dot in the loaded crystal, and a tensile state stress (blue box) that correspond to the blue dot. Passimng from a condiion to the other the elliptical shapes changes, in particular it changes the horizontal section of each ellipse. By a sphenoscopic scan of the crystal along the induced stress gradient (d) it is possible to see a fringes curvature, and the relative distances locally corresponds to the horizontal section of the elliptical fringe in conoscopy. This behaviour is coherent with the model (b) in wich are presented the sphenoscopic fringes with the relative ellipse shaped fringes. The dotted vertical straight lines represent the theoretical shape of the fringes in unloaded condition, instead the continuous lines are the result of the mathematical simulation of the sphenoscopical fringes for this type of applied load.

It is possible to see that fringe spacing variation in Sphenoscopy by inducing a stress gradient by means of 4-point bend test (Fig. 4.36a) [30], [39], [48]. In this manner the stress varies linearly along the y direction, passing from a compressive to a tensile condition. Scanning the sample along this reference direction in Conoscopy, the elliptical shaped fringe patterns change progressively. In particular in Fig. 4.36c it is possible to see the two representative condition: at the top the compressive and at the bottom the tensile, with the ellipses that are rotated of π/2 one respect to the other [28], [30], [48]. In Fig. 4.36d it is possible to see the sphenoscopic acquisition along the same y direction, the fringes obtained are the envelope of the diametric dimension of the conoscopic ones. In Fig. 4.36b we have the model that represent this behaviour in a stressed condition [30]. In the bottom side of the pattern in Fig. 4.36b the traces of the optic axes are recognizable in the thicker black curve because in the tensile area the optic axes open along the direction of the load. In the compressive area the ellipses are rotated by π/2 and for this reason no trace of the optical axes can be seen [30]. The model representing the above behaviour in Fig. 4.36b has been presented in [30], here are reported some steps. Since n_o variates linearly with the stress, by the relation in (2.35) the angle β will variate as well as:

$$tan^2\beta = \frac{n_o^2-(n_o+ky)^2}{(1-(\frac{n_o}{n_e})^2)(n_o+ky)^2} \qquad (4.39)$$

with k linearly dependent by the load.

The equation (4.38) is reported hereafter, but this time the semi-angle β is a function of y:

$$H^2(n_x)N^2(x^2+z^2)(1+tan^2\beta(y))^2 = (x^2 - z^2 tan^2\beta(y))^2 \qquad (4.40)$$

4.3.2 Observation perpendicular to the optic axis direction

The advantage to inspect an entire line by Sphenoscopy instead of a series of point by Conoscopy is also applicable on the field of the observations orthogonal to the optic axis [2], [4], [48]. Also in this case, the wedge of light can be thought as the superimposition of light sheets all with the same common edge of departure. In each sheet we observe the intensity profile across a section of the isocromate fringe pattern. In our case the fringe pattern is composed by quartic curves with the shape similar to branches of hyperbole (Fig. 4.37b). Recompiling the light sheets in the starting wedge, the Bertin surfaces become planes obtained as the envelope of the distances between the branches of the quartic curves in each light sheet (Fig. 4.37a) [2], [4], [48].

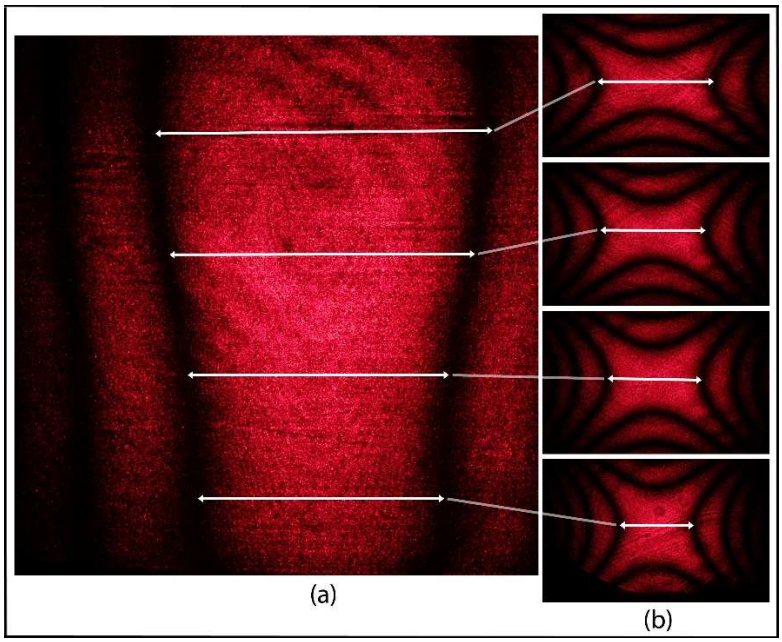

Fig. 4. 37: In (a) we have an acquisition in Sphenocopy in direction hortogonal respect to he optic axis. Also in this case is possible to correlate the distance between the spenoscopyc fringes with the conoscopic ones. In (b) we have the result of a conoscopic scan along the same direction of Sphenoscopy. The trend of the horizontal distances between the fringes in Conoscopy correspond with the trend of the sphenoscopic fringes.

Through a scan of a vertical line using the Conoscopy, it is possible to correlate the parameter of the horizontal distances between the fringes branches with the position of the conoscopic acquisition along this vertical line (Fig. 4.37b). Using a single acquisition in Sphenoscopy, focusing the light

wedge along the same vertical line, it is possible to obtain the same information of the previous conoscopic scan, studying the distance between the vertical fringes (Fig. 4.37a). By iterating this process along the whole sample, it is possible to compare the gradient of the distances in Conoscopy and in Sphenoscopy (Fig. 4.38) [2], [4], [48].

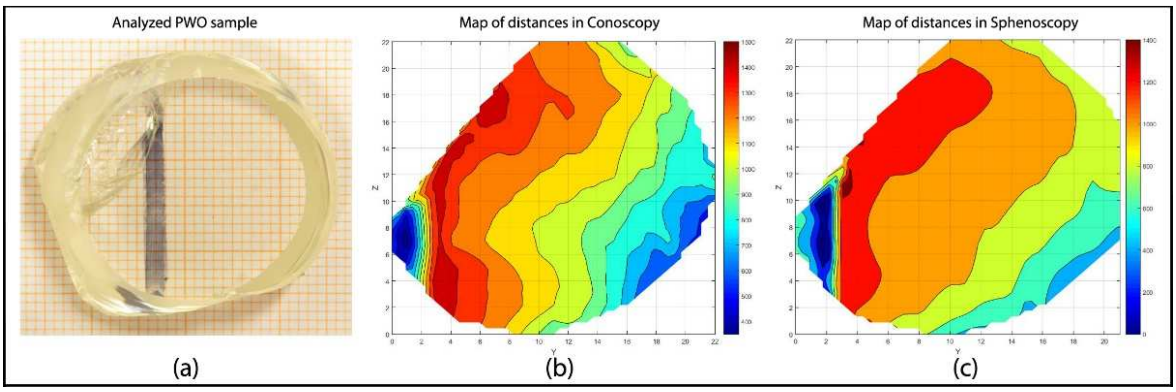

Fig. 4. 38: Starting from a crystal sample (a), by the analysis of a grid of points is possible to obtain the map of the conoscopic distances between fringes. This map can be superimposed to the starting crystal (b). By a scan with Sphenoscopy, so not on a grid of points but along parallel lines, it is possible to obtain the same informations (c). Even if Sphenoscopy produces a similar but less detailed map of the conoscopic one, it results a much faster investigation technique, being able, with a single acquisition, to give information regarding a line instead of a point of the crystal.

Making a scan in Conoscopy, being a punctual analysis, it is possible to obtain a lot of details respect to the Sphenoscopy (Fig. 4.38b). This because with the Conoscopy it is possible to increase the acquisition grid as much as desired. However, by Sphenoscopy it is possible to have sample information with a sufficient level of detail but saving a lot of time, being the sphenoscopic technique able to obtain information from an entire line with only one acquisition (Fig. 4.38c). For example, if it needs to make a scan of a sample with a grid of equidistant points, the Conoscopy need a number of nxn points (Fig. 4.39a). Instead the Sphenoscopy need n vertical lines + n horizontal lines (n+n) (Fig. 4.39b). With each vertical inspection in Spenoscopy are obtained the relative horizontal distances between the conoscopic fringes along the same line, contrariwise in each horizontal inspection are obtained the vertical distances between the conoscopic fringes along the same line.

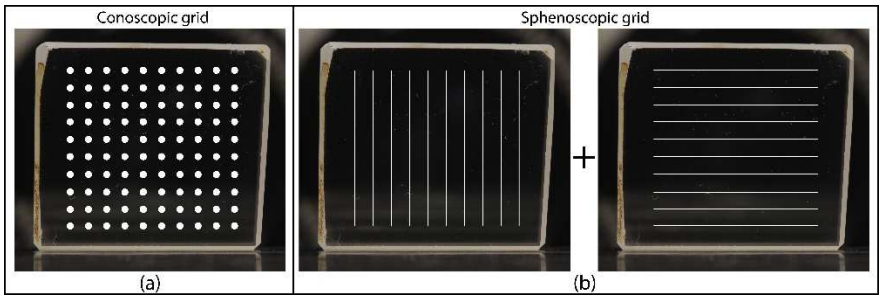

Fig. 4. 39: To have informations from an entire crystal sample, in order to obtain a stress map, a lot of acquisitions are needed. In particular in Conoscopy, being a punctual analysis, we must refer to a grid of equidistant points (a) in which the acquisitions are made. If the sample is a square, then we need nxn acquisitions. With Sphenoscopy, being a technique that investigates an entire line instead of a point, inside the same sample we need n horizontal acquisitions and n vertical acquisitions in order to have the same spatial resolution of the Conoscopy.

4.3.3 Observation along a random direction

With the aim of have another comparison between the conoscopic technique and the sphenoscopic, have been carried out some observations along a random position with respect to the optic axis (Fig. 4.40a). This to compare the two type of fringe pattern coming from each technique [2], [48].

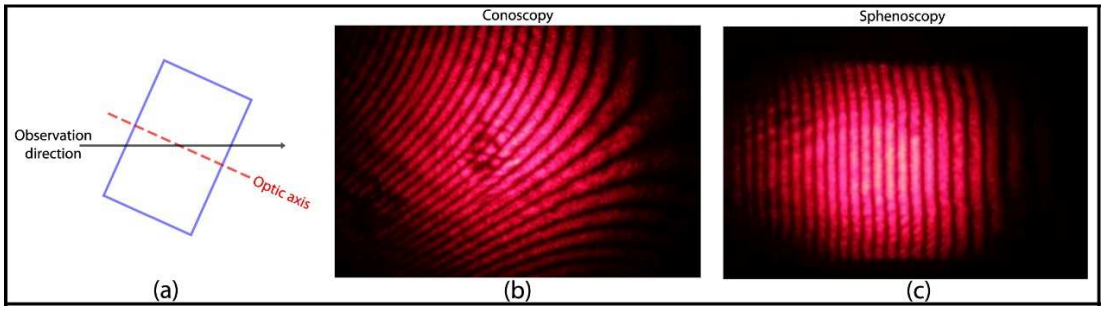

Fig. 4. 40: (a) Scheme of observation in a random position with respect to the optic axis. (b) Conoscopic fringe pattern carried out by one pointwise acquisition. (c) Sphenoscopic fringe pattern obtained by observing the sample in the same direction of the previous case in Conoscopy. The conoscopic pattern appears not easy to interpret; contrariwise, by the sphenoscopic acquired lines, a simplified analysis is possible.

In particular, in Fig. 4.40b is represented the pattern from the conoscopic acquisition, which is a pointwise inspection. This type of pattern is really complex to interpret and hard to correlate with the Bertin surfaces. We do not have closed fringes or reference profiles that are repeated in the image. Contrariwise, looking at the fringe pattern in Fig. 4.40c coming from the sphenoscopic acquisition, it is easier to give a fringes interpretation. In this case, in fact, we have parallel fringes that are repeated throughout the image. In this manner a simplified analysis is possible. In fact, the slight curvature close to the edges confirms the presence of the residual stress.

4.3.4 Fringe analysis

The characterizing requirement for the sphenoscopic analysis in each studied orientation, is the detection of the trend of the distance between a couple of fringes. Starting from an acquisition made by Sphenoscopy (Fig. 4.41a), the first step is to acquire points that belongs to the fringes of interest. This in order to digitalize the fringes shape. Also in this case we have the spackle noise influence, therefore, before any operation, we have to remove it via image filters [1], [43], [44]. Once that these points belonging each sphenoscopic fringe of the filtered image are acquired, each fringe is fitted through an equation that minimize the standard deviation with the founded points (Fig. 4.41b).

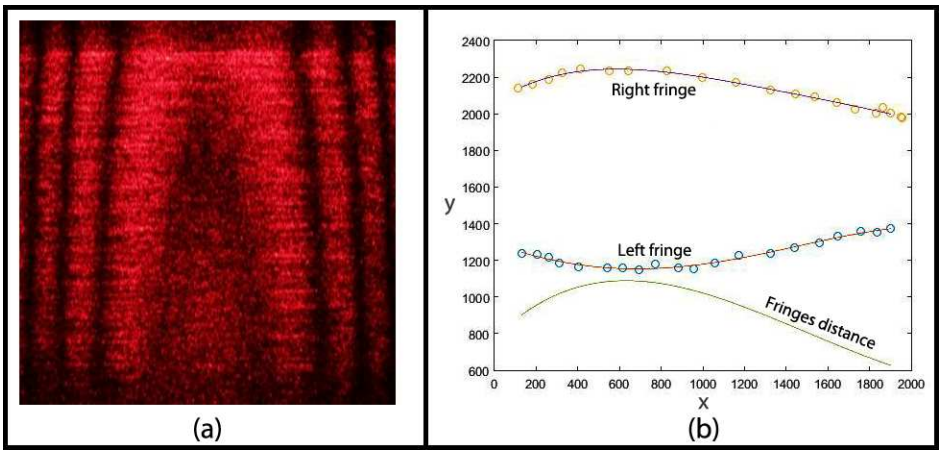

Fig. 4. 41: Starting from an image obtained in Sphenoscopy (a), the first thing to do is an image processing in order to make more easy the acquisition of the points that belongs to each fringe, wich are obtained as points of minimum light intensity (b). Using these obtained points, each fringes are fitted with a mathematical function that minimize the standard deviation with the selected points (b). Once that the fringes are digitalized as mathematical funtion, is easy to obtain the trend of the distance between the fringes.

Once that the fringes are transformed in a mathematical function, is easy to extrapolate the trend of the distances between the fringes [2], [4], [48].

4.4 Observations in collimated light in direction normal to the optic axis.

This developed system is aimed to examine with another technique, in direction orthogonal to the optic axis, seven PWO samples, six of which came from the same production family.

4.4.1. Photoelastic System Set-up

The system is very simple, being composed only of a laser source, an observer and an analyser placed in a dark field configuration with the laser. What described above represents the basic set-up 1 of the system (Fig. 4.42), starting from it a beam expander can also be added to the source, obtaining the configuration in Fig. 4.43 (set-up 2).

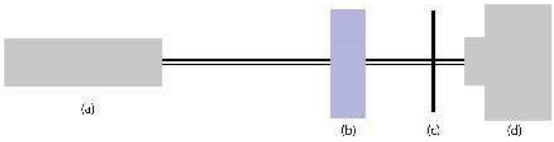

Fig. 4. 42: Set-up in configuration 1, composed by: a) laser, b) sample, c) analyser, d) observer.

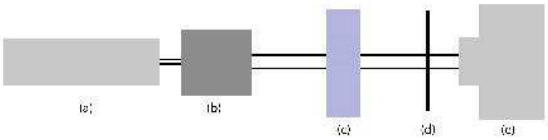

Fig. 4. 43: Set-up in configuration 2, composed by: a) laser, b) beam expander, c) sample, d) analyser, e) observer.

4.4.2 Photoelastic observation performed

4.4.2.1 Measures without beam expander (set-up 1)

The crystals under examination have an orientation of the optical axis parallel to the surface in exam. The sample is inserted into the set-up 1 and positioned with the surface orthogonal to the incident laser beam. Under these conditions, the observer obtain acquisitions such as those in Fig. 4.44, where it is possible to observe the presence of a fringe passing through the laser spot.

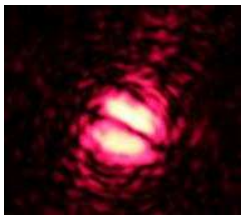

Fig. 4. 44: Example of acquisition obtained by the Set-up 1, it is possible to see a fringe that cross the laser spot.

In order to understand if this fringe is fix with the sample, different orientations of the samples are analysed, maintaining the surface in exam orthogonal to the laser beam. Once defined a reference system (Fig. 4.45), to ensure that the laser spot always invests the same sample portion as it is rotated, the centre of rotation is made to coincide with the laser spot (Fig. 4.45). The analysis was then performed in a range between -18° and +18°, studying what happened in every variation of 1°

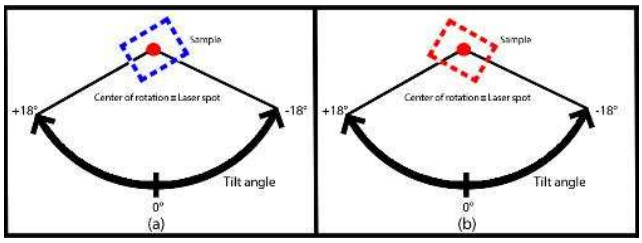

Fig. 4. 45: Reference system used for the analysis of the crystal in different orientations. Mantaining the surface of interest hortogonal to the laser spot, the sample was tilted in order to acquire the sample in different conditions.

The different inclination conditions are presented in Fig. 4.46. It is clear that the fringe, observed in a static condition, also results to rotate as the sample. This type of fringe is therefore integral with the samples.

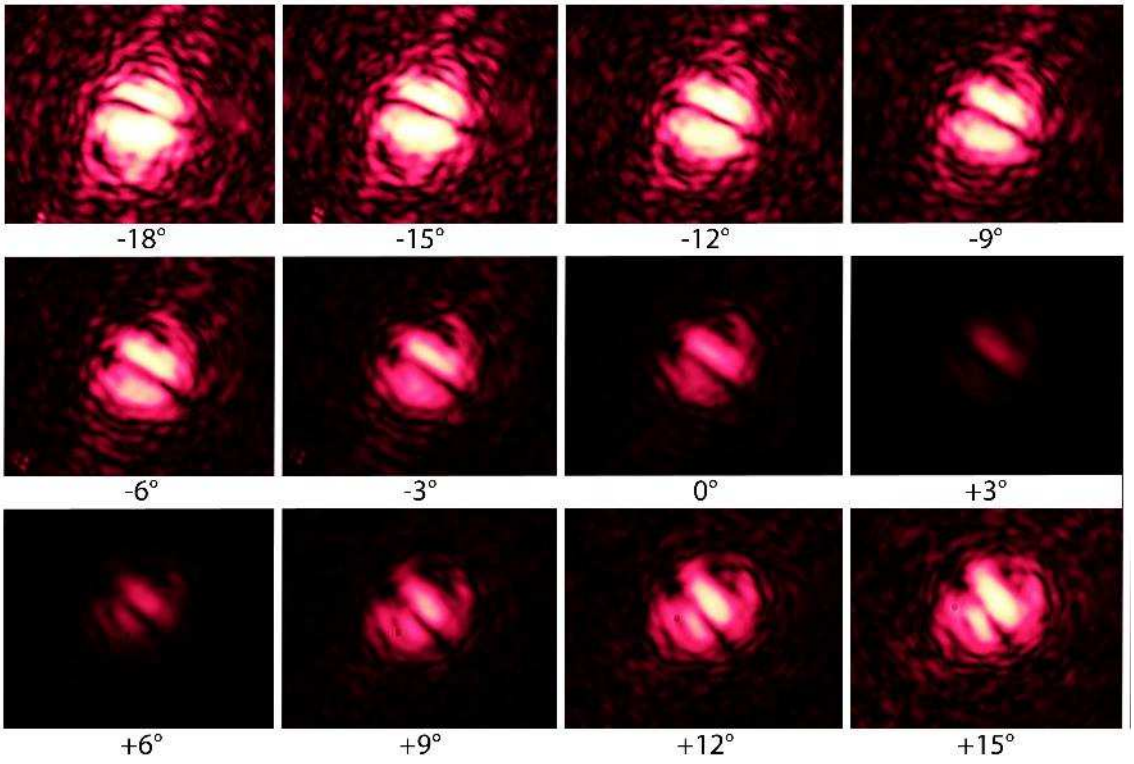

Fig. 4. 46: The behaviour of the fringe is studied by rotating the crystal, in order to understand if the interference figure is solidal respect to the surface. The results is that y increasing the orientation angle of the sample, it is possible to see that also the fringe orientation angle increase by the same amount.

4.4.2.2 Measures with beam expander (set-up 2)

The same type of samples is studied, maintaining the same orientation but using the set-up 2. The laser beam is then positioned orthogonal to the crystal surface and therefore to the optic axes. Using this configuration, it is possible to obtain acquisitions like this shown in Fig. 4.47. In this way, parallel fringes with the same frequency equally distributed along the whole area of the sample are observed.

Fig. 4. 47: Acquisition obtainable using set-up 2. It is possible to observe a series of parallel fringes that are equally distributed along the whole area of the sample.

As in the previous case the sample in exam was tilted following the reference system in Fig. 4.45. This to validate the results obtained with the set-up 1 (without beam expander). Hence, looking at the crystal for increasing inclinations, it is possible to obtain what is schematized in Fig. 4.48.

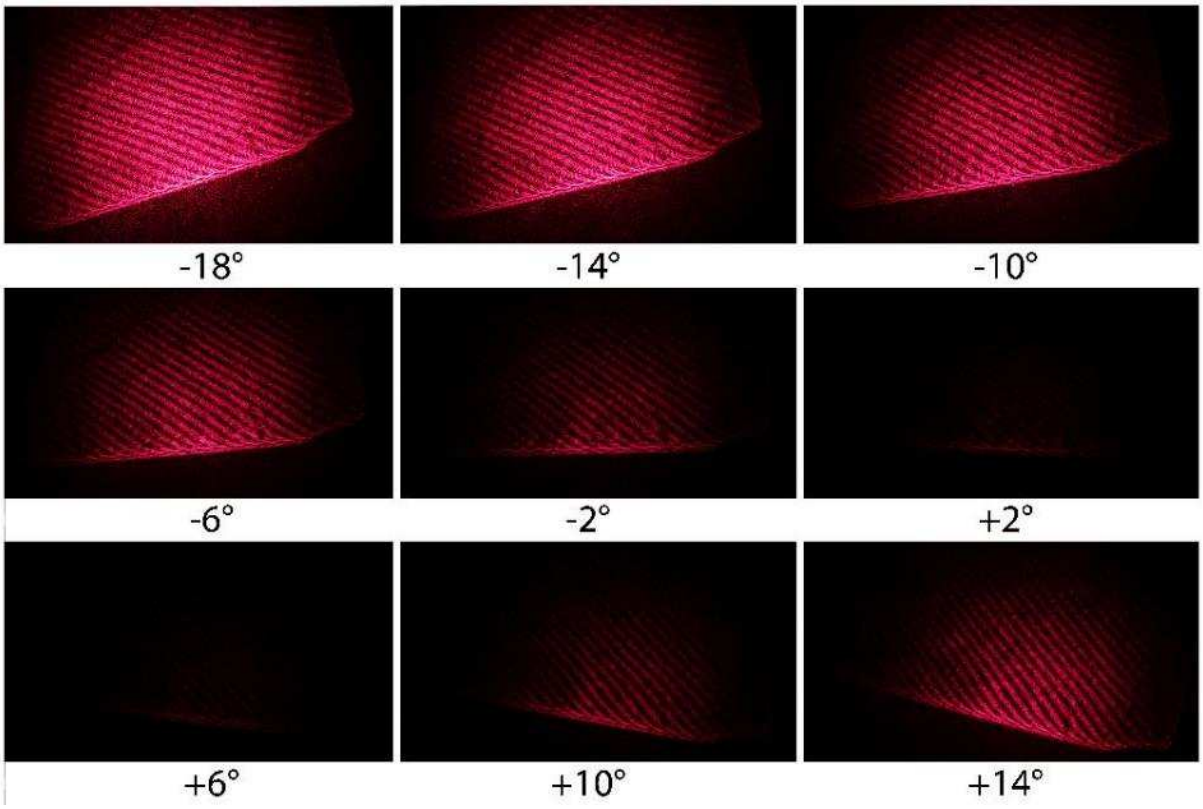

Fig. 4. 48: It is shown that, when the orientation of the sample is varied, the inclination of the fringes also varies by the same amount in the measure condition with beam expander

The results coming from this analysis confirm that, by increasing the rotation of the sample by 1°, the fringes angle increases by the same amount. It is therefore verified, also in this case, that the fringes turn together with the sample. In order to test the spatial frequency of this fringes, a further test is made in the same configuration of the optical bench but changing the laser source. In this

way it is possible to verify if decreasing the wavelength of the source, the spatial frequency of the fringes increases.

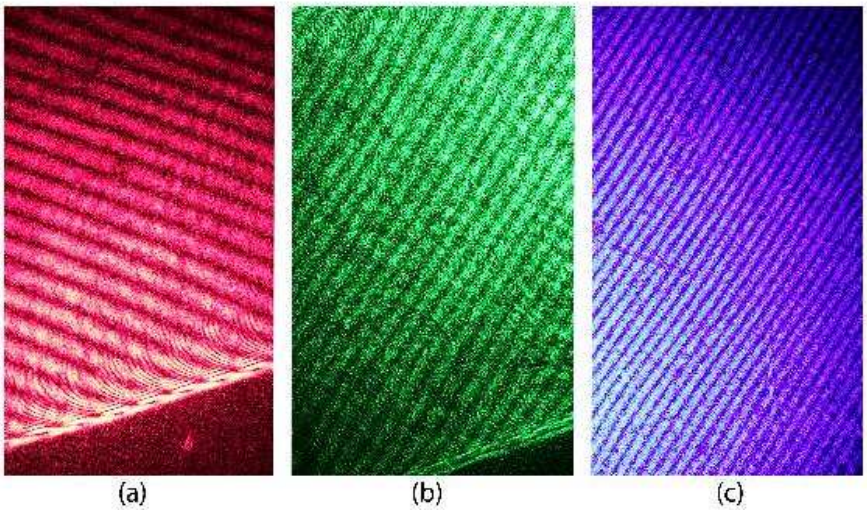

Fig. 4. 49: Sample analysis with different wavelenght laser source. In (a) a 633nm laser source was used, in (b) a source of 532nm and finally in (c) a source of 473nm. Looking at the different conditions, it is clear that decreasing the wavelenght of the laser, the spacial frequency of the fringes increase.

The proportionality between the laser source wavelength and the fringes spatial frequency is shown in Fig. 4.49. Passing from a red laser (633nm) (Fig. 4.49a) to a green laser (532nm) (Fig. 4.49b) and then to a blue laser (473nm) (Fig. 4.49c), thus decreasing the wavelength of the source, it is possible to see that, observing the same spatial portion of the sample, the fringes appears with an increasing frequency.

4.4.3 Geometric analysis of the samples

A dimensional analysis is carried out on the six samples of the same family to geometrically evaluate any non-coplanarity of the surfaces crossed by the laser beam. For the measurements, the reference system used is this in Fig. 4.50, where the z axis coincides with the beam direction and verse of the previous laser measurements. The two surfaces A and B, with their parallels, are considered parallel respectively to the reference plane ‘x-z’ and ‘y-z’. Contrarywise, the surface opposite to D is considered parallel to the plane ‘x-y’ (and also normal to the laser direction) but the surface D is constructed randomly oriented.

In order to perform easily the necessary geometrical measures, considerations must be made to calculate the not coplanarity of the surface D (Fig. 4.50). The sample is projected onto the 'x-z' and 'y-z' planes (Fig. 4.51a - b). Then, in each of the two projections the difference in length of the edges parallel to the z axis is measured. Once these quantities are known, in the projection respect to the plane 'x-z' in obtained the inclination α of the projection edge ‘g’ with respect to the x axis (Fig. 4.51a). In the other projection 'y-z' is instead calculated the angle β of the projection edge ‘h’ respect to the y axis (Fig. 4.51b). Once the inclinations of the edges with respect to the two projections are known, the vector $\underline{n_1}$ normal to the edge ‘g’ in ‘x-z’ and the vector $\underline{n_2}$ normal respect to the edge ‘h’ in ’y-z’ are constructed. From the vector $\underline{n_1}$ it is possible to obtain the component $\underline{n_{1n}}$ parallel to the x axis, instead from the vector $\underline{n_2}$ can be calculated the component $\underline{n_{2n}}$ parallel to the y axis (Fig. 4.51c). Considering now the sample projection on the 'x-y' plane, the visible part of the vectors $\underline{n_1}$ and $\underline{n_2}$ on this plane are the just considered $\underline{n_{1n}}$ and $\underline{n_{2n}}$ components, which results, as a matter of fact, the projections of the original vectors on the plane ‘x-y’ (Fig. 4.51d). By the composing of these two vectors $\underline{n_{1n}}$ and $\underline{n_{2n}}$, it is possible to obtain the normal $\underline{n}$ respect to the surface D, that is randomly oriented respect to the ‘x-y’ plane. This vector $\underline{n}$ has an angle respect to the y axis, named γ (Fig. 4.51d).

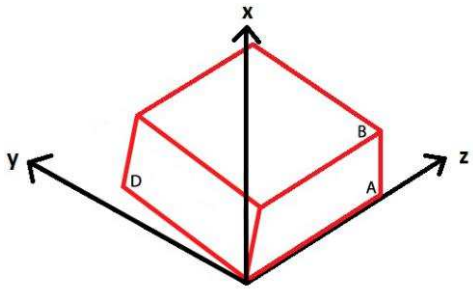

Fig. 4. 50: Reference system used for the sample geometrical measurements, the z axis was chosen with the same direction of the laser beam in the previous analisis.

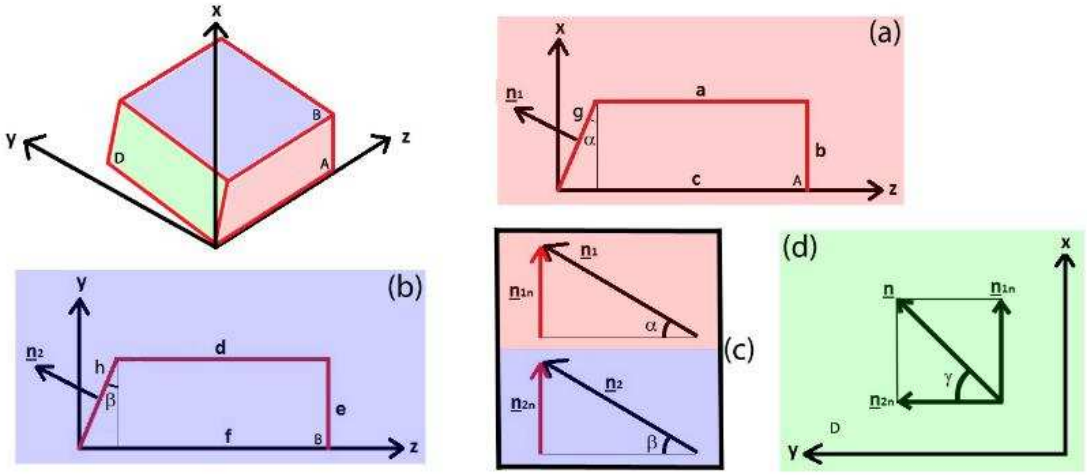

Fig. 4. 51: Starting from the crystal inserted into the reference system, by the projections of the sample respect to the 'x-z' plane (a) and 'y-z' plane (b) it is possible to obtain respectively the two inclinations α and β of the projection edges g and h that belonging to the surface D. Once constructed the normal $\underline{n_1}$ and $\underline{n_2}$ to the edges g and h, trough the angles α and β it is possible to obtain their components $\underline{n_{1n}}$ and $\underline{n_{2n}}$ parallel respectively to the x and the y axis (c). The found components, are used in the plane 'x-y' to find the vector $\underline{n}$ normal to the surface D and its inclination γ respect to the y axis.

From the trigonometric point of view, the angles α and β were calculated:

$$\alpha = atan\frac{(a-c)}{b} \tag{4.41}$$

$$\beta = atan\frac{(d-f)}{e} \tag{4.42}$$

To obtain the components $\underline{n_{1n}}$ and $\underline{n_{2n}}$ we have:

$$\underline{n_{1n}} = sen(\alpha) \tag{4.43}$$

$$\underline{n_{2n}} = sen(\beta) \tag{4.44}$$

hence:

$$\underline{n_{1n}} = sen\left[atan\frac{(a-c)}{b}\right] \tag{4.45}$$

$$\underline{n_{2n}} = sen\left[atan\frac{(d-f)}{e}\right] \tag{4.46}$$

Therefore, in order to obtain the angle γ we have:

$$\gamma = \text{atan}\left(\frac{n_{1n}}{\underline{n_{2n}}}\right) = atan\left\{\frac{sen\left[atan\left(^{(a-c)}/_{b}\right)\right]}{sen\left[atan\left(^{(d-f)}/_{e}\right)\right]}\right\} \tag{4.47}$$

By means of equation (4.47) then, the angle γ is calculated in each of the six samples coming from the same family. Tre results are presented in the Table 4.2.

γ smpl1	γ smpl2	γ smpl3	γ smpl4	γ smpl5	γ smpl6
351,28°	294,84°	299,54°	296,14°	294,99°	246,5°

Table 4. 2: Results from the calculation of the angle γ in each sample from the same family.

4.4.4 Calculation of fringe inclinations and comparison with geometric results

Using the usual reference system in Fig. 4.50, the samples were observed with the laser spot in the same direction and verse of the z axis and normal to the first incident crystal surface. In this manner, using the set-up 2 (Fig. 4.43), the transversal fringes are acquired in each of the six samples belonging the same family. Then, in every acquisition coming from the relative crystal, was calculated the angles of the normal to the fringes respect to the y axis (Fig. 4.52).

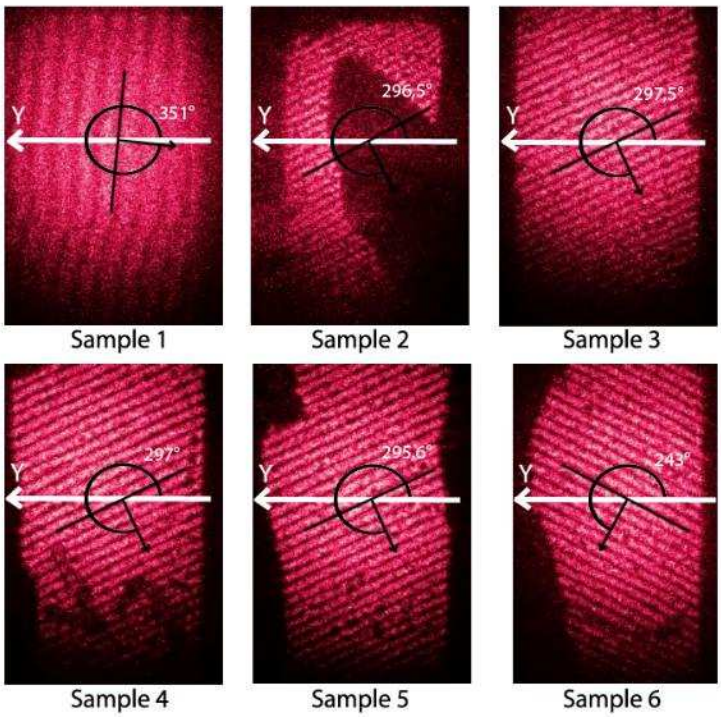

Fig. 4. 52: In each sample was extracted the parallel fringes and then was calculated, from each acquisition coming from the relative crystal, the angle between the y axis and the normal to the fringes direction.

Putting together the last results with the results coming from the geometrical analysis, it is possible to obtain the following Table 4.3.

	γ smpl1	γ smpl2	γ smpl3	γ smpl4	γ smpl5	γ smpl6
Geometric analysis	351,28°	294,84°	299,54°	296,14°	294,99°	246,5°
Fringe analysis	351°	296,5°	297,5°	297°	296,5°	243°

Table 4. 3: Comparison of the results coming from the geometrical analysis and the fringe analysis. From the geometrical analysis we have the angle between the normal to the surface D and the y axis. In the fringe analysis we have the angle between the normal to the fringes directions and the same y axis.

In order to understand the correlation between the two measures is important to make an optical analysis of the problem. In a crossed axes plane polariscope (Fig. 4.42, Fig. 4.43) the light intensity that arrives to the observer is given by the equation [22], [50]:

$$I = A^2 sin^2(2(\theta - \omega)) sin^2(\pi\delta) \quad (4.48)$$

where:

$$\delta = \frac{d}{\lambda}(n_1 - n_2) \quad (4.49)$$

having considered:

d = thickness of the sample in exam

λ = wavelength of the laser source used

δ = spatial delay related to λ

θ = angle formed between the x axis and the cross of tensions

ω = angle between the axis x and the polarization plane of the analyser

n_1 and n_2 = refractive indices of the material

The intensity of light becomes zero when:

$\delta = n$ (with n integer number) (4.50)

$\theta = \omega$ (4.51)

The fringes corresponding to the relation (4.50) are the locus of points where the delay δ is constant and equal to the integer number (n=1,2,3...) called fringe order. It must be considered that, as we observed, the quantity d changes along the surface of the samples, then also the quantity δ changes, being a function of the parameter d ($\delta(d)$) (4.49). Furthermore, it should be noted that, since the fringes are normal to the projection on the plane 'x-y' of the vector normal to the surface D (geometrically calculated) (Fig. 4.51), they can be seen as lines of equal thickness of the sample. Knowing that the inclination of the fringes agrees with the geometrical measurements and that δ is a function of d (4.49), it is possible to consider the series of parallel fringes as increasing or decreasing fringe orders. In order to be clearer, from the optical point of view, in each fringe the quantity δ is equal to an integer number. The same fringe is also, from the geometrical point of view, a locus of points where the thickness of the sample is constant. Passing from a fringe to the next one, we find another locus of equal thickness, but that is different from the previous one. Between these two fringes, considering the other parameters almost constant, the parameter that is changed is d. Therefore, if the thickness is increased we have the fringe that represent the next fringe order δ+1, if it is decreased we have the previous fringe order δ-1.

4.4.5. Comparison between collimated light fringes and acquisitions in Conoscopy

In the remaining sample of PWO was performed a more deepen analysis to understand the fringes acquired with the collimated light test though the comparison with the conoscopic test. At first was used the set up in Fig. 4.43 to acquire the fringes in collimated light using a beam expander (Fig. 4.53b), in order to have a starting image for the further analysis. This Image was acquired observing the crystal along the 'a' crystallographic plane. Once completed this operation, the laser has been turned off with the aim of acquire the sample surface illuminated by the ambient light, with the reference of the graph paper resting on the sample surface (Fig. 4.53a). If the sample remains in the same position between the measurement with and without the laser source, it is possible to superimpose the two images with the purpose of having an idea of the geometrical fringes size (Fig. 4.53c).

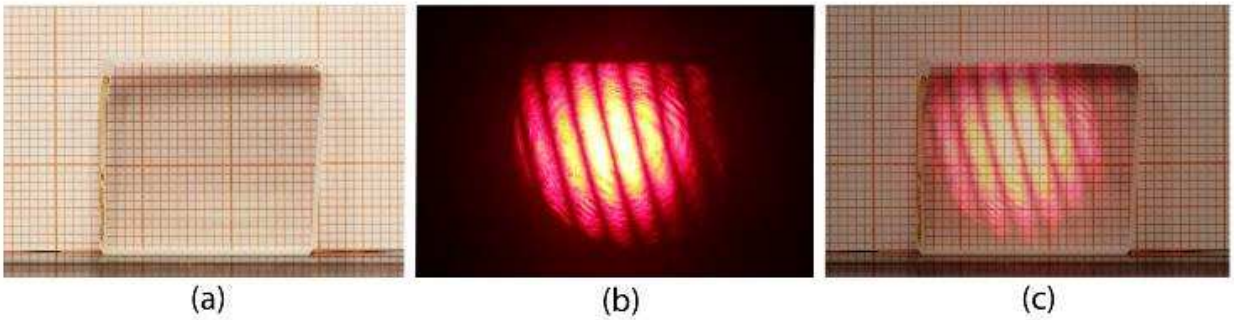

Fig. 4. 53: (a) Fringes acquired using a collimated light beam with beam expander, in (b) is shown the sample in the same position after turning off the laser source, illuminated by ambient light and with the presence of graph paper resting to the sample surface. In (c) we have the superimposition of (a) and (b) in order to see the approximately the fringes size.

The superimposing of the graph paper with the sample is useful because it can be used also as a reference for a conoscopic analysis. For this purpose, a test bench was implemented using the traditional scheme for a conoscopic analysis [2], [4], [48] (Fig. 4.54a). Therefore, through the laser focused on the crystal to produce the probe cone volume (Fig. 4.54b), was performed a scan of a horizontal line inside the sample, observing the crystal in the same 'a' crystallographic direction (Fig. 4.54c). The acquisitions along this inspected line are one millimetre equidistant, in order to make it comparable with the graph paper grid.

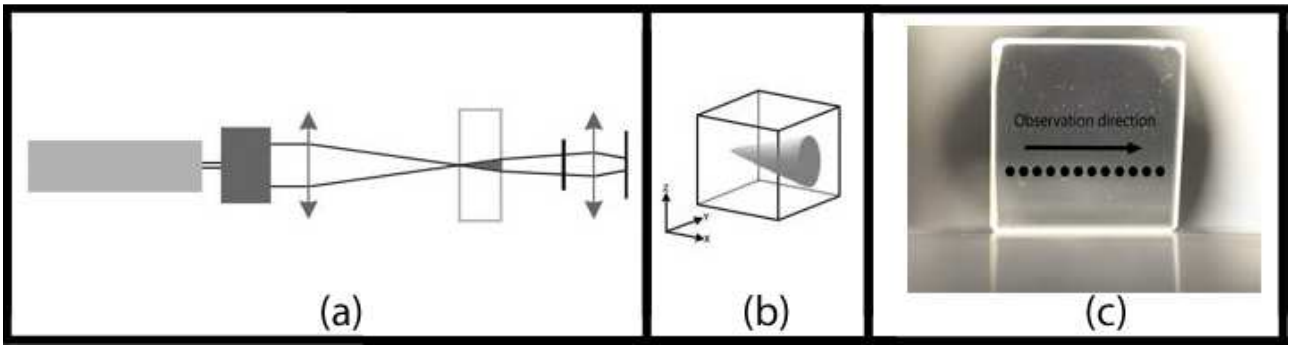

Fig. 4. 54: (a) Typical layout of a conoscopic test, that produce a laser cone inside the sample (b) where the interference fringes appears. This punctual analysis was performed along a line, with the measurement points one millimetre equidistant (c).

With this kind of orientation along the 'a' crystallographic axis, through Conoscopy is possible to obtain acquisition images like in Fig. 4.55, where the two measurable parameters are the horizontal distance Δy and the vertical distance Δz between the fringes vertices [2], [4], [48].

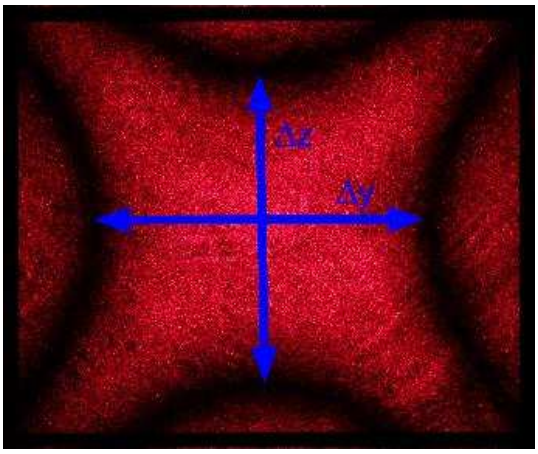

Fig. 4. 55: Example of conoscopic acquisition observing he sample along the 'a' crystallographic axis. In the image is shown also the measurable parameters Δy and Δz that represents the distances between the vertices of the fringes.

By organizing all the acquisitions obtained along the reference line, it is possible to obtain the graphs in Fig. 4.56 that describes the trend of the parameters Δy and Δz in function of their position along the measurement line.

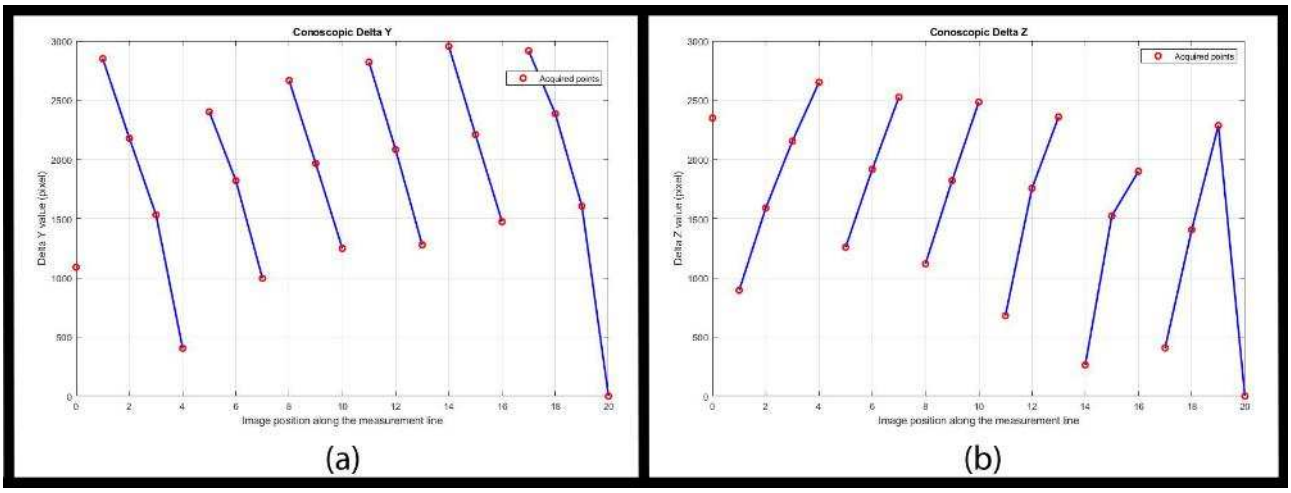

Fig. 4. 56: In (a) we have the trend of the measured Δy parameter in function of the acquisition position along the horizontal reference line. In (b), as same, we have the trend of the Δz parameter in function of the acquisition position along the horizontal reference line.

The measured distances Δy produces a series of six broken lines, all equidistant and with the same orientation. Contrariwise, regarding the distances Δz we have similarly a series of six equidistant broken lines, but with an opposite orientation compared to the Δy case (Fig. 4.56). It is important to note that there is a point (in correspondence with the twentieth millimetre in the graph) where both the distances results collapsed. In this case Δy and Δz are considered zero (Fig. 4.57).

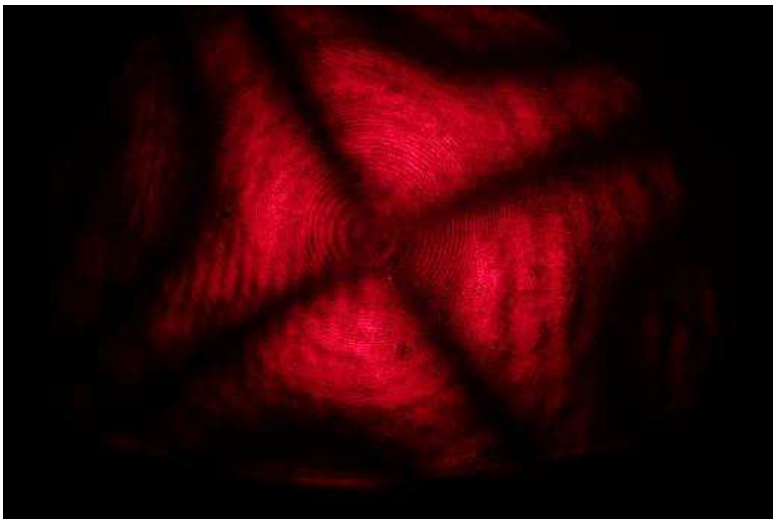

Fig. 4. 57: Example of acquired images where the distances Δy and Δz results collapsed to zero

Utilizing the same previous concept, was performed also a conoscopic scan [2], [4], [48] along a vertical line inside the sample, using the same direction of observation, that is the 'a' crystallographic plane (Fig. 4.58 a – b - c). Also in this case, the acquisitions were made equidistant one millimetre along the reference line.

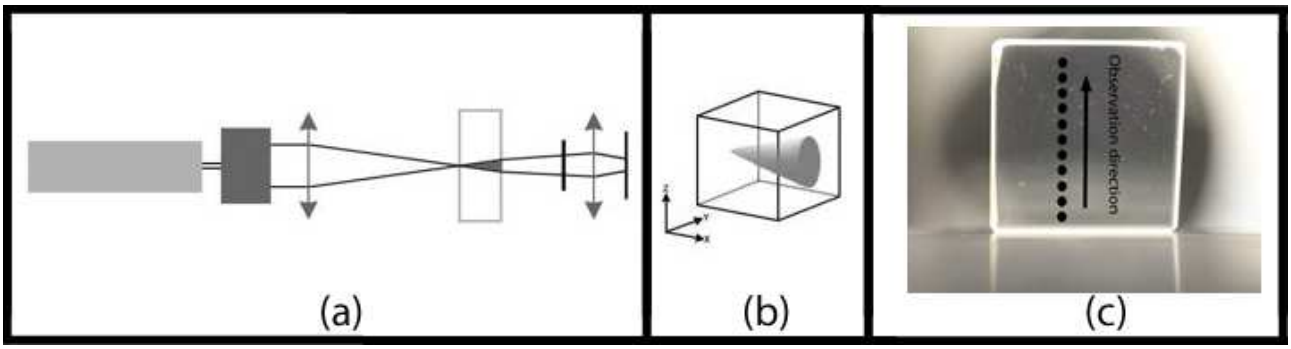

Fig. 4. 58: (a) same layout used in the previous conoscopic scan, in order to produce within the sample, the laser cone (b) where the interference fringes are formed. This time the scan direction is vertical, with the acquisitions equidistant one millimetre (c).

The obtainable acquisitions even in this case are like that in Fig. 4.55, thus, putting together all the acquisitions along the new scan direction, it is possible to obtain the graphics of Δy and Δz in function of their position along the measurement line (Fig. 4.59).

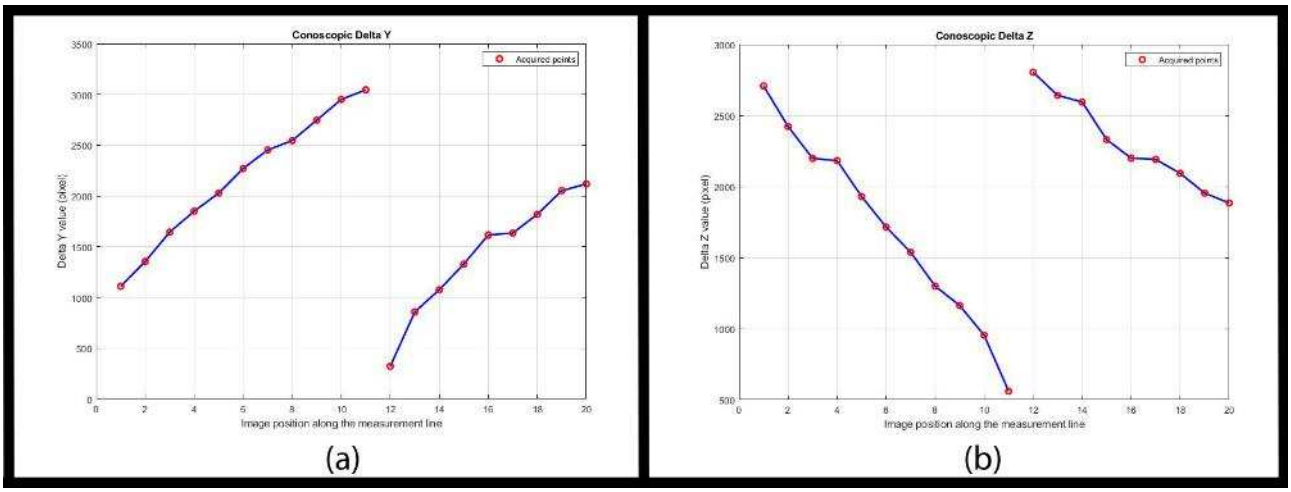

Fig. 4. 59: In (a) we have the trend of the measured Δy parameter in function of the acquisition position along the vertical reference line. In (b), as same, we have the trend of the Δz parameter in function of the acquisition position along the vertical reference line.

In this case for the parameter Δy we have two similarly oriented broken lines. Still for Δz we have two similarly oriented broken lines, but this orientation is opposite to the orientation of the broken lines that describe the Δy trend along the vertical line. To understand better the phenomenon, the graph of the distances in Conoscopy must be compared with the respective area of the sample illuminated by collimated light. Considering the horizontal scanned line, it is possible to see the respective investigated zone inside the image where the collimated light fringes are superimposed to the sample with the graph paper. In Fig. 4.60a the black line represents the scanned area in Conoscopy inside the sample, and this distance, from the left to the right, correspond to the x axis in the graphs in Fig. 4.60b for the conoscopic distances. It is important to remark that the acquisitions in Conoscopy have been made equidistant one millimetre, then the conoscopic acquisition scheme corresponds to the graphic paper grid. Comparing the two type of measure it is possible to see that, passing from a black fringe to the next in collimated light reference, the trend of Δy and Δz regarding the relative conoscopic acquisitions path remains the same. Instead, to cross a black fringe acquired in collimated light produces a discontinuity in the conoscopic graphs on the relative spatial reference. Summarizing, between each black fringe in collimated light it is present the same relative behaviour in Conoscopy, but the crossing of a fringe in collimated light produces a discontinuity in the relative conoscopic graphs (Fig. 4.60b).

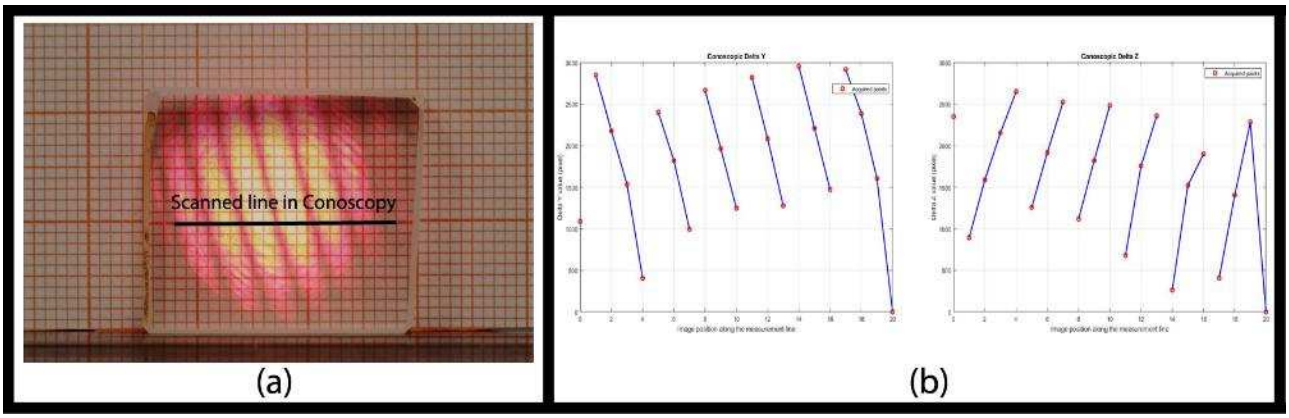

Fig. 4. 60: Comparison between (a) the fringes acquired in collimated light with a graph paper of reference, where the horizontal line of acquisition in Conoscopy is traced, and (b) the relative graphs of Δy and Δz. It is possible to see that both Δy and Δz has the same period of the fringes in collimated light.

The same procedure was done for the conoscopic vertical acquisition line inside the sample (Fig. 4.61a). Comparing the collimated light fringes with the graphs in Conoscopy (Fig. 4.61b) it is possible to see that is confirmed the behaviour discussed with the horizontal line in Fig. 4.60. As above, in fact, the distances in Conoscopy presents a discontinuity when cross the point relative to the black fringe in the collimated light reference, producing two broken lines with the same trend between the black fringes.

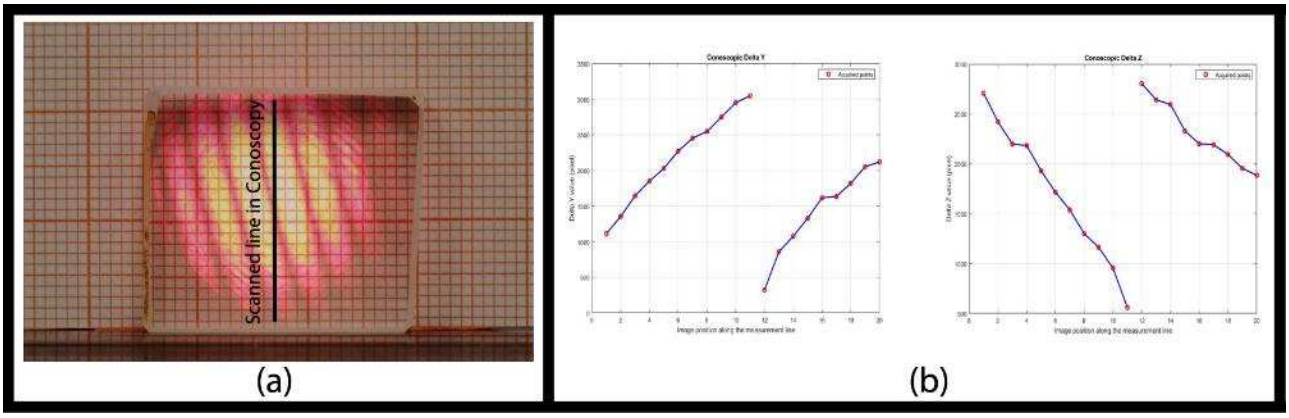

Fig. 4. 61: Comparison between (a) the fringes acquired in collimated light with a graph paper of reference, where the vertical line of acquisition in Conoscopy is traced, and (b) the relative graphs of Δy and Δz. It is possible to see that both Δy and Δz presents a discontinuity when crossing the black fringe.

Through the study of these two cases, is possible to confirm the hypothesis that the black fringes in collimated light represent the transition to another fringe order. Because of this, when a black fringe is crossed in Conoscopy, a discontinuity is generated in Δy and Δz graphs. This passage from one fringe order to the other is caused by the non-coplanarity of the two surfaces crossed by the laser. This is easily verifiable trough the measure of the thickness variations inside the sample. Using these values of thickness, it is possible to study the variation of the parameters Δy and Δz in function of

'd' inside (4.19)(4.20), being these equations a function of the angle β and of the parameter $N^{(-)}$ and $N^{(+)}$ respectively. These last two parameters are function of β and of the studied thickness 'd' (4.18). Using a micrometric calliper is easily possible to obtain the data in Fig. 4.62.

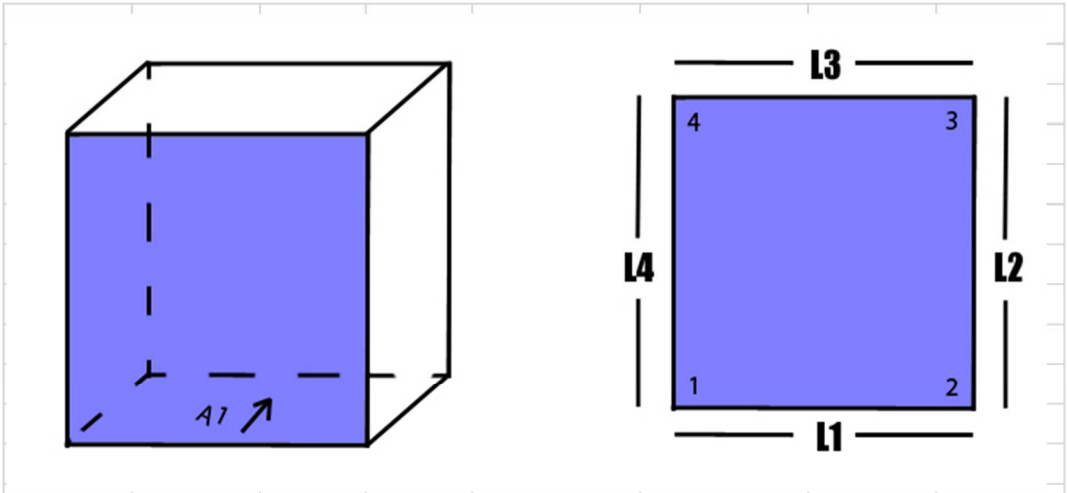

		Caplier (mm)		Thickness difference			
Point				Point1-2	Point2-3	Point3-4	Point4-1
1		6,662		0,047	-0,015	-0,045	0,013
2		6,615					
3		6,63					
4		6,675					

Fig. 4. 62: Geometrical analysis of the used sample.

Through the obtained geometrical parameters, it is possible to extrapolate from (4.19)(4.20), once defined a reasonable value for the β parameter in a PWO sample, the trends of Δy and Δz in each case in exam, in function of the thickness variation. Regarding the horizontal investigated line in Fig. 4.60a, they are measurable from the left to the right two different thickness, that is respectively 6.662mm and 6.615mm (Fig. 4.62). These values were used inside the (4.19)(4.20), as explained, in order to extrapolate the Δy and Δz values in function of the aforementioned thickness variation. It is important to show the results obtained from the mathematical model next to the same results calculated in Conoscopy. Regarding the Δy distances, we have in Fig. 4.63a what can be obtained from the mathematical model using the obtained data and in Fig. 4.63b the same parameter trend calculated along the conoscopic line in exam.

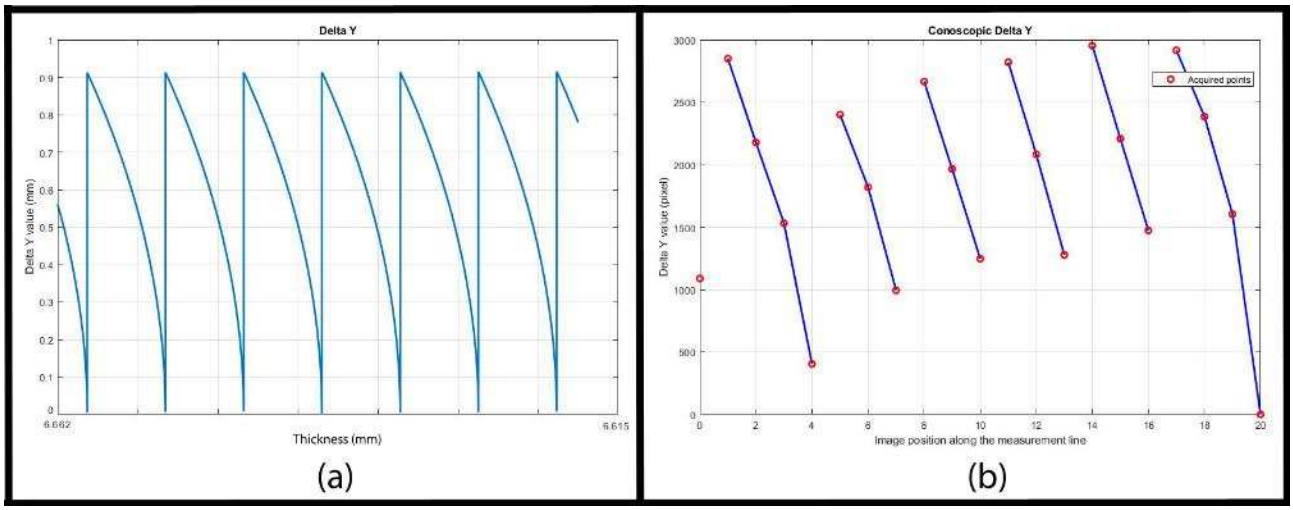

Fig. 4. 63: Comparison between the (a) Δy distances obtainable using the measured thickness of the sample inside the mathematical model and (b) the relative distances calculated using the conoscopic technique. The two graphs shows that the same quantity, obtained using two different way, has the same behaviour.

The two graphs appear with the same period of discontinuities and they are partially overlappable, the slight differences are due to possible variations of the parameter β related to the stress state [4], [48]. But nevertheless, the curve obtainable from the mathematical model seems to be the detailed representation of what happens by measuring the same datum with the Conoscopy. Also studying the comparison of the Δz parameter simulated (Fig. 4.64a) with the related distances calculated in Conoscopy (Fig. 4.64b), we have the same results of the distance dy.

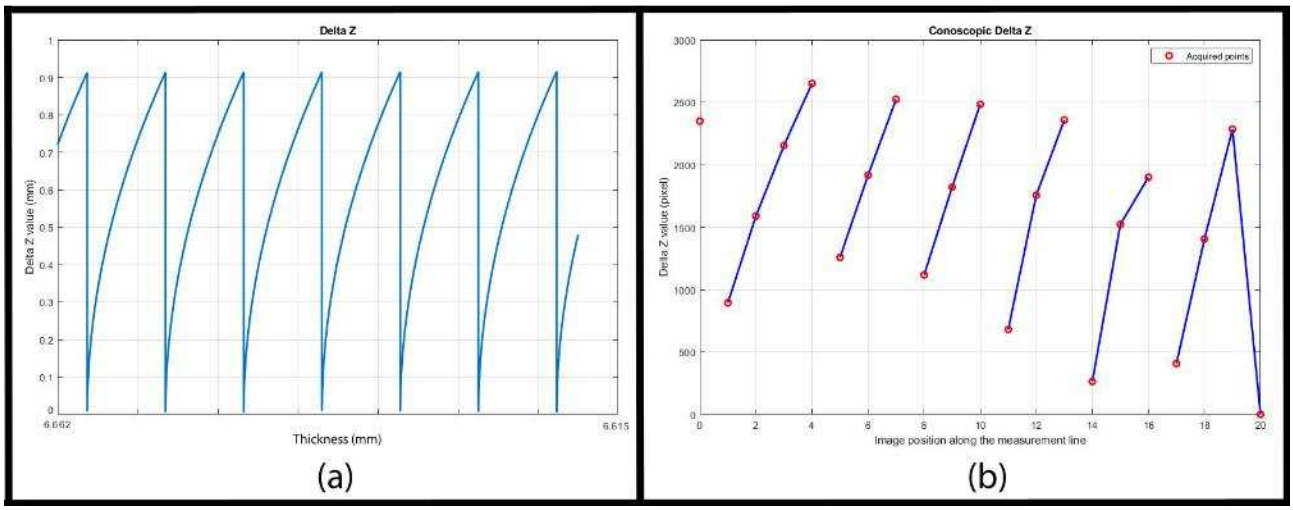

Fig. 4. 64: Comparison between the (a) Δz distances obtainable using the measured thickness of the sample inside the mathematical model and (b) the relative distances calculated using the conoscopic technique. Also in this case the teoretical trend with the practical trend are overlappable

The discontinuities, represented as vertical line in the mathematical model graph (Fig. 4.63a, Fig. 4.64a, Fig. 4.65a, Gig. 4.66a) are related to the changing of the fringe order. In those points the

distances Δy and Δz collapses as in Fig. 4.57. Before this point in Conoscopy we calculate the distance between two couple of fringes defined respectively by two fringe orders. After this point we calculate the distances between two couple of fringes defined by two different fringe orders respect to the previous case. Because of this, the graph is periodic, moving from one fringe order to another. When the parameter d varies within a certain range, we can see by (4.19)(4.20) that the quantities Δy and Δz vary in a linearizable way. On the other hand, if the variation of the parameter goes outside this range, there are collapses of the distances Δy and Δz, with relative change of the reference fringe orders. With the aim of continuing the analysis, it has been studied what happens along the vertical investigation line in Fig. 61a. In this case the thickness variation is lower, passing from 6.615mm to 6.630mm. In fact, studying what happens in the mathematical equations (4.19)(4.20), we have only one point of discontinuity in the graph in each distance Δy and Δz (Fig. 4.65a, Fig. 4.66a). The relative distances in Conoscopy (Fig. 4.65b, Fig. 4.66b) confirm these trends of the mathematical model. Also in this case, the two distances can be superimposed with the mathematical model, except for variations of the beta parameter [4], [48].

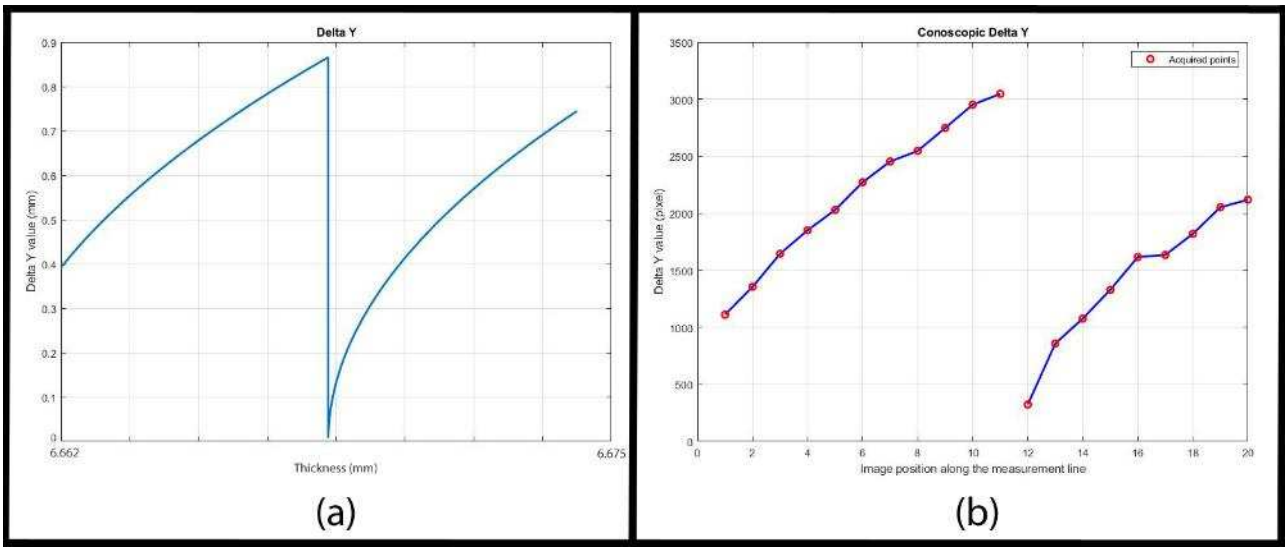

Fig. 4. 65: Comparison between the (a) Δy distances obtainable using the measured thickness of the sample inside the mathematical model and (b) the relative distances calculated using the conoscopic technique In this case the difference of thickness is less, cause of that we have only one discontinuity point confirmed by both the techniques. Regardless of this the two graphs also in this case are symilar.

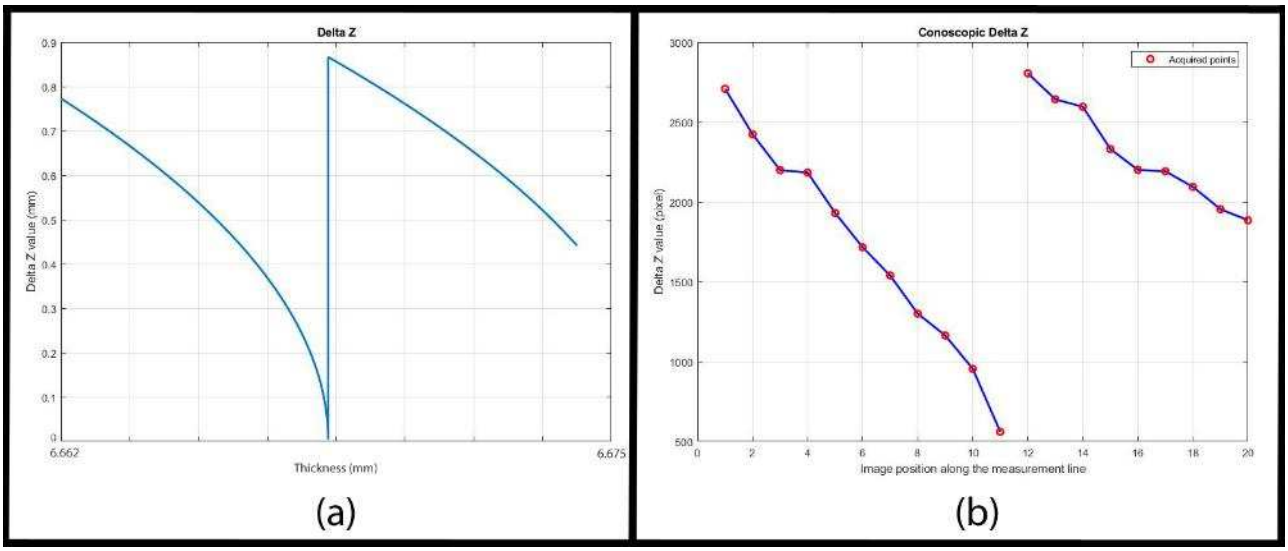

Fig. 4. 66: Comparison between the (a) Δz distances obtainable using the measured thickness of the sample inside the mathematical model and (b) the relative distances calculated using the conoscopic technique. Also in this case the teoretical trend with the practical trend are overlappable.

The collimated light fringes show a passage from a fringe order to the next one. This is caused by a non-coplanarity of the faces of sample crossed by the laser source, confirmed by the comparison with the geometrical shape of the samples. This changing of the fringe order is confirmed by the study of the light intensity equation and even more with the comparison with the conoscopic technique. In this comparison is possible to use both conoscopic acquisitions and the related mathematical model. In the first possible comparison the collimated light fringes appear in Conoscopy as discontinuity of the Δy and Δz parameter trend. Through the comparison between what obtained through the conoscopic technique with the relative mathematical model, it is possible to observe that the discontinuity appears as changes of the fringe order. Putting together all of the observations, it is possible to define the observed fringes as related to different fringe order. If no variation of the beta angle is present, the observation of these fringes can be used to determine the non-coplanarity between the observed surfaces crossed by the laser beam. In addition to the presence of non-coplanarity, it is also possible to define the angles of relative inclination between the two non-coplanar surfaces.

Chapter 5

5 Applications

Even the applications, as well as the aforementioned analysis systems, have been developed for the most part within the Università Politecnica delle Marche. This allowed to interact within its collaboration network like the 'Crystal Clear Collaboration' and the COST Action TD1410 'FAST' coordinated by the CERN. This gave the opportunity to test the developed techniques at the FH Aachen University of Jülich, comparing them with their decay time measurement techniques. Furthermore, strong collaboration with companies (Crytur), allowed our techniques to be applied to the detailed quality control of the entire sample. Here, the results of some activities are reported.

5.1 Evaluation of piezo optic parameters and photoelastic constant in Tetragonal PWO

Photoelasticity is today the fastest and not destructive technique that allows to analyse the macroscopic internal stress distribution [37], [51], [52]. But it can also be fruitful applied to extract from the experimental data the parameters which appear in the mathematical models that describe the interaction of polarized light with the crystal lattice [27], [35], [36]. In particular, the quantitative knowledge of the piezo-optic properties or the crystal, described by the piezo optic tensor Π is crucial. This set of parameters, for most crystals, is not fully known mainly due to the complexity of the necessary experimental approach arising from crystal anisotropy. What we are going to do is to evaluate, for a PWO crystals, the components π_{16} and the difference between the components π_{12} and π_{11} of the piezo optic tensor Π [3], the γ rotation angle of the optic plane under stress with respect to the crystallographic directions and the measure of the photoelastic constant f_σ [3], [26].

5.1.1 Photoelastic model

At first, we assume that the crystallographic frame (a-b-c) coincides with the sample frame (x-y-z) as in Fig. 5.1.

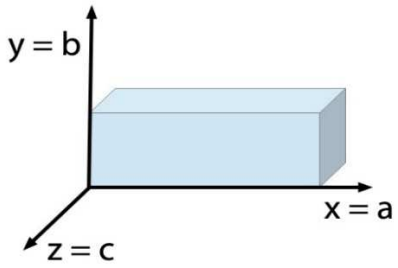

Fig. 5. 1: Crystallographic frame (a-b-c) that coincides with the sample frame (x-y-z).

If the crystal is stressed, by internal residual stress or applied loads, the dielectric impermeability changes according to the Maxwell constitutive relation, which is linear in the Cauchy symmetric stress tensor T:

$$B(T) = B_0 + \Pi[T] \tag{5.1}$$

where the tensor Π, for this class of crystal, admits the following non-null components [32], [46], [47]:

$$\Pi = \begin{bmatrix} \pi_{11} & \pi_{12} & \pi_{13} & 0 & 0 & \pi_{16} \\ \pi_{12} & \pi_{11} & \pi_{13} & 0 & 0 & -\pi_{16} \\ \pi_{31} & \pi_{31} & \pi_{33} & 0 & 0 & 0 \\ 0 & 0 & 0 & \pi_{44} & \pi_{45} & 0 \\ 0 & 0 & 0 & -\pi_{45} & \pi_{44} & 0 \\ \pi_{61} & -\pi_{61} & 0 & 0 & 0 & \pi_{66} \end{bmatrix} \tag{5.2}$$

If the stress is uniaxial, with the only component σ_{xx} along the direction a=x different to zero, by (5.1) and (5.2) we obtain the matrix of B(T) as:

$$B = \begin{vmatrix} B_x + \pi_{11}\sigma_{xx} & \pi_{61}\sigma_{xx} & 0 \\ \pi_{61}\sigma_{xx} & B_x + \pi_{12}\sigma_{xx} & 0 \\ 0 & 0 & B_z + \pi_{31}\sigma_{xx} \end{vmatrix} \tag{5.3}$$

From this matrix is possible to calculate the eigencouples (B_k, $\mathbf{u}_k$), k=1,2,3, that are:

$$B_1 = B_x + \sigma_{xx}\frac{(\pi_{11}+\pi_{12}) - \sqrt{(\pi_{12}-\pi_{11})^2 + 4\pi_{61}^2}}{2} \qquad u_1 = \left[\sqrt{1-tan^2\gamma} \quad tan\gamma \quad 0\right]$$

$$B_2 = B_x + \sigma_{xx}\frac{(\pi_{11}+\pi_{12}) - \sqrt{(\pi_{12}-\pi_{11})^2 + 4\pi_{61}^2}}{2} \qquad u_2 = \left[tan\gamma \quad -\sqrt{1-tan^2\gamma} \quad 0\right] \tag{5.4}$$

$$B_3 = B_z + \pi_{31}\sigma_{xx} \qquad u_3 = [0 \quad 0 \quad 1]$$

where:

$$tan\gamma = \frac{\pi_{11}+\pi_{12}\pm\sqrt{(\pi_{12}-\pi_{11})^2+4\pi_{61}^2}}{2\pi_{61}} \qquad (5.5)$$

The tree eigenvectors are different, so the crystal becomes optically biaxial [32], [46], [47]. The frame U of the eigenvectors is rotated with respect to the reference system x-y-z of an angle γ about z; the two optic axes both lie in the Optic Plane which is crossed by the eigenvectors associated with the highest and the lowest eigenvalues. Since (5.3) is valid for small stress and considering that in PWO $B_z>B_x$, therefore B3 remains the higher eigenvalue and the optic plane is spanned by $\mathbf{u_3}$ and the eigenvector $\mathbf{u_j}$ associated with the lowest eigenvalue $B_j=\min\{B1, B2\}$. From (5.5) it is possible to understand that under the uniaxial stress σ_{xx} the rotation angle is independent on the stress magnitude. In particular for a compressive stress ($\sigma_{xx}<0$) we have B1>B2, whereas B2>B1 for tensile stress ($\sigma_{xx}>0$) (Fig. 5.2).

In the case of tensile stress then the angle γ defined by (5.5) is between ($\mathbf{u_2}$,y) (Fig.2b) whereas for compressive stress it is between ($\mathbf{u_1}$,x) (Fig.2a) and is given by γ+π/2.

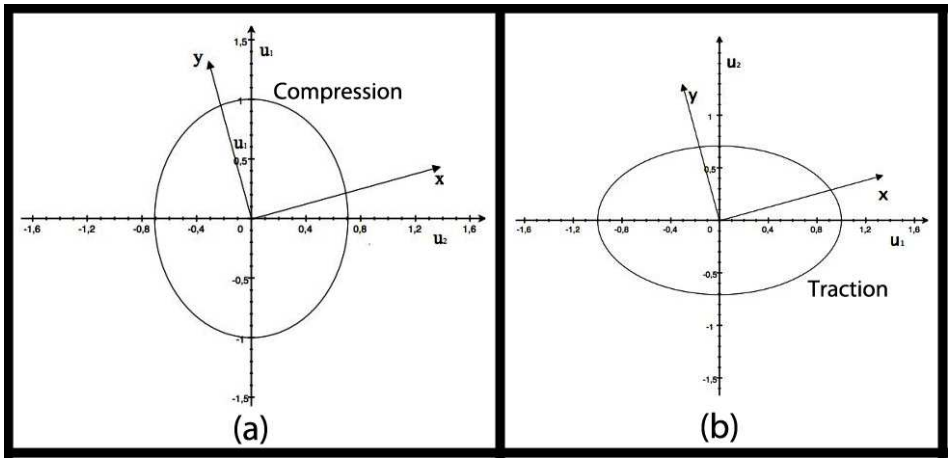

Fig. 5. 2: Section of the optic indicatrix in the frame U. In this frame the plane (u1, u2) is normal to the c crystallographic axis which coincides with the z-axis in the crystallographic frame S. They are therefore represented the cases of a) traction and b) compression.

The Bertin surfaces [23], as stress induced interference surfaces [22], can be observed by means of Laser Conoscopy as intersection with a crystal surface plane, generating an interference pattern [27], [35], [36]. Using the coordinates U = ($\mathbf{u_1}$, $\mathbf{u_2}$, $\mathbf{u_3}$) renamed as (x', y', z'), the Bertin surfaces equation is [27], [35], [36]:

$$cos^4\beta x'^4 + y'^4 + sin^4\beta z'^4 + 2cos^2\beta x'^2 y'^2 + 2sin^2\beta z'^2 y'^2 - 2sin^2 cos^2\beta z'^2 x'^2 - N^2H^2(x'^2 + y'^2 + z'^2) = 0 \quad (5.6)$$

with:

$$H = \frac{\lambda}{n_e - n_o} \quad (5.7)$$

Where β is the semi-angle between the optical axes (optic angle), λ is the wavelength and N is an integer number that represent the fringe order. The optic angle depends on the eigenvalues of (5.3), and either for positive or negative crystal, with respectively $B_1>B_2>B_3$ and $B_3>B_2>B_1$ it is [23]:

$$cos\beta = \sqrt{\frac{B_2 - B_3}{B_1 - B_3}}, \qquad sin\beta = \sqrt{\frac{B_1 - B_2}{B_1 - B_3}} \qquad tan^2\beta = \frac{B_1 - B_2}{B_2 - B_3} \quad (5.8)$$

For negative crystals like the PWO in exam, the equations (5.7) can be rewritten as follows:

$$tan^2\beta = \frac{B_{\min(1,2)} - B_{\max(1,2)}}{B_{\max(1,2)} - B_3} \quad (5.9)$$

The equation (5.9) depends on the two possible cases: if we have compressive stress ($\sigma_{xx}<0$) we have $B_1>B_2$, if the stress is tensile ($\sigma_{xx}>0$) we have $B_2>B_1$ (Fig. 5.2). In order to evaluate the stress by the means of these interference fringes, a phenomenological measure is given by the elliptical ratio C, defined as [26]:

$$C = \frac{a}{b} - 1 \quad (5.10)$$

where a and b are respectively the major and the minor axis of the Cassini-like curves [27] in the frame U=(x', y', z'). The parameter C at first order can be written as a function of the stress magnitude by means of (5.6) and (5.10) as [26]:

$$C = f_\sigma \sigma \quad (5.11)$$

were f_σ is the photoelastic constant for the material and σ is a measure of stress. When the measure is performed along the c crystallographic axis that coincides with z we get [26], [36], [53]:

$$C = \frac{1}{1 - sin^2\beta}\sqrt{\frac{1 + 2K^2 sin^2\beta cos^2\beta + \sqrt{1 + 4K^2 cos^2\beta}}{1 - 2K^2 sin^2\beta + \sqrt{1 + 4K^2 cos^2\beta}}} - 1 \quad (5.12)$$

where K = z_o/H with z_0 = z that describe the sample thickness. For the uniaxial load $\sigma=\sigma_{xx}$, by linearizing (5.12) with respect to the stress measure we arrive at:

$$C = f_\sigma \sigma = (1 + \frac{2K^2}{1+\sqrt{1+4K^2}}) \frac{\sqrt{(\pi_{11}-\pi_{12})^2+4\pi_{16}^2}}{B_X - B_Z} \sigma_{xx} \quad (5.13)$$

The last relation (5.13) is the theoretical tool that can be used to link the model with the photoelastic measurements. Indeed, it depends directly on the sample thickness z_o and on the components π_{11}-π_{12} and π_{16} of Π, as well as on the optic properties of the unstressed crystal [53].

5.1.2 Experimental method

Once defined the parameters γ. π_{11}-π_{12} and π_{16} as a relation between the mathematical model and the Photoelasticity, a set of PWO samples have been studied after checking their quality with these latest techniques.

5.1.2.1 Angle γ evaluation

To calculate the γ angle, the sample utilized for the test is a PbWO4 with 9,93x14,73x44.70mm dimensions (Fig. 5.3a). Among the possible bend tests, it was chosen to use the four points one [3], [39]. The sample is positioned between two couples of cylinders, the first one closer and the second one more distant (Fig. 5.3b). Applying a uniform load over the superior couple is possible to produce a bending momentum that is constant in the central area (Fig. 5.3b) along the sample length. In this region the momentum induces a stress state which varies linearly along the y dimension (Fig. 5.3c). In particular it passes from a traction condition at the bottom area to a compression condition at the top [54]. The choice of this test was motivated by its characteristic of producing a stress state in the central area that does not vary in each section orthogonal to the x axis.

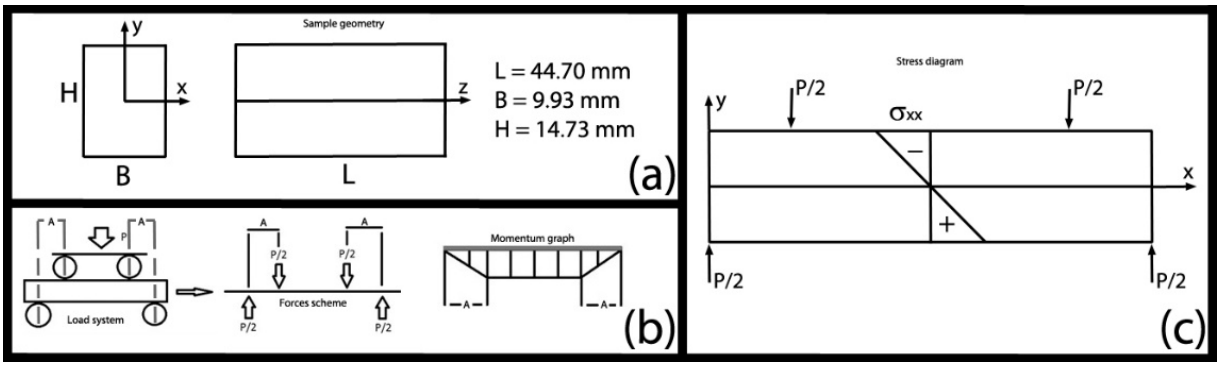

Fig. 5. 3: (a) Geometry of the sample used for the gamma angle detection. (b) Scheme of the four points bend test used to apply a load inside the sample in order to induce a uniaxial stress σ_{xx}. We have also the forces scheme and the respective momentum graph. (c) Produced uniaxial stress state which varies linearly along the y axis, induced by the bend test.

The maximum tensile stress $\sigma_{xx(max)}$ produced at the borders of the samples is only function of the applied load P, of the dimensions of the sample and the geometry of the load scheme From the load scheme we need the distance A between the upper and lower support points (Fig. 5.3b), from the sample geometry the two dimensions B and H (Fig. 5.3a). Through these parameters is possible to obtain [54]:

$$\sigma_{xx(\max)} = \pm\frac{3PA}{bh^2} \tag{5.14}$$

Instead the local stress σ_{xx}, being linear along the y dimension, is a function of the measuring position along y and it is obtainable, once known σ_{xx}, through [54]:

$$\sigma_{xx}(y) = \frac{\sigma_{xx(\max)} * y}{h/_2} \tag{5.15}$$

Considering that the sample is oriented with the optic axis coincident with the x reference axis of the sample in exam, is possible to inspect the sample with the conoscopic technique along the optic axis [28]. In order to know exactly the magnitude of the P parameter that defines the applied load, a load cell was applied in the system [55]. Once the load is applied, through this photoelastic technique is possible to perform a scan along the y axis in the sample area where the stress is linear respect to the y axis (Fig. 5.3c) [28].

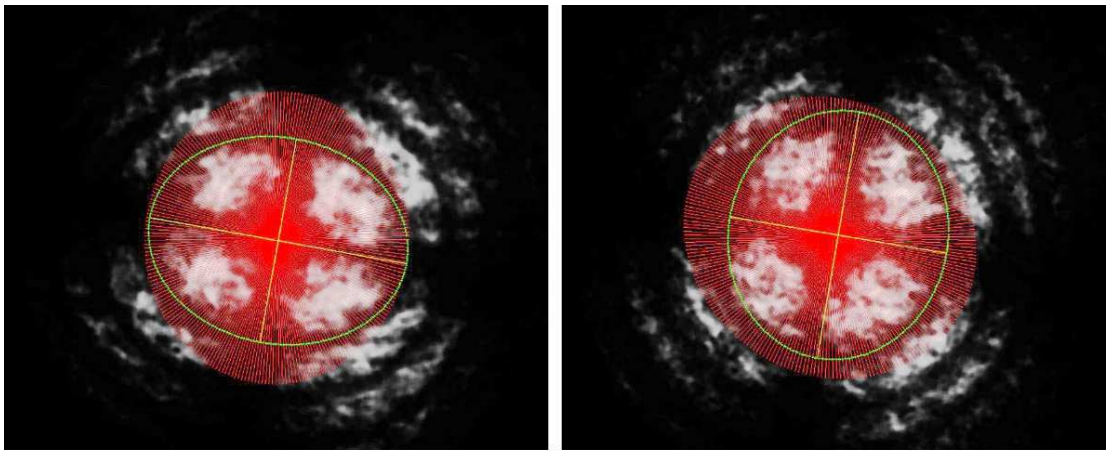

Fig. 5. 4: Example of conoscopic images acquired during the bend test in the linear stress area. Over each image is traced in green the fit of the first fringe order produced automatically by the custom- made software, that use the red lines as reference. In particular we have in (a) a tensile stress condition and in (b) a compressive stress condition.

In Fig. 5.4 we have an example of images acquirable by Conoscopy. Superimposed at these images are the red lines that the custom-made software uses to fit the fringe order (green lines). In particular in Fig. 5.4a we have an acquisition in the area of tensile stress, in Fig. 5.4b the compressive stress condition. Therefore, by the use of different loads and inside each load condition by the calculation of the stress state at different y (Fig. 5.3c) trough Conoscopy and (5.15), it is possible to obtain the results showed in Table 5.1.

	1	2	3	4
Load (MPa)	2.26	1.88	1.41	-0.73
Angle (Deg.)	-9.04	-11.25	-10.20	100.14
StDev Angle	0.041	0.033	0.039	0.259

Table 5. 1: Table of results obtained by applying different loads level, in order to evaluate the angle γ and their standard deviation.

Coherently with (5.5), under an uniaxial stress the γ_1 and γ_2 angles are independent to the stress intensity and the experimental measurements lead to:

$$\gamma_1 = -0.1733 \pm 0.0158\, rad \qquad \gamma_2 = \gamma_1 + \frac{\pi}{2} \tag{5.16}$$

5.1.2.2 Evaluation of the Π components with the photoelastic constant for the uniaxial load.

Using the data obtained from the bend test, coupled with data found in bibliography on the PhD thesis of Andrea Ciriaco [56], is possible to link the experimental evidence with the theoretical assessment of the piezo optical effect. Using the relations for the eigenvalues (5.4) inside the (5.9) it is possible to obtain:

$$tan^2\beta = \frac{\pm\sigma_{xx}\sqrt{(\pi_{11}-\pi_{12})^2+4\pi_{61}^2}}{\Delta B+\sigma_{xx}(\pi_{31}+\frac{1}{2}(\pi_{11}+\pi_{12})-\frac{1}{2}\sqrt{(\pi_{11}-\pi_{12})^2+4\pi_{61}^2})} \tag{5.17}$$

It is possible from (5.17) to assume that in the denominator the piezo-optic effect can be disregarded, being this negligible with respect to the difference $\Delta B = n_e^{-2} - n_o^{-2}$ [35], [46], thus obtaining the relation [35], [46]:

$$tan^2\beta = \pm\frac{\sigma_{xx}\sqrt{(\pi_{11}-\pi_{12})^2+4\pi_{61}^2}}{\Delta B} = \pm\sigma_{xx}\frac{R}{\Delta B} \tag{5.18}$$

The relation (5.18) is proposed with the assumption that no residual stress is present in the specimen. If a residual stress $\sigma_{xx} = \sigma_{xx}^o$ is observable, then (5.18) becomes:

$$tan^2\beta = \pm\sigma_{xx}\frac{R}{\Delta B} + \sigma_{xx}^o\frac{R}{\Delta B} \tag{5.19}$$

Using the fit taken from the [56] of the Cassini-Like curves to the equation (5.6), we first obtain an estimate of the angle beta, and then through (5.18) and (5.19) we obtain respectively:

$R = (0.98 \pm 0.11) \cdot 10^{-12} Pa^{-1}$, eq. (5.18),

$R = (0.976 \pm 0.054) \cdot 10^{-12} Pa^{-1}$, eq. (5.19),

It is important to note that both equations give a similar value, but the (5.19) produces a smaller error. Cause of this in the sequel we use the results of equation (5.19). Comparing the results obtained from the bibliographic data with the results of the bend test, we have a fully compatibility that confirms the theory. Moreover, using the definition of R mentioned in (5.18) which is:

$$R = \sqrt{(\pi_{11} - \pi_{12})^2 + 4\pi_{61}^2} \tag{5.20}$$

and by the (5.19) is possible to obtain the searched parameters:

$$\pi_{16} = (0.1736 \pm 0.0507) \cdot 10^{-12} Pa^{-1} \qquad \pi_{12} - \pi_{11} = (0.9234 \pm 0.1548) \cdot 10^{-12} Pa^{-1} \tag{5.21}$$

Once know these parameters, by (5.13) we can rewrite the photoelastic constant as:

$$f_\sigma = f_K \frac{R}{\Delta B}, \qquad f_K = 1 + \frac{2K^2}{1+\sqrt{1+4K^2}} \tag{5.22}$$

to obtain:

$$f_\sigma = f_K (73.4286 \pm 12.1579) \cdot 10^{12} Pa^{-1} \tag{5.23}$$

The photoelastic constant f_σ we obtained is valid for uniaxial stress directed

The photoelastic constant f_σ we obtained is valid for uniaxial stress directed not only along the 'a' crystallographic direction, but even for the direction 'b', namely respectively σ_{xx} and σ_{yy}. It is important to note that the constant f_σ depends also on z_o and on the wavelength λ of the test light. So, the thickness becomes a parameter to be measured with care. These results are a step towards a deeper knowledge of elasto-optical properties of PWO. Furthermore, it is important to say that what has been discussed can be applied on every tetragonal crystal.

5.2 Testing and characterization of PWO from a Crytur pre-series

The sample inspected is a pre-series PWO that presents a general bad quality by a visual inspection, scratching and chipping are recognizable on the surface. Moreover, the geometry is not a regular cylinder, as one would expect (Fig. 5.5) [4], [48].

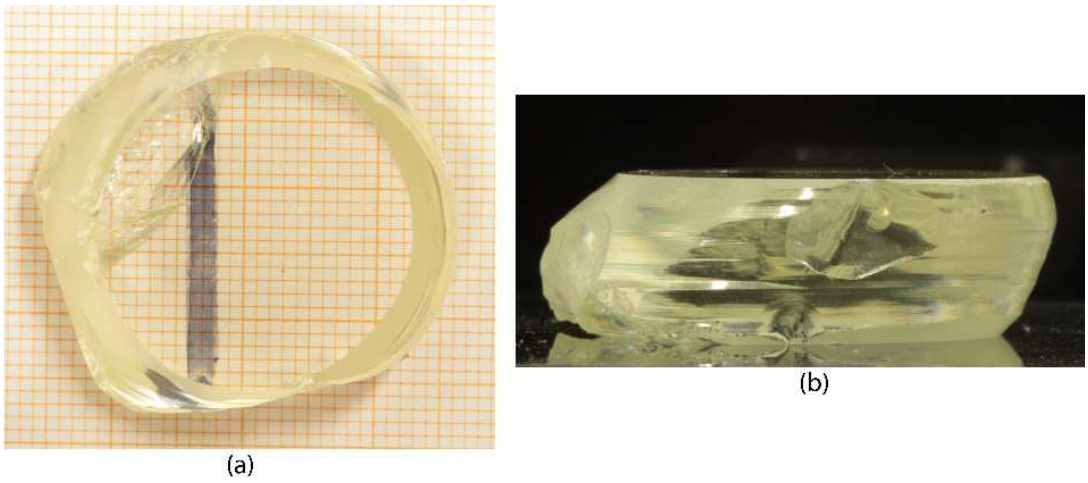

Fig. 5. 5: Pictures of the inspected PWO sample are shown. In (a) looking at the surface chipping and scratches are evident. (b) The lateral point of view shows the sliding of the sample which deviates from a classical cylinder. This phenomenon is probably caused by the non-correct growth parameters which has generated macroscopic distortions. Is expected thus a complex distribution of the residual stress.

Considered the crystal condition, is not expected a homogeneous state but rather a complex distribution of stress and defectiveness. The intention is to study point by point the sample with its fringe pattern. Therefore, a grid of 392 points with a resolution of 1mm has been created over the sample on the irregular surface (Fig. 5.6b). These points are then inspected by Laser Conoscopy technique orthogonally with respect to the optical axis [2], [4], [48].

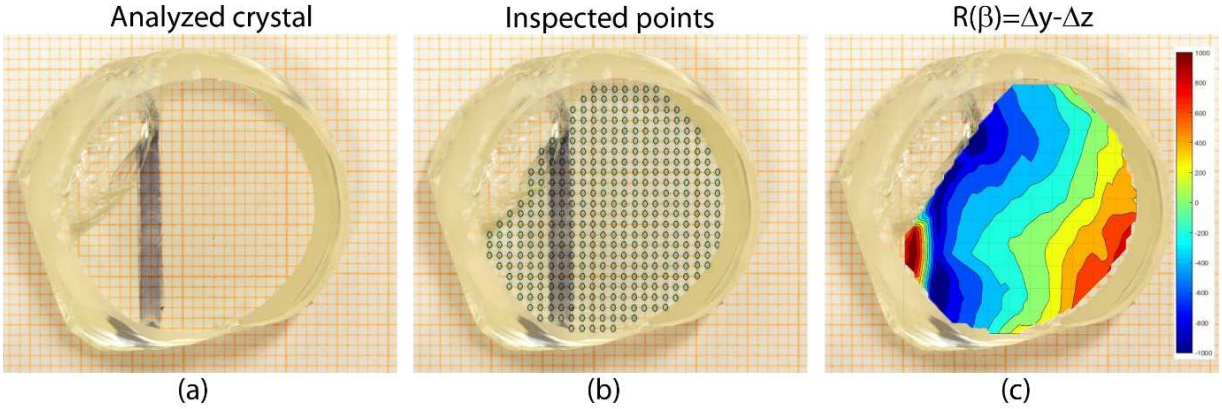

Fig. 5. 6: In (a) we have the surface of the analysed crystal. Over this surface in (b) is superimposed the reference grid of 392 points for the conoscopic analysis. (c) Results from the conoscopic analysis in terms of R parameter obtained in each acquisition point and reported as a map over the sample.

Point by point, from the fringe pattern the distances Δy and Δz have been obtained, and with these the parameter R = Δy – Δz [4], [48]. Putting together the values of R in reference with the coordinates of the relative acquisition point on the grid is possible to obtain the magnitude map of R superimposed to the crystal surface in Fig. 5.6c. In Fig. 5.7 are reported as exemplum the acquisitions from three equidistant points along the crystal diameter in horizontal direction. In these

images are clearly visible the variation of the distances Δy and Δz indicated with white arrows, which are shown as parameter R on the map in Fig. 5.6c.

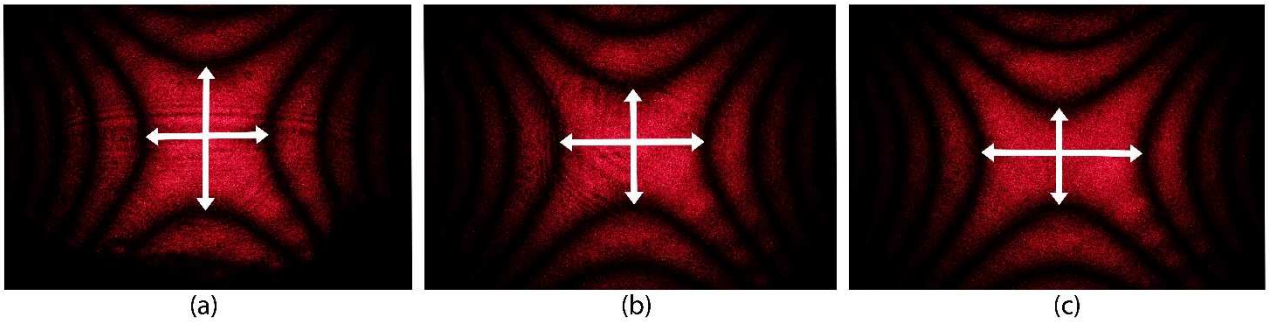

Fig. 5. 7: Results obtained from three equidistant acquisition points along the crystal diameter in horizontal direction. (a) comes from the left border, (b) comes from the middle and (c) comes from the right border. It is clearly visible the variation of the parameters Δy and Δz, showed with white arrows, passing from an image representative of a crystal area to the others.

The sample is than inspected by the Laser Sphenoscopy technique in order to evaluate the applicability of a faster but less detailed technique with respect to the previous described Conoscopy [2], [4], [29], [30], [48]. Therefore, over the crystal surface is created a reference path of 23 vertical and parallel lines equidistant 1mm (Fig. 5.8b). These lines are then inspected by Sphenoscopy, along each line is possible to obtain a pair of fringes with this technique. By the study of the distance distributions between this pair of fringes in each acquisition and by the correlation between the distances with the relative position of the reference path line is possible to obtain the map of distances in Fig. 5.8c.

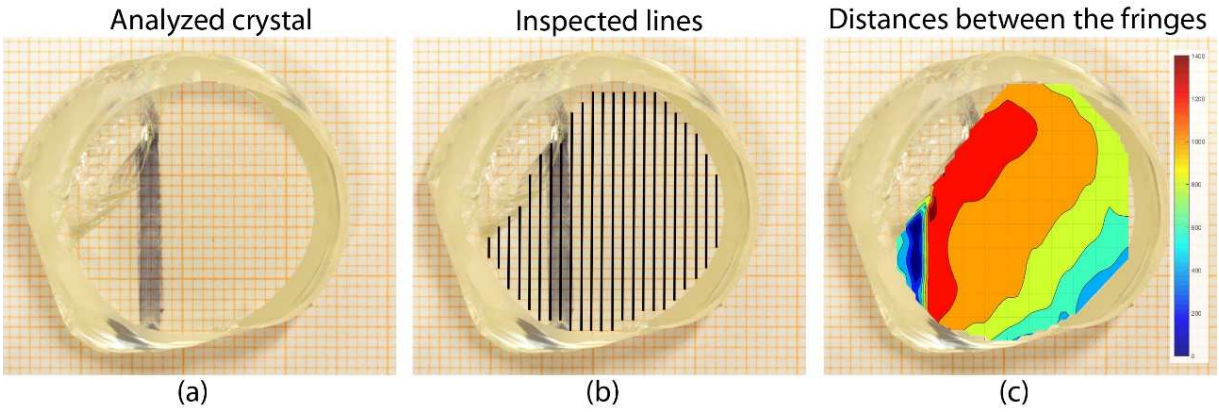

Fig. 5. 8: In (a) we have the crystal under analysis, over this in (b) is superimposed the reference path for Sphenoscopy. (c) shows the results coming from the data analysis, starting from the distances acquired in each line path and reporting these in the respective spatial position. By integrating the results from each line path, the map of distances is obtained.

In order to see some details, in Fig. 9a – b - c we have three sphenoscopic acquisition respectively from the left side, the centre and the right side of the sample. Using the white arrows is possible to

see better the fringes distance trend. It is clearly visible a difference between each condition, which are large-scale map details.

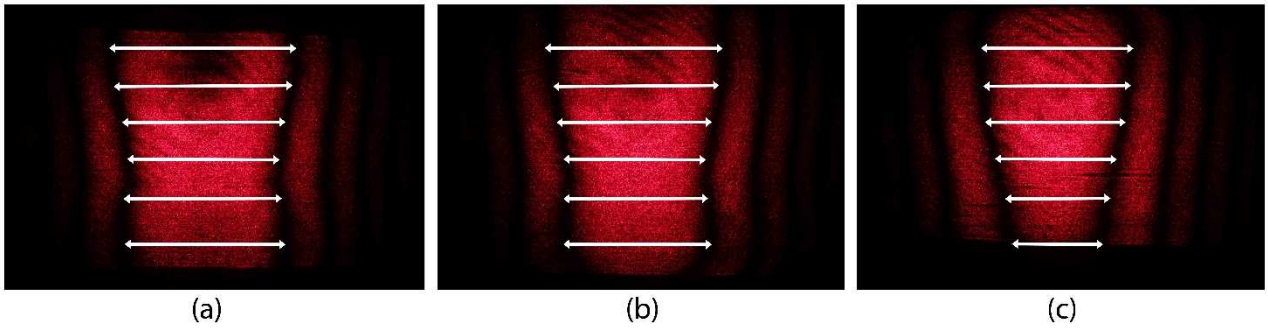

Fig. 5. 9: Results obtained from three equidistant acquisition along the crystal. (a) comes from the left border, (b) comes from the middle and (c) comes from the right border. In each image the distances between fringes are highlighted with white arrows. It is clearly visible the distances differences passing from an image coming from a crystal area to the others.

Summarizing the two results, even though Conoscopy offers more details in the analysis, the results carried out by Sphenoscopy are more than compatible with them. In both type of analysis, the map of stress is shown superimposed to the crystal geometry in order to relate directly the residual stress trend to the sample (Fig. 5.6c, 5.8c). The stress gradient seems to have a preferential direction along the sliding direction of the crystal (the deviation direction from the expected cylindrical shape). Furthermore, as a further point of connection with the geometry of the sample, it is easily observable that the faster gradient is close to the higher defectiveness area of the sample. The choice of one technique rather than the other depends by the balance between details and time which is suitable to the user needs. With the purpose of having quantitative values of the stress in each point inspected, it would be necessary a calibration. But nevertheless, the maps carried out in the test are well representative of the crystal state and stress distribution, which are indicators of defects and/or lattice distortion. In fact, a monochromatic map is expected in case of residual stress absence (with linked defects or lattice distortions).

5.3 Comparative analysis between Photoelastic measurements and Timing properties in LYSO samples

The hypothesis that motivated the arrangement of multiple analyses is that in the Scintillating Crystals the cell orientation and the overall quality are parameters that can be correlated to scintillating efficiency and timing issues [57]. To deepen these aspects, 20 LYSO samples coming

from the same ingot and with the same dimensions were compared. In order to be more precise each crystal is cut with a base of 1x1mm and a height of 10mm.

5.3.1 Extinction angle detection through collimated light Photoelasticity

The first bench test is built to perform a measure of the extinction angle inside the samples. The set-up is composed by a laser, a beam expander to illuminate the whole sample by collimated light, an analyser in dark field respect to the laser polarization and at the end a system of acquisition (Fig. 5.10a). The sample, with their own reference system (Fig. 5.10b) is positioned between the beam expander and the analyser, with the laser crossed surface orthogonal to the beam. To perform this type of measure in each face of the sample, the probe volume is decomposed into its numbered faces (Fig. 5.10b).

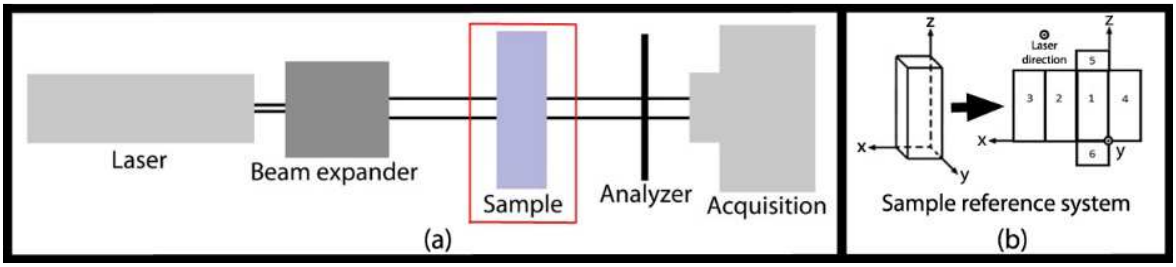

Fig. 5. 10: (a) Photoelastic system developed to detect the extinction angles inside a sample. It is composed by a Laser source with wavelength of 633 nm coupled with a beam expander to make the laser spot comparable with the sample dimension. The specimen is oriented with the surface, where the extinction angle will be detected, orthogonal to the laser beam. The analyser is positioned after the crystal, in dark field respect to the polarization of the laser light. At the end there is a system of acquisition to detect the light coming from the crystal. (b) Reference system integral respect to the crystal with the reference numbering given to each face.

Once that a face of the sample is oriented orthogonal to the laser beam, the crystal is rotated with respect to the axis that coincides with the same laser direction. During the imposed rotation, from the acquisition system is possible to observe the sample illuminated by the laser source (Fig. 5.11a - c). But for a certain angle of the crystal the light emitted decrease until a minimum. The rotation angle that correspond to this minimum of light is called extinction angle (Fig. 2b). Extinction angle is the angle at which all light travels through the crystal undisturbed, without undergoing polarization changes, and is therefore not allowed to pass through the Analyzer. When the Crystal is at a minimum, it seems to disappear; contrariwise, for an angle different to the extinction, the light is allowed to pass through the Analyzer, having the crystal changed the polarization of light. This condition of minimum of light, peculiarity for the Extinction angle detection, is motivated by the fact that this angle represents one of the principal crystal directions.

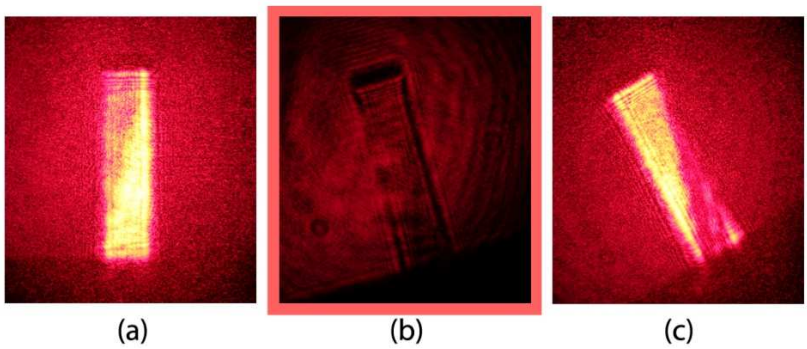

Fig. 5. 11: Example of different inclinations applied at the Crystal inside the measurement system. In (a) and (c) the crystal modifies the polarization of light coming from the laser source and therefore is visible from the analyser. In (b) we are in the extinction angle condition. The laser light travels through the crystal undisturbed, without undergoing polarization changes, and is therefore not allowed to pass through the analyser. This behaviour is due to the fact that this angle represents one of the principal crystal directions.

Being the crystal birefringent monoclinic, only one of the principal directions will coincide with a crystallographic axis. The others will be at some angle to the crystallographic axes. Therefore, this extinction angle parameter is a peculiarity of each face of the specimen. Iterating the procedure for the calculus of the extinction angle in every face of each sample is possible to obtain the results shown in Tab. 5.2, using the reference system for the sign of the angles in Fig. 5.12.

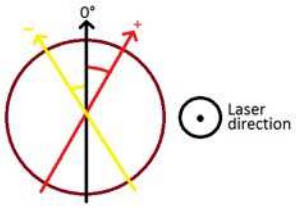

Fig. 5. 12: Reference system used to assign the value of the extinction angle.

Face number \ Sample number	1	2	3	4	5	6	7	8	9	10	11	12	13	14	15	16	17	18	19	20	21	22
1	45	-14	29	30,5	-15,5	30,5	-14	-15	28	-13	29	29	30	-14	-13,5	31	-11	31	32	35	-18	31
2	-13	-15	-15	31	31,5	-16	-16,5	28	32	34	-16	-15	36	-16	45	-16	-18,5	-14	32	29	-14	33,5
3	29	31	-11,5	-16	26	-12	28,5	35	-10	30	-13,5	-13	-10,5	45	29,5	-13,5	31	-11	-13	-17	33	-11
4	-16	18	34	-11,5	-15	32	31	-13	-16,5	-17,5	33	34	-16	40	-14,5	32	34	31,5	-16	-10	28	-11
5	-31	45	-31	-31,5	-30,5	-31	45	45	45	-28	-31	-29,5	45	45	-31	-30	-37	-32	45	-36	-29	45
6	45	-30	45	45	-35	45	-29	-30,5	-32	45	45	45	-31	-29,5	45	-38	-31	45	-29	-37	-37	-31,5

Tab. 5. 2: Table of the extinction angles measured, each column represents the data of each crystal studied, each raw instead represents a face from the fixed reference system.

Starting from these raw values obtained, it is possible to make them comparable by reorganizing the values calculated in each crystal. Inside each sample we used the same reference system in Fig. 5.10b. Passing from a crystal to the following we use the same reference system, but the choice of the starting face named '1' is arbitrary. To make all the measurements confrontable, we use in each

sample as face '1', the face that gives the highest value of the extinction angle. The other faces follow as the reference system. With this new reorganization we get the Tab. 5.3.

Sample number																																					
1		2		3		4		5		6		7		8		9		10		11		12		13		14		15		16		17		18		19		20		21		22	
°	Face	°	Face	°	Face	°	Face	°	Face	°	Face	°	Face	°	Face	°	Face	°	Face	°	Face	°	Face	°	Face	°	Face	°	Face	°	Face	°	Face	°	Face	°	Face	°	Face	°	Face
45	1	31	3	34	4	31	2	32	2	32	4	31	4	35	3	32	2	34	2	33	4	34	4	36	2	45	3	45	2	32	4	34	4	32	4	32	1	35	1	33	3	34	2
-13	2	18	4	29	1	-16	3	26	3	31	1	-14	1	-13	4	-10	3	30	3	29	1	29	1	-11	3	40	4	30	3	31	1	-11	1	31	1	32	2	29	2	28	4	-11	3
29	3	-14	1	-15	2	-12	4	-15	4	-16	2	-17	2	-15	1	-17	4	-18	4	-16	2	-15	2	-16	4	-14	1	-15	4	-16	2	-19	2	-14	2	-13	3	-17	3	-18	1	-11	4
-16	4	-15	2	-12	3	31	1	-16	1	-12	3	29	3	28	2	28	1	-13	1	-14	3	-13	3	30	1	-16	2	-14	1	-14	3	31	3	-11	3	-16	4	-10	4	-14	2	31	1

Tab. 5. 3: Table of the reordered extinction angles. Each couple of column represents one crystal. Within these, in the first column are represented the extinction angles starting from the highest value measured and than , cascading, the other values, following the measurement sequence. In the second column is represented the face number of the relative extinction angle.

With this kind of data is possible to compare the extinction angles of the samples. In particular is possible to build a matrix composed by the differences between the extinction angles in each sample (Tab. 5.4).

	Sample number																					
	1	2	3	4	5	6	7	8	9	10	11	12	13	14	15	16	17	18	19	20	21	22
1		89	101,5	104	97	105,5	105	98	105,5	103,5	101,5	100	102,5	96	88,5	104,5	107,5	105,5	100	104	102	100,5
2	89		18,5	82	10	18,5	78	79	74,5	20,5	16,5	17	80,5	37	27,5	17,5	82,5	17,5	17	23	17	80,5
3	101,5	18,5		93,5	9,5	5	87,5	82,5	82	5	4	1,5	84	27,5	14	7	86	6	11,5	4,5	7,5	87
4	104	82	93,5		92	94,5	9	13	14,5	98,5	95,5	95	15,5	119	106,5	96,5	15,5	91,5	97	95	97	8,5
5	97	10	9,5	92		9,5	86	86	81,5	11,5	7,5	8	87,5	29	19,5	8,5	89,5	10,5	9	14	8	89,5
6	105,5	18,5	5	94,5	9,5		86,5	87,5	81	5	4	5,5	87	28,5	17	2	89	4	8,5	7,5	7,5	91
7	105	78	87,5	9	86	86,5		7	5,5	89,5	87,5	89	10,5	115	101,5	88,5	10,5	87,5	95	86	88	13,5
8	98	79	82,5	13	86	87,5	7		7,5	87,5	86,5	84	6,5	108	94,5	89,5	9,5	87,5	94	82	88	10,5
9	105,5	74,5	82	14,5	81,5	81	5,5	7,5		84	82	83,5	7	109,5	96	83	8	83	89,5	80,5	82,5	11
10	103,5	20,5	5	98,5	11,5	5	89,5	87,5	84		4	3,5	87	27,5	15	5	86	9	11,5	5,5	4,5	92
11	101,5	16,5	4	95,5	7,5	4	87,5	86,5	82	4		2,5	86	27,5	14	3	88	8	9,5	6,5	3,5	90
12	100	17	1,5	95	8	5,5	89	84	83,5	3,5	2,5		85,5	26	12,5	5,5	87,5	7,5	10	6	6	88,5
13	102,5	80,5	84	15,5	87,5	87	10,5	6,5	7	87	86	85,5		107,5	94	89	6	89	95,5	81,5	87,5	9
14	96	37	27,5	119	29	28,5	115	108	109,5	27,5	27,5	26	107,5		13,5	26,5	113,5	27,5	22	30	30	112,5
15	88,5	27,5	14	106,5	19,5	17	101,5	94,5	96	15	14	12,5	94	13,5		16	100	18	19,5	16,5	17,5	100
16	104,5	17,5	7	96,5	8,5	2	88,5	89,5	83	5	3	5,5	89	26,5	16		91	5	6,5	9,5	6,5	93
17	107,5	82,5	86	15,5	89,5	89	10,5	9,5	8	86	88	87,5	6	113,5	100	91		91	97,5	83,5	85,5	8
18	105,5	17,5	6	91,5	10,5	4	87,5	87,5	83	9	8	7,5	89	27,5	18	5	91		7,5	9,5	11,5	89
19	100	17	11,5	97	9	8,5	95	94	89,5	11,5	9,5	10	95,5	22	19,5	6,5	97,5	7,5		16	12	93,5
20	104	23	4,5	95	14	7,5	86	82	80,5	5,5	6,5	6	81,5	30	16,5	9,5	83,5	9,5	16		8	88,5
21	102	17	7,5	97	8	7,5	88	88	82,5	4,5	3,5	6	87,5	30	17,5	6,5	85,5	11,5	12	8		91,5
22	100,5	80,5	87	8,5	89,5	91	13,5	10,5	11	92	90	88,5	9	112,5	100	93	8	89	93,5	88,5	91,5	

Tab.5. 4: Comparison between the extinction angles of the different samples, performed by calculating the differences between the different values. It is possible to see in yellow a family of Crystal who have each other low values of that differences.

Without making a deepen analysis is possible to see that we have a series of samples with similar extinction angles, (in particular the crystals named 3, 6, 10, 11, 12, 16, 18, 20, 21) but we have also some crystals that differs from this family. So, from the entire collection of crystals analysed, we have a group with similar lattice orientations, and others randomly oriented.

5.3.2 Comparative analysis of Decay times

To evaluate the crystal timing properties [58], [59], it is necessary to develop a system capable of acquiring light impulses coming from the crystal. These pulses are very fast, so the system must have a very high acquisition rate. To cover this aspect without lose light sensitivity is used an Hamamatsu Silicon Photomultiplier [60] (Fig. 5.13b) powered by an APDPI board in NIM standard to set-up the bias operating voltage the SiPM [61] (Fig. 5.13a). To collect the signal is chosen a DRS4 evaluation board [62] (Fig. 5.13c) which can be connected directly to the PC via a USB port and using the appropriate software released (Fig. 5.13d). This board is capable of digitizing eight channels at sampling speeds up to 5 GSPS and 1024 sampling points. In order to position the sample over the SiPM sensor was built a special sample-grip by a 3D printer. This grip has been designed to keep the sample almost completely covered, allowing the positioning above the sensor (Fig. 5.13b).

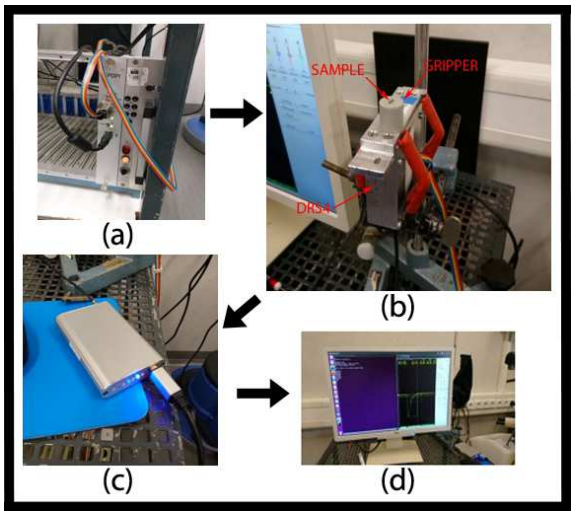

Fig. 5. 13: Acquisition system used for the analysis composed by an (a) APDPI board in NIM stand in order to power supply the bias operating voltage of the (b) Hamamatsu Silicon Photomultiplier. The signal from the SiPM is acquired by a (c) DRS4 evaluation board with a sampling speed of 5GSPS. This board is connected directly through USB to the (d) user interface.

To stimulate the emission of light inside the crystal we used an ultraviolet pulsed laser. In this manner it is possible to drive the light impulse emitted and acquire only the component of light transmitted due to the laser excitation by synchronizing the acquisition with the laser trigger. Even in this case we use the same reference system of the extinction angle detection (Fig. 5.10b), pointing the laser spot at the top of each of the four side faces parallel to the z axis, with the base x-y of the sample mounted over the SiPM. Furthermore, the same measurement was carried out by inverting the sample mounting the other x-y base on the SiPM and measuring the other top of each of the four lateral sides parallel to the z axis. In order to synthetize, in this manner it is possible to obtain

information from the eight points described in Fig. 5.14, where each point hit by the laser has the same distance from the SiPM; maintaining the same reference system of the extinction angle detection (Fig. 5.10b).

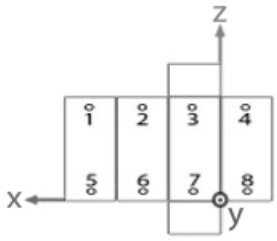

Fig. 5. 14: Reference system for the ultraviolet pulsed laser excitation. In each crystal are performed eight tests in the four lateral faces, four at the top of the faces and four at the bottom. Each numbered point represents the spot area for the laser in the selected test by the eight.

With this measurement chain it is possible to measure the pulse emitted by the crystal (Fig. 5.15a) when it is excited by a pulse of the ultraviolet laser. In order to understand if the sample rate is adequate, it is studied the raw points acquired, without using any interpolation (Fig. 5.15b). By comparing the last two figures, Fig. 5.15a of the pulse interpolated by a broken line, and Fig. 5.15b of the source point acquired, it is possible to see that we have enough points to fit each pulse.

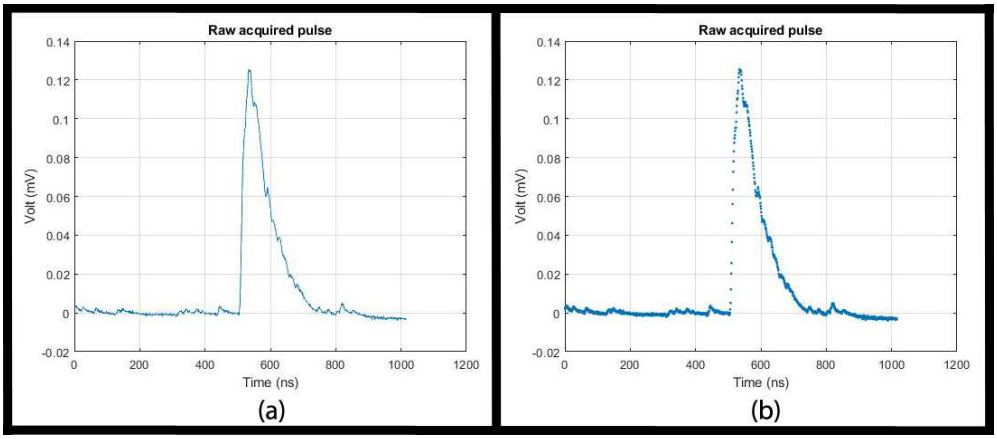

Fig. 5. 15: Example of pulse acquirable from the crystal when excited by a laser pulse using the developed system. In (a) we have the pulse represented with a broken line, in (b) the raw points acquired that describes the same pulse. The acquisition frequency is sufficient to describe the impulses to be acquired.

Going forward, with one thousand pulses from the laser in each point described in the reference system in Fig. 5.14, is possible to produce respectively one thousand pulses from the excited crystal. These one thousand pulses, that comes from a single test, are all synchronized with respect to the trigger provided by the laser. They therefore all have the same initial position along the x axis but have different amplitude (Fig. 5.16).

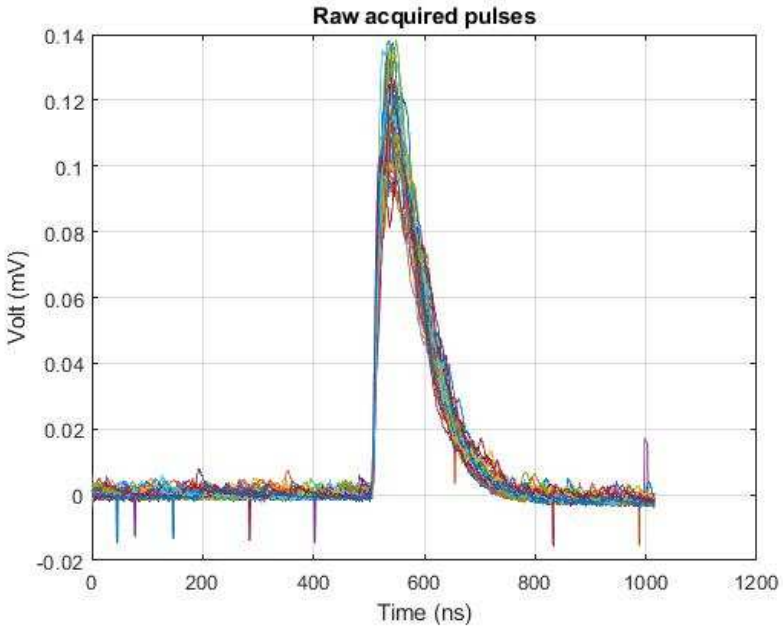

Fig. 5. 16: Example of the thousand rough pulses that can be acquired from a single test in a reference frame of the crystal.

The first step in order to manipulate the signal is therefore to normalize with respect to the amplitude, producing all the pulses with the same width (Fig. 5.17).

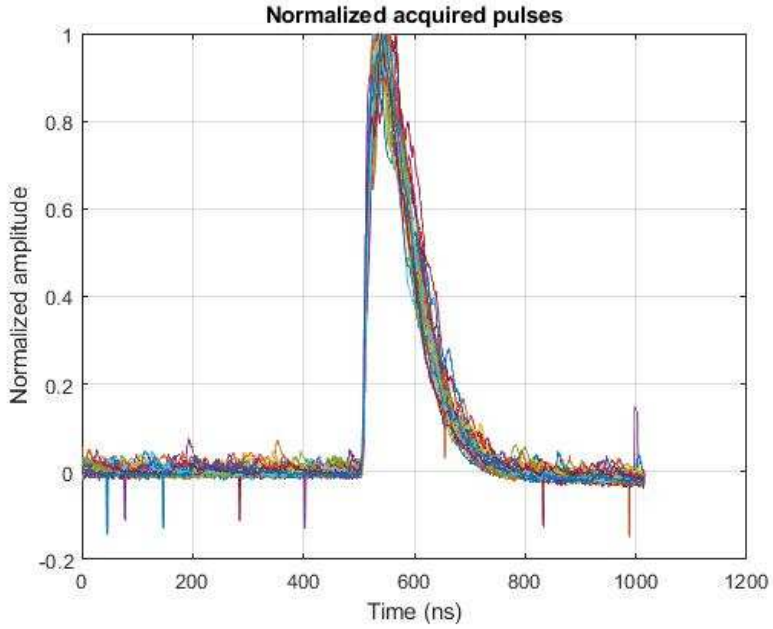

Fig. 5. 17: Same pulses coming from a test normalized respect to the amplitude, in order to make them comparable.

Once the maximum value of each pulse has been calculated, only the part following this value is selected (Fig. 5.18a). Subsequently, to ignore the noisy behaviour of the curves near the maximum, only the part after 90% of the maximum value is considered in each pulse (Fig. 5.18b).

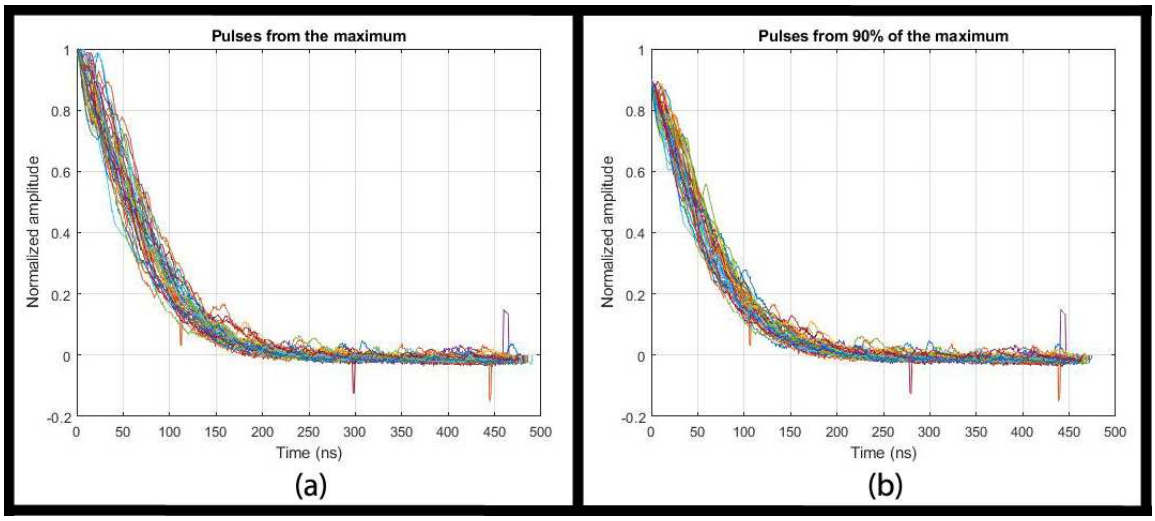

Fig. 5. 18: Some manipulation from the normalized pulses data. in (a) we have from each pulse the part that goes from the maximum onwards. In (b) compared to the previous point, the part that goes from the maximum to the value corresponding to its 90% is cut because it is affected by a lot of noise.

With the last data is possible to fit a curve in order to have an unambiguous result that describes the behaviour of the crystal in the test point. To extrapolate directly the decay constant of the crystal, as curve to fit is chosen an exponential with equation:

$$y = e^{-\frac{t}{\tau}} \tag{5.24}$$

where τ is the searched decay constant. By applying this equation to the data acquired is possible to obtain a result as in Fig. 5.19 where the red curve represents the trend of the fitted exponential.

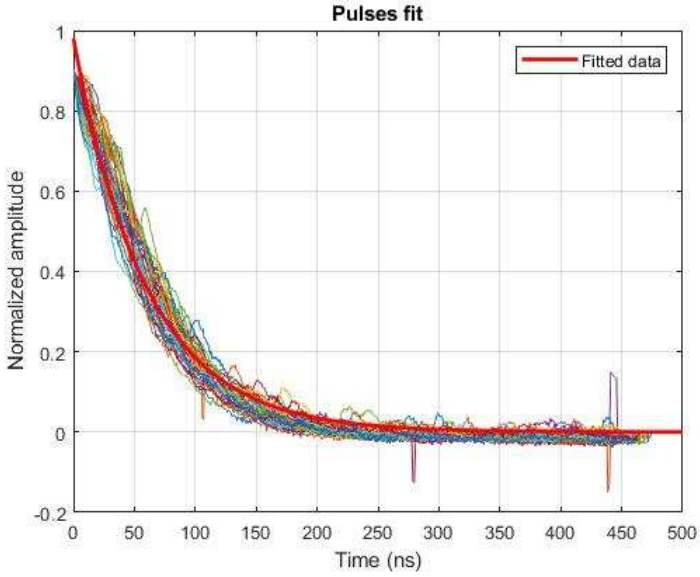

Fig. 5. 19: Normalized pulses from the 90% of their maximum, starting point for the relative fitted exponential curve in red.

With this instrument is possible to obtain a decay constant from an acquisition point inside a crystal. By iterating the procedure inside the desired eight points of the sample (Fig. 5.14) it is obtained an overall information of the whole crystal. Using the same procedure for the whole family of samples it is possible to graph the decay constants of each specimen in function of the face number (Fig. 5.20).

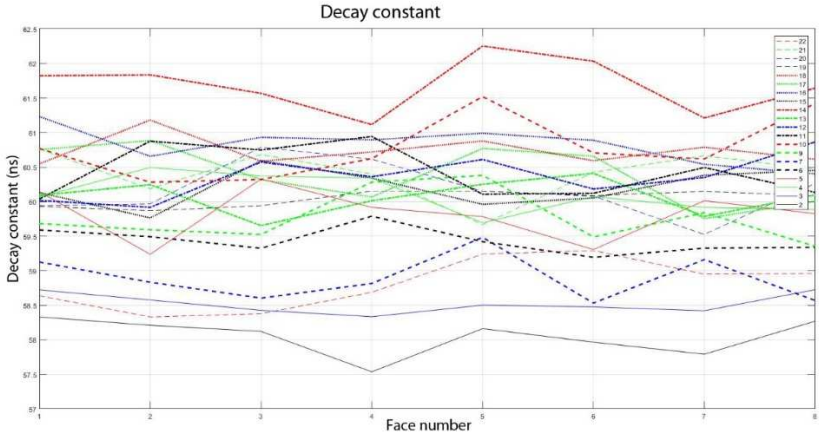

Fig. 5. 20: Each line represents a sample with its decay constant values in each reference test number. It is possible to notice an intermediate region that corresponds with the average values of the decay constant. But there are also samples that deviate from the average, possessing higher or lower values

To keep the environmental conditions under control, between the test of a crystal and the other a reference measurement is made on the same face of a reference sample to check if the system always provides the same constant response (Fig.5.21).

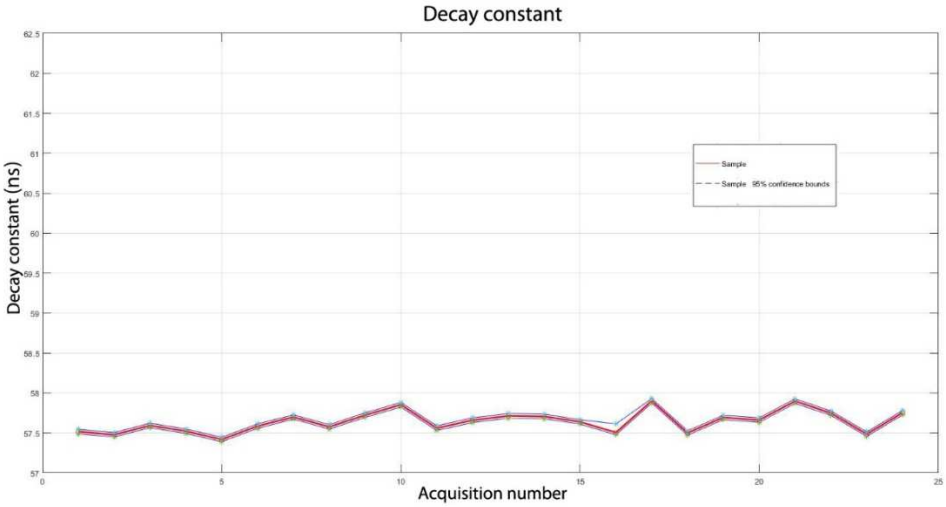

Fig. 5. 21: Trend of the decay constant measured in a specified test sample used each time in the same condition during the test of the crystals, in order to check the environmental influences, the system condition and stability. The violet line represents the acquired measures, the dotted lines the 95% of confidence bound error.

The magnitude order of the differences between these control measures is lower than the differences in Decay constant that can be seen by comparing some samples. This aspect is clearly visible if we take the values of samples 2 5 and 14 with the relative 95% of confidence bounds (Fig. 5.22). From the entire group of analysed crystals, the 2 and the 14 are respectively the faster and the slower, whereas 5 represents an intermediate condition of timing.

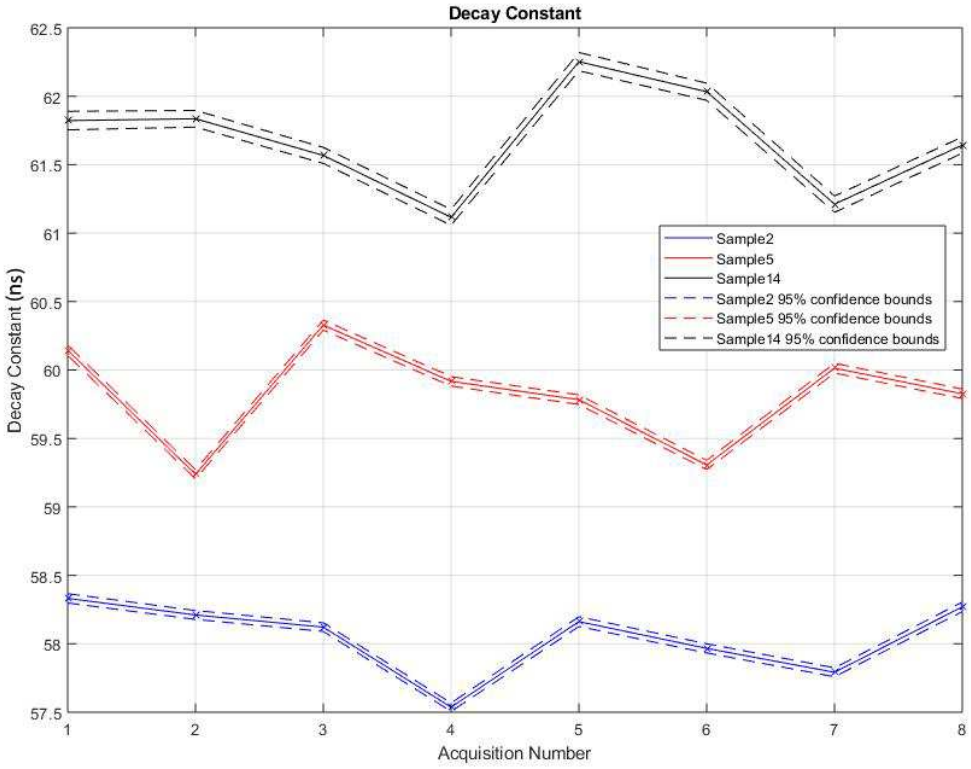

Fig. 5. 22: Three samples chosen by the whole family as representative of different conditions. The number two is the one with the lower decay constant, the number fourteen is the one with the highest decay constant and the five represents the condition of the samples with behavior close to the average line. With the lines that represents the decay constant in each sample,are present in dotted line the relative 95% confidence bounds.

Putting in ascending order the measures inside each sample and showing the relative mean value, the differences between one sample and another are even clearer (Fig. 5.23).

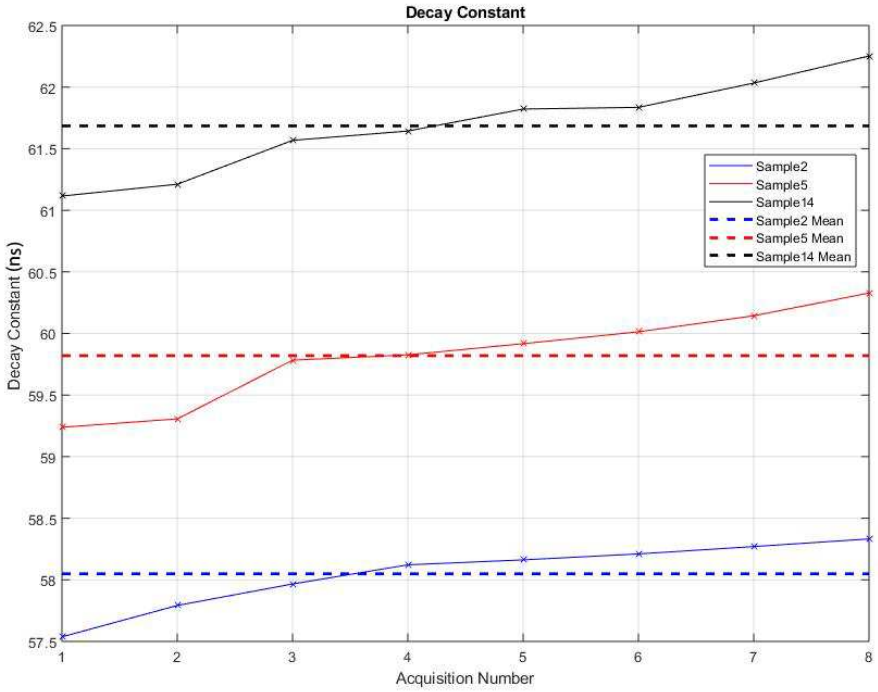

Fig. 5. 23: For the same three samples the relative decay constant values are shown with a continuous line in increasing order, while in the dotted line their average value is presented.

5.3.3 Optic axes detection through Conoscopic - Index-matching technique

The Conoscopy is a consolidated photoelastic technique that admit investigating the sample with the aim of finding the orientation of the optical axes. Because of the small samples size and in order to make possible the conoscopic observation even in the edges of the Crystal, the conoscopic technique is enriched by the index-matching technique. The acquisition system is composed by a Laser with coupled a beam expander and a converging lens, that is the usual acquisition system of the Conoscopy. The sample is mounted on a series of controlled tilts (Fig. 5.24a) respect to the z-y-z axes of the reference system in Fig. 5.10b which is integral with the specimen. These axes will be renamed for convenience z y z' as in Fig. 5.24a. The crystal is furthermore immersed in an index-matching fluid (Fig. 5.25b). This kind of liquid has the same refractive index of the sample; therefore, optically it behaves like a continuum with the specimen. Because of this property it is possible to use the Laser Conoscopy even in the edges of the Crystal. It is important to note that is fundamental to use a tube for the index matching that has no photoelastic behaviours, like a quartz tube as in our case.

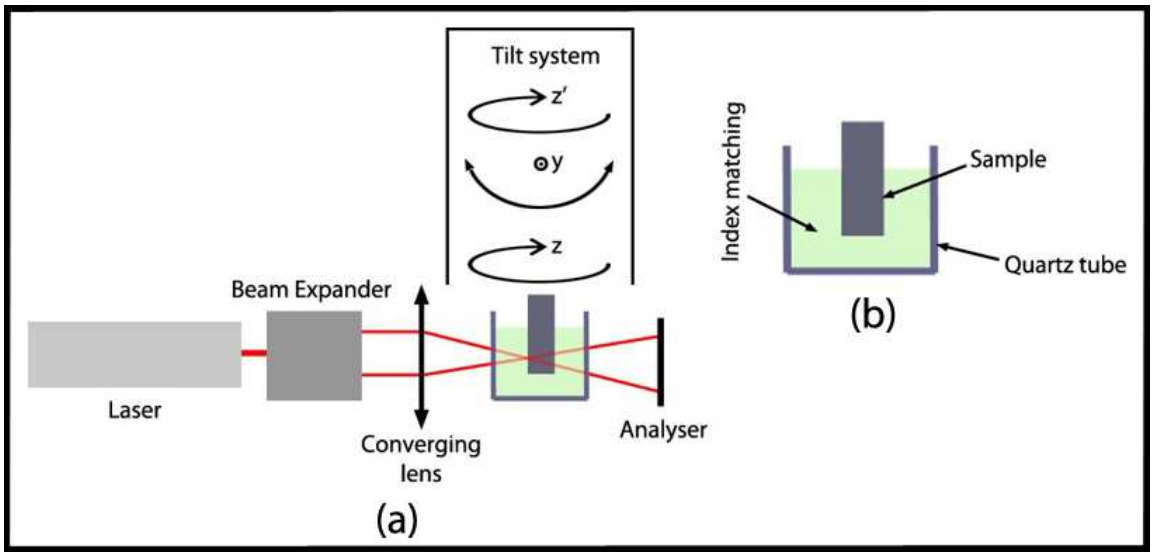

Fig. 5. 24: Photoelastic device developed for the laser Conoscopy, with the aim of detect the optical axes inside each crystals. In (a) we have the classical conoscopic set-up composed by a laser, a beam expander and a converging lens that focuses the laser beam to the sample surface. The sample furthermore is mounted on a tilt sistem that admit to rotate the crystal around the three axes z-y-z' solidal respect to the system. In order to make applicable the conoscopic system in the sample area near to the edges, (b) the crystal is immersed in an index matching fluid contained in a quartz tube. This fluid, having the same index of the sample, behaves like a continuum with the crystal.

In order to maintain a reference with the other tests, the crystal is mounted into the system with the x axis of the Sample reference system in Fig. 5.10b coincident in direction and verse with the laser beam and with the z axis facing up. Once the sample is placed in the system, it must first be rotated around the axis called z, then around the y and at the end around the z' axis if necessary (Fig. 5.24a). Through this rotation system it is possible to identify the two melatopes and therefore to know the orientation of the two optical axes. The samples chosen for the analysis are the same of Fig. 5.22, that show the most relevant differences in term of Decay constant. In order to make easier the representation of the results, the sample shape is decomposed in two projections (Fig. 5.25a). With this system is easier to represents the inclination angles of the optical axes of each sample. In particular, for the sample 2, 5 and 15 the results are shown in Fig. 5.25b – c - d respectively.

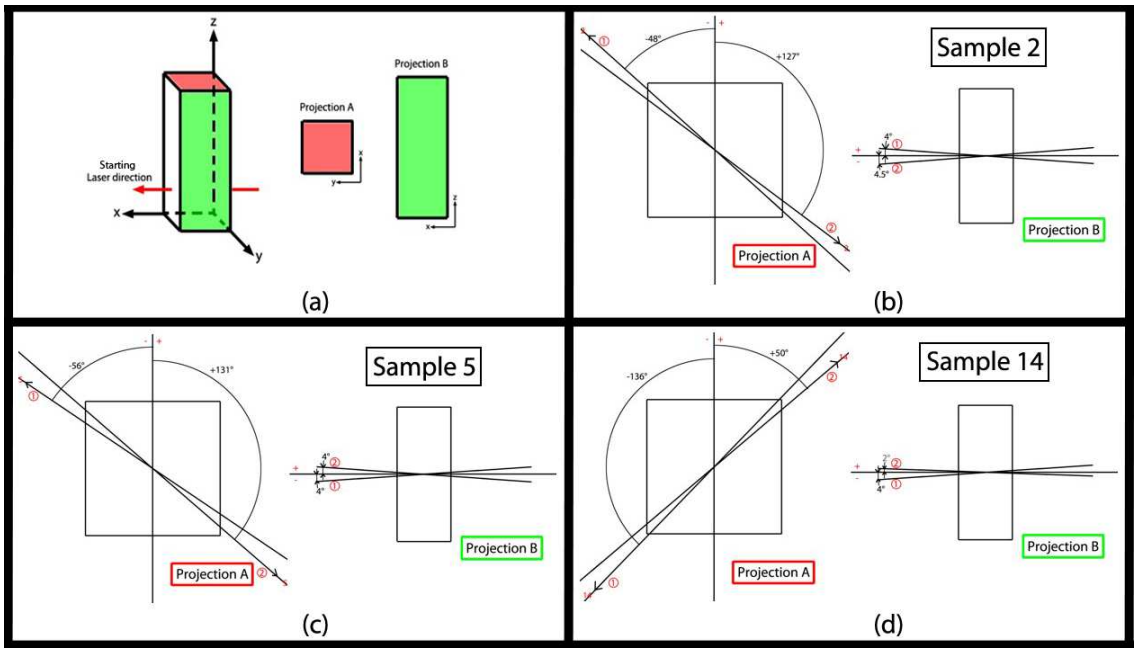

Fig. 5. 25: In order to make it easier to visualize the orientation of the optical axes, the sample is decomposed into the two projections A and B (a). In (b) we have the orientation of the two optical axes in the sample 2, in (c) and (d) respectively the orientation of the optical axes in sample 5 and 14.

The numbering 1 and 2 of the axes is in order to provide a reference of the same axis in the two different projections A and B. Studying the projection B, the difference between the samples are clear. The projection A needs more attention. This because we refer to a reference system integral with the sample but chosen in an arbitrary way in each crystal. To understand this projection, we must consider the crossing points between the optical axis directions and the crystal silhouette. These points, respect to the nearest sample edge, appear positioned differently in each crystal. Thus, by synthesizing, each of the three samples presents an orientation of the optical axes different from the others considered. This aspect is in agreement with the different Decay Time measured in each sample in exam.

Chapter 6

6 Concluding remarks

6.1 Conclusions

Scintillating crystals are involved in fields like the nuclear and high energy physics (for instance, CERN), medical and general bio-imaging (PET-positron emission tomography for cancer diagnosis), geologic research, security and laser technology. Performances of the scintillators rule the behaviour of the instruments and the systems exploited in those fields. Hence, the quality of the material itself and the production efficiency determine the cost and the feasibility of the above-mentioned activities. Therefore, reliable and precise instruments and methods are required by researchers, users and producers to achieve deeper knowledge of the material and its state and to get feedback so as to improve the efficiency of the production system and the quality of the end-product. The residual stress state is indeed an indicator parameter of the crystal quality, which is a critical quantity to be monitored and kept under control for an optimal production (growth and machining); furthermore, it is strictly related to the durability and to the functional behaviour (light production and transport). For this reason, in this work, non-invasive techniques have been developed and validated for the measurement of the residual stress condition of the studied birefringent transparent material. The reliability and the accuracy of the developed methods have been validated by experimental tests. The methods developed starts from the theories inside the Optical Crystallography and inside the Photoelasticity, that lead to the Diffused Light Polariscope concepts, precursor of the laser Photoelasticity, that involves the conoscopic technique. The development of a laser Conoscopy, has overcome the limitations about the sensitivity and the spatial resolution of the classical diffuse light polariscope technique. The method gives the possibility to control the conic probe volume confining the light in a precise part of the crystal volume with known dimensions. Considering that the fringe pattern is due uniquely by the probe volume, reducing its volume the sensitivity and the spatial resolution are enhanced. The only limitations in the technique are dictated by the measurement environment, in fact the condition of the samples surfaces and the quality of the optics highly affect the quality of the fringe images patterns acquired. These aspects can be processed and improved during image processing phase. In this work tools have been provided to improve these disturbing aspects, in order to reduce the measurement uncertainty. Once known the described benefits on the laser conoscopic technique,

used up until now to analyse the crystals along the optical axis direction, it was expanded its field of application in other two direction orthogonal to the optic axis. By observing the crystal in the crystallographic directions orthogonal to the optic axis, a different fringe pattern is produced respect to the previous one. A model has been therefore developed to understand that fringe pattern and correlate to the stress state of the probe volume. In parallel, a new image acquisition and processing system has been developed. The set of developed methods is completed by a new technique named Sphenoscopy, which provides reliable inspection of the crystal in a faster and simplified way whatever orientation of the crystallographic and optic axes. This technique is a modified Conoscopy, which makes use of a wedge-shaped probe volume instead of the conic one. This volume inspects a larger zone with respect to the pointwise Conoscopy and allows to inspect stress state along a line, rather than at a single point. The technique has been tested and compared with the Conoscopy; the results are less detailed than the conoscopic one but compatible and still reliable, suitable for a fast inspection. A new technique was then developed, using observations in collimated light in direction normal to the optic axis, with the different purpose of analysing the sample from a dimensional point of view, with the aim of determining any non-coplanarity between the surfaces, which is an aspect that may disturb the previous measurement techniques. This technique has been treated by comparing it with the mathematical model presented and used for the Conoscopy, with the direct geometrical measurements of the surfaces and with the theories of the optical crystallography. All these activities are based on a strong theoretical approach that has led to a development as well to the modelling of the phenomena. With the developed techniques it was possible to build an analysis system with the aim of produce maps of the stress state, coherently coming from different techniques, for the analysis of the Crytur pre-series P_bWO_2 samples. Using the same techniques, was possible to evaluate the piezo optic parameters and the photoelastic constant in tetragonal P_bWO_2, in order to expand the theoretical knowledge of this material. Concluding, comparative measures using Photoelasticity and the Decay Time measurement were carried out, in order to find a possible correlation between the crystal lattice orientation and the timing properties of the relative crystal.

6.1 Future possible improvements

Regarding the conoscopic technique, will be useful to make the system able to perform all the measurement and image processing autonomously in each studied direction of observation. Moreover, using the mathematical simulations created for the latest analysis in Conoscopy, could

be studied more deepen the fringes behaviour in order to make possible the conoscopic measurements in each direction of observation. Regarding the practical aspects, different shape and dimensions (bulk, pixels, prismatic and cylindrical fibres also with sub millimetric section) of the crystalline birefringent materials are requested by the applications; suitable techniques for the purpose of the characterization are under development, in order to overtake the limitation of having to observe flat surfaces of the sample. For example, the photoelastic index matching techniques and scattered light methods are promising in order to accomplish to these needs.

References

[1] P. P. Natali, L. Montalto, F. Davi, N. Paone, D. Rinaldi, and L. Scalise, "Optimization of the photoelastic fringe pattern processing for the stress evaluation in scintillating anisotropic media," in *I2MTC 2017 - 2017 IEEE International Instrumentation and Measurement Technology Conference, Proceedings*, 2017.

[2] P. P. Natali, L. Montalto, D. Rinaldi, F. Davi, N. Paone, and L. Scalise, "Noninvasive Inspection of Anisotropic Crystals: Innovative Photoelasticity-Based Methods," *IEEE Trans. Nucl. Sci.*, vol. 65, no. 8, 2018.

[3] P. P. Natali *et al.*, "Theoretical and experimental evaluation of piezo-optic parameters and photoelastic constant in tetragonal PWO," *Appl. Opt.*, vol. 57, no. 4, p. 730, 2018.

[4] L. Montalto, P. P. Natali, F. Daví, P. Mengucci., N. Paone, and D. Rinaldi, "Characterization of a defective PbWO 4 crystal cut along the a-c crystallographic plane: structural assessment and a novel photoelastic stress analysis," *J. Instrum.*, vol. 12, no. 12, p. P12035, 2017.

[5] P. Lecoq, A. Annenkov, A. Gektin, M. Korzhik, and C. Pedrini, *Inorganic scintillators for detector systems: physical principles and crystal engineering (Particle acceleration and detection*. Springer, 2006.

[6] D. Rinaldi, M. Lebeau, N. Paone, L. Scalise, and P. Pietroni, "Quality Control and Characterization of Scintillating Crystals for High Energy Physics and Medical Applications."

[7] Z. I. Kolar and W. den Hollander, "2003: A centennial of spinthariscope and scintillation counting," *Appl. Radiat. Isot.*, vol. 61, no. 2–3, pp. 261–266, Aug. 2004.

[8] CERN/LHCC, “CMS -The Electromagnetic Calorimeter Project, Technical Design Report,” 1997.

[9] LHC Experiments Committee, *CMS, the Compact Muon Solenoid: technical proposal*. Geneva, CERN, 1994.

[10] P. PANDA Collaboration *et al.*, “Technical Design Report for the: PANDA Straw Tube Tracker,” May 2012.

[11] D. Hooper, F. Petriello, K. M. Zurek, and M. Kamionkowski, “New DAMA dark-matter window and energetic-neutrino searches,” *Phys. Rev. D*, vol. 79, no. 1, p. 015010, Jan. 2009.

[12] S. Akkoyun *et al.*, “AGATA—Advanced GAmma Tracking Array,” *Nucl. Instruments Methods Phys. Res. Sect. A Accel. Spectrometers, Detect. Assoc. Equip.*, vol. 668, pp. 26–58, Mar. 2012.

[13] A. DE ANGELIS, “GLAST, THE GAMMA-RAY LARGE AREA SPACE TELESCOPE,” in *New Worlds in Astroparticle Physics*, 2001, pp. 140–145.

[14] Z. Nahas, M. S. George, J. P. Lorberbaum, S. C. Risch, and K. M. Spicer, “SPECT and PET in Neuropsychiatry.”

[15] D. L. Bailey, J. S. Karp, and S. Surti, “Physics and Instrumentation in PET,” in *Positron Emission Tomography*, London: Springer-Verlag, 2005, pp. 13–39.

[16] D. L. Bailey, D. W. Townsend, P. E. Valk, and M. N. Maisey, Eds., *Positron Emission Tomography*. London: Springer-Verlag, 2005.

[17] R. J. Jaszczak, R. E. Coleman, and C. Bin Lim, “SPECT: Single Photon Emission Computed Tomography,” *IEEE Trans. Nucl. Sci.*, vol. 27, no. 3, pp. 1137–1153, 1980.

[18] J. Glodo *et al.*, “New Developments in Scintillators for Security Applications,” *Phys. Procedia*, vol. 90, pp. 285–290, Jan. 2017.

[19] P. Lecoq, A. Gektin, and M. Korzhik, *Inorganic scintillators for detector systems : physical principles and crystal engineering*. Springer, 2017.

[20] W. Bradsley and D. T. J. Hurle, *Crystal growth: a tutorial approach*. North-Holland Publishing

Company, 1979.

[21] C. L. Melcher, J. S. Schweitzer, C. A. Peterson, R. A. Manente, H. Suzuki, and S.-D. Research, “Crystal growth and scintillation properties of the rare earth oxyoorthosilicates,” *CT06877-41018,USA*.

[22] M. Born and E. Wolf, *Principles Of Optics, 6th edition*. New York: Pergamon press, 1975.

[23] E.E. Walhstrom, *Optical Crystallography*. New York: Wiley, 1960.

[24] R. Caciuffo and S. Melone, *Fisica generale II volume, ottica ed elettromagnetismo*. Masson, 1996.

[25] H. Aben and C. Guillemet, *Photoelasticity of Glass*. Springer Berlin Heidelberg, 1993.

[26] A. Ciriaco *et al.*, “PWO photo-elastic parameter calibration by laser-based polariscope,” *Nucl. Instruments Methods Phys. Res. Sect. A Accel. Spectrometers, Detect. Assoc. Equip.*, vol. 570, no. 1, pp. 55–60, 2007.

[27] D. Rinaldi, P. Pietroni, and F. Davì, “Isochromate fringes simulation by Cassini-like curves for photoelastic analysis of birefringent crystals,” *Nucl. Instruments Methods Phys. Res. Sect. A Accel. Spectrometers, Detect. Assoc. Equip.*, vol. 603, no. 3, pp. 294–300, 2009.

[28] L. Montalto, N. Paone, D. Rinaldi, and L. Scalise, “Inspection of birefringent media by photoelasticity: from diffuse light polariscope to laser conoscopic technique,” *Opt. Eng.*, vol. 54, no. 8, p. 081210, 2015.

[29] L. Montalto, D. Rinaldi, L. Scalise, N. Paone, and F. Davì, “From Conoscopy to Sphenoscopy: New Experimental Methods in Crystals Inspections,” in *18th Italian National Conference on Photonic Technologies (Fotonica 2016)*, 2016, p. 40 (5 .)-40 (5 .).

[30] L. Montalto, D. Rinaldi, L. Scalise, N. Paone, and F. Davì, “Photoelastic sphenoscopic analysis of crystals,” *Rev. Sci. Instrum.*, vol. 87, no. 1, 2016.

[31] S. Khorasani and B. Rashidian, “Energy approach to the propagation of light waves in anisotropic crystals, SPIE Conference on Design, Fabrication and Characterization of Photonic

Davices," *SPIE*, vol. 3896, 1999.

[32] N. V. Perelomova and M. M. Tagieva, *Problems in crystal physics with solutions, Edited by M.P. Shaskol'skaya translated from the Russian by V.I. Kisin*. Moscow: Mir Publisher.

[33] Wood E. A., *Crystal And Light*. New Jersey: Van Nostrand Company, 1964.

[34] A. I. Kolesnikov *et al.*, "Isochrome Shapes in the Conoscopic Patterns of Uniaxial Crystals," *Ferroelectrics*, vol. 441, no. 1, pp. 75–83, Jan. 2012.

[35] F. Daví, "On the Bertin surfaces of photoelastic crystals," *J. Opt. Soc. Am. A*, vol. 32, no. 12, p. 2323, Dec. 2015.

[36] F. Daví and D. Rinaldi, "Mechanical and Optical Properties of Anisotropic Single-Crystal Prisms," *J. Elast.*, vol. 120, no. 2, pp. 197–224, Aug. 2015.

[37] H. Aben, J. Anton, and A. Errapart, "Modern Photoelasticity for Residual Stress Measurement in Glass," *Strain*, vol. 44, no. 1, pp. 40–48, Jan. 2008.

[38] K. Ramesh and G. Lewis, *Digital photoelasticity: advanced techniques and applications*. American Society of Mechanical Engineers, 2002.

[39] J. E. Shigley, C. R. Mischke, and R. G. Budynas, *Mechanical Engineering Design*. New York: McGraw-Hill, 2004.

[40] A. S. Jayatilaka, *Fracture of Engineering Brittle Materials*. Applied Science Publishers, 1979.

[41] L. Montalto, N. Paone, L. Scalise, and D. Rinaldi, "A photoelastic measurement system for residual stress analysis in scintillating crystals by conoscopic imaging," *Rev. Sci. Instrum.*, vol. 86, no. 6, 2015.

[42] N. Cocozzella, M. Lebeau, G. Majni, N. Paone, and D. Rinaldi, "Quality inspection of anisotropic scintillating lead tungstate (PbWO4) crystals through measurement of interferometric fringe pattern parameters," *Nucl. Instruments Methods Phys. Res. Sect. A Accel. Spectrometers, Detect. Assoc. Equip.*, vol. 469, no. 3, pp. 331–339, Aug. 2001.

[43] Vision LabVIEW Machine, *Image Processing Course Manual*. Course Software version, 2004.

[44] National Instruments, “Imaq Vision Concepts Manual.” 2014.

[45] G. Casella and R. L. Berger, *Statistical inference*. Duxbury/Thomson Learning, 2002.

[46] Y. I. Sirotin and M. P. Shaskolskaya, *Fundamentals of Crystal Physics*. Moscow, 1982.

[47] J. F. Nye, *Physical properties of crystals*. Clarendon Press, 1985.

[48] L. Montalto, “Inspection and characterization of birefringent materials : development of methods and systems for scintillating anisotropic crystals,” Università Politecnica delle Marche, 2017.

[49] B. Spain, *Analytical conics*. Dover Publications, 2007.

[50] Augusto Ajovalasit, *Analisi sperimentale delle tensioni con la FOTOMECCANICA Fotoelasticità, moiré, olografia speckle, correlazione immagini Seconda edizione*. .

[51] M. M. Frocht, *Photoelasticity Wiley*. New York, 1941.

[52] J. W. Dally and W. F. Riley, *Experimental Stress Analysis, 2nd edition*. Singapore: McGraw-Hill Book Company, 1987.

[53] D. Rinaldi, F. Daví, and L. Montalto, “On the photoelastic constants and the Brewster law for stressed tetragonal crystals,” *Math. Methods Appl. Sci.*, vol. 41, no. 8, pp. 3103–3116, 2018.

[54] S. Lenci, *Lezioni di meccanica strutturale*. Pitagora Editrice, 2009.

[55] E. O. Doebelin, *Measurement systems : application and design*. McGraw-Hill, 2004.

[56] A. Ciriaco, “Piezo-optical characterization of uniaxial crystals by means of Laser based photoelasticity: application to PWO scintillators,” Università Politecnica delle Marche, 2008.

[57] D. Ding *et al.*, “Effects of anisotropy on structural and optical characteristics of LYSO:Ce crystal,” *Phys. status solidi*, vol. 251, no. 6, pp. 1202–1211, Jun. 2014.

[58] S. Gundacker, E. Auffray, K. Pauwels, and P. Lecoq, “Measurement of intrinsic rise times for various L(Y)SO and LuAG scintillators with a general study of prompt photons to achieve 10 ps in TOF-PET,” *Phys. Med. Biol.*, vol. 61, no. 7, pp. 2802–2837, Apr. 2016.

[59] J. Saeterstøl, “Characterization of Scintillation Crystals for Positron Emission Tomography,” 2010.

[60] P. Buzhan *et al.*, “Silicon photomultiplier and its possible applications,” *Nucl. Instruments Methods Phys. Res. Sect. A Accel. Spectrometers, Detect. Assoc. Equip.*, vol. 504, no. 1–3, pp. 48–52, May 2003.

[61] L. S. Weinstock, “Regulierung der Versorgungsspannung von Silizium-Photomultipliern anhand ihrer charakteristischen Spektren,” 2012.

[62] S. Ritt, R. Dinapoli, and U. Hartmann, “Application of the DRS chip for fast waveform digitizing,” *Nucl. Instruments Methods Phys. Res. Sect. A Accel. Spectrometers, Detect. Assoc. Equip.*, vol. 623, no. 1, pp. 486–488, Nov. 2010.

Acknowledgments

As a conclusion I would like to thank the people who, in various ways, have made my journey possible. First of all, thanks to Prof. Nicola Paone and Luigi Montalto, who firstly introduced me and made me passionate about this discipline. Thanks to Prof. Fabrizio Davì and Prof. Daniele Rinaldi, for their guidance and their advices, about academic arguments, and Pub arguments.

Thanks to Prof. Ziemons who welcomed me at his University and gave me a continuous support.

This work was done within the Crystal Clear Collaboration and was part of the COST ACTION FAST TD1401. This aspect gave me the opportunity to meet people who have expanded my knowledge and improved my professional and personal experience. In particular, I thank Dr. Etiennette Auffray for her attention and the visibility granted to me.

Ringraziamenti

Come conclusione vorrei ringraziare coloro che, in diversi modi, hanno reso possibile questo mio percorso. In primis ringrazio il Prof. Nicola Paone e Luigi Montalto, i quali per primi mi hanno introdotto e fatto appassionare a questa disciplina. Ringrazio poi Prof. Fabrizio Davì e Prof. Daniele Rinaldi, per la loro guida ed i loro consigli, sia accademici che leggeri al Pub.

Grazie al Prof. Ziemons che mi ha accolto nella sua Università e mi ha fornito un supporto continuo.

Questo lavoro è stato svolto all'interno della Crystal Clear Collaboration ed è stato parte della COST ACTION FAST TD1401. Questo aspetto mi ha dato l'opportunità di incontrare persone che hanno ampliato le mie conoscenze e migliorato la mia esperienza professionale e personale. In particolare, ringrazio la Dr. Etiennette Auffray per la sua attenzione e la visibilità accordatami.

Ringrazio i miei genitori, che mi hanno sorretto nei momenti più difficili di questo lungo percorso di studio, durante il quale sono sempre stati in grado di comprendermi, e questa di per sé è opera piuttosto ardua se non impossibile.

Ringrazio Arianna, conosciuta in un periodo molto brutto della mia vita, che mi ha preso per mano e mi ha fatto riprovare il piacere di essere me stesso.

Un sincero grazie ai miei amici fidati ed a tutti quelli che, anche per poco, hanno condiviso con me una risata.

In particolare, ringrazio Alessandro, mio cugino ed amico fidato, la persona migliore con cui fare campeggi illegali all'avventura; Andrea Piantoni, semplicemente la persona migliore con cui condividere una birra dopo una lunga giornata; Laura, la persona migliore con cui condividere un buon bicchiere di vino.

Grazie a Luigi Colombo, la persona migliore con cui condividere uno Spritz mentre si maledice l'Università.

Ringrazio poi Andrea Rocchi, con lui ho fatto l'asilo, le scuole medie, il Liceo e l'Università. Siamo passati assieme dal pongo alle equazioni differenziali, fino ad arrivare al dottorato ed infine ad essere colleghi. Come non bastasse siamo stati coinquilini per più di dieci anni, passando ogni tipo di serata immaginabile assieme. In poche parole, ho visto più spesso la sua faccia che quella di mia madre, quante altre ce ne toccheranno ancora assieme?

Ringrazio inoltre Roberto, quando penso alla parola amico non mi puoi che venire in mente te. Con lui ringrazio anche Sara e Sole, l'unica femminuccia che mi sorride sempre e senza lo scopo di chiedermi qualcosa.

Ringrazio poi Beatrice, fidata consulente fitness e culinaria, spalla ideale agli all you can eat, dove mi ha visto fare seriamente schifo senza mai giudicarmi.

Ringrazio il Direttore, che mi ha sapientemente guidato e tuttora mi segue per i sentieri del treme.

Ringrazio infine Kali, so che non lo leggerai mai, ma dal tuo bar scrauso sono partite le serate più memorabili, di quelle che esci di casa solo per un amaro in tranquillità, e l'unica cosa di cui ti ricordi la mattina dopo è l'insegna 'Bar Ancona'.